Medical Applications for Particle Physics

Hin Tung Lau

Department of Physics
Imperial College London

A thesis submitted to Imperial College London
for the degree of Doctor of Philosophy

February 2022

Abstract

The technologies developed for particle physics experiments have found numerous medical applications, particularly in the field of radiotherapy. Simulation results and analysis for several of these medical applications will be presented which include: commissioning of a carbon ion beam at MedAustron, design and development of LhARA, preliminary design and work on a new detector called the SmartPhantom. Simulations played a key role to the carbon commissioning effort, and paved the way for MedAustron to treat their first patient with carbon ions during the summer of 2019. Beam line simulations also played a critical role for a proposed state of the art facility, LhARA. These simulations were used to characterise the beam that a laser source delivers, improving upon previous analysis and supporting ongoing developments for LhARA. Finally, work has gone into the design of an instrumented water phantom incorporating scintillating fibres. Simulation work has shown that placing thin scintillating fibres at several locations in a water phantom upstream of a cell culture sample could allow one to reconstruct a Bragg peak. If fully realised, the detector could serve as an online monitor capable of monitoring the dose for each shot. This detector would be useful to evaluate the reproducibility of the beam LhARA delivers, and could also find use in radiobiological experiments.

Declaration

I hereby declare that the material presented in this thesis is my own work unless otherwise stated or referenced.

Hin Tung Lau

February 2022

Copyright

Acknowledgements

The work presented in this thesis would not have been possible without the excellent support and supervision of my supervisor Professor Kenneth Long. Despite your busy schedule you have always been ready to lend an ear to answer any questions or concerns I had. Furthermore, your guidance has been a constant source of inspiration and motivation over the course of my PhD. I am incredibly grateful to have had the opportunity to work with you. In addition, I am also grateful to have worked with the Imperial Accelerator group: Jaroslaw, Jürgen, Ajit, Titus, and Paul. The expertise the group provided was invaluable, always providing me with useful inputs and suggestions.

I also want to thank the beam commissioning group at MedAustron particularly: Mauro, Ivan, Alex, Greta, Laurids, and Andrea. Despite my inexperience, everyone welcomed me and helped to teach and guide me to become a useful temporary member of the team and allowed me to contribute to the carbon commissioning effort. Special thanks also goes to William Shields and the other developers for their support and development of BDSIM, which has played a key role throughout my PhD.

The LhARA Consortium has also been an invaluable source of support. In particular, I would like to thank Ollie, George, Bob, Colin, Elisabetta, and Jason who provided valuable insight and expertise into the laser source simulations.

In addition, I want to thank everyone who helped with the design of the SmartPhantom. Particularly, Liam, Johan, Geoff, Dan, Colin, Cyril, and Oliver.

Finally, and most importantly, I want to thank my parents and brother. Without your continued support I would never have been able to reach where I am today. This thesis is dedicated to you all.

Contents

List of Tables

List of Figures

Chapter 1

Introduction

Cancer ranks as one of the leading causes of death globally, estimated to account for close to 10 million deaths and 19 million new cases in 2020 alone [1]. The burden of cancer is expected to grow due to an ageing population as well as other socio-economic factors [2, 3], with an estimated increase to 28 million new cases in the year 2040 [4]. A variety of cancer treatments are currently available including: surgery, chemotherapy, radiotherapy, and immunotherapy. Novel treatments are also being developed [5, 6]. This thesis will focus on aspects of radiotherapy where particle physics plays a prominent role.

1.1 Radiotherapy Context

Radiotherapy uses radiation to target and kill cancer cells and approximately 50% of cancer patients receive it at some point in their treatment [7]. Ever since the first cancer treatment with radiation therapy in 1898 [8], radiotherapy has developed in tandem with technological advancements. Computed Tomography (CT) scans allow for a 3D reconstruction of structures inside the body. Intensity modulated radiation therapy (IMRT) uses these scan images to tailor the treatment to the tumour. Image-guided radiotherapy (IGRT) corrects for organ motion based on imaging taken before each session.

Another important development is the use of beams of protons and other ions for radiotherapy (hadron therapy), first proposed in 1946 by Wilson [9]. Conventional treatments irradiate with photons, which are sparsely ionising radiations. In contrast, due to the Bragg peak, charged particles are capable of delivering higher energies to a tumour site, whilst sparing the surrounding normal tissue.

In recent years there has been a growing interest in FLASH radiotherapy ($> 40\,\mathrm{Gy/s}$) [10] which

may improve normal tissue sparing and bring treatment times down to a few milliseconds. This phenomenon was first noted by Dewey and Boag in 1959 [11] from experiments with bacteria. When bacteria were irradiated with a normal dose of 1000 rads/min ($\approx$ 0.2 Gy/s) in a nitrogen-oxygen environment, the bacteria was found to be more radiosensitive compared to the same irradiation in a pure nitrogen environment. But when a much higher instantaneous dose rate of over 10 kilorads/2 µs ($\approx 5 \times 10^7$ Gy/s) was delivered, there was an observed decrease in the radiosensitivity of the bacteria in the nitrogen-oxygen environment. These results showed that a high dose rate could be beneficial for tissue sparing and was supported by other experiments for mammalian cells [12,13]. In 2014, Favaudon applied FLASH radiotherapy to treat lung tumours in mice, where a reduction in toxicity affecting healthy lung tissue was seen [14]. This sparked a renewed interest to understand the underlying biological mechanisms behind FLASH and applying it to clinical treatment.

Another development that may improve normal tissue sparing is minibeam radiotherapy [15] using submillimetre beams with photons. Proton minibeam radiotherapy (pMBRT) could further improve normal tissue sparing [16] by taking advantage of the Bragg peak and angular straggling which widens the beam with depth. Experiments with rats have shown that a high dose delivered with pMBRT leads to a decrease in neurotoxicity compared to conventional proton therapy [17].

1.2 Accelerator Technologies Context

Technological advances resulting from multidisciplinary research play a key role in developing radiotherapy. These advances include new imaging methodologies, more powerful computers for treatment planning and simulations, sophisticated detectors for measuring dose, and most importantly the accelerators that deliver the beam to a patient.

Crookes tube paved the way for the discovery of electrons and X-rays. It consists of a vacuum sealed glass container where a voltage could be applied between the cathode and anode to generate electrons by ionisation. If the voltage applied is high enough, electrons are accelerated to high velocities and generate X-rays upon hitting the anode or walls of the tube which can pass through the glass. It was these rays that Röentgen observed in 1895 when he noticed a nearby fluorescent screen glowing [18]. With this discovery, Crookes tubes became a common source of X-rays which were used in imaging and early radiotherapy where energies of about about 20 keV could be produced [19]. However, there was a need for a better source of high energy X-rays.

Driven by an interest to generate high energy particles for fundamental physics, Hansen helped develop a linear accelerator (linac) for electrons in the 1940s [20]. The electron linac allowed for much higher X-ray energies to be produced by accelerating electrons into a metal target. Kaplan [21] recognised that a particle accelerator could provide reliable, focused, and high energy X-rays for

radiotherapy. Together with Ginzton who worked with Hansen, they developed a medical linac and treated the first patient, a young boy with retinoblastoma in 1956 [21]. Such a treatment would not have been possible without the invention of the linac. It is worth mentioning that developments in the UK occurred in parallel, where Fry independently developed an electron linac [22]. In 1952 a clinical linac using this design was installed at the Hammersmith Hospital in London and soon began treating patients [23]. The versatility of the linac led to it quickly becoming the mainstay of modern radiotherapy.

Another important development in particle physics that found applications in radiotherapy was the cyclotron. Driven by a need to generate large amounts of highly energetic particles, Lawrence developed the cyclotron in 1932 [24]. Cyclotrons save space by accelerating particles along a spiral. In the medical field, it quickly found use as a proton and ion source for the treatment of patients. However, cyclotrons are limited in the energies that can be reached. In order to accelerate heavy ions, synchrotrons are used where particles are instead accelerated in a closed loop. But compared to the clinical linacs for conventional radiotherapy, cyclotrons and synchrotrons take up a larger footprint and are thus more costly. There is ongoing design work to improve the performance and lower the costs of these accelerators. In addition, there is an interest in developing novel techniques for acceleration.

A novel technique that has gained recent popularity is laser-driven acceleration, capable of achieving high acceleration gradients over short distances. There are a variety of laser-driven schemes that can be used, with target normal sheath acceleration (TNSA) the most studied scheme [25–27]. In TNSA, a laser impinging on a thin foil generates ionises the foil generating energetic electrons on the front. These electrons propagate through the foil and accumulate on the rear, creating a strong electric field and accelerating ions normal to the target. The energies that can be achieved with this method depend on the laser system and the target material and thickness. A survey of maximum energies in TNSA experiments was performed by Borghesi [28] and showed that proton energies at several tens of MeV can be measured with the highest energies achieved on laser systems that can deliver high energies in a long pulse ($> 300\,\mathrm{fs}$). With the TNSA mechanism, Wagner *et al.* measured proton beams with energies up to 85 MeV using the PHELIX laser at GSI Helmholtzzentrum für Schwerionenforschung GmbH in 2016 [29]. There are also other acceleration mechanisms like radiation pressure acceleration (RPA) that can achieve higher energies [30]. Higginson *et al.* [31] achieved proton energies exceeding 94 MeV using a hybrid acceleration scheme that combines TNSA and RPA mechanisms at Rutherford Appleton Laboratory in 2018. But there are challenges which need to be addressed in order to apply these acceleration schemes into a clinical setting which include beam reproducibility, cut-off energy, beam divergence, and beam emittance.

It is clear that the development of treatment methodologies for cancer requires a multidisciplinary approach. In particular, the technologies developed for particle physics research have found numerous applications in radiotherapy and will continue to play a key role for future developments.

1.3 Summary of Thesis

The focus of this thesis is on a variety of simulation work for MedAustron [32], one of the cutting-edge centres for cancer therapy, as well as for the Laser-hybrid Accelerator for Radiobiological Applications (LhARA) [33, 34], a proposed facility dedicated to research which aims to combine laser-driven acceleration and post acceleration with a fixed field alternating gradient accelerator (FFA). Some of the work for the design of a scintillating fibre detector, the SmartPhantom will also be presented.

Chapter 2 presents a background on the theory of accelerators and beam dynamics. Chapter 3 continues with an overview of the physics of particle therapy. Chapter 4 then provides an overview of the laser-driven acceleration with a focus on the TNSA interaction. Chapter 5 looks at the conventional accelerators used for hadron therapy and an outlook of other novel methods. A description of the MedAustron facility will also be given. Chapter 6 presents beam line optimisation work for the carbon ion commissioning effort at MedAustron. A rematch procedure was developed which could provide an approximate beam with relatively good agreement to measurements. A risk assessment was also carried out to ensure the safe delivery of carbon ions. Chapter 7 goes into detail of various design and simulations of LhARA. Simulations of the TNSA interaction and the resulting beam which was tracked through the Stage 1 beam line. Design work for Stage 2 is then outlined and supported by tracking simulations. Chapter 8 presents the design and work on an instrumented phantom, the SmartPhantom. Chapter 9 concludes by summarising the work presented in this thesis, with a discussion of future avenues of research.

Chapter 2

Accelerator Dynamics

This chapter gives an outline of general accelerator dynamic principles. It begins with the fundamental principles, then introduces some common accelerator magnets. This will be followed by the equations of motion that govern individual particle motion and extended to describe the entire beam which can be parametrised by the Twiss parameters. This chapter concludes with a discussion of space-charge effects.

Twiss parameters are useful quantities to define a beam. If the initial Twiss parameters of a beam are known, they can be calculated at any other point in the beam line. The evolution of these parameters form an important part of beam line simulation programs like MAD-X [35], where matrix elements can be calculated for a beam line and matching algorithms used to optimise beam sizes. Twiss parameters can also be used to approximate complex beams, a useful property as will be discussed in chapter 6 and chapter 7.

2.1 Frenet–Serret Coordinates

In a beam line, magnets and other elements are aligned along the ideal path a particle will take. However, particles deviate from this design orbit which requires correction. Since the design orbit is typically well defined, the deviation of a particle from the ideal path is often of greater interest.

It is convenient to define a coordinate system that moves along the ideal path to simplify the mathematics. A curvilinear coordinate system known as the Frenet-Serret reference system is commonly used [36] and is visualised in fig. 2.1. In this system, the motion along the design orbit is represented by s, while the three unit vectors defined as $(\hat{\mathbf{x}}, \hat{\mathbf{y}}, \hat{\mathbf{z}})$ form an orthogonal coordinate system. The direction given by $\hat{\mathbf{x}}$ is defined to be perpendicular to the trajectory and $\hat{\mathbf{z}}$ parallel to the trajectory. Together these define the horizontal plane. The plane orthogonal to it is the vertical plane defined

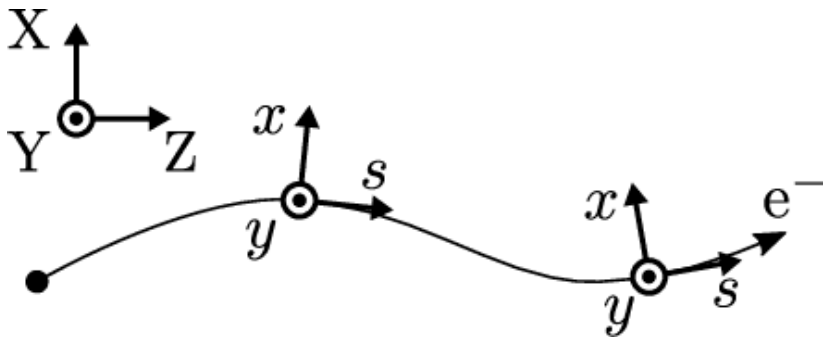

Figure 2.1: The Frenet-Serret curvilinear coordinate system for the trajectory of a reference particle [37].

by $\hat{\mathbf{y}}$ and $\hat{\mathbf{z}}$. The coordinates (x, y) describe the deviation of a particle from the reference trajectory.

2.2 Lorentz Force

A particle carrying a charge e, experiences the Lorentz force expressed by

$$\mathbf{F} = e\mathbf{E} + e\left(\mathbf{v} \times \mathbf{B}\right), \tag{2.1}$$

where $\mathbf{E}$ and $\mathbf{B}$ are the electric and magnetic field vectors respectively, and $\mathbf{v}$ is the velocity vector of the particle.

The Lorentz force both guides and focuses particles along an ideal path. It is typically easier to base beam line elements on magnetic fields to achieve a desired force. However, for low energy particles with velocities much less than the speed of light, electric fields can become more practical [36].

2.2.1 Beam Bending

In order to bend and deflect particles, a magnetic field is required. From the Lorentz force, the bending radius can be expressed by:

$$\frac{1}{\rho} = \left|\frac{e}{p}B\right| = \left|\frac{ec}{\beta E}B\right|, \tag{2.2}$$

where ρ is the radius of curvature, p is the momentum of the particle, β is the ratio of the velocity to the speed of light c, and E is the energy. Another useful quantity is the beam rigidity, $B\rho$, which describes the difficulty of bending a beam and can also be used to normalise the magnetic strength:

$$|B\rho| = \frac{p}{e}. \tag{2.3}$$

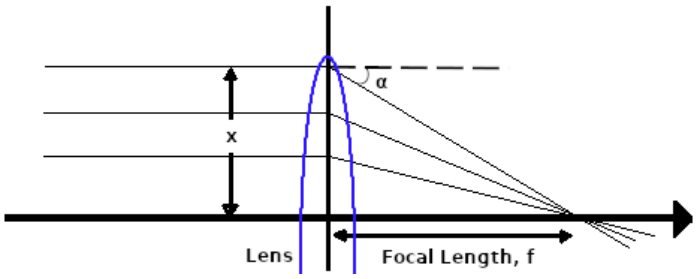

Figure 2.2: Optical analogy of focusing a ray of light through a lens.

2.2.2 Beam Focusing

As beams naturally diverge, focusing elements are necessary to control their evolution. A typical analogy to consider is the focusing effect of a light ray passing through a glass lens. The light rays are focused with a focal length, f, and a deflection angle, α, depending on the distance from the center of the lens x as seen in fig. 2.2. The deflection angle is then defined as

$$\alpha = -\arctan\left(\frac{x}{f}\right) \approx -\frac{x}{f}, \tag{2.4}$$

where the paraxial approximation can be made when x is small. Extending this optical analogy to charged particle beams for a path s, and a magnetic field, B, gives a deflection angle:

$$\alpha = -\frac{\ell}{\rho} = -\frac{e}{p}\int B\,\mathrm{d}s. \tag{2.5}$$

If the magnetic field strength does not change significantly, the integral can be approximated by the product $B\ell$, where ℓ is the path length of the particle in the magnetic field [36]. By comparing to the deflection angle defined in eq. 2.4 it can be seen that a higher magnetic field is needed for particles far from the central axis to achieve the same focusing.

2.3 Common Accelerator Magnets

Magnets are key components of beam lines to deflect and focus charged particles. There are combined function magnets that can both deflect and focus, as well as separated function magnets that primarily deflect or focus. Separated function magnets tend to be better suited for higher energy particles because these magnets often saturate at higher fields [38], providing more flexibility for optimisations. An overview of common magnetic elements will be presented, but will neglect fringe field effects which can lead to a mismatch of beam parameters. An analytical expression that includes fringe fields is discussed by Muratori *et al.* [39].

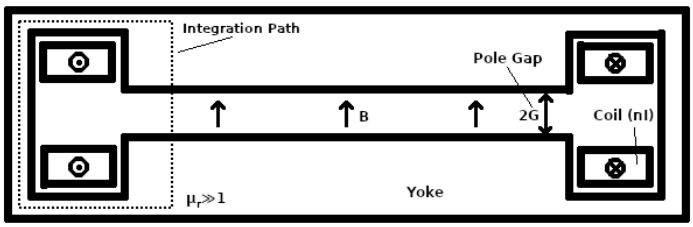

Figure 2.3: Schematic cross-section diagram of a dipole magnet. The cross and point denote the direction of the current in the coil. Figure adapted from Wiedemann [36].

2.3.1 Dipole Magnet

A dipole field is generated by current-carrying wires surrounded by a ferromagnetic yoke with a high permeability μ_r. Integrating Ampere's law along the path in fig. 2.3 gives

$$(2G)B_\perp + \oint \frac{\mathbf{B}}{\mu_r}\,\mathrm{d}s = \mu_0(2nI), \tag{2.6}$$

where $B_\perp$ is the magnetic field normal to the magnet poles with a gap of $2G$ and a total current of $2nI$ for n coils, and μ_0 is the vacuum permeability. For a large permeability, the integral term becomes negligible which gives the current in each coil, I_{coil}, as:

$$I_{\mathrm{coil}}[\mathrm{A}] = \frac{1}{n\mu_0} B_\perp[\mathrm{T}]G[\mathrm{m}]. \tag{2.7}$$

This yields a magnetic field of

$$B_\perp = \frac{\mu_0 n I_{\mathrm{coil}}}{G}. \tag{2.8}$$

From the magnetic field, the radius of curvature of a particle travelling through a dipole magnet is given by eq. 2.2,

$$\frac{1}{\rho}[\mathrm{m}^{-1}] = \frac{eB_\perp}{p} \approx 0.3\frac{B_\perp[\mathrm{T}]}{p[\mathrm{GeV/c}]}. \tag{2.9}$$

2.3.2 Quadrupole Magnets

Quadrupole magnets are used to focus particles. These magnets consist of coils wrapped around four pole tips with alternating north and south poles as represented in fig. 2.4. From the polarity shown, the magnet will focus a positively charged particle in the x-axis and defocus in the y-axis.

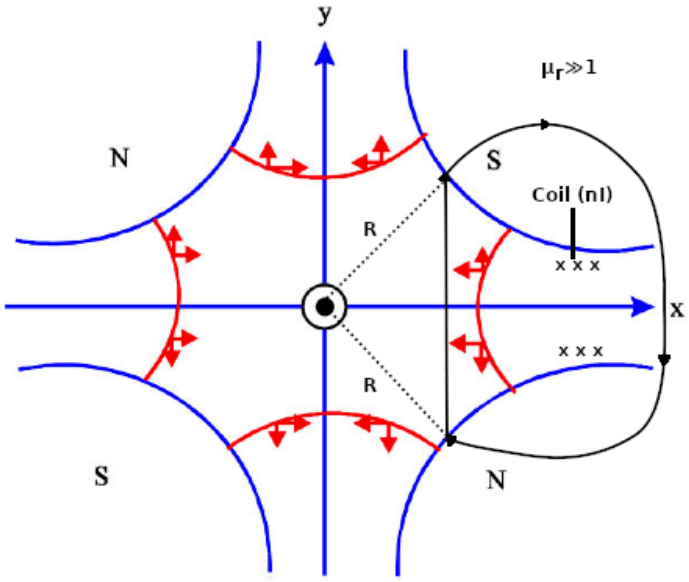

Figure 2.4: Schematic diagram of a quadrupole magnet looking down the centre. The red arrows show the direction of the force for a positively charged particle coming out of the page. Black loop represents the integration path. Blue hyperbolic contour designate the poles. Adapted from Kain [40].

From the potential given by [36]:

$$V = -gxy, \tag{2.10}$$

where the equipotential lines are lines from the hyperbolas of $xy = \text{const.}$ and g is a field gradient, the magnetic fields can be determined by

$$B_x = -\frac{\partial V}{\partial x} = gy, \tag{2.11}$$

$$B_y = -\frac{\partial V}{\partial y} = gx. \tag{2.12}$$

It can be noted that the strength of the magnetic field varies in proportion to the distance from the central axis. To compute the quadrupole gradient, g, we take the path integral as given in fig. 2.4 and separate the field in the gap between poles and the iron of the magnet:

$$\begin{aligned}\oint \frac{\mathbf{B}}{\mu_0}\,\mathrm{d}r = 2nI &= \int_0^{\sqrt{2}R} \frac{\mathbf{B}_{\text{gap}}}{\mu_0}\,\mathrm{d}r_{\text{gap}} + \int \frac{\mathbf{B}_{\text{iron}}}{\mu_r}\,\mathrm{d}r_{\text{iron}}, \\ &= \frac{1}{\mu_0}\int_0^{\sqrt{2}R} (gx)\,\mathrm{d}y,\end{aligned} \tag{2.13}$$

where the second integral term is negligible under the assumption $\mu_r \gg 1$ and we substitute the

magnetic field component from eq. 2.12. Solving the integral and rearranging terms gives

$$\begin{aligned} 2nI =& \frac{1}{\mu_0}\left(\frac{1}{2}g\left(\sqrt{2}R\right)^2\right) \\ \Rightarrow g =& \frac{2\mu_0 nI}{R^2} \end{aligned} \tag{2.14}$$

The field gradient can be normalised to the particle momentum, giving the strength of a quadrupole by

$$k = \frac{eg}{p}, \tag{2.15}$$

and expressed in practical units by:

$$k[m^{-2}] \simeq 0.3\frac{g[\mathrm{T/m}]}{\beta E[GeV]}. \tag{2.16}$$

For a quadrupole with length, ℓ, and assuming that the magnet field strength does not change significantly, we get from eq. 2.5:

$$\alpha = -\frac{e}{p}B_y\ell = -\frac{eg}{p}x\ell = -kx\ell, \tag{2.17}$$

when related to eq. 2.4, this gives a focal length of

$$\frac{1}{f} = k\ell. \tag{2.18}$$

These results show that the focal length of a quadrupole increases with the energy of the beam. However, a single quadrupole alone can only focus in one plane, while defocusing in the other. But a system of quadrupole magnets in certain configurations can provide an overall focusing effect in both planes [36].

2.3.3 Solenoid Lens

A solenoid can act as a magnetic lens to focus charged particles. When a current is passed through the wire, a near uniform magnetic field is generated at the centre of the solenoid and falls outside the coil. An off-axis charged particle which enters the solenoid will experience periodic focusing. This results from a helical trajectory whilst traversing the solenoid with a radius of curvature smaller than

the initial displacement [41]. The focal length of a solenoid lens is given by [38]:

$$\frac{1}{f_{\text{sol}}} = \int \left(\frac{eB_s}{2p}\right)^2 \mathrm{d}s, \tag{2.19}$$

where B_s is the longitudinal component of the magnetic field. Since the focal length increases with the square of the total momentum p, solenoid lenses tend to be most effective for low momentum particles. A comparison of the performance of solenoids against doublet and triplet configurations of quadrupole magnets can be seen in Hofmann [42].

2.4 Equations of Motion

The reference trajectory travelled by an ideal particle is dictated by the geometry of the beam line, and specified in terms of the path length, s. Hill's equation [36, 38, 43] gives the motion governing the deviation from the reference trajectory.

2.4.1 Hill's Equation

Hill's equations of motion gives the motion for a beam where higher order terms are neglected. These neglected terms include: magnet errors, fringe fields, dispersion, and chromatic effects. Using the Frenet-Serret system (sec. 2.1), Hill's equation is expressed by:

$$x'' + K_x(s)x = 0, \qquad K_x(s) = k(s) + \frac{1}{\rho(s)^2}, \tag{2.20}$$

$$y'' + K_y(s)y = 0, \qquad K_y(s) = -k(s), \tag{2.21}$$

where $k(s)$ represents the focusing term. The $1/\rho(s)^2$ term describes the *weak focusing* from a bending magnet. This originates from the circular paths charged particles take when passing through a uniform magnetic field, this can lead to the orbits of two particles to cross. This term can be neglected at high energies compared to the *strong focusing* that results from a quadrupole. We can recast the equations as

$$u'' + K(s)u = 0, \tag{2.22}$$

where the variable, u, can refer to either the transverse x or y position. Hill's equation describes the motion of a particle acting like a spring with a restoring force that varies over the distance of the accelerator.

Every solution $u(s)$ to Hill's equation is a linear combination of two arbitrary solutions: $C(s)$

and $S(s)$, which will be defined later. In order for $C(s)$ and $S(s)$ to be linearly independent, the Wronskian, W has to satisfy:

$$W = \begin{vmatrix} C(s) & S(s) \\ C'(s) & S'(s) \end{vmatrix} \neq 0 \qquad \text{and} \qquad \frac{\mathrm{d}W}{\mathrm{d}s} = C(s)S''(s) - S(s)C''(s) = 0. \tag{2.23}$$

The value of the Wronskian is determined by the initial conditions. A fundamental set of solutions $C_0(s)$ and $S_0(s)$ that satisfy convenient initial conditions at position $s = s_0$:

$$C_0(s_0) = 1 \qquad C_0'(s_0) = 0 \qquad S_0(s_0) = 0 \qquad S_0'(s_0) = 1, \tag{2.24}$$

are referred to as *Cosinelike* and *Sinelike* [38, 43, 44]. The solution to Hill's equation with initial conditions u_0 and u_0' at s_0 can be expressed by,

$$u(s) = u_0 C_0(s) + u_0' S_0(s), \tag{2.25}$$

$$u'(s) = u_0 C_0'(s) + u_0' S_0'(s). \tag{2.26}$$

Rewriting this as

$$\begin{pmatrix} u(s) \\ u'(s) \end{pmatrix} = \underbrace{\begin{pmatrix} C_0(s) & S_0(s) \\ C_0'(s) & S_0'(s) \end{pmatrix}}_{M(s/s_0)} \begin{pmatrix} u_0 \\ u_0' \end{pmatrix}, \tag{2.27}$$

gives a transfer matrix $M(s/s_0)$ from s_0 to s. These equations hold for $K(s)$ whether or not it is periodic. We can also note that for another position s_1, a transfer matrix can be built with $C_1(s)$ and $S_1(s)$, which will satisfy

$$C_1(s_1) = 1 \qquad C_1'(s_1) = 0 \qquad S_1(s_1) = 0 \qquad S_1'(s_1) = 1. \tag{2.28}$$

2.4.2 Piecewise Constant Transport

To simplify the mathematics, the *piecewise constant approximation* can be used [38, 43]. In this approximation, a single element of the accelerator is represented with a constant K, which allows $C(s)$ and $S(s)$ to be written as [38],

$$K > 0: \qquad C(s) = \cos\left(\sqrt{K}s\right), \quad S(s) = \frac{1}{\sqrt{K}} \sin\left(\sqrt{K}s\right), \tag{2.29}$$

$$K < 0: \qquad C(s) = \cosh\left(\sqrt{|K|}s\right), \quad S(s) = \frac{1}{\sqrt{|K|}} \sinh\left(\sqrt{|K|}s\right). \tag{2.30}$$

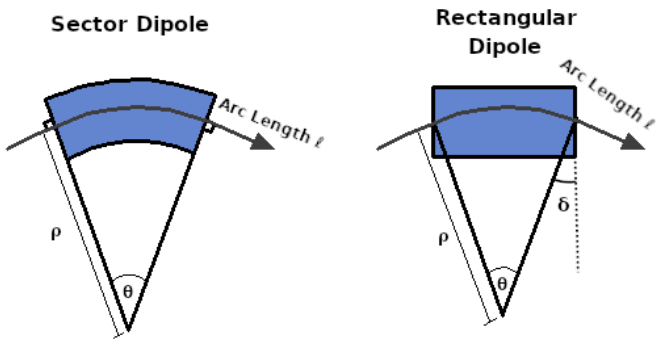

Figure 2.5: Schematic diagram of a dipole sector magnet (left) and a dipole rectangular magnet (right).

The transfer matrices for some of the common elements of an accelerator will be presented.

Drift Space

A drift space of distance ℓ without any magnetic elements gives $K = 0$. This gives the transfer matrix:

$$M_{\text{drift}} = \begin{pmatrix} 1 & \ell \\ 0 & 1 \end{pmatrix}. \tag{2.31}$$

Dipole Magnet

There are two types of dipole magnet, one is a sector magnet, another is a rectangular dipole as seen in fig. 2.5. For a sector magnet, the ends of the magnet are perpendicular to the trajectory. Particles on the exterior end of the central trajectory will undergo more bending, while particles on the interior end of the trajectory undergo less bending. In the plane of the bend (assumed to be x here) the transfer matrices are:

$$M_{x,\text{sector}} = \begin{pmatrix} \cos(\theta) & \rho \sin(\theta) \\ -\frac{1}{\rho}\sin(\theta) & \cos(\theta) \end{pmatrix}, \qquad M_{y,\text{sector}} = \begin{pmatrix} 1 & \ell \\ 0 & 1 \end{pmatrix}, \tag{2.32}$$

where $\theta = \frac{\ell}{\rho}$ and the y-plane is the transfer matrix of a drift space.

For a rectangular dipole magnet, the ends of the magnet are not perpendicular to the trajectory. Because of this, the fringe field term, $\tan(\delta)/\rho$ must be considered, giving the transfer matrix:

$$M_{\text{rect}} = M_{\text{exit}} \cdot M_{\text{sector}} \cdot M_{\text{entrance}}, \qquad \text{where } M_{\text{entry,exit}} = \begin{pmatrix} 1 & 0 \\ \frac{\tan(\delta_{\text{entry,exit}})}{\rho} & 1 \end{pmatrix}. \tag{2.33}$$

In the case where the angle is small and the magnet is symmetric about the reference trajectory ($\theta \ll 1$ and $\delta = \theta/2$), the transfer matrices are [36]:

$$M_{x,\text{rect}} = \begin{pmatrix} 1 & \rho\sin(\theta) \\ 0 & 1 \end{pmatrix}, \qquad M_{y,\text{rect}} = \begin{pmatrix} \cos(\theta) & \rho\sin(\theta) \\ -\frac{1}{\rho}\sin(\theta) & \cos(\theta) \end{pmatrix}. \tag{2.34}$$

Quadrupole Magnet

A quadrupole does not provide bending so the strength term is given by eq. 2.15. The transfer matrices for focusing and defocusing quadrupoles of length ℓ and positive strength k are

$$M_{\text{QF}} = \begin{pmatrix} \cos\left(\sqrt{k}\ell\right) & \frac{1}{\sqrt{k}}\sin\left(\sqrt{k}\ell\right) \\ -\sqrt{k}\sin\left(\sqrt{k}\ell\right) & \cos\left(\sqrt{k}\ell\right) \end{pmatrix}, \tag{2.35}$$

$$M_{\text{QD}} = \begin{pmatrix} \cosh\left(\sqrt{|k|}\ell\right) & \frac{1}{\sqrt{|k|}}\sinh\left(\sqrt{|k|}\ell\right) \\ \sqrt{|k|}\sinh\left(\sqrt{|k|}\ell\right) & \cosh\left(|k|\,\ell\right) \end{pmatrix}. \tag{2.36}$$

For a negative strength k, the matrices are interchanged such that $M_{\text{QF}} \leftrightarrow M_{\text{QD}}$. A further approximation can be made when the focal length of the quadrupole is larger than the length of the lens ($f = (k\ell)^{-1} \gg \ell$), which simplifies the transfer matrices to

$$M_{\text{QF}} = \begin{pmatrix} 1 & 0 \\ \frac{1}{f} & 1 \end{pmatrix}, \qquad M_{\text{QD}} = \begin{pmatrix} 1 & 0 \\ -\frac{1}{f} & 1 \end{pmatrix}. \tag{2.37}$$

Multiple Elements

From the matrix representation in eq. 2.27, the motion through consecutive elements can be easily combined as long as the transfer matrices for each element is known. For two consecutive elements with magnet strengths K_1 and K_2, the transport from u_0 to u_2 can be described element by element by,

$$\begin{pmatrix} u_1 \\ u_1' \end{pmatrix} = M(s_1/s_0)\begin{pmatrix} u_0 \\ u_0' \end{pmatrix}, \qquad \begin{pmatrix} u_2 \\ u_2' \end{pmatrix} = M(s_2/s_1)\begin{pmatrix} u_1 \\ u_1' \end{pmatrix}. \tag{2.38}$$

These solutions can be combined to give,

$$\begin{pmatrix} u_2 \\ u_2' \end{pmatrix} = M(s_2/s_1)\left(M(s_1/s_0)\begin{pmatrix} u_0 \\ u_0' \end{pmatrix}\right) = M(s_2/s_0)\begin{pmatrix} u_0 \\ u_0' \end{pmatrix}, \tag{2.39}$$

where $M(s_2/s_0) = M(s_2/s_1)M(s_1/s_0)$. This can be extended for an arbitrary number of transport elements. Hence, splitting the beam line into piecewise constant sections gives the particle transport equation.

2.4.3 Stability Criterion

Beam line lattices are often arranged to repeat, particularly in a circular accelerator. It is of interest to know if the lattice design leads to stable oscillations, over a large number of revolutions. This is expressed by the stability criterion. To derive this criterion, we define a periodic transfer matrix for n turns by:

$$M(s) = \left(M(s)\right)^n. \tag{2.40}$$

To be stable, the elements of M^n must be bounded as $n \to \infty$. The necessary conditions can be found by examining the eigenvalues λ of:

$$MU = \lambda U, \qquad \text{where } M = \begin{pmatrix} C & S \\ C' & S' \end{pmatrix},\ U = \begin{pmatrix} u \\ u' \end{pmatrix}. \tag{2.41}$$

The eigenvalues are,

$$\lambda_{\pm} = \cos(\mu) \pm i \sin(\mu) = e^{\pm i\mu}, \tag{2.42}$$

where the substitution $(C + S')/2 = \cos(\mu)$ was applied. The matrix M can generally be expressed in a more useful form called the Twiss form by,

$$M = \mathbb{1}\cos(\mu) + J\sin(\mu), \qquad \text{where } \mathbb{1} = \begin{pmatrix} 1 & 0 \\ 0 & 1 \end{pmatrix},\ J = \begin{pmatrix} \alpha & \beta \\ -\gamma & -\alpha \end{pmatrix}, \tag{2.43}$$

where

$$\alpha = \frac{C - S'}{2\sin(\mu)}, \qquad \beta = \frac{S}{\sin(\mu)}, \qquad \gamma = -\frac{C'}{\sin(\mu)}, \tag{2.44}$$

and the number of free parameters can be reduced by considering the determinant:

$$\beta\gamma - \alpha^2 = 1. \tag{2.45}$$

This Twiss form allows the n-th power of M to be expressed by:

$$M^n = \mathbb{1}\cos(n\mu) + J\sin(n\mu)\,. \tag{2.46}$$

As the limit $n \to \infty$, the matrix elements will be bounded if and only if μ is real. This gives the stability condition on the trace of M:

$$|\mathrm{Tr}\,(M)| = |C + S'| \leq 2. \tag{2.47}$$

Under the stability criterion it can be seen that for a real value of μ, the matrix elements execute a bound oscillation. If μ was imaginary, the motion would become unbound and the terms would increase exponentially with n and be lost.

2.4.4 The Beta Function

The transfer matrix $M(s)$, expressed in the Twiss form with a dependence on s is:

$$M(s) = \begin{pmatrix} 1 & 0 \\ 0 & 1 \end{pmatrix} \cos(\mu) + \begin{pmatrix} \alpha(s) & \beta(s) \\ -\gamma(s) & -\alpha(s) \end{pmatrix} \sin(\mu). \tag{2.48}$$

The terms in the matrix can be expressed in terms of the function $\beta(s)$, which due to the periodicity of the transfer matrix for a period L, has the property:

$$\beta(s + L) = \beta(s). \tag{2.49}$$

The two other terms can be expressed in terms of the beta function by considering eq. 2.41 and eq. 2.45 to get:

$$\alpha(s) = -\frac{\beta'(s)}{2}, \tag{2.50}$$

$$\text{and} \qquad \gamma(s) = \frac{1 + \alpha^2(s)}{\beta(s)}. \tag{2.51}$$

From Floquet's theorem two independent solutions can be expressed in terms of the beta function [38, 43, 44]:

$$u_{1,2}(s) = a\sqrt{\beta(s)}e^{\pm i\mu(s)} \qquad \text{where } \mu(s) = \int_{s_0}^{s} \frac{\mathrm{d}t}{\beta(t)}, \tag{2.52}$$

where a is a constant. Hence, a particle trajectory can be described by the real solution to Hill's

equation:

$$u(s) = a\sqrt{\beta(s)}\cos\left(\mu(s) - \delta\right), \tag{2.53}$$

$$u'(s) = -\frac{a}{\sqrt{\beta(s)}}\left(\sin\left(\mu(s) - \delta\right) + \alpha(s)\cos\left(\mu(s) - \delta\right)\right), \tag{2.54}$$

which for an arbitrary constant phase, δ, gives a parametric representation of an ellipse in the transverse trace space plane. In other words, the trajectory of a particle is described by the Twiss parameters. From this point onwards, it will be implied that the Twiss parameters have an implicit dependence on s.

2.5 Beam Distributions

Sec. 2.4 focused on describing the transport equation for a single particle. However, it is often more useful to describe the entire beam.

2.5.1 Beam Emittance and Twiss Parameters

The transport equation from sec. 2.4.4 can be used to trace the outline of an ellipse in the transverse trace space (u, u'). A varying amplitude and phase will fill the insides of the ellipse. Hence, an entire beam is described by an ellipse in trace space.

Liouville's Theorem

To describe the trace space ellipse, it is useful to introduce a fundamental theorem of classical mechanics, Liouville's theorem [45]. The theorem states that under the influence of conservative and differentiable forces, all configurations beginning in a phase space volume $\mathrm{d}\Gamma$, will after a period of time end up in a volume $\mathrm{d}\Gamma'$. The two states will have the same volume, but may not share the same shape. Often the longitudinal plane can be treated independently of the transverse planes. In the longitudinal plane it is natural to use the energy as a variable along with time, its canonical conjugate. According to Liouville and under Hamiltonian forces, the area occupied by the beam will be conserved. For the transverse planes, the trace space variables (u, u') are not the canonical conjugate variables. Instead, the ellipse needs to be described with the canonical conjugate variables of position and momentum (u, p_u) for the area to be conserved when accelerated.

2.5.2 Courant-Snyder Invariant

The Courant-Snyder invariant has the form of a rotated ellipse which is centred at the origin in the trace space (u, u') and is defined by:

$$\gamma u(s)^2 + 2\alpha u(s)u'(s) + \beta u'(s)^2 = a^2 = \epsilon. \tag{2.55}$$

A physical interpretation of this invariant is that an ellipse can be described by four parameters: β, α, γ, and ϵ, with the area of the ellipse given by $\pi\epsilon$. The term ϵ is called the *emittance* and the other terms referred to as the Twiss parameters with the same definitions as given in sec. 2.4.4. As the beam evolves, the form of the ellipse changes, but emittance stays constant under Liouville's theorem. As a result, particles stay within the ellipse as it changes. Hence, all particles inside the ellipse have an amplitude factor $a \leq \sqrt{\epsilon}$. This description is quite useful as it shows that a beam of particles can be described with the previous formulae for a single particle.

As discussed above, for the transverse plane the canonical conjugate variables are not position and angle. Thus, when solely considering the transverse emittance, the emittance decreases inversely with the momentum as particles are accelerated [38]. The relation between the angle and momentum is through: $p_u = p_0 u'$, where p_0 is the total momentum. If instead the ellipse is described with the phase space (u, p_u), one still gets an ellipse, but with an area given by $\pi p_0 \epsilon$. This is defined as a *normalised emittance*:

$$\epsilon_N = \left(\frac{p_0}{m_0 c}\right)\epsilon, \tag{2.56}$$

where m_0 is the mass of the particle and c is the speed of light. In contrast to the emittance, the normalised emittance remains invariant as the beam is accelerated.

Statistical Definition of Beam Emittance

The definition of the beam emittance in the Courant-Snyder invariant in eq. 2.55 can sometimes be difficult to apply. A definition based on a beam distribution is often more practical, particularly when the coordinates of all particles in a beam is known such as in simulations.

Given that the beam emittance describes the spread of particles, it is conceptually similar to the standard deviation which measures the dispersion:

$$\sigma_u = \sqrt{\frac{1}{N}\sum_{i=1}^{N}(u_i - \overline{u})^2}, \tag{2.57}$$

where the overline in $\overline{u}$ represents the average. If the average position and angle are zero, then the

root mean square (RMS) emittance for the distribution of points can be defined as the product of the standard deviation in u and u':

$$\epsilon = \sigma_u \sigma_{u'}. \tag{2.58}$$

A scaling factor can be added to include a larger majority of points within the ellipse. Generally, the distribution of particles may be rotated such that there exists a correlation between the position and angle. Also, the origin of the coordinate axis may not be at the barycentre of the distribution. A definition for the RMS emittance for a rotated distribution is derived in Buon [46] and given by:

$$\epsilon = \sqrt{\sigma_{uu}\sigma_{u'u'} - (\sigma_{uu'})^2} = \sqrt{\begin{vmatrix} \sigma_{uu} & \sigma_{uu'} \\ \sigma_{u'u} & \sigma_{u'u'} \end{vmatrix}} \tag{2.59}$$

where the emittance is defined in terms of the variance and correlation of position and angle. These terms are defined by:

$$\sigma_{uu} = \langle u^2 \rangle = \frac{1}{N}\sum_{i=1}^{N} (u_i - \overline{u})^2, \tag{2.60}$$

$$\sigma_{u'u'} = \left\langle u'^2 \right\rangle = \frac{1}{N}\sum_{i=1}^{N} \left(u'_i - \overline{u'}\right)^2, \tag{2.61}$$

$$\sigma_{uu'} = \langle uu' \rangle = \frac{1}{N}\sum_{i=1}^{N} (u_i - \overline{u})\left(u'_i - \overline{u'}\right). \tag{2.62}$$

A full expression for the beam emittance in a six dimensional phase space is given by:

$$\epsilon^2 = \begin{vmatrix} \sigma_{xx} & \sigma_{xx'} & \sigma_{xy} & \sigma_{xy'} & \sigma_{xz} & \sigma_{xz'} \\ \sigma_{x'x} & \sigma_{x'x'} & \sigma_{x'y} & \sigma_{x'y'} & \sigma_{x'z} & \sigma_{x'z'} \\ \sigma_{yx} & \sigma_{yx'} & \sigma_{yy} & \sigma_{yy'} & \sigma_{yz} & \sigma_{yz'} \\ \sigma_{y'x} & \sigma_{y'x'} & \sigma_{y'y} & \sigma_{y'y'} & \sigma_{y'z} & \sigma_{y'z'} \\ \sigma_{zx} & \sigma_{zx'} & \sigma_{zy} & \sigma_{zy'} & \sigma_{zz} & \sigma_{zz'} \\ \sigma_{z'x} & \sigma_{z'x'} & \sigma_{z'y} & \sigma_{z'y'} & \sigma_{z'z} & \sigma_{z'z'} \end{vmatrix}. \tag{2.63}$$

In the case of no correlation between the planes, the off-diagonal terms are zero, which splits the determinant into three 2×2 determinants. A comparison to the Courant-Snyder invariant gives a

relationships between the Twiss parameters and the standard deviations:

$$\sigma_u = \sqrt{\epsilon\beta}, \tag{2.64}$$

$$\sigma_{u'} = \sqrt{\epsilon\gamma}, \tag{2.65}$$

$$r\sigma_{uu'} = -\alpha\epsilon, \tag{2.66}$$

where $r = \sigma_{uu'}/\sqrt{\sigma_{uu}\sigma_{u'u'}}$ is the correlation coefficient.

2.5.3 Beam Envelope and Divergence

As has been shown, an arbitrary particle, i, lying within an ellipse will follow a trajectory given by

$$u_i(s) = \sqrt{\epsilon\beta}\cos\left(\mu(s) + \delta_i\right). \tag{2.67}$$

The cosine term will have a maximum and minimum value of ± 1, which allows the *beam envelope*, $E(s)$, to be defined for all particles:

$$E(s) = \sqrt{\epsilon\beta}. \tag{2.68}$$

As the beam envelope depends on the beta function, knowledge and manipulation of the beta function is critical to the design of beam lines. Similarly, the *beam divergence*, $A(s)$, is defined by:

$$A(s) = \sqrt{\epsilon}\sqrt{\frac{1+\alpha^2}{\beta}} = \sqrt{\epsilon\gamma}. \tag{2.69}$$

The relation of the Twiss parameters to the ellipse is summarised in fig. 2.6. When $\alpha = 0$, the beam envelope has a local minimum called the waist. Taking the ratio of the beam size to beam divergence at this point gives the beta function:

$$\frac{E_{\text{waist}}(s)}{A_{\text{waist}}(s)} = \frac{\sqrt{\epsilon\beta}}{\sqrt{\frac{\epsilon}{\beta}}} = \beta. \tag{2.70}$$

2.5.4 Twiss Parameter Transformation

Since the Twiss parameters β, α, γ, and emittance ϵ characterize the beam ellipse, an understanding of how the parameters transform is of importance. Using the property that a cosine wave can be decomposed into a linear combination of a sine and cosine, the solution to Hill's equation can be

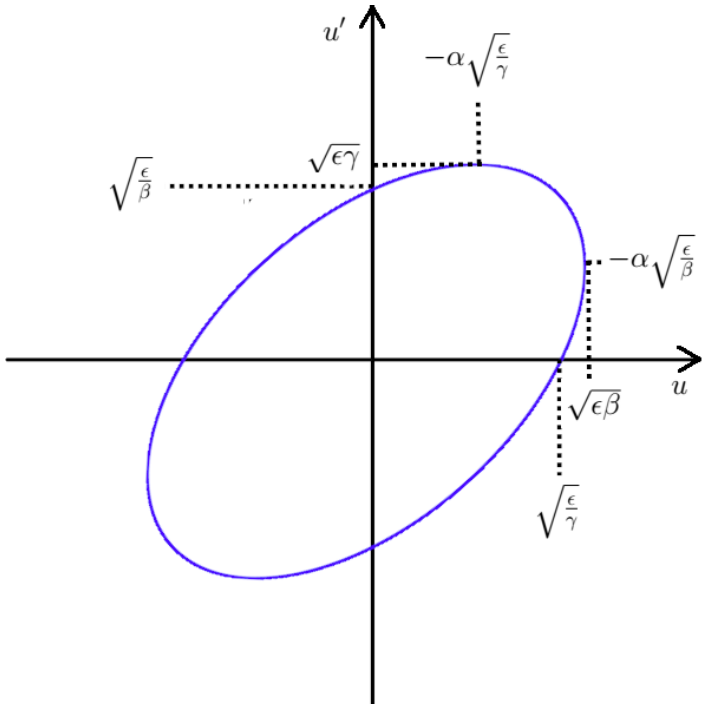

Figure 2.6: Beam ellipse in trace space.

expressed by:

$$u(s) = a\sqrt{\beta}\cos(\mu(s)) + b\sqrt{\beta}\sin(\mu(s)). \tag{2.71}$$

Setting initial conditions at position $s = 0$:

$$\mu(0) = 0, \quad \beta(0) = \beta_0, \quad \alpha(0) = \alpha_0, \quad u(0) = u_0, \quad u'(0) = u'_0, \tag{2.72}$$

gives for the amplitude factors:

$$a = \frac{1}{\sqrt{\beta_0}} u_0, \tag{2.73}$$

$$b = \frac{\alpha_0}{\sqrt{\beta_0}} u_0 + \sqrt{\beta_0} u'_0. \tag{2.74}$$

Substitution of the amplitude factors gives:

$$u(s) = \sqrt{\frac{\beta}{\beta_0}} \left[\cos(\mu(s)) + \alpha_0 \sin(\mu(s))\right] + \sqrt{\beta\beta_0}\sin(\mu(s))u'_0, \tag{2.75}$$

$$u'(s) = \left[\frac{(\alpha_0 - \alpha)\cos(\mu(s))}{\sqrt{\beta_0\beta}} - \frac{(1 + \alpha\alpha_0)\sin(\mu(s))}{\sqrt{\beta_0\beta}}\right] u_0 + \sqrt{\frac{\beta_0}{\beta}} \left[\cos(\mu(s)) - \alpha\sin(\mu(s))\right] u'_0, \tag{2.76}$$

this can be succinctly expressed in matrix formulation as:

$$\begin{pmatrix} C(s) & S(s) \\ C'(s) & S'(s) \end{pmatrix} = \begin{pmatrix} \sqrt{\frac{\beta}{\beta_0}}\left[\cos(\mu(s)) + \alpha_0 \sin(\mu(s))\right] & \sqrt{\beta\beta_0}\sin(\mu(s)) \\ \frac{(\alpha_0-\alpha)\cos(\mu(s))}{\sqrt{\beta_0\beta}} - \frac{(1+\alpha\alpha_0)\sin(\mu(s))}{\sqrt{\beta_0\beta}} & \sqrt{\frac{\beta_0}{\beta}}\left[\cos(\mu(s)) - \alpha\sin(\mu(s))\right] \end{pmatrix}. \tag{2.77}$$

By considering the inverse of the transformation matrix and substituting into the Courant-Snyder invariant allows the Twiss parameters to be expressed in matrix formalism by:

$$\begin{pmatrix} \beta \\ \alpha \\ \gamma \end{pmatrix} = \begin{pmatrix} C^2 & -2SC & S^2 \\ -CC' & SC' + S'C & -SS' \\ C'^2 & -2S'C' & S'^2 \end{pmatrix} \begin{pmatrix} \beta_0 \\ \alpha_0 \\ \gamma_0 \end{pmatrix}. \tag{2.78}$$

These results show that the Twiss parameters can be transformed in a piecewise manner through the beam line. As long as the initial Twiss values are known, the values at any point in the beam line can be calculated.

2.6 Space-Charge Effects

Collective effects also need to be considered for beams. One example is space-charge which arises from the charge and current of the beam. As will be shown, the result of space-charge can lead to an increase of the beam size.

2.6.1 Self-Fields

Space-charge originates from the particles in a beam interacting with each other, where two particles with the same charge experience a repulsive Coulomb force. If the particles are also travelling, there will be an attractive force from the magnetic fields. The sum of these two forces will give an overall repulsive force, which decreases as the particle velocity increases. An expression for the sum of these two forces was derived by Schindl [47], with the result:

$$F_u = \frac{eI}{2\pi\varepsilon_0\beta c\gamma^2 a^2}u, \tag{2.79}$$

where e is the charge, I the current, ε_0 the vacuum permittivity, β the ratio of the velocity to speed of light, c the speed of light, γ the Lorentz factor, a the beam radius, and u representing either transverse coordinate. Fig. 2.7 shows the space-charge force acting on a uniform and Gaussian beam, with a comparison to a focusing quadrupole.

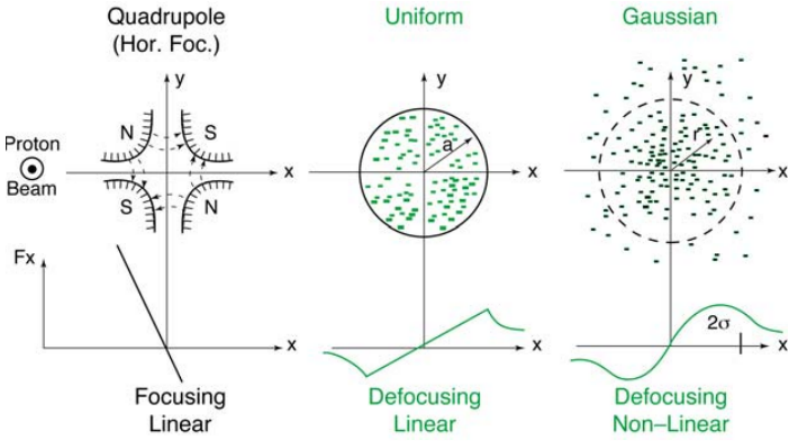

Figure 2.7: Comparison of the horizontal force of a quadrupole (left), space-charge on a uniform beam (middle), and space-charge on a Gaussian beam (right). Image taken from Schindl [47].

Hill's equation can be modified to include space-charge [47, 48]:

$$u'' + (K(s) + K_{\mathrm{SC}}(s))\, u = 0 \qquad \text{where } K_{\mathrm{SC}} = -\frac{2r_0 I}{ea^2\beta^3\gamma^3 c}, \tag{2.80}$$

where r_0 is the classical particle radius. As can be seen, the focusing term, $K(s)$ is reduced due to the presence of the space-charge. In addition to self-fields, there are also additional space-charge effects that can arise due to interactions with the environment, such as the beam pipe, magnets, and diagnostic equipment.

2.6.2 Space-Charge Limit

As space-charge depends on the beam intensity, there will be a limit on the maximum intensity, known as the space-charge limit. Exceeding this limit may lead to a significant increase of the beam size and emittance and lead to beam losses. To counter the space-charge effect, it is typical either to lower the beam intensity or to increase the beam energy.

Chapter 3

Particle Therapy

Hadrons are composite particles which are made up of two or more quarks. Two well known hadrons are protons and neutrons which compose the atomic nuclei. Charged particle therapy typically refers to therapy where patients are irradiated with protons and other *heavy* ions. The definition of a heavy particle is a bit arbitrary and can change depending on the context. In the context of particle therapy, it often refers to any particle heavier than protons [49].

This chapter will introduce some of the common terms as well as underlying physics used in radiation oncology. Introducing these terms will help to establish the context for radiotherapy and the chapter will conclude with a discussion of common dosimeters currently in use for proton beams. These underlying physics form the basis of particle simulations codes like Geant4 [50].

3.1 Particle Interactions with Matter

Ionising radiation directed at a tumour causes DNA lesions which damage the structure of cancer cells. Of the type of lesions that can occur, double-strand breaks (DSB) are quite effective in inhibiting DNA repair pathways. Erroneous repair of DNA structures negatively affects the stability of a genome and leads to the formation of aberrations which may lead to cell death. A detailed overview of DSB repair pathways is discussed in Mladenov *et al.* [51]. The interactions between ionising radiation and DNA structures is a key role for radiation oncologists. A deeper understanding could allow for targeted elimination of specific repair pathways in tumour cells, increasing treatment efficiency.

Ionising radiation is grouped as either directly or indirectly ionising. Indirectly ionising radiation occurs from neutral particles which ionise particles through secondary interactions. For example, photons interact with cellular water to produce free radicals and electrons which can interact with the medium. In contrast, charged particles are directly ionising and can interact directly with the

cells. Examples of charged particles include: alpha particles, beta particles, protons, and other charged nuclei. Directly ionising radiation will be the primary focus for this chapter and thesis.

3.1.1 Energy Loss

Charged particles lose energy when moving through a medium primarily through excitation and ionisation. The scattering processes of a charged particle experiences will dictate the amount of energy lost. The maximum transferable kinetic energy for a relativistic incident particle to transfer to an electron in a head-on collision can be found by considering the conservation of energy and momentum [52]:

$$T_{\max} = \frac{2m_e c^2 \beta^2 \gamma^2}{1 + \frac{2\gamma m_e}{m_0} + \left(\frac{m_e}{m_0}\right)^2}, \tag{3.1}$$

where m_e is the mass of an electron, m_0 and p, are the mass and momentum of the incident particle, c is the speed of light, β is the ratio of the speed of the particle and c, and γ is the Lorentz factor. For reference, the maximum transferable kinetic energy for a 10 MeV proton is about 0.0219 MeV, and for 100 MeV is about 0.229 MeV. The maximum percentage of energy transferred increases with energy, such that a 1 TeV proton can transfer over half of its energy.

3.1.2 Bethe-Bloch Formula

The Bethe-Bloch formula gives a description of the mean energy loss of a charged particle ($m_0 \gg m_e$) travelling through a medium [53]:

$$-\frac{\mathrm{d}E}{\mathrm{d}x} = K z^2 \frac{Z}{A} \frac{1}{\beta^2} \left[\frac{1}{2} \ln \left(\frac{2m_e c^2 \beta^2 \gamma^2 T_{\max}}{I^2} \right) - \beta^2 - \frac{\delta(\beta\gamma)}{2} \right]. \tag{3.2}$$

This gives the mass stopping power with the units $\mathrm{MeV\,g^{-1}cm^2}$, which is plotted in fig. 3.1. The terms that appear in the formula are:

$K = 4\pi N_A r_e^2 m_e c^2$

N_A – The Avogadro constant

r_e – Classical electron radius

z – Charge of the incident particle

Z, A – Atomic number and weight of absorber material

I – Mean excitation energy

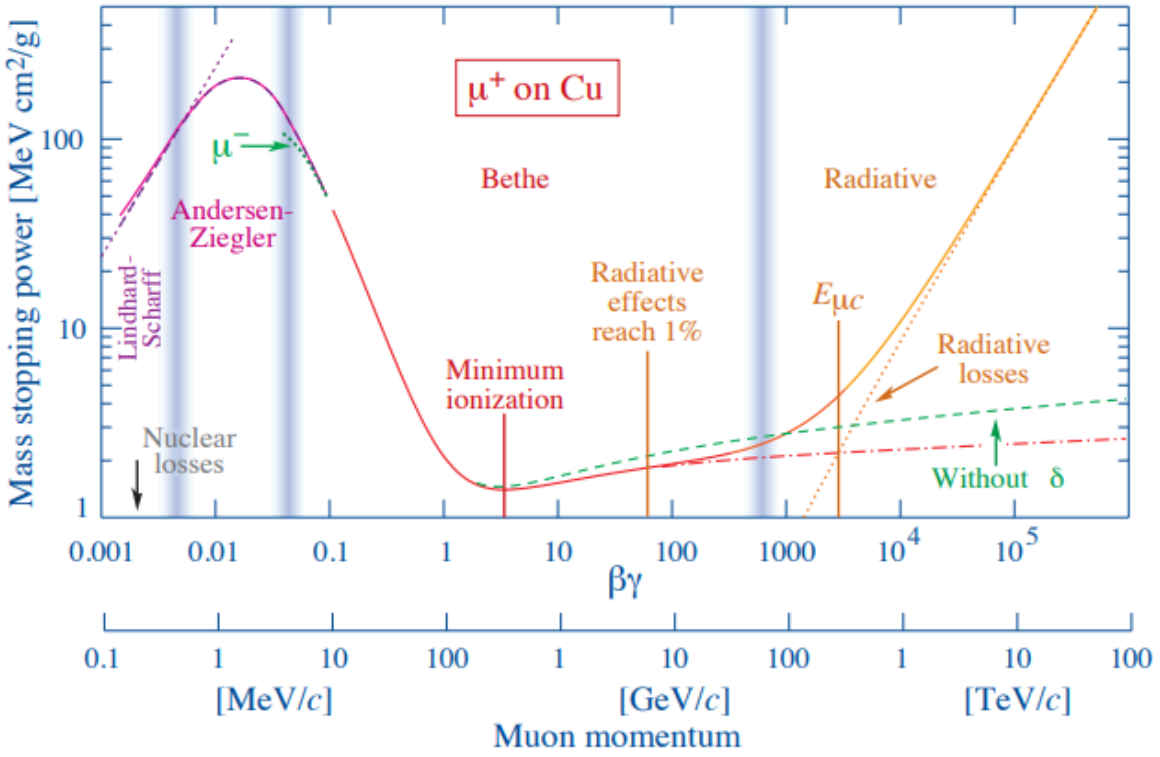

Figure 3.1: Mass stopping power plot for positive muons in copper as a function of momentum. Taken from the 2020 published review by the Particle Data Group (PDG) [53].

$\delta(\beta\gamma)$ – Density effect correction due to polarisation

Comparing eq. 3.2 to the plot it can be seen that as $1/\beta^2$ increases, the stopping power initially decreases. This continues for low energy particles until a minimum is reached. Relativistic particles with an energy loss in this minimum region are called minimum-ionising particles (MIPs). But as the energy of the particle increases beyond this point, the energy loss starts to rise. This is described by the logarithmic term in the equation, which dominates at high energies. From the equation, it can be seen that the absorber material will have an influence on the energy loss and is directly proportional to the density of electrons in the absorber. As a result, the loss rate in a human body will have a strong dependence on the composition and density. The Bethe-Bloch formula in eq. 3.2 can be a good approximation in the regions of $0.1 \leq \beta\gamma \leq 1000$. But for lower energies, higher order corrections need to be included [53]. Furthermore, only the energy loss from ionisation and excitation is described, whereas at higher energies, losses from radiation will dominate.

The Bethe-Bloch formula only gives the mean energy loss of charged particles. Due to the statistical nature of ionisation, a thin absorber (relative to the mean free path) would see a strong fluctuation around the average energy loss. The distribution of the energy loss in the layer of material can be approximated according to the Landau distribution. However, in experiments the actual distribution tends to be broader [54]. For thicker absorbers, the tail in the Landau distribution will reduce and a

Gaussian distribution becomes a better approximation to model the energy loss distribution.

3.2 Common Interaction and Dosimetric Quantities

Radiation dosimetry deals with measurements and calculations for energy depositions in a medium for ionising radiation. Various quantities are used to characterise the radiation. Some of the common quantities will be presented below.

3.2.1 Fluence

The particle fluence Φ, represents the number of protons, N, incident on a small sphere with infinitesimal area $\mathrm{d}A$. Similarly, an energy fluence Ψ, can be defined for the radiant energy $\mathrm{d}E_{\mathrm{kin}}$. The two quantities are expressed by:

$$\Phi = \frac{\mathrm{d}N}{\mathrm{d}A}, \tag{3.3}$$

$$\Psi = \frac{\mathrm{d}E_{\mathrm{kin}}}{\mathrm{d}A} = \Phi E_{\mathrm{kin}}. \tag{3.4}$$

The reason that a sphere is considered is because the area perpendicular to the direction of the particle will be independent of the incident angle. For beams with an energy spread, the fluence are spectrums. The particle and energy fluence rate are the time derivatives for the two fluence quantities:

$$\dot{\Phi} = \frac{\mathrm{d}\Phi}{\mathrm{d}t}, \tag{3.5}$$

$$\dot{\Psi} = \frac{\mathrm{d}\Psi}{\mathrm{d}t}. \tag{3.6}$$

3.2.2 Stopping Power

The stopping power defines the amount of energy lost to a medium by a charged particle. Dividing the stopping power by the density of the absorbing medium gives the *mass stopping power*. There are two types of stopping powers: collisional and radiative.

For the collisional stopping power, collisions can be defined as soft or hard. A soft collision is when the interaction occurs at a distance considerably greater than the atomic radius. This leads to a collision with a small energy transfer. A hard collision is when the interaction occurs close to the atomic radius, and can produce secondary electrons with high energies (delta rays). Radiative stopping power correspond to the nuclear interactions that occur between charged particles and atomic nuclei.

It is normally of interest to determine the energy deposited within a volume. However, high energy delta electrons may escape and carry energy away from the volume. Because of this, it becomes useful to define a *restricted collisional stopping power*. This definition excludes any interactions that take energy away from the interaction volume. The Bethe-Bloch equation can be modified to account for delta electrons carrying energy away up to a limit T_{cut}:

$$-\left.\frac{\mathrm{d}E}{\mathrm{d}x}\right|_{T<T_{\text{cut}}} = Kz^2\frac{Z}{A}\frac{1}{\beta^2}\left[\frac{1}{2}\ln\left(\frac{2m_e c^2\beta^2\gamma^2 T_{\text{cut}}}{I^2}\right) - \frac{\beta^2}{2}\left(1+\frac{T_{\text{cut}}}{T_{\text{max}}}\right) - \frac{\delta(\beta\gamma)}{2}\right]. \tag{3.7}$$

3.2.3 Linear Energy Transfer

The linear energy transfer (LET) is the average energy transferred locally to an absorbing medium. From the definition alone, it can be seen that LET is very similar to the stopping power. The key difference is that LET does not consider nuclear interactions. According to ICRU report 85 [55], the LET is the same quantity as the restricted linear collisional stopping power. The unrestricted linear energy transfer is defined when no limit is placed on the energy carried away. In this case, the unrestricted linear energy transfer is equal to the total electronic stopping power.

LET has another definition which is used to describe the mean value of the collisional stopping power [56]. This value can be calculated along the track of a single particle, or by averaging the stopping powers of all particles at a particular point. Two common implementations are: track averaged LET and dose averaged LET. The track averaged LET is the mean value of the stopping power weighted by the fluence. The dose averaged LET is the stopping power for each individual proton weighted by its contribution to the dose.

3.2.4 Kerma and Cema

As photons are indirectly ionising radiation, they impart energy in two steps: first by transferring energy to secondary charged particles, then by transferring energy to the medium. To describe the average kinetic energy transferred to the liberated charged particles, the kinetic energy released per unit mass (kerma), K is defined by:

$$K = \frac{\mathrm{d}E_{\text{tr}}}{\mathrm{d}m}, \tag{3.8}$$

where $\mathrm{d}E_{\text{tr}}$ is the average sum of the kinetic energies of all charged particles liberated in a material of mass $\mathrm{d}m$.

A similar quantity is the converted energy per unit mass (cema) for directly ionising radiation. In contrast to the kerma, the cema describes the energy lost by charged particles but excludes secondary

electrons. The cema C is defined by:

$$C = \frac{\mathrm{d}E_c}{\mathrm{d}m}, \tag{3.9}$$

where $\mathrm{d}E_c$ is the energy lost by charged particles.

3.2.5 Absorbed Dose

The absorbed dose in a volume is the average energy $\overline{E}$ lost by ionising radiation to an absorbing medium with mass m:

$$D = \frac{\mathrm{d}\,\overline{E}}{\mathrm{d}m}. \tag{3.10}$$

Typically the dose is expressed in units of Gray (= J/kg).

Looking at the units for the dose it can be seen that the absorbed dose is similar to the kerma and cema. The key difference lies within the definition of these terms. The dose is the sum of *all* energies entering the volume minus the energy leaving the volume. The kerma disregards the energy transport of longer ranged charged particles, so these particles are still included in the quantity. In contrast, the cema disregards the energy dissipation of secondary electrons. A *reduced cema*, C_Δ, can also be defined with a cutoff in energy for all electrons of Δ. In general, the difference between the dose and cema is small compared to the difference between dose and kerma [57].

Relationship of Dosimetric Terms to Dose

From dimensional analysis, one can relate the dose to the fluence and stopping power [58]. For an infinitesimal cylinder with $\mathrm{d}N$ particles passing through a cross sectional area $\mathrm{d}A$, of thickness of $\mathrm{d}x$, and density ρ, gives a dose of:

$$\begin{aligned} D = \frac{\text{energy}}{\text{mass}} =& \frac{-\left(\frac{\mathrm{d}E}{\mathrm{d}x}\right) \times \mathrm{d}x \times \mathrm{d}N}{\rho \times \mathrm{d}A \times \mathrm{d}x}, \\ =& \Phi \frac{S}{\rho}. \end{aligned} \tag{3.11}$$

Here Φ is the fluence and S/ρ is the mass stopping power.

3.2.6 Range

The range of a particle refers to the distance a charged particle travels in a medium until it stops. But a charged particle interacts with multiple electrons as it proceeds through a medium. During each interaction, a small fraction of the kinetic energy of the incident particle will be lost. Because

the energy loss occurs as a result of a finite number of individual interactions, the particle does not stop at the same depth. This makes the range an average quantity. This phenomenon is referred to as range straggling (or energy straggling). Since it is convenient to treat the particle as losing energy gradually and continuously, an approximation called the continuous slowing down approximation (CSDA) is often used. It represents the average path length along the particle trajectory for it to come to a stop. The CSDA range is the integral of the inverse of the stopping power for a charged particle with an initial kinetic energy of T_0 [59, 60]:

$$R_{\mathrm{CSDA}} = \int_0^{T_0} \left[\frac{S(E)}{\rho}\right]^{-1} \mathrm{d}E. \tag{3.12}$$

For heavily charged particles, a projected range can also be defined. The projected range refers to the penetration depth in absorbers. One definition of the projected range is the mean projected range $\overline{R}$. This refers to the thickness of the absorber where 50% of incident particles are stopped. Another definition is the extrapolated projected range R_0, which is the distance for the particle energy to fall to zero. It is extrapolated from the penetration curve and is particularly useful for experimental measurements. Finally, the maximum depth of penetration R_{max}, represents the thickness of the absorber sufficient to attenuate the incident particles to an *undetectable* level, though this level is not precisely defined.

Databases such as PSTAR [59] by the National Institute of Standards and Technology can be used to generate stopping powers and ranges for protons. A comparison of the CSDA range and R_{max} plotted against the incident energy can be generated from PSTAR for protons in water as can be seen in fig. 3.2. For high energy protons, the difference between the two quantities is negligible, but a difference can be observed at low energies. Water is typically used to estimate the beam penetration because water and tissue have a similar density and effective Z/A. As a result, proton energy loss and range is often measured in terms of their water-equivalence. This is measured by placing a degrader upstream of a water phantom and measuring how the Bragg peak shifts.

From fig. 3.2 it can be seen that at higher energies, the logarithm of energy and range appears to be linear. Bragg and Kleeman observed this and approximated the range of protons to energy by the Bragg-Kleeman rule [61]:

$$R = \alpha E^p, \tag{3.13}$$

where α is a constant dependent on the material, E is the initial energy of the proton beam, and p is an energy dependent parameter.

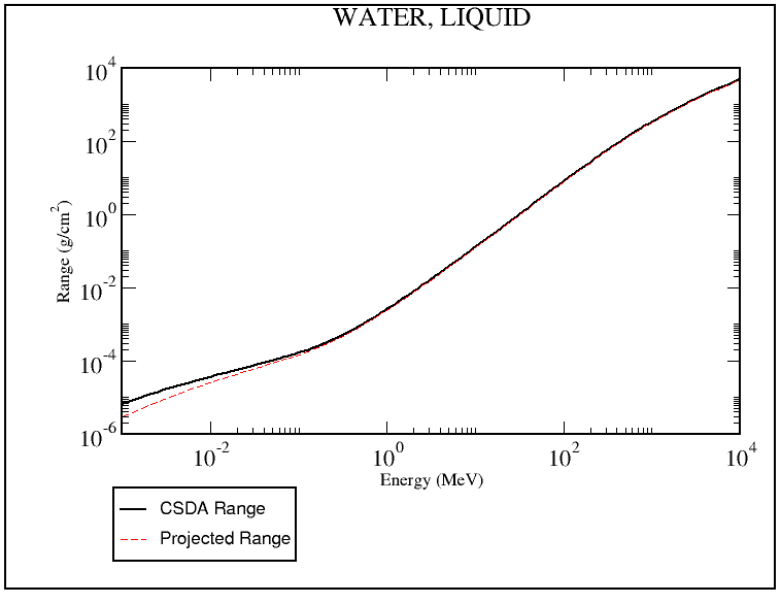

Figure 3.2: Range table for protons in water. The difference comes from the definition of the range where the projected range is the average penetration depth from the surface. While the CSDA range is the average path length travelled. Generated from PSTAR [59].

3.2.7 Relative Biological Effectiveness

Since conventional photon therapy is better understood compared to hadron therapy, many treatment schemes with hadrons are planned based on photon treatments. Doses for protons are often compared to the photon doses needed to achieve the same biological effect. This quantity is the relative biological effectiveness (RBE) which is the ratio of the reference radiation, D_{X}, to a radiation of type R, D_{R}:

$$\mathrm{RBE\ (endpoint)} = \frac{D_{\mathrm{X}}}{D_{\mathrm{R}}}. \tag{3.14}$$

An RBE adjusted dose is then defined as the product of the physical dose and the RBE. In other words, prescription doses are defined in reference to photons.

Protons are typically assumed to have an RBE value of 1.1, which means patients receive a dose about 10% lower than a comparable treatment with photons. This value is based on experiments in the early days of proton therapy [62]. Although the use of a single value for the proton RBE greatly simplifies treatment planning, it is well-known that the RBE is not constant [63]. This is corroborated by experimental results as seen in fig. 3.3. As RBE is affected by the type of tissue, this can lead to an extension in the depth of a few millimetres [64]. Furthermore, RBE is known to depend on a large number of factors which include: dose, biological endpoint, and LET. The relationships of these factors to the RBE still needs to be better understood in order for treatment planning to incorporate

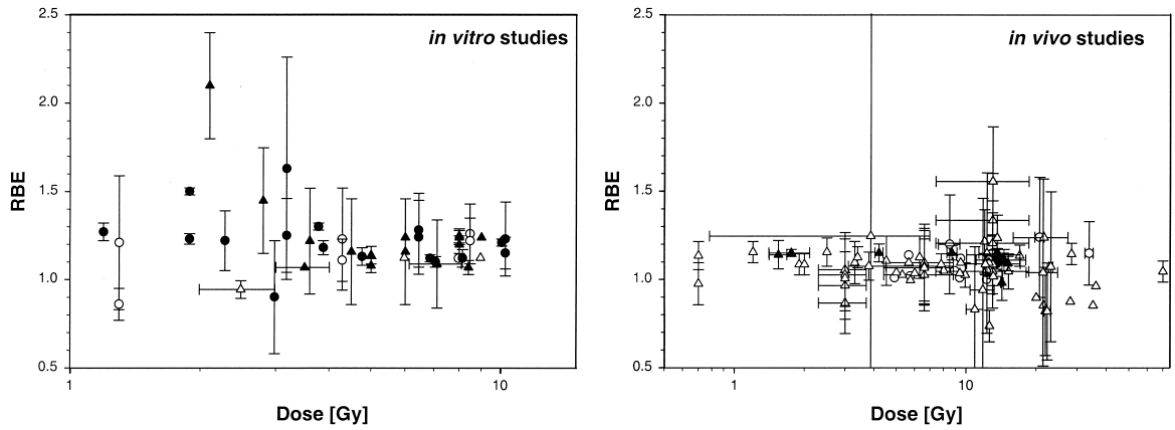

Figure 3.3: Experimental RBE values (relative to ^{60}Co) taken from Paganetti *et al.* [63]. Left: *In vitro* measurements using Chinese Hamster cell lines (closed symbols) and other cell lines (open symbols). Right: RBE values for jejunal crypt cells (closed symbols) and other tissues (open symbols).

RBE variations.

3.3 Proton Interactions

In a radiotherapy context, protons interact with matter in three ways [58]: slowing due to collisions with atomic electrons (stopping), deflection by collisions with atomic nuclei (scattering), and head-on collisions with a nucleus (nuclear interactions). Although proton Bremsstrahlung can occur, for therapeutic energies this effect is often neglected since it only becomes prominent at highly relativistic energies. A summary of the proton interactions [65] is presented in table 3.1. These interactions when combined together lead to the pronounced peak in the solid red line shape in fig. 3.4 called the *Bragg peak*. The shape of the depth-dose distribution can be exploited to concentrate the majority of the delivered dose into a volume.

Stopping

Protons primarily lose energy due to frequent inelastic Coulomb interactions with atomic electrons. At a certain depth (range), the protons stop, and any loss becomes negligible beyond the stopping point. Due to range straggling, there will be a spread in the range. From the Bethe-Bloch equation, the rate of energy loss increases as the proton slows down.

Scattering

A proton passing close to the atomic nucleus will experience a repulsive elastic Coulomb interaction. The deflection is small for a single interaction, but a combination of these deflections will lead to an observable angular spread. Multiple Coulomb scattering (MCS) for protons in a slab of material

Table 3.1: Summary of the interactions of a proton at therapeutic energies.

	Target	**Products**	**Primary Proton Effect**	**Dosimetry**
Inelastic Coulomb scattering	Atomic electrons	Primary proton, electrons	Quasi-continuous energy loss	Range in patient
Elastic Coulomb scattering	Atomic nucleus	Primary proton, recoil nucleus	Deflection	Penumbral sharpness
Non-elastic nuclear reactions	Atomic nucleus	Secondary proton, neutrons, heavy ions, etc.	Loss of primary proton	Fluence, generation of neutrons
Bremsstrahlung	Atomic nucleus	Primary proton, Photons	Energy loss, deflection	Negligible

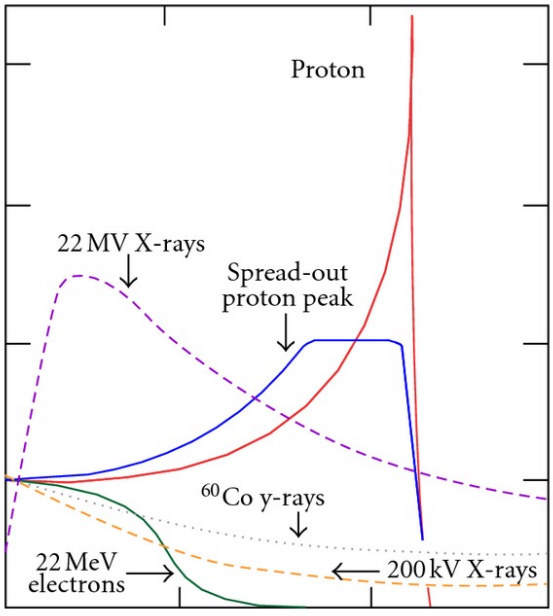

Figure 3.4: The depth-dose distribution for protons (solid red line = pristine Bragg peak, solid blue line = spread-out Bragg peak) compared against photons and electrons. Plot taken from Cianchetti [66].

leads to a spatial spread that looks approximately Gaussian. This is because the scattering angle is typically small [58], but can depend on the type of absorbing material.

Nuclear Interactions

Although non-elastic nuclear reactions between protons and the atomic nucleus occur less often compared to electromagnetic interactions, they can have more profound effects. In these interactions, the nucleus is transformed and will eject secondaries such as protons, deuterons, and other ions. These secondaries have lower energies and larger angles compared to the primary proton. Secondary protons can comprise as much as 10% of the absorbed dose in a treatment [65], with deuterons and other heavy ions comprising a much smaller proportion and depositing their energy locally. However, neutrons can also be produced which have high biological effectiveness, and may lead to significant side effects in patients [67, 68].

3.4 Multiple Coulomb Scattering

Multiple Coulomb scattering (MCS) is the sum of multiple small-angle deflections due to interactions of protons with the atomic nuclei. Most protons will have an angular distribution that resembles a Gaussian distribution, but this will not be exact due to the occurrence of rare large single scatters.

3.4.1 Molière's Theory

There are a variety of theories proposed to predict the form of the MCS angular distribution with the most comprehensive theory proposed by Molière in 1948 [69]. However, there are limits to the application of this theory as it generalises the scattering to arbitrarily thick targets composed of compounds and mixtures. The mathematics behind the theory is quite involved and requires the introduction of several quantities. One of these quantities is the *characteristic single scattering angle*, χ_c. It represents a limit on the maximum angle a proton will be deflected by for a single event whilst traversing a target. Though it is possible for a rare single scattering event to occur which exceeds this angle. This quantity is expressed by [58]:

$$\chi_c{}^2 = \frac{c_3 t}{(pv)^2} \qquad \text{where } c_3 = 4\pi N_A \left(\frac{e^2}{\hbar c}\right)^2 (\hbar c)^2 \frac{z^2 Z^2}{A}, \tag{3.15}$$

where N_A is Avogadro's constant, $(e^2/\hbar c) \sim 1/137$ is the fine structure constant, z is the proton charge number, Z is the target atomic number, A is the target atomic weight, p is the proton momentum, and v is the proton speed.

Another quantity is the *screening angle* χ_a. This is the angle where the single scattering cross section differs from Rutherford's law and due to effects from the nuclear charge of atomic electrons. Molière's theory used the Thomas-Fermi model to account for electron screening, but a more precise results was later calculated with the Hartree-Fock approach by Striganov [70]. Molière's approach gives an expression of [58]:

$$\chi_a{}^2 = \frac{c_2}{(pc)^2}\left(1.13 + 3.76\alpha^2\right), \qquad \text{where } c_2 = \left(\frac{\hbar c}{a}\right) = \left[\frac{1}{0.885}\left(\frac{e^2}{\hbar c}\right)\left(m_e c^2\right) Z^{1/3}\right]^2, \tag{3.16}$$

where a is the Thomas-Fermi radius and α is the *Born parameter*:

$$\alpha^2 = \left(\frac{\frac{e^2}{\hbar c} zZ}{v/c}\right)^2. \tag{3.17}$$

This leads to the quantity:

$$b = \ln\left(\frac{\chi_c{}^2}{1.167\chi_a{}^2}\right), \tag{3.18}$$

which represents the natural logarithm of the effective number of collisions in the target. For convenience, the *reduced target thickness*, B, can be defined through the equation:

$$B - \ln(B) = b. \tag{3.19}$$

Molière's *characteristic multiple scattering angle* can then be expressed:

$$\theta_M = \frac{1}{\sqrt{2}}\left(\chi_c\sqrt{B}\right). \tag{3.20}$$

The $1/\sqrt{2}$ follows the convention in Paganetti [58] to allow for it to be associated to the standard deviation in the Gaussian function. This allows for a reduced angle to be introduced:

$$\theta' = \frac{\theta}{\chi_c\sqrt{B}}. \tag{3.21}$$

Using these newly defined quantities allows an approximation of the distribution function $f(\theta)$ by a power series:

$$f(\theta) = \frac{1}{2\pi\theta_M{}^2}\frac{1}{2}\left[f^{(0)}(\theta') + \frac{f^{(1)}(\theta')}{B} + \frac{f^{(2)}(\theta')}{B^2}\right], \tag{3.22}$$

where

$$f^{(n)}(\theta') = \frac{1}{n!}\int_0^\infty y \mathrm{d}y J_0(\theta' y)\exp\left(\frac{y^2}{4}\right)\left[\frac{y^2}{4}\ln\left(\frac{y^2}{4}\right)\right]^n, \tag{3.23}$$

$$f^{(0)}(\theta') = 2\exp\left(-(\theta')^2\right). \tag{3.24}$$

The Molière/Bethe approach [71] from 1953 modified the theory to allow one to evaluate targets with low-Z by substituting $Z(Z+1)$ instead of Z^2 in all the previous formulae. Another modification was proposed by Fano in 1954 [72] which makes corrections for b and Z^2 based on the target material.

3.4.2 Highland's Formula

Although Molière's theory provided a good match to experimental results, it is complicated to use. Since the angular distribution resembles a Gaussian, an approximation can be made. Despite the first term in Molière's being a Gaussian term, Hanson [73] found that only retaining the first term in Molière does not provide a good approximation to experiments and results. Instead, Hanson introduced a Gaussian width parameter for small angles:

$$\theta_{\text{Hanson}} = \frac{1}{\sqrt{2}}\left(\chi_c\sqrt{B-1.2}\right), \tag{3.25}$$

This provided a good approximation, but the presence of the B term means that the entire Molière computation is needed. Highland [74] parametrised the Molière/Bethe/Hanson theory with:

$$\theta_{\text{Highland}} = \frac{14.1\,\text{MeV}}{pv}\sqrt{\frac{L}{L_R}}\left[1+\frac{1}{9}\log_{10}\left(\frac{L}{L_R}\right)\right], \tag{3.26}$$

where L is the target thickness and L_R is the radiation length of the target material[1].

Highland's formula was found to fit well to experiments, particularly for thin targets. Highland's formula was later generalised by Gottschalk [76] for thicker targets by:

$$\theta_{\text{Gottschalk}} = \left(1+\frac{1}{9}\log_{10}\left(\frac{L}{L_R}\right)\right)\sqrt{\int_0^L\left(\frac{14.1\,\text{MeV}}{pv(x')}\right)^2\frac{1}{L_R}dx'}. \tag{3.27}$$

There have also been other attempts to improve upon Highland's formula such as dropping the dependence on radiation length [77], or using a scattering power approach [58].

[1] Some numbers in eq. 3.26 are not the same as given by Highland. One of these differences is the constant of 14.1 MeV. The value as given by Highland should be 13.9 MeV, but 14.1 MeV was quoted in the 1986 Particle Data Book, which has since been commonly adopted [75]. Another difference is the $\frac{1}{9}$ term instead of $\frac{1}{8}$.

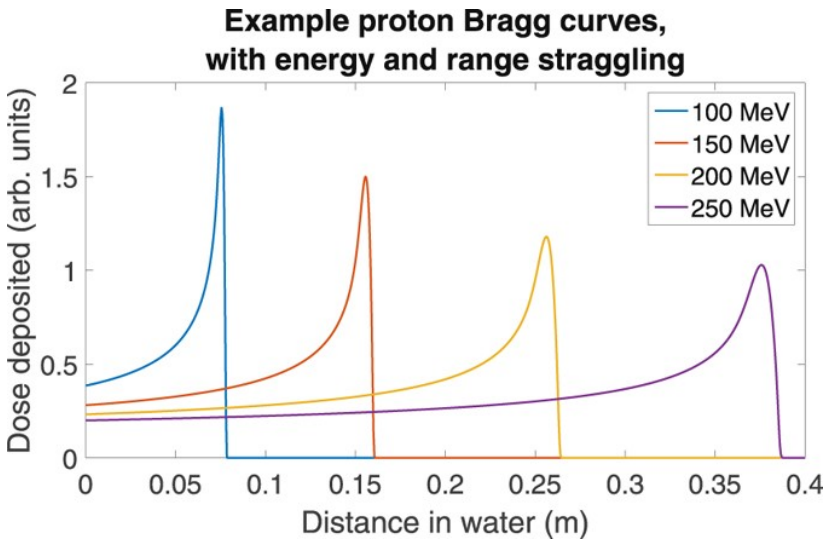

Figure 3.5: Proton Bragg curves travelling through water. Taken from Grimes *et al.* [78].

3.5 The Bragg Peak

The Bragg curve refers to the entire depth-dose distribution which includes the characteristic Bragg peak. This distribution arises as a result of a combination of stopping, scattering, and nuclear reactions. In order to uniformly irradiate a volume, a range modulator can be used to create a spread-out Bragg peak (SOBP).

From the Bragg-Kleeman rule (eq. 3.13), it can be seen that the depth of the peak is controlled by the beam energy. As protons slow down, the stopping power increases which leads to the characteristic rise in the Bragg peak. Since nonelastic nuclear reactions remove protons from the primary beam, this has the effect of lowering the peak and raising the buildup region upstream of the peak. The width of the peak is related to range straggling and spread in energy. There are various widths to characterise the peak, but the two common ones are: the 80 %-to-20 % distal-falloff length d_{80-20}, and the 80 %-to-80 % peak width. According to Paganetti [58], a relation for the d_{80-20} width is:

$$d_{80-20} = 1.3 \times \sqrt{{\sigma_{\mathrm{RS}}}^2 + {\sigma_{\mathrm{beam}}}^2}, \tag{3.28}$$

where σ_{RS} and σ_{beam} are the range straggling and energy spread respectively. Furthermore, the width of the Bragg peak increases with the range as can be seen in fig. 3.5.

MCS will also affect the Bragg peak. As the beam scatters, the fluence decreases with depth according to $1/r^2$ since the surface area of a sphere is proportional to the square of the radius, with r representing the distance from the origin to the region of analysis. Since dose is a product of the fluence and mass stopping power, the decrease in fluence can counteract the increase of stopping

power with depth. This results in the Bragg peak being less pronounced for larger transverse beam sizes.

3.6 Conventional Dosimeters for Proton Beams

Characterisation and dosimetry of treatment beams is critical for treatment planning. Radiation dosimeters are devices that measure various quantities of ionising radiation such as the dose. Some conventional detectors used for dosimetry of proton beams will be introduced below. Most dosimeters are destructive, such that the radiation particles ceases to exist after measurement. The choice of radiation dosimeter used depends on the requirements of the user.

3.6.1 Calorimeters

Calorimeters can be used to measure the absorbed dose in a medium. As the dose-to-water is an important quantity for radiotherapy, a conversion from a dose-to-medium to dose-to-water needs to be made, which can be a major source of uncertainty. A calorimeter measures the change in temperature of a medium, ΔT_{medium}, which changes due to the deposition of energy. Multiplying the change in temperature by the specific heat capacity of the medium c_{medium}, and applying correction factors gives the absorbed dose in the medium:

$$D_{\text{medium}} = c_{\text{medium}} \times \Delta T_{\text{medium}} \times \frac{\prod k_i}{1-h}, \tag{3.29}$$

where h is the heat defect and $\prod k_i$ represents the product of various correction factors [58]. The heat defect is defined as:

$$h = \frac{E_a - E_h}{E_a}, \tag{3.30}$$

where E_a is the energy absorbed locally and E_h is the energy in the form of heat. The heat defect corrects for temperature changes due to radiation-induced chemical changes in the medium. The heat defect can be calculated analytically or by simulating the chemical changes in an irradiated medium. Although the heat defect has a dependence on the LET, the relationship is not known precisely. Another source of concern with calorimeters is related to how heat conduction can affect measurements. Due to heat conduction, heat can be transferred both away from or towards the measurement point. To mitigate this, a medium with low thermal diffusivity such as water can be used.

Solid calorimeters composed of crystalline materials are another option for calorimeters. As an

example, graphite has a thermal diffusivity three order of magnitudes greater than water, causing heat conduction to become a more prominent effect. However, the dose needs to be converted to dose-to-water.

It is interesting to note that calorimeters are also commonly used in particle physics. They are often used to detect and identify individual particles in a beam. However, a single calorie corresponds to $\sim 10^7$ TeV, far higher than the energies seen in modern experiments. Hence, a single particle alone would only give a negligible rise in temperature for detecting particles. Instead of measuring the temperature change, other processes are used to convert the energy deposited into a detectable response. An example is scintillation light resulting from ionisation of the calorimeter medium. From the energy deposited, information about the particle can be determined.

3.6.2 Faraday Cups

To measure the particle fluence of a proton beam, a Faraday cup can be used. The Faraday cup measures the electric current of the protons interacting with the metal in the cup, which determines the number of particles. The relationship of dose to fluence in eq. 3.11 and the inclusion of correction factors $\prod k_i$ [58], gives a dose of,

$$D_w(z) = \Phi \times \frac{S_w(z)}{\rho_w} \times \prod k_i. \tag{3.31}$$

The subscripts refer to the dose delivered to water. A concern arises due to the generation of electrons which may reduce or increase the signal in the collecting electrode. To counter this effect, a guard electrode is used to suppress this effect. If the beam characteristics are well defined, the dose can be determined with good accuracy [79].

3.6.3 Ionisation Chambers

Ionisation chambers are gas-filled cavities surrounded by a conductive outer wall. When the gas is ionised, the movement of ions to the collecting electrodes gives a measure of the current. Guard electrodes are also added to reduce leakage of current. Both the Bragg-Gray and Spencer-Attix cavity theory can be applied to ionisation chambers.

The Bragg-Gray cavity theory [80] relates the dose in a dosimeter to the medium surrounding it. For this theory to be applicable two conditions must be satisfied:

1. The presence of the cavity does not perturb the fluence of charged particles (small cavity compared to charged particle range).

2. Only charged particles cross the cavity deposit dose.

Under these two conditions, the dose delivered to a medium can be related to the dose delivered to the cavity through,

$$D_{\text{med}} = D_{\text{cav}} \left(\frac{\overline{S}}{\rho} \right)_{\text{cav}}^{\text{med}} p, \tag{3.32}$$

where $\left(\frac{\overline{S}}{\rho} \right)_{\text{cav}}^{\text{med}}$ is the ratio of the average unrestricted mass collisional stopping power of the medium to the cavity and p is an ionisation chamber perturbation factor. The perturbation factor corrects for deviations from the Bragg-Gray condition [81]. For an ionisation chamber, the dose to the cavity is given by:

$$D_{\text{cav}} = \frac{Q}{m} \left(\frac{\overline{W}}{e} \right)_{\text{cav}}, \tag{3.33}$$

where Q is the ionization per unit volume, m is the mass of the medium in the cavity, and $\left(\overline{W} / e \right)_{\text{cav}}$ is the mean energy to produce an ion pair in the medium.

The Spencer-Attix cavity theory [82] generalises the Bragg-Gray cavity theory by accounting for delta electrons which may take energy away from the cavity. The two conditions for the Bragg-Gray theory must still hold and now must also be applicable to the delta electrons. In particular, the delta electrons must have sufficient energy to cross the cavity. This is done by specifying a threshold value, Δ, for the electron energy. The Spencer-Attix relation is similar to the Bragg-Gray relation and is given by:

$$D_{\text{med}} = D_{\text{cav}} \left(\frac{\overline{L_{\Delta}}}{\rho} \right)_{\text{cav}}^{\text{med}} p, \tag{3.34}$$

where $\left(\frac{\overline{L_{\Delta}}}{\rho} \right)_{\text{cav}}^{\text{med}}$ is the ratio of the average restricted mass collisional stopping power of the medium to the cavity.

3.6.4 Radiographic/Radiochromic Films

Radiographic and radiochromic films darken when exposed to radiation. Lookup tables are used to convert the optical density (degree of darkening) into the absorbed dose. The relationship between optical density and absorbed dose is typically nonlinear. Since the LET for protons can vary over the range, the response of the film will vary. In order to reconstruct the dose, information needs to be known about the beam and the response of the film needs to be modelled.

The main difference between radiographic and radiochromic film is that radiochromic films can be irradiated under ambient light. Radiochromic films also exhibit a linear response for a larger dose

range [83].

3.6.5 Detector Arrays

2D detector arrays are easy to use and can be used for fast real-time measurements, making them common for quality assurance purposes. The 2D detector arrays are equipped with a series of ionization chambers or diodes. A downside of these detectors is that the resolution is limited based on the size and distance of the detectors. The main challenges with using these detectors is in verifying the outputs and measured profiles.

Chapter 4

Laser Plasma Ion Acceleration

The target normal sheath acceleration (TNSA) interaction will be a key focus of the Stage 1 source simulations for LhARA in chapter 7. To provide context, basic laser and plasma concepts will be presented. This will be followed by an introduction to the interactions between lasers and plasmas. Finally, a brief overview of a typical implementation of particle in cell (PIC) codes will be given.

4.1 Plasma Properties

Plasmas are one of the states of matter and commonly consist of a population of positively charged ions and electrons. The definition given by Chen [84] is a: "quasineutral gas of charged particles which exhibits collective behaviour". Quasineutrality refers to the overall charge density of free electrons and ions cancelling out in equilibrium. In a plasma, the motion of charged particles leads to local concentrations of charge which generate currents, giving rise to electromagnetic fields. Collective behaviour refers to how macroscopic fields will dominate the microscopic fluctuations. In other words, long ranged electromagnetic forces dominate the short ranged collisional interactions.

A plasma can be classified according to its temperature and density. At thermal equilibrium, the most probable distribution for particles is the Maxwellian distribution [84]. In a plasma, ions and electrons can have different Maxwellian distributions which correspond to different temperatures within a plasma.

4.1.1 Electron Plasma Frequency

A plasma will maintain quasineutrality by readjusting to a disturbance. This can be understood by considering that when a population of electrons within a plasma is displaced, the resulting separation of charge creates a field with a restoring force [85]. Due to this restoring force, electrons will be pulled

back to their initial positions. However, due to inertia the electrons will overshoot and reverse the electric field. This leads to an oscillation which is characterised by the electron plasma frequency ω_{pe}. In a simple ideal case of fixed ions, no thermal effects, and no magnetic fields, the electron plasma frequency is given by:

$$\omega_{pe} = \sqrt{\frac{n_e e^2}{\gamma \varepsilon_0 m_e}}, \tag{4.1}$$

where n_e is the electron number density, e the electron charge, ε_0 the permittivity of free space, γ is the Lorentz factor for relativistic effects from the electron quiver motion, and m_e the mass of an electron. If thermal effects are included, the oscillations propagate with a frequency given by the dispersion relation [84]:

$$\omega^2 = \omega_{pe}^2 + \frac{3}{2}k^2 v_{\text{th}}^2, \qquad v_{\text{th}} = \sqrt{\frac{2k_B T_e}{m_e}}, \tag{4.2}$$

where k is the wavenumber, k_B is the Boltzmann constant, and T_e is the temperature of electrons.

4.1.2 Critical Density

The critical density is the density in a plasma into which light can no longer penetrate. This quantity can be determined by first considering the dispersion relation for an electromagnetic wave which has a magnetic field orthogonal to the electric field propagating through a plasma [84]:

$$\omega_L^2 = \omega_{pe}^2 + c^2 k^2. \tag{4.3}$$

From the dispersion relation, the phase velocity v_p, and group velocity v_g, can be calculated:

$$v_p = \frac{c}{\sqrt{1 - \frac{\omega_{pe}^2}{\omega_L^2}}}, \qquad v_g = c\sqrt{1 - \frac{\omega_{pe}^2}{\omega_L^2}}. \tag{4.4}$$

The electron plasma frequency and laser frequency gives several timescales to consider. If the laser frequency is smaller than the electron plasma frequency ($\omega_L < \omega_{pe}$), the plasma is described as being *overdense*. The group velocity becomes imaginary, so the laser can no longer propagate in the plasma. This is due to the electron oscillations cancelling the electric field of the laser, and results in the plasma reflecting the majority of the laser. If instead the laser frequency is greater than the plasma frequency ($\omega_L > \omega_{pe}$), the plasma is *underdense*. In this case, the electrons are unable to fully cancel the electric field of the laser. This allows the laser to propagate through the plasma. The boundary between the two conditions is when the laser frequency equals the plasma frequency

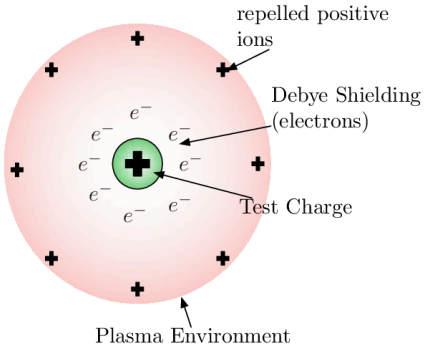

Figure 4.1: Illustration of Debye shielding from Schaub *et al.* [86].

($\omega_L = \omega_{pe}$). At this point, the group velocity drops to zero and gives the critical density,

$$n_{\mathrm{cr}} = \gamma \frac{\varepsilon_0 m_e \omega_L^2}{e^2}. \tag{4.5}$$

4.1.3 Debye Length

Another important property to consider is how plasmas screen external electric fields. This phenomenon is known as Debye shielding [84]. One can consider a ball of positively charged particles introduced into a plasma. A cloud of electrons will be attracted and surround the ball, damping the electric field. This shielding effect can be seen in fig. 4.1.

At thermal equilibrium, the electron and ion density will be distributed according to the Maxwell-Boltzmann law [84], which for electrons is given by:

$$n_e = n_i \exp\left(\frac{e\Phi}{k_B T_e}\right), \tag{4.6}$$

where n_i is the ion number density , Φ is the electrostatic potential by an external disturbance, and T_e is the temperature of the electrons. Poisson's equation gives:

$$\nabla^2 \Phi = -\frac{\rho}{\varepsilon_0} = -\frac{e}{\varepsilon_0}\left(n_i - n_e\right). \tag{4.7}$$

In the absence of a potential, we assume the electron density is the same as ions ($n_i = n_0$). By substituting the Boltzmann relation into Poisson's equation and solving the differential equation we get in spherical geometry:

$$\Phi(r) = \frac{1}{4\pi\varepsilon_0 r} \exp\left(-\frac{r}{\lambda_D}\right), \tag{4.8}$$

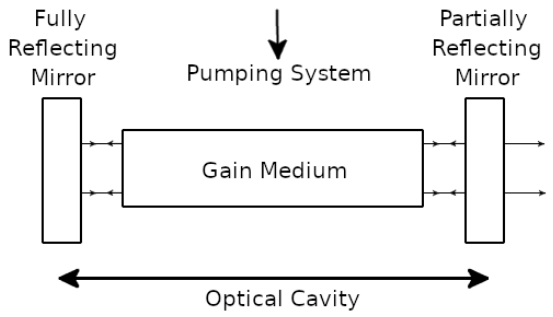

Figure 4.2: Basic structure of a laser system.

where r is the radial distance and the quantity λ_D is the Debye length given by:

$$\lambda_D = \sqrt{\frac{\varepsilon_0 k_B T_e}{e^2 n_0}}, \tag{4.9}$$

This definition of the Debye length neglects the ion contribution when the ion temperature is much lower than electrons. From eq. 4.8, it can be seen that the Debye length gives the distance over which the electrostatic potential is screened. A sphere with a radius given by the Debye length is known as a Debye sphere. The number of particles within the Debye sphere, N_D, parametrises the interactions that dominate. For an ideal plasma,

$$N_D \equiv n_e \frac{4\pi}{3} {\lambda_D}^3 \gg 1. \tag{4.10}$$

where n_e is the number density of electrons. It can be seen that an ideal plasma has high temperatures. Furthermore, if one considers the collision rate of electrons and ions [85], an ideal plasma will also have low densities. This arises from the fact that when the number density increases, the mean distance between particles decreases, increasing collisional interactions. A plasma becomes non-ideal when the mean energy of the interparticle interactions becomes comparable to the thermal motion.

4.2 Laser Properties

The laser was proposed by Towns and Schawlow in 1958 [87] to extend the maser to optical frequencies. The basic elements of a laser are [88]: a laser medium (gain medium), a pumping process to excite atoms, and optical feedback elements to either reflect or transmit radiation. The optical cavity refers to the arrangement of these elements, with the simplest configuration consisting of two mirrors surrounding a gain medium. These mirrors are given coatings where one mirror will primarily reflect light, while the other can both reflect and transmit. Such an optical cavity can be seen in fig. 4.2.

4.2.1 Electron Motion in a Laser Field

The electromagnetic fields cause particle motion which is governed by the Lorentz force. The equation of motion for electrons is given by:

$$\mathbf{F} = \frac{\mathrm{d}\mathbf{p}}{\mathrm{d}t} = -\,e\,(\mathbf{E} + \mathbf{v} \times \mathbf{B})\,, \tag{4.11}$$

where e, $\mathbf{p}$, and $\mathbf{v}$ are the magnitude of charge, momentum, and velocity of an electron. In the non-relativistic regime, the electric field component dominates, but as the velocity approaches the speed of light, the contribution of the magnetic field component increases. These two components will affect the type of interactions that can occur.

The amplitude of the electron oscillation motion for a linearly polarised laser is [88, 89]:

$$a_0 \equiv \frac{eE_L}{m_e\omega_L c} = \frac{e}{m_e c}\frac{\lambda_L}{2\pi c}\left(\frac{2I_L}{\varepsilon_0 c}\right)^{1/2} \simeq 0.85\sqrt{I_L[10^{18}\ \mathrm{W/cm^2}] \times (\lambda_L[\mu\mathrm{m}])^2}, \tag{4.12}$$

where E_L is the amplitude of the electric field, m_e is the mass of an electron, ω_L is the frequency of the laser, λ_L is the wavelength of the laser, $I_L = \varepsilon_0 c|\mathbf{E}|^2/2$ is the laser intensity, and c is the speed of light. The quantity a_0, is the normalised peak vector potential or the laser strength parameter. For a value $a_0 \gg 1$, the electron motion is highly relativistic. Such a regime generally requires laser intensities much greater than 10^{18} W/cm^2. A useful aspect of this parameter is how it can be used to compare laser systems, as it relates the electromagnetic field to the electron response.

4.2.2 Laser Beam Characteristics

An important property of a laser is the polarisation, which gives the direction of the electric field. Light has three types of polarisations: linear, circular, and elliptical. For linear polarisation, there are two orthogonal states: p- and s-polarisation. These states are defined relative to the plane of incidence as seen in fig. 4.3. P-polarised light has its electric field polarised parallel to the plane of incidence, while s-polarisation is perpendicular to the plane. As will be discussed, different interactions can occur based on the polarisation.

Laser beams are typically modelled by Gaussian beams where the profile of the intensity is described by a Gaussian function:

$$I(r,z) = I_0 \exp\left(-\frac{2r^2}{w(z)^2}\right) = \frac{2P_0}{\pi w(z)^2}\exp\left(-\frac{2r^2}{w(z)^2}\right), \tag{4.13}$$

where I_0 is the peak intensity, P_0 is the total power transmitted by the beam, $w(z)$ is the radius of

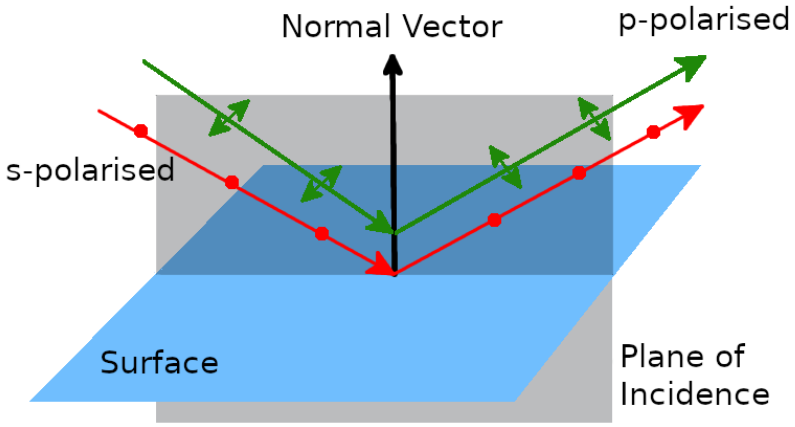

Figure 4.3: Two beams with p- (green with arrows along the plane of incidence) and s-polarisation (red with arrows going into the plane of incidence) relative to the plane of incidence containing the normal vector to the surface.

the beam where the intensity falls to $1/e^2$, r is the radial distance from the axis, and z is the distance along the direction of propagation.

The radius of the beam is given by:

$$w(z) = w_0 \sqrt{1 + \left(\frac{\lambda_L z}{\pi {w_0}^2}\right)^2}, \tag{4.14}$$

where w_0 is the minimum spot size at a position $z = 0$ and is known as the beam waist, while λ_L is the wavelength of the laser. Another beam size quantity used is the full width at half maximum (FWHM), w_{FWHM}. This quantity gives the size of the beam when the intensity falls to half the maximum value and can be related to $w(z)$ by considering the Gaussian equation for the intensity to give:

$$w(z) = \frac{w_{\mathrm{FWHM}}}{\sqrt{2 \ln 2}}. \tag{4.15}$$

For a Gaussian beam, the peak power of the laser, P_{peak}, is related to the energy of the laser pulse E by:

$$P_{\mathrm{peak}} = 2\sqrt{\frac{\ln 2}{\pi}} \frac{E}{\tau_0} \simeq 0.94 \frac{E}{\tau_0}, \tag{4.16}$$

where τ_0 is the duration of the laser pulse at FWHM.

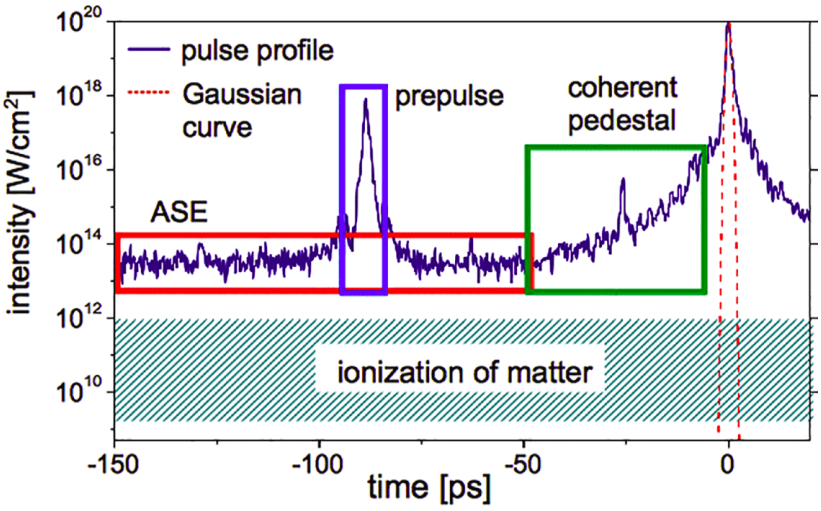

Figure 4.4: Temporal profile of the PHELIX pulse with various structures highlighted. The shaded region shows the ionisation threshold for typical materials, and the red dashed line is a fitted Gaussian function to the main pulse. Figure taken from Wagner *et al.* [93].

Generating Intense Laser Pulses

Innovations with technology led to the development of more intense lasers and the delivery of shorter pulses. Some of these technological innovations are: Q-switching, mode locking, and chirped pulse amplification. As the laser intensities increased, self focusing (as will be described in sec. 4.2.5) becomes a bigger problem and could lead to the laser gain becoming damaged.

A solution to this problem is with chirped pulse amplification (CPA), proposed by Strickland and Mourou [90]. The CPA technique stretches the ultrashort laser pulse in time by a dispersive element. This allows the light to be amplified to a higher power while still having a relatively low intensity. The amplified laser pulse is then compressed to the original pulse width, producing an intense and ultrashort pulse.

However, for pulses generated by chirped pulse amplification, a pedestal of light can be generated forming prepulses and postpulses before and after the main pulse. These structures tend to have lower intensities and different durations, affecting the temporal intensity contrast of the laser. These can also lead to effects such as generating a preplasma on the front of solid targets [91, 92]. The temporal profile of a pulse from the PHELIX laser from 2010 [93] can be seen in fig. 4.4 which shows the pedestal and prepulses that precede the main pulse.

The contributions that affect the temporal intensity contrast can be divided into four categories [94]: (i) Prepulses generated due to pulses leaking from the laser system, (ii) pre/post-pulses generated by secondary reflections that overlap with the main pulse, (iii) deterioration of the main pulse due to scattered light from the gratings, and (iv) amplified spontaneous emission (ASE) from fluorescence emitted during amplification. Of these contributions, ASE is the most difficult to sup-

press. ASE occurs when the gain medium is pumped to achieve population inversion and allow stimulated emission. When spontaneous emission occurs, photons are emitted in random directions. Some of these photons will be emitted with an angle that enables light to be amplified. This leads to a substantial prepulse which arrives ahead of the main pulse. A solution to improve the contrast is with plasma mirrors [95]. When the prepulse is incident on a plasma mirror, the prepulse will be transmitted and ionise the surface of the mirror. This creates a plasma which can reflect the main pulse. Another solution is to use optical parametric chirped pulse amplification (OPCPA) [96] which avoids the problems of ASE.

4.2.3 Motion of an Electron in a Laser Field

For an electron in an electromagnetic field, it will experience the Lorentz force. For a linearly polarised laser propagating in the z direction, it will have an electric and magnetic field of the form:

$$\mathbf{E} = E_0 \cos(kz - \omega_L t)\,\hat{\mathbf{x}}, \tag{4.17}$$

$$\mathbf{B} = B_0 \cos(kz - \omega_L t)\,\hat{\mathbf{y}}. \tag{4.18}$$

The magnitudes of tghe electric and magnetic field can be related by $E_0 = cB_0$. This gives equations of motion as:

$$m_e \dot{v_x} = -eE_0 \cos(kz - \omega_L t), \tag{4.19}$$

$$m_e \dot{v_y} = 0, \tag{4.20}$$

$$m_e \dot{v_z} = -\frac{ev_x E_0}{c} \cos(kz - \omega_L t). \tag{4.21}$$

Integrating the equations of motions above by time and assuming an initial case where the electron is at rest will give the velocities:

$$v_x = -\frac{eE_0}{m_e \omega_L} \sin(kz - \omega_L t) + constant = a_0 c \sin(kz - \omega_L t), \tag{4.22}$$

$$v_y = 0, \tag{4.23}$$

$$v_z = \left(\frac{a_0^2 c}{4}\right) \cos[2(kz - \omega_L t)] + constant = -\left(\frac{a_0^2 c}{2}\right) \sin^2(kz - \omega_L t), \tag{4.24}$$

where the normalised vector potential a_0 was substituted into the expressions. Finally the position

of the electron motion can be found by integrating again to give:

$$x = \frac{a_0 c}{\omega_L}\left[\cos\left(kz - \omega_L t\right) - 1\right] \tag{4.25}$$

$$y = 0 \tag{4.26}$$

$$z = \frac{a_0^2 c}{4} t - \left(\frac{a_0^2 c}{8\omega_L}\right)\sin\left[2\left(kz - \omega_L t\right)\right] \tag{4.27}$$

4.2.4 Ponderomotive Force

The ponderomotive force is a nonlinear force acting on a plasma due to inhomogeneous oscillating electromagnetic fields. This results in electrons being pushed away from the centre of the beam to regions with weaker electromagnetic fields. Since the laser intensity is reduced at the new region, the restoring force is also less, leading to electrons being pushed further away. The ponderomotive force, $\mathbf{F}_{\mathrm{pm}}$, acting on an electron is given by [89]:

$$\mathbf{F}_{\mathrm{pm}} = -\frac{e^2}{2m_e{\omega_L}^2}\nabla\left\langle \mathbf{E}^2 \right\rangle = -\frac{e^2}{4m_e{\omega_L}^2}\nabla\left\langle E_0(x)^2\left(1 - \cos(2\omega_L t)\right)\right\rangle, \tag{4.28}$$

$$= -\frac{e^2}{4m_e{\omega_L}^2}\nabla E_0(x)^2 = -\nabla U_p, \tag{4.29}$$

where the cycle-average was taken for a linearly polarised electromagnetic wave, $\mathbf{E} = E_0(x)\cos\left(\omega_L t\right)$, propagating in the longitudinal direction in order to get from eq. 4.28 to eq. 4.29, and U_p is the ponderomotive potential. The relativistic ponderomotive force in the lab frame is given by Mora and Antonsen [97]:

$$\mathbf{F}_{\mathrm{pm,rel}} = -\frac{1}{\overline{\gamma}}\nabla U_p, \qquad \overline{\gamma} = \sqrt{1 + \frac{\overline{p}^2}{m_e^2 c^2} + \frac{2}{m_e^2 c^2}U_p}, \tag{4.30}$$

where $\overline{p}$ is the cycle averaged momentum.

4.2.5 Self Focusing

Self focusing arises from a change in the local refractive index of a plasma due to a laser pulse. When the refractive index varies, the laser beam gains curvature, and the plasma acts as a converging lens [98]. Two important cases for self focusing are Kerr-induced self focusing and plasma self focusing.

Kerr-induced self focusing occurs when an intense laser interacts with the surrounding medium. This causes a variation in the refractive index which can be described by [98]:

$$\eta = \eta_0 + \eta_2 I, \tag{4.31}$$

where η_0 and η_2 are the linear and non-linear parts of the refractive index, and I is the laser intensity. From the expression it can be seen that the refractive index becomes larger in regions where the intensity is highest.

Plasma self focusing primarily occurs in three forms [98]: thermal, relativistic, and ponderomotive. Thermal self focusing occurs when strong electromagnetic radiation interactions generate collisional heating of the plasma. The rise in the plasma temperature leads to an increase in the refractive index.

Relativistic self focusing occurs due to the mass of electrons increasing as they approach the speed of light which leads to a change in the refractive index by:

$$\eta = \sqrt{1 - \frac{{\omega_{pe,\mathrm{rel}}}^2}{\omega_L^2}} = \sqrt{1 - \frac{1}{\gamma}\frac{{\omega_{pe}}^2}{\omega_L^2}}. \tag{4.32}$$

The refractive index is maximised where the Lorentz factor is greatest (along the laser axis). The intensity of laser falls transversely away from the axis, which is accompanied by a drop in the refractive index.

Finally, ponderomotive self focusing is due to the ponderomotive force pushing electrons away from high intensity regions as was discussed in sec. 4.2.4. This fall in the electron density leads to an increase of the refractive index by [98]:

$$\eta = \sqrt{1 - \frac{n_e}{n_{\mathrm{cr}}}}. \tag{4.33}$$

4.3 Laser Plasma Absorption Interactions

There are many interactions that can occur when a laser interacts with a plasma. These effects depend on the properties of the laser and plasma. Some of these absorption interactions will be described below.

4.3.1 Inverse Bremsstrahlung

The laser can be absorbed in a plasma through non-adiabatic interactions with electrons in the plasma through inverse Bremsstrahlung (IB), also referred to as collisional absorption [89]. The electrons which oscillate in the laser field can collide with the ions in the plasma, which results in energy transferred to the plasma [99].

This effect becomes less dominant for faster electrons which undergo fewer collisions. As the frequency of IB interactions is largest for dense and cool plasmas at low laser intensities, this effect is most relevant during the early stages of the laser interaction. At laser intensities above 10^{16} W/cm^2 [100], the laser becomes inefficient at transferring energy to the electrons through IB heating.

4.3.2 Resonance Absorption

Resonant absorption occurs for a laser with p-polarisation incident at a non-zero angle, θ, when the component of the electric field normal to a surface couples with the plasma oscillations. The laser penetrates the surface up to a density given by the relation $n = n_{cr}\cos(\theta)^2$ [101]. An evanescent field will extend beyond this surface, driving a plasma wave resonant near the critical density, and heats the plasma [101]. For a laser with s-polarisation, no component of electric field is normal to the surface, so no induced resonance will occur.

An approximation of the absorption rate of energy into the plasma, $\eta_{\text{abs,ra}}$, is given by [89, 102] where:

$$\eta_{\text{abs,ra}} = \frac{\Phi(\tau)^2}{2}, \tag{4.34}$$

$$\Phi(\tau) = 2.3\tau \exp\left(-\frac{2\tau^3}{3}\right), \tag{4.35}$$

$$\tau = (k_L L)^{\frac{1}{3}} \sin\theta. \tag{4.36}$$

In the formulae, $\Phi(\tau)$ is the Ginzburg curve, k_L is the wavenumber of the laser, L is the density scale of the plasma, and θ is the angle of incidence. It can be seen from the definition of τ and η_{abs} that the absorption rate drops to zero when $\theta = 0$, corresponding to normal incidence. Resonance heating appears to increase with the incidence angle, but at large angles there are competing effects from the plasma density through the relation $n = n_{cr}\cos(\theta)^2$, which can reduce the heating.

This is supported by investigations conducted by Ping *et al.* [103] on the absorption rates of solid targets for laser pulses at intensities ($> 10^{17}$ W/cm^2). It was found that the absorption was enhanced with a maximum laser absorption of 90% for an incident angle of 45° compared to 60% for a near incidence angle of 6°.

4.3.3 Vacuum Heating

A similar mechanism to resonance heating is vacuum or Brunel heating. This mechanism occurs for an ultra-short laser pulse, p-polarised, at high intensity, and incident at an oblique angle for a steep electron density profile [89, 104]. Electrons near the plasma boundary heated by the p-polarised laser field are dragged out to the vacuum according to the period of the laser. After half a cycle, the laser field reverses and accelerates these electrons back into the plasma. These electrons can acquire high energies and penetrate deep into the target until absorbed through collisions [105]. This effect results in bunches of electrons accelerated into the target at the frequency of the laser pulse.

Brunel modelled this with a capacitor model where it was assumed the target is a perfect conduc-

tor. In a relativistic regime, the fractional absorption rate for vacuum heating is [89, 104]:

$$\eta_{\mathrm{abs,vh}} = \frac{4\pi \left(\frac{\sin^2(\theta)}{\cos(\theta)}\right)}{\left(\pi + \frac{\sin^2(\theta)}{\cos(\theta)}\right)^2}. \tag{4.37}$$

Cai *et al.* [105] later extended this model to give a self-consistent analytical model.

4.3.4 J×B Heating

For linearly polarised light at high laser intensities, the magnetic field component of the Lorentz force becomes comparable to the transverse motion of the electric field. This results in a significant push to the electrons in the longitudinal direction. The main difference between vacuum heating and $\mathbf{J} \times \mathbf{B}$ heating is the oscillation frequency. From the longitudinal motion given in eq. 4.27, it can be seen that there are two components to the forward motion. The laser pulse will accelerate electrons on the surface into the target at twice the laser frequency [106]. It can also be seen from eq. 4.24 that it depends on a_0^2, which indicates this mechanism becoming prevalent for high a_0 [107].

4.4 Target Normal Sheath Acceleration

Three pioneering experiments reported multi-MeV proton energies with beam-like properties in 2000: Clark *et al.* [25], Maksimchuk *et al.* [26], and Snavely *et al.* [27]. A large number of experimental results have since been reported by various groups using a variety of laser parameters. Many of these experiments rely on the target normal sheath acceleration (TNSA) mechanism. The term was first coined by Wilks *et al.* [108] when modelling the mechanism. In addition to TNSA, there are other acceleration mechanisms such as radiation pressure acceleration [30], break-out afterburner [109], and shock acceleration. However, these alternative mechanisms tend to require much higher laser intensities than are needed for TNSA.

The TNSA mechanism occurs when an intense laser pulse ($\gg 10^{18}\,\mathrm{W/cm^2}$) interacts with a solid thin target foil that has a thickness on the order of a few microns [108, 110]. The prepulse ionises the target surface and forms a preplasma on the front surface, helping to transfer the laser energy to electrons. The main pulse then propagates through the plasma. Interactions between the laser pulse and the plasma generates hot electrons which penetrates through the foil to the rear surface. A fraction of the electrons will have sufficient energy to leave the rear of the target, which builds up a potential that traps the rest of the electrons. Then the electrons circulate between the front and rear of the target, producing a sheath field on both sides (typically on the order of a few teravolts per metre) [110] to shield the field from the bulk plasma. The electrostatic fields on the front and

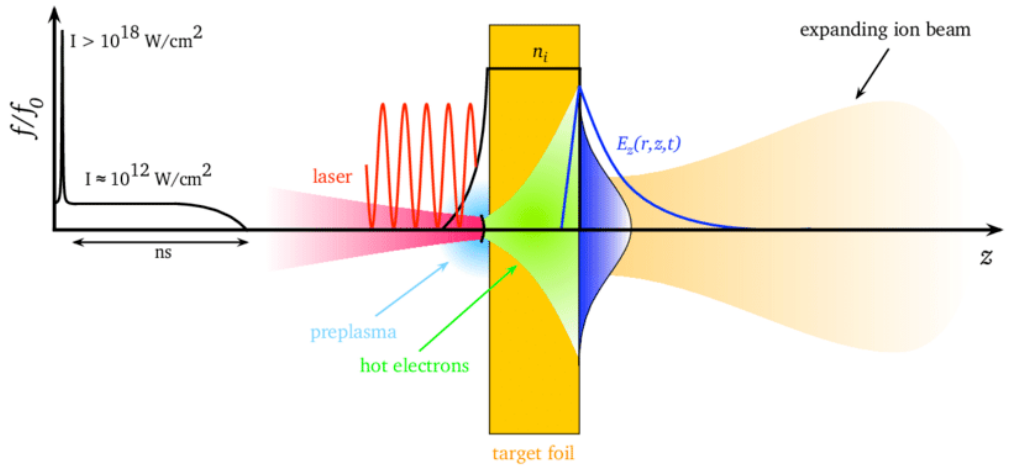

Figure 4.5: Schematic diagram of the target normal sheath acceleration (TNSA) interaction. The prepulse of an intense laser pulse creates a preplasma on the surface of the target foil. The main pulse interacts with the plasma and accelerates electrons to create a sheath field on the other side. Ions on the rear surface are then accelerated in the target normal direction. Figure taken from Roth *et al.* [110].

rear surface ionises atoms and accelerates ions out of the foil. Ions on the surface are primarily accelerated normal to the rear surface due to the direction of the charge separation field (giving rise to the name of the mechanism). However, in the early stages of the interaction there is a pronounced correlation of the ion distribution with the incident laser direction which can lead to non-target normal emission [111]. A schematic diagram of this interaction can be seen in fig. 4.5.

Typically, higher electron temperatures form stronger sheath fields, increasing the maximum ion energies achievable. Surface contaminants such as hydrocarbons are ionised and accelerated. Protons are predominantly accelerated due to its high charge-to-mass ratio [112]. Heavier ions are also accelerated but not as efficiently due to screening from the lighter ions. This can be improved through a stronger sheath field or by ridding the surface of unwanted contaminants. Particles accelerated by the TNSA mechanism will have a cut-off energy as can be seen in the energy spectrum in fig. 4.6.

It can be noted that laser plasma interactions create a current that typically exceeds the Alfvén limit [114, 115]. The Alfvén limit is the maximum current a beam can propagate in a plasma before it acquires a net backward motion due to its self-generated magnetic field. In the absence of return currents, these hot electrons would only propagate a short distance before moving backwards. For TNSA, the source for the return currents originates from the charge separation due to the hot electrons

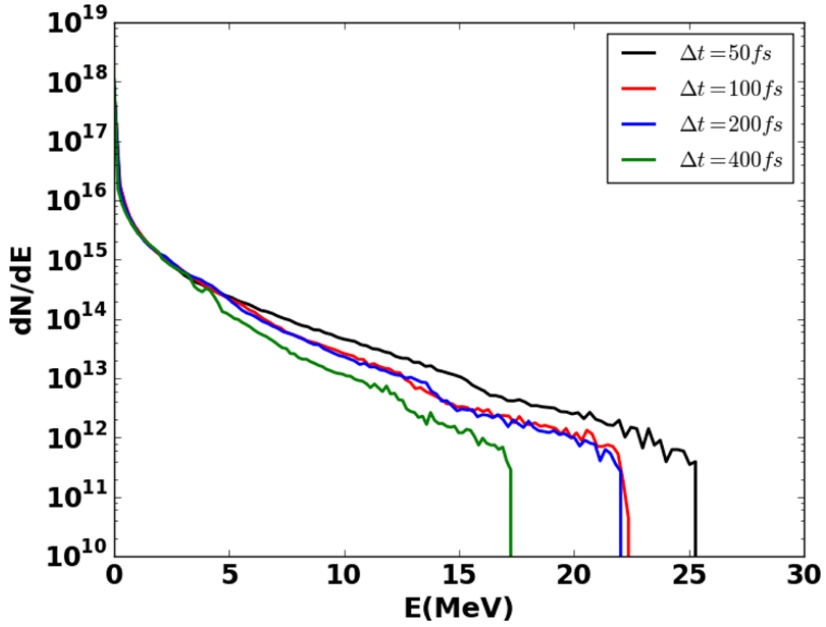

Figure 4.6: Example of the proton energy spectra for protons accelerated by the TNSA interaction from Kumar *et al.* [113].

ionising parts of the target [115]. This leads to a net current lower than the Alfvén limit, and allowing some of the electrons to escape the target.

4.4.1 Theoretical Models

An isothermal expansion model to describe the acceleration of ions was provided by Mora [116, 117]. This model for a collisionless plasma allows for the position and velocity of the ion front to be determined, under the assumption that the electron distribution corresponds to a Boltzmann distribution. The maximum energy for ions can be calculated from the ion plasma frequency, ω_{pi}, at a given time t much greater than 1 ($\omega_{pi}t \gg 1$) by [116]:

$$E_{i,\max} \simeq 2Zk_BT_e \left[\ln\left(\tau + \sqrt{\tau^2+1}\right)\right]^2 \approx 2Zk_BT_e \left[\ln\left(2\tau\right)\right]^2, \tag{4.38}$$

$$\text{where } \tau = \frac{\omega_{\mathrm{pi}}t}{\sqrt{2\exp(1)}}, \tag{4.39}$$

Z is the ion charge number, and $\exp(1)$ is Euler's number. The ion plasma frequency, ω_{pi}, is given by [116]:

$$\omega_{pi} = \left(\frac{n_{e0}Zk_BT_e}{m_i\varepsilon_0}\right)^{1/2}, \tag{4.40}$$

where m_i is the mass of the ion and n_{e0} is the electron density for an unperturbed plasma at time $t = 0$. However, a complication with the Mora model is the reliance on the hot electron temperature

T_e, which may not be known. A scaling of the hot electron temperature with the laser intensity was provided by Kluge *et al.* [118]:

$$T_e = \left(\frac{a_0^2}{4}\right) m_e c^2 \qquad (a_0 \ll 1), \tag{4.41}$$

$$T_e = \left(\frac{\pi a_0}{2\ln 16 + 2\ln a_0} - 1\right) m_e c^2 \qquad (a_0 \gg 1). \tag{4.42}$$

The temperature of the hot electrons from ultra intense laser interactions can also be described by the ponderomotive scaling given by Wilks *et al* [106]:

$$T_e = \left(\sqrt{1 + {a_0}^2} - 1\right) m_e c^2. \tag{4.43}$$

There are other models such as the Schreiber model [119] which gives a general expression relating the duration of the laser pulse to the maximum ion energy and gives good agreement to experiments with various ions. The Passoni-Lontano model [112, 120] uses a quasi-static approach where a static electron sheath only acts on light ions. It is also based on the electron distribution with a Maxwell-Jüttner relativistic electron distribution function. This avoids the problem in the Mora model where the accelerating electric field extends to infinity resulting in quantities diverging. It has been found that the model by Passoni *et al.* [112, 120] can provide good agreement with experimental results for laser intensities ranging between $10^{18} - 10^{21}\,\mathrm{W/cm^2}$.

Perego *et al.* [121] reviewed various models and compared model predictions to a database of experimental parameters and results. It was found that the quasi-static models provided better predictions for the maximum ion energy, particularly for the Passoni-Lontano model. But it was noted that the different models that were studied relied upon different quantities, with some of these quantities having to be estimated. Such quantities included the divergence of the electrons and the hot electron temperature.

4.5 Particle-In-Cell (PIC) Simulations

To model kinetic plasma interactions, particle-in-cell (PIC) codes are used. Particle-in-cell (PIC) codes simulate the dynamics of ensembles of particles using a number of *macroparticles*. This is useful for modelling plasmas which are ensembles of many particles interacting with each other. A typical implementation of PIC codes such as with Smilei [122] will be presented in this section.

The distribution function of the macroparticles, f_s, satisfies the Vlasov-Maxwell system of equa-

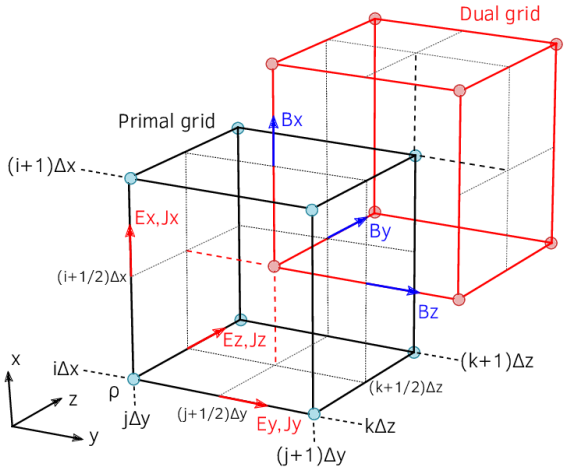

Figure 4.7: A representation of the staggered Yee grids taken from Massimo *et al.* [124].

tions [123]. Vlasov's equation is given by [122]:

$$\frac{\partial f_s}{\partial t} + \frac{\mathbf{p}}{m_s \gamma} \cdot \nabla f_s + \mathbf{F}_L \cdot \frac{\partial f_s}{\partial \mathbf{p}} = 0, \tag{4.44}$$

where $\mathbf{p}$ is the momentum, m_s is the mass of a species, γ is the Lorentz factor, and $\mathbf{F}_L$ is the Lorentz force. Instead of calculating the Coulomb force directly for each particle, the force can be calculated from the electric and magnetic fields. Maxwell's equations are calculated over a discrete spatial grid, with the space between points called *cells*.

The distribution functions are expressed as a discrete sum of macroparticles [122]:

$$f_s(t, \mathbf{x}, \mathbf{p}) = \sum_{p=1}^{N_s} w_p S\left(\mathbf{x} - \mathbf{x}_p(t)\right) \delta\left(\mathbf{p} - \mathbf{p}_p(t)\right), \tag{4.45}$$

where t is time, $\mathbf{x}_p$ is the position, $\mathbf{p}_p$ is the momentum, N_s is the number of macroparticles for a species, w_p is the numerical weight, $S(\mathbf{x})$ is the macroparticle shape function, and $\delta(\mathbf{p})$ is the Dirac delta function.

4.5.1 PIC Algorithm

PIC simulations start with an initialisation step. This involves: loading the macroparticle's position and momentum, computing the initial charge and current densities, computing the initial electric and magnetic fields, and adding user defined fields such as the laser field. The electromagnetic fields are discretised onto a Yee grid which helps to ensure the magnetic field is divergence free. The Yee grid staggers the field components within a grid cell, this allows for one field's components to be encircled by the other as can be seen in fig. 4.7.

After initialisation, the main PIC loop begins:

1. Compute the electromagnetic fields.
2. Update the position and momentum.
3. Calculate the charge and current density.
4. Solve Maxwell's equations to calculate the electromagnetic fields for the grid.
5. Apply boundary conditions for particles located outside the grid.

Particle Pusher

A solver called the particle pusher is used to advance the macroparticles. Typically a leap-frog integrator is used to calculate the momentum and position from the electromagnetic fields according to [122]:

$$\mathbf{u}_p^{(n+\frac{1}{2})} = \mathbf{u}_p^{(n-\frac{1}{2})} + \frac{q_s}{m_s}\Delta t\left[\mathbf{E}_p^{(n)} + \frac{\mathbf{u}^{(n+\frac{1}{2})} + \mathbf{u}^{(n-\frac{1}{2})}}{2\gamma^{(n)}} \times \mathbf{B}_p^{(n)}\right], \tag{4.46}$$

$$\mathbf{x}^{(n+1)} = \mathbf{x}^{(n)} + \Delta t\frac{\mathbf{u}_p^{(n+\frac{1}{2})}}{\gamma_p}, \tag{4.47}$$

where $\mathbf{u}_p = \mathbf{p}_p/m_s$ is the reduced momentum, q_s is the charge, $\gamma^{(n)} = \left(\gamma^{(n-1/2)} + \gamma^{(n+1/2)}\right)/2$ is the discretised Lorentz factor, and Δt is the timestep. As can be seen the particle is calculated every timestep, while the momentum is calculated at each half timestep.

Charge Conservation

Once the momentum and positions are calculated, the current and charge density is calculated. A charge-conserving algorithm proposed by Esirkepov [125] can be used to calculate the current and charge densities.

Maxwell Solvers

To solve Maxwell's equations, the Finite Difference Time Domain (FDTD) technique formulated by Yee [126] can be used [122]:

$$\mathbf{E}^{(n+1)} = \mathbf{E}^{(n)} + \Delta t\left[(\nabla \times \mathbf{B})^{(n+\frac{1}{2})} - \mathbf{J}^{(n+\frac{1}{2})}\right], \tag{4.48}$$

$$\mathbf{B}^{(n+\frac{3}{2})} = \mathbf{B}^{(n+\frac{1}{2})} - \Delta t\,(\nabla \times \mathbf{E})^{(n+1)}. \tag{4.49}$$

This technique is useful due to its straightforwardness and computational efficiency.

4.5.2 Numerical Heating

The discretisation of physical models in space and time (such as in PIC simulations) can lead to energy not being conserved, which is referred to as numerical heating [127]. One can consider a simulation in which a small number of macroparticle are used, then macroparticles moving from one cell to an adjacent one can lead to a significant fluctuation in the electric field. Grid aliasing is another cause of numerical heating where important details are not resolved if the grid spacing is too coarse. Typical solutions which overcome these instabilities includes: employing a large number of macroparticles per cell, and ensuring that the grid spacing resolves the Debye length.

The timestep of the simulation also plays an important role. Since the FDTD approach is used to calculate the electromagnetic fields as outlined above, the Courant-Friedrich-Lewy (CFL) condition [128] must be satisfied for stability, ensuring that electromagnetic waves only travel to adjacent cells. To satisfy this condition, a limit on the timestep for a 3D case is given by:

$$\Delta t \leq \frac{1}{c\sqrt{\frac{1}{\Delta x^2} + \frac{1}{\Delta y^2} + \frac{1}{\Delta z^2}}}. \tag{4.50}$$

As can be seen, there will be restrictions on the timestep for a given grid size.

Chapter 5

Current Day Hadron Therapy Accelerators

Accelerators have and continue to play a significant role in the development of cancer therapy. Hadron therapy was first proposed by Wilson in 1946 [9] and its development relied upon past technological breakthroughs which include [129]: the discovery of X-rays, the invention of the electron linac, and the invention of the cyclotron.

Röentgen first detected X-rays in 1895 [18]. When he conducted experiments with cathode rays he observed a glow coming from a fluorescent sheet. Due to the unknown nature of the radiation, he called it X-rays. After further investigation, Röentgen found that X-rays could penetrate into human flesh and be photographed. Soon after, Jones and Lodge used X-rays to image a bullet in the hand of a boy [130]. Following this, X-rays have since been used for tumour therapy [131, 132] and continue to be a common means of treatment.

Hansen first developed the idea of an electron accelerator in the 1930s but found existing microwave generators inadequate for particle acceleration. The klystron, a tube to amplify microwaves, was invented in 1939 by the Varian brothers [133] and it enabled Hansen to design and create an electron linear accelerator (linac) [20]. Using an electron linac, X-rays could be produced by accelerating electrons into a target. Alternatively, electron beams could also be used directly for therapy. This takes advantage of electrons having a shallow penetration depth accompanied with a rapid dose fall off. Hence, making electron beams particularly useful to treat tumours close to the skin surface.

Particularly critical to hadron therapy was the invention of the cyclotron. The development of accelerators was driven by a need in the particle physics community to generate a copious supply of particles more energetic than could be obtained from naturally radioactive sources for research. In 1928, Wideröe [134] proposed applying a radio-frequency voltage to drift tubes. Lawrence built upon

this concept but recognised a linear accelerator would be impractical. This led to the development of a cyclotron [24]. Cyclotrons quickly found use in medical applications, such as studies into the effect of fast neutrons on rats conducted in 1936 [135].

Brief mention will be made of various accelerators used in hadron therapy facilities. This will be followed by an overview of the beam line at MedAustron, a treatment facility making use of conventional technologies to deliver both protons and carbon ions for treatment.

5.1 Treatment Facility Accelerators

Hadron therapy treatment facilities consist of two essential sections, the accelerator and the treatment room. The accelerators needed to accelerate protons or ions tend to be large, requiring larger facilities compared to facilities delivering photons. To maximise the number of patients treated, these facilities often contain several treatment rooms.

5.1.1 Cyclotrons

Cyclotrons accelerate particles along a spiral track. At the centre of the cyclotron are two D-shaped electrodes (referred to as *dees*) as can be seen in fig. 5.1. Particles are injected between the two dees and when a voltage is applied, particles are accelerated towards one of the electrodes. Due to the magnetic field, the particles will bend as they travel through the dees. After the particles emerge from the electrode, the polarity of the voltage is reversed. This results in the particles being accelerated towards the other electrode where the process repeats until the beam is extracted. Since the extraction is determined by the radius, cyclotrons deliver a fixed energy. For treatment, the energy needs to be varied in order to irradiate the entire tumour volume. An energy degrader which consists of wedges is inserted into the beam line where energy will be lost due to interactions with the degrader material. The degree to which the degrader is moved into the beam path will dictate the amount of energy lost. The loss in energy is accompanied by a growth in the beam emittance due to scattering. Furthermore, the energy degradation can lead to a significant loss in the beam intensity. This requires the beam to be extracted at high currents in order to ensure a low energy beam can be delivered with sufficient intensity.

The period, T, for the particles to complete an orbit can be calculated:

$$T = \frac{2\pi r}{v} = \frac{2\pi}{v}\frac{mv}{qB} = \frac{2\pi m}{qB}, \tag{5.1}$$

where r is the radius, v is the speed, m is the particle mass, q is the particle charge, and B is the

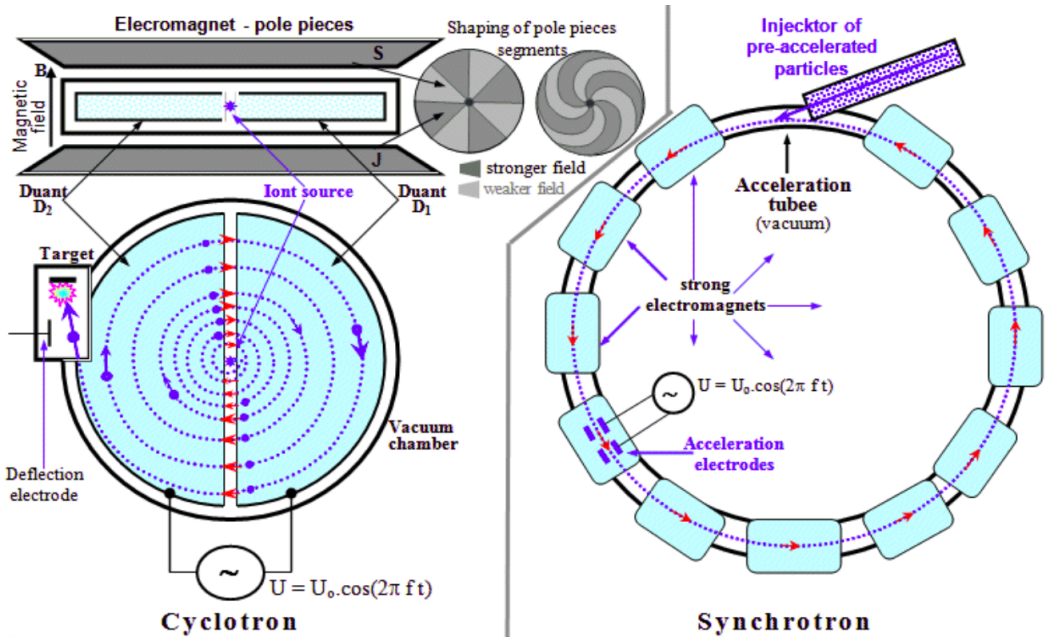

Figure 5.1: Schematic diagram of a cyclotron (left) and a synchrotron (right). Image taken from Ullmann [136].

magnetic field. The frequency, f, can then be calculated:

$$f = \frac{1}{T} = \frac{qB}{2\pi m}. \tag{5.2}$$

This is the cyclotron frequency and is independent of both speed and radius. As long as a voltage with the cyclotron frequency, f, is applied, the energy of the beam of particles will be boosted when the particles traverse the gap. This results in an outward spiral motion which increases with velocity. For protons above about 20 MeV [137], relativity cannot be neglected and modifies the frequency by:

$$f_{\text{rel}} = \frac{qB}{2\pi\gamma m}, \tag{5.3}$$

where γ is the Lorentz factor. From eq. 5.3, it can be seen that the frequency is no longer fixed but decreases as the energy increases. In order to accelerate relativistic particles, this effect needs to be compensated for. A *synchrocyclotron* has an oscillating electric field that decreases as the velocity increases to account for this. However, a drawback is that only one bunch can be accelerated at a time. This leads to a reduced beam intensity compared to a classical cyclotron. An alternative is the *isochronous cyclotron* which has a magnetic field that increases with radius so that the frequency can be kept constant, but can lead to beam instability.

5.1.2 Synchrotrons

In a synchrotron, particles move around a circular ring at a fixed radius. To achieve this, the magnetic field strength scales with the particle energy. As a result, unlike cyclotrons with a fixed extraction energy, the extraction energy can be varied in a synchrotron. The advantage of this is that energy degradation is not required. This results in a smaller beam emittance and energy spread compared to a cyclotron.

The dependence of the magnetic field with the energy can be found from the beam rigidity in eq. 2.9:

$$\frac{1}{\rho\,[m]} \simeq 0.3\frac{B\,[T]}{\beta E\,[GeV]} = 0.3\frac{B\,[T]}{cp\,[\mathrm{GeV}]}. \tag{5.4}$$

The magnetic field strength and frequency need to increase with the momentum to keep the radius constant. After the beam has been accelerated to the desired energy, the magnetic fields are kept constant (flat top). This allows for the beam to be slowly extracted over a few seconds which is beneficial for patient treatment.

5.1.3 Novel Developments

Linacs

Linacs have not typically been used for accelerating protons or heavier ions because reaching high energies would have required a very long accelerator. However, developments have recently been made for linac-based systems for particle therapy. A linac solution provides several advantages [138] which includes: an output energy that can be varied per pulse, an advantageous time structure for beam scanning, and a small transverse beam emittance. A project led by the TERA Foundation was to design a 3 GHz[1] compact proton linac (LIBO) [138]. A prototype was constructed and tested with a length of 13.5 m. It was shown that a beam of protons from a cyclotron could be boosted from 62 to 72 MeV [140]. Building upon this, the LIGHT (Linac for Image-Guided Hadron Therapy) accelerator is being designed as an industrial product to accelerate protons by ADAM (Application of Detectors and Accelerators to Medicine) [141].

Fixed-Field Alternating Gradient Accelerators

Fixed-field alternating gradient accelerators (FFA) combine aspects of cyclotrons and synchrotrons. The frequency is modulated and the magnet is split into sectors, allowing for higher energies to be

[1] The 3 GHz corresponds to the RF frequency commonly used in electron linacs. It is difficult to apply to protons due to the greater mass compared to electrons which would require very short cell lengths [139].

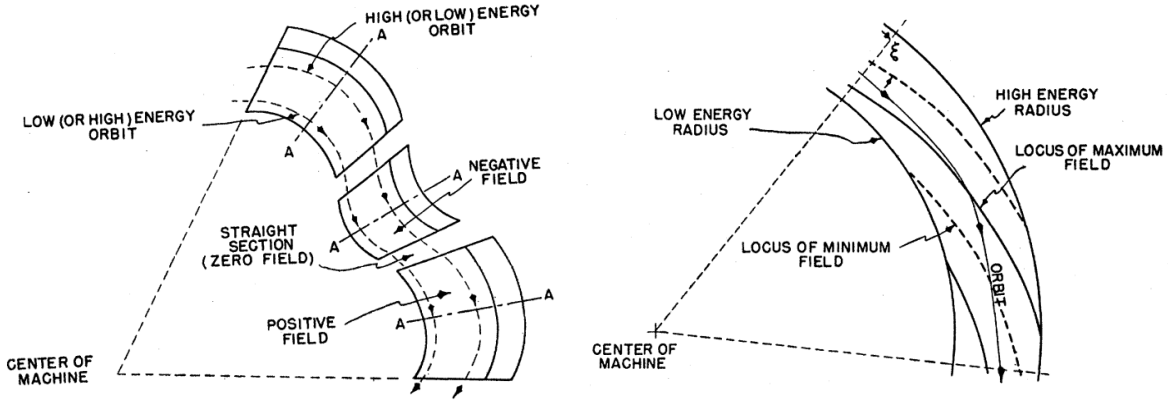

Figure 5.2: Plan view of FFA radial sector magnets (left) and spiral magnets (right) [144].

attained. The FFA concept was first proposed in the 1950s [142], but due to the complexities in the design, it only saw active develop in the 2000s [143].

An FFA makes use of radial or spiral sector magnets which are designed to have fields that vary in space as shown in fig. 5.2. The field increases towards the edge such that the orbits of accelerated particles will be confined. Compared to synchrotrons, FFAs allow for a larger acceptance and a higher repetition rate.

The tune of an accelerator corresponds to the frequency of beam oscillations during each pass in an accelerator. Normally betatron tunes are designed to be constant over acceleration and fixed away from resonance lines to prevent errors in magnets from building up. The first FFAs were designed to have constant tunes and are called *scaling* FFAs. The constraints placed on a scaling FFA makes the orbit shape at different energies similar and stable, but require complex magnets to achieve the required fields. In addition, the aperture and circumference of the machine must be made larger to accommodate the different orbits. Several scaling FFAs have been constructed, this includes two proton FFAs by Mori's group at KEK [145, 146].

Non-scaling FFAs relax the scaling laws. This means the orbit shapes for different energies do not have to be made similar, allowing for more compact orbits. However, this means the betatron tunes are no longer constant with energy, and vary throughout the acceleration cycle. This would normally be a concern, but if the acceleration is fast enough, the beam may cross the resonance lines fast enough to mitigate growth of the beam amplitude. EMMA (Electron Model for Many Applications) [147, 148] demonstrated this principle and the feasibility of non-scaling FFAs. PAMELA (Particle Accelerator for Medical Applications) [149] was a design study to apply the non-scaling FFA principles of EMMA to charged particle therapy for protons and carbon ions. Building upon the design of PAMELA was NORMA (Normal conducting Racetrack Medical Accelerator) [150], which used normal conducting magnets as opposed to superconducting magnets, but was only designed for protons.

Laser Driven Acceleration

Laser-driven acceleration can achieve a high accelerating gradient over a small length. There are several laser-based acceleration methods that can be used, but the most common method is target normal sheath acceleration (TNSA) [110]. In this method, the laser energy heats a thin foil to generate a large density of electrons. Proton energies of several tens of MeV can be achieved, with near-100 MeV energies obtained through a hybrid method of TNSA and radiation pressure acceleration (RPA) [31]. These electrons generate an intense electric field which ionises and accelerates ions from the foil. There are challenges associated with laser-driven acceleration which include the bulk of the ions having low energies and shot-to-shot fluctuations.

A non-exhaustive list of groups and projects making use of laser driven accelerators includes SCAPA [151], who focuses on the development of accelerator technologies and uses the beams for a variety of applications. HZDR [152] conducts experiments with the DRACO laser system (a Ti:Sapphire laser system) and aims to develop a laser system capable of attaining energies above 100 MeV [153]. ELIMAIA [154] operates in the RPA regime and aims to provide a stable and tuneable beam for multidisciplinary applications. A-SAIL [155] also operates in the RPA regime and incorporates other acceleration methods including hole-boring and shock acceleration. LhARA [33, 34] operates in the TNSA regime to create a large flux of protons or light ions which are captured by a series of strong-focusing plasma lenses. Post acceleration can be performed with an FFA to accelerate the beam to higher energies. More detail on LhARA will be provided in chapter 7.

5.2 Treatment Considerations

Modern radiotherapy divides treatment into several sessions, where 2 Gy is typically delivered per fraction [156]. Heavier ions could allow for fewer fractions, but must be accelerated to much higher energies to achieve the same treatment depths as with protons. Furthermore, for heavier ions the distal fall-off (region after the Bragg peak) is affected by processes like fragmentation.

The field size for treatment needs to cover the entire volume in terms of the lateral area and depth. One way is to passively scatter the treatment beam with scattering foils. Absorbers such as ridge filters or modulator wheels can also be used to form a spread-out Bragg peak (SOBP). Collimators are then used to shape the beam.

An alternative to passive scattering is instead to scan a narrow pencil beam across a target volume. Treatment typically starts with the highest energy to cover the deepest layer, then the energy is decreased sequentially to paint the rest of the volume. There are various techniques for scanning. One technique is discrete spot scanning, where the beam is switched off between spots.

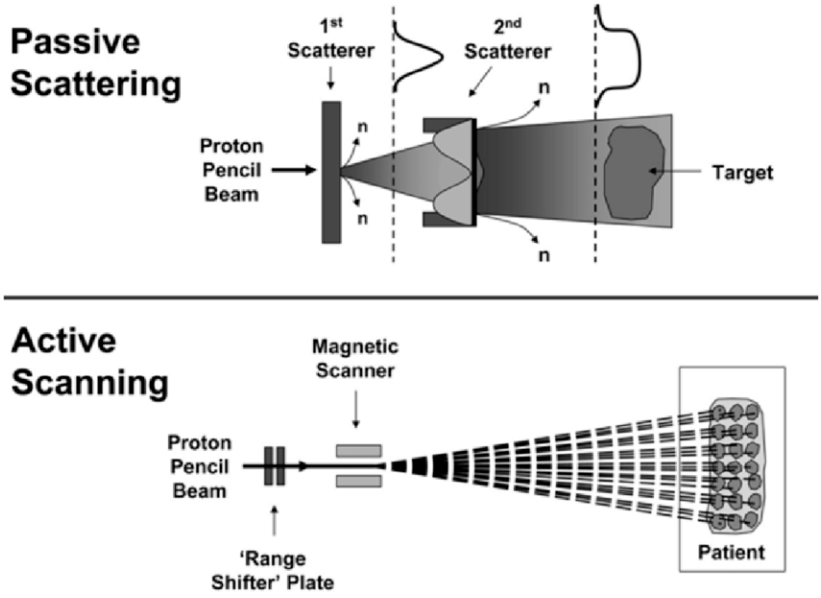

Figure 5.3: Schematic diagrams of passive scattering and active scanning beam delivery systems from Leroy *et al.* [157].

Another technique is raster scanning which is similar to discrete spot scanning but the beam is kept on. A schematic diagram comparing passive scattering with active beam scanning can be seen in fig. 5.3.

The direction of delivery can be varied by either moving the patient or delivering the dose at multiple angles. Gantries which bend the beam around a patient are useful in this regard. However, ion species plays an important role as heavy ions have a larger magnetic rigidity and require larger magnetic fields, which increase the gantry size.

5.3 MedAustron

5.3.1 Overview

The Proton-Ion Medical Machine Study (PIMMS) was formed in 1996 between MedAustron and the TERA Foundation to design a cancer therapy synchrotron, with CERN hosting the study [158]. The study focused on slow extraction and other techniques to obtain a smooth beam spill with sub-millimetre accuracy for use in beam scanning by proton and carbon ion beams. The design of MedAustron as well as the facility at the National Centre of Oncological Hadrontherapy (CNAO) are both based upon the PIMMS study [32].

The MedAustron Particle Therapy Accelerator (MAPTA) is located in Wiener Neustadt in Lower Austria and delivers both proton and carbon ion beams for cancer treatment. The facility delivers protons between 62.4 MeV and 252.7 MeV and carbon ions in the range of 120 MeV/u to 402.8 MeV/u

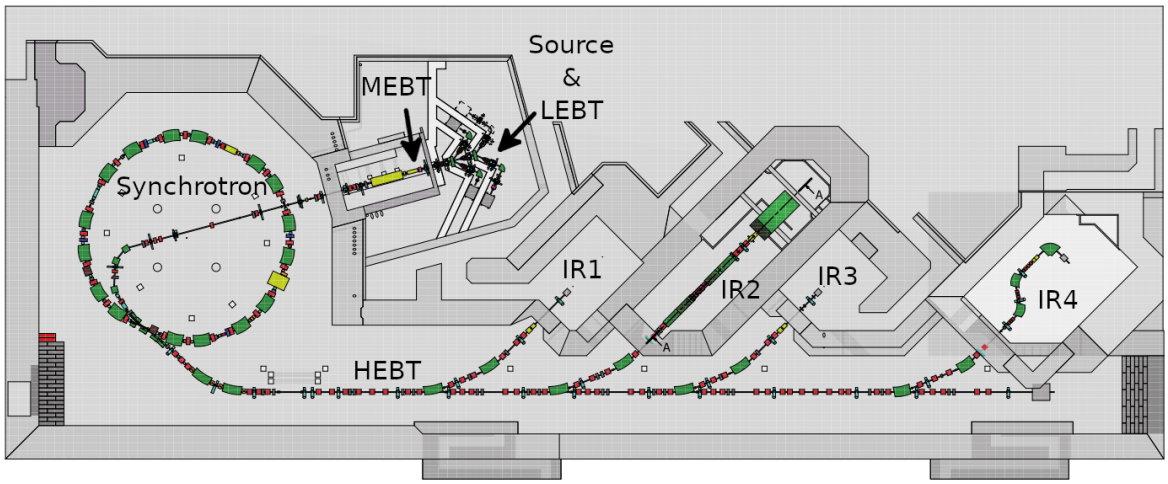

Figure 5.4: Layout of the MedAustron facility, showcasing the accelerator components [160].

[159]. Beyond the clinical energy ranges, the synchrotron accelerator is capable of energies up to 800 MeV for research purposes [32]. It first began clinical operation with proton beams as well as non-clinical research at the end of 2016 while carbon ions were first used for clinical operations in the middle of 2019. MedAustron contains four irradiation rooms (which will be subsequently referred to by IR1 - IR4). IR1 only contains a horizontal beam line and is dedicated to non-clinical research. IR2 consists of both a horizontal beam line and a vertical beam line. IR3 consists of just a horizontal beam line and was the first treatment room commissioned for clinical operations. IR4 is the only treatment room with a proton gantry and is used solely for proton beams. A layout of the MedAustron facility can be seen in fig. 5.4.

5.3.2 Accelerator Sections

Source and Low Energy Beam Transfer Line (LEBT)

MedAustron contains four independent source arms. One of the arms is for protons, the other for carbon, and the remaining two were originally intended to serve as redundant backups. Currently one is kept as a redundant backup, the other is planned to be used to test other ions [161]. Electron cyclotron resonance is used to energise free electrons from the low pressure gas in the source to produce H_3^+ and C^{4+} ions which are selected by a spectrometer dipole.

The four source arms each contain quadrupole triplets and switching dipoles to connect each arm to a common section of the LEBT. The common straight section of the LEBT consists of a series of quadrupole triplets and solenoids to control and transport the beam to match the acceptance of the radio frequency quadrupole (RFQ) [161]. The RFQ is used to focus, bunch, and accelerate the DC beam from the source up to 400 keV/u [162]. The beam then enters the Interdigital H-Mode drift Tube LINAC (IH-DTL) to accelerate the beam to 7 MeV/u where a stripping foil absorbs or strips

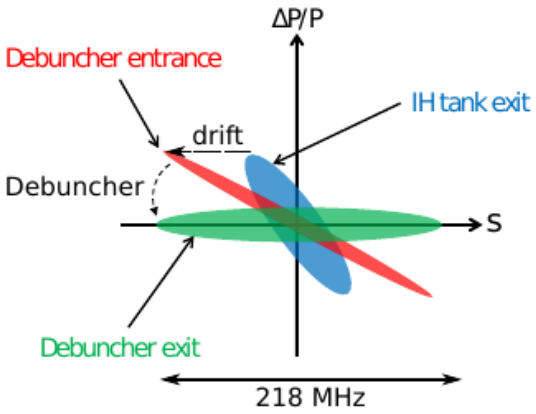

Figure 5.5: Diagram of a rotation of the longitudinal phase space in the MEBT [164].

electrons from the H_3^+ and C^{4+} ions to produce protons and C^{6+} ions respectively [163]. The energy was chosen to maximise the stripping efficiency [161].

Medium Energy Beam Transfer Line (MEBT)

The MEBT contains the beam line sections located between the stripping foil and the injection to the synchrotron [164]. To reduce the energy spread in the beam, a debunching cavity is used to rotate the beam in longitudinal phase space. This rotation reduces the momentum spread of lower energy beams and is visualised in fig. 5.5. In the figure, the beam coming from the LEBT is bunched and represented in blue. As the beam propagates in drift space, the beam elongates and higher momentum particles move ahead while the lower momentum particles fall behind as depicted in red. In the debunching cavity the RF voltage is adiabatically (slowly) lowered, resulting in the beam shown in green. The reduction in the momentum spread comes at a cost of the bunch length, but this is not a major concern as the multi-turn injection process will smear out the bunch length [164].

A degrader before the synchrotron attenuates the beam intensity to limit the number of particles entering the synchrotron. There are four settings available: 10%, 20%, 50%, and 100%, which correspond to the percentage of the beam current that is transmitted (with 100% representing no beam degradation). For clinical operations, typically only degraders for 10% and 20% are used to suit the requirements for treatment [164].

Synchrotron

The main ring synchrotron accelerates the beam to the energies required for treatment. From the MEBT, multi-turn injection is used to fill the available phase space. An advantage of this technique is that changes in the beam emittance at the MEBT mainly affects the injected beam current, but

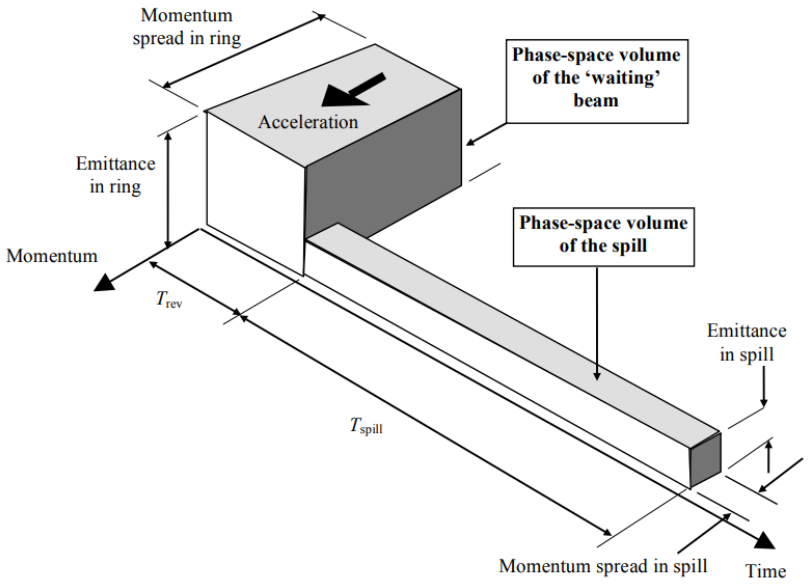

Figure 5.6: Schematic view of the phase space volume during slow extraction. Figure from the PIMMS study [158].

not the emittance in the synchrotron.

The magnets in the ring are ramped synchronously at up to 3 T/s [163], with a field-stabilisation time required to allow eddy currents to decay. After the desired energy is attained, the beam is debunched before slow extraction is employed to extract the beam into the High Energy Beam Transport line (HEBT). To achieve the slow resonant extraction, a betatron core is used [158]. The betatron core accelerates the particles to an unstable resonance, this causes the amplitude of the beam to increase, and after a certain number of turns the particles on the edge will reach the electrostatic septum. This septum applies a small deflection to a magnetic septum which applies a larger kick to extract the beam towards the HEBT. As can be seen in fig. 5.6, the extracted beam will have a small emittance and long spill time.

The phase space of the extracted beam differs from conventional beams as can be seen in fig. 5.7. In the extraction plane, the segment of the separatrix that is deflected by the electrostatic septum has a phase space shape that is rectangular, and is referred to as a *bar of charge* [158].

High Energy Beam Transfer Line (HEBT)

The HEBT comprises the beam line from extraction to the four irradiation rooms. Within the HEBT is the chopper, which contains a block of tungsten to prevent the beam from unintentionally entering any of the irradiation rooms. As seen in fig. 5.8, for beam to reach an irradiation room, four kicker magnets need to be powered in order to divert the beam around the beam dump and back onto the central axis [158]. Following the chopper is the phase shifter-stepper (PSS) which consists of

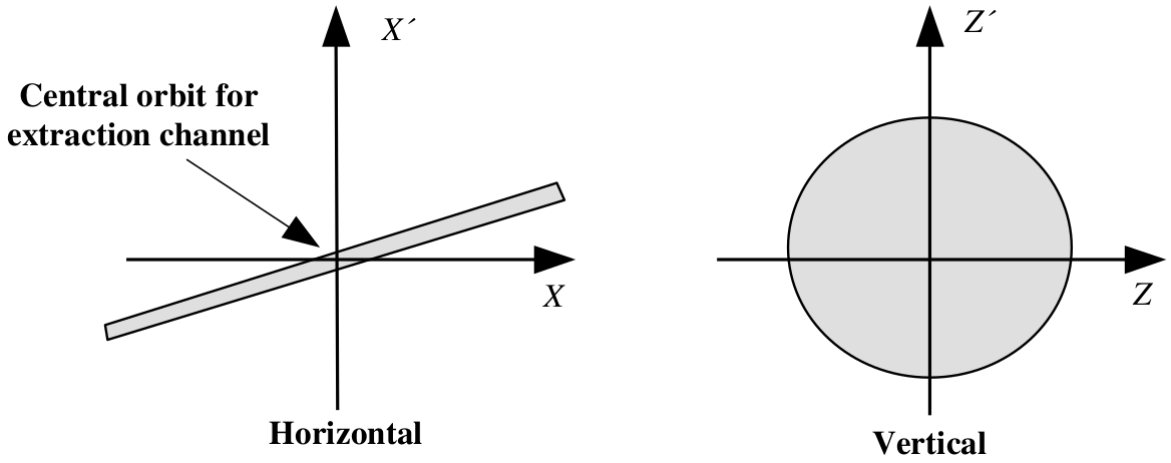

Figure 5.7: Schematic representation of the phase space of the beam after extraction. Figure from the PIMMS study [158].

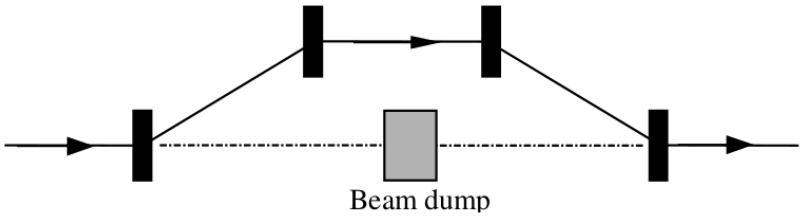

Figure 5.8: Schematic view of the chopper [158].

six independently powered quadrupoles. This module was designed to manipulate the beam size to satisfy the clinical requirements. The PSS marks the end of the common section of the beam line, before it diverts to the different rooms through the use of switching dipoles. The maximum number of particles that reach the irradiation room is 2×10^{10} protons or 1×10^{9} carbon ions, which is scanned over a target volume through the use of scanning magnets [165].

5.3.3 Diagnostic Devices

Various beam diagnostic devices are positioned throughout the beam line to ensure the safety of the patient and allow successful treatment. An overview of various beam monitors in use are given in Table 5.1.

Wire scanners measure the beam profile and position through the use of a pair of thin wires which move through the beam for measurements in the horizontal and vertical plane. As the wire passes through the beam, secondary particles are generated. From these secondaries, the transverse distribution and position of the beam can be determined.

Slit plates are used to measure the beam emittance. As the beam passes through the plates with horizontal or vertical slits, it is split into smaller pieces which drift to a screen. From the measured

Table 5.1: Overview of beam monitors located in the beam line at MedAustron. Adapted from [166, 167].

Beam Monitor	**Location**	**Quantity**	**Purpose**
Wire Scanners	LEBT	28	Measures beam intensity
Slit Plates	LEBT, MEBT	40	Collimates beam and measures emittance
Faraday Cups	LEBT, MEBT	11	Measures beam intensity
Cylindrical Faraday Cup	LEBT	1	Measures beam intensity
Current Transformer	LEBT, MEBT, MR	5	Measures beam intensity and fluence
Profile Grid Monitors	LEBT, MEBT	7	Measures beam profile, emittance, and position
Position Pickup	MEBT, MR	21	Measures beam position
Stripping Foil	MEBT	1	Strips particles of electrons
Degraders	MEBT	3	Regulates beam intensity
Schottky Pickup	MR	2	Measures beam velocity and momentum spread
Luminescent Screen	MR	2	Measures beam position and intensity
Septum Shadow Monitor	MR	1	Measures beam profile
Silicon Diode	MR	1	Measures beam loss
Scintillating Fibre Hodoscope	HEBT	29	Measures beam profile and position
Qualification Monitor	HEBT	1	Measures beam profile, position and intensity
In total		**153**	

intensity for the different slits, the angular distribution can be determined.

Faraday cups measure the current of the beam destructively by stopping the beam. The incoming beam will collide with the cup material and be absorbed. The beam current can be determined by discharging the cup.

Current transformers consist of a torus wound with wire through which a beam passes. The beam current is measured by observing how the magnetic field changes. To shield against external fields, the current transformer is housed in a metal housing.

The Profile Grid Monitor (PGX) was developed at MedAustron to measure the beam profile for a pulsed beam [168]. The PGX consists of harp grids (wires stretched in one plane) to cover the transverse plane of the beam. These monitors can be moved into the beam path in order to do measurements. Similar to wire scanners, the secondary particles generated are measured and converted into the beam intensity, which subsequently gives the beam profile and position.

Position pickups consists of pairs of electrodes onto which signals are induced by a beam. The ratio of the amplitudes of the induced signals allows for the beam position to be calculated. Key to the operation is defining the signal amplitudes.

Schottky signals originate from fluctuations or noise in the beam current due to the movement of individual particles. From these signals, the relative momentum spread or transverse velocity spread can be extracted [166].

Luminescent screens provide a destructive means to measure the transverse beam profile. When the beam interacts with the screen, light emission can be captured by a camera. These screens are placed at the injection to the synchrotron to study the injected beam.

At extraction, a diode detector made of hydrogenated amorphous silicon is used to measure the beam loss on the extraction septum. A monitor after the extraction septum measures the profile of the beam that is extracted [166].

Scintillating fibre hodoscopes (SFX) measure the transverse position and profile of the beam. A SFX consists of planes of scintillating fibres grouped together. As a particle hits the scintillating material, the emitted light from collisions are detected by a CCD camera. However, a limitation of hodoscopes are in the spatial resolution, which is limited by the size of the fibres. At MedAustron, the SFX monitors are composed of 128 fibres, each fibre has a diameter of 0.5 mm and no gap between adjacent fibres [166].

The Qualification Monitor consists of two scintillating fibre planes to measure the beam position. This is followed by a scintillator plate used to measure the beam intensity. The monitor is mainly used to measure the head of the treatment beam.

In addition to the aforementioned monitors, each irradiation room at MedAustron is equipped

with a Dose Delivery System (DDS) which was developed at CNAO. The DDS helps to ensure the proper delivery of a prescribed dose. The DDS consists of five parallel plate ionisation chambers housed in two independent boxes (DDM). Box 1 contains a large area integral chamber to measure the beam fluence, followed by two chambers with segmented anodes to measure the beam profile and position. Box 2 contains another large area integral chamber followed by a chamber segmented into 32×32 pixels [169].

Chapter 6

MedAustron Spot Size Commissioning

One of the key challenges to beam commissioning is to make the most of the time available, in particular when commissioning for a facility that treats patients. Due to time constraints, simulations were essential to make the most of a commissioning session. The work in this chapter will present the simulation efforts and measurement results for beam spot size commissioning at MedAustron from the year 2018 to 2019. The main focus was for MedAustron to commission a carbon ion beam suitable for patient treatment for the first time. Part of the work also included commissioning a 800 MeV proton beam for the research room.

The Methodical Accelerator Design (MAD-X) is a useful simulation code for particle accelerator design [35, 170]. A particularly useful aspect of MAD-X is its optics matching module which can calculate the Twiss parameters at all parts of the beam line. Beam Delivery Simulation (BDSIM) uses the Monte Carlo simulation toolkit Geant4 [50] to simulate the transport of particles in an accelerator as well as simulating various interaction processes with materials [37]. BDSIM has been designed to use an ASCII text input with a syntax similar to MAD-X making it easy to use both simulations in tandem. In addition, BDSIM includes a visual model in 3D to better visualize particle tracks. Analysis in this chapter was performed using MAD-X v5.04.00, BDSIM v1.0.0, and Geant4 v10.04.p01.

6.1 Slow Extraction Beam Distribution

A key component to obtaining useful results from beam simulations are the initial parameters of the beam. The beam distribution will affect the evolution of the beam as it propagates through the

beam line. Hence, being able to model accurately the beam which is delivered is crucial to make the most of the commissioning session. For conventional beams, a Gaussian distribution for phase space parameters is a good approximation to a beam described by the Twiss parameters. However, for the beam extracted from the MedAustron synchrotron, this is only a good approximation for the vertical phase space (refer to sec. 5.3.2). In this case, the particles can be generated according to:

$$y = a\sqrt{\epsilon_y \beta_y} \tag{6.1}$$

$$y' = (b - \alpha_y a)\sqrt{\frac{\epsilon_y}{\beta_y}} \tag{6.2}$$

where y is the position, y' is the normalised vertical momentum, and p is the momentum. α_y, β_y are the vertical Twiss parameters and ϵ_y is the vertical emittance. a and b are Gaussian random numbers generated with a mean value of 0 and a standard deviation of 1. Appendix A shows how these values are derived.

In comparison to the vertical plane, the horizontal phase space does not have a Gaussian spread but is instead a *bar of charge* which does not correspond precisely to the Twiss parameters. To characterise this distribution, there are three main degrees of freedom to specify: position distribution, angular distribution, and orientation of the bar.

From the PIMMS study [158], a method to couple the Twiss parameters to the bar of charge is by *indirect fitting*. The bar of charge is enclosed within an ellipse described by the Twiss parameters, this approximates the beam evolution through the beam line. But this method was difficult to implement in practice. In order to best fit an ellipse to the bar of charge, the orientation of the bar needs to be horizontal with a small divergence. However, it was not known at what position in the HEBT this was the case as the angular distribution was difficult to determine. A different but similar method based on *direct fitting* was attempted [158]; instead of enclosing the bar of charge with an ellipse, the ellipse itself was fitted within the bar of charge. By coupling the Twiss parameters to the bar, the horizontal phase space could be approximated by a Gaussian distribution and will be discussed in sec. 6.2.2.

As both transverse planes could be approximated with Twiss parameters, the challenge to the simulations was in determining the initial parameters which differed from the design values. Initially a manual fitting scheme was performed by varying initial Twiss parameters to fit to measurements. Although time consuming, this method had a small measure of success. But it was abundantly clear that a more methodical approach was needed to determine the Twiss parameters at an arbitrary location in the beam line.

6.2 Fitting Measured Beam with Twiss Parameters

Two methods were attempted to approximate the beam with the Twiss parameters. One method was to use the results of a quadrupole scan, the other method was to fit Twiss parameters and beam emittance to detector measurements along the beam line.

6.2.1 Quadrupole Scan Method

The quadrupole scan method [36,171] relies upon a single beam profile monitor close to a quadrupole. The beam emittance can be determined by varying the quadrupole strength and observing how the beam size changes. In addition, based on how the the beam position changes, the offset of the beam from the center can also be determined. Consider a point, i, where a transverse plane of the beam can be represented by the beam matrix:

$$\Sigma = \begin{pmatrix} \sigma_{11} & \sigma_{12} \\ \sigma_{21} & \sigma_{22} \end{pmatrix}, \tag{6.3}$$

where,

$$\sigma_{11} = \langle {x_i}^2 \rangle = \epsilon\beta, \tag{6.4}$$

$$\sigma_{12} = \sigma_{21} = \langle x_i x_i' \rangle = -\epsilon\alpha, \tag{6.5}$$

$$\sigma_{22} = \langle x_i'^2 \rangle = \epsilon\gamma. \tag{6.6}$$

Here, x_i is the position, x_i' the divergence, ϵ the geometrical emittance and (β, γ, α) represent the Twiss parameters. The geometrical emittance is defined by:

$$\epsilon = \det(\Sigma) = \sqrt{\sigma_{11}\sigma_{22} - \sigma_{12}^2} = \sqrt{\langle x_i^2 \rangle \langle x_i'^2 \rangle - \langle x_i^2 x_i'^2 \rangle}. \tag{6.7}$$

A beam matrix, Σ_0 will transform to Σ_1 according to:

$$\Sigma_1 = R\Sigma_0 R^T. \tag{6.8}$$

If the initial beam matrix is known, the evolution of the beam will be determined by the transfer matrix, R. A simple scenario is to consider the beam matrix Σ_0, located at the entrance to a

quadrupole:

$$\Sigma_0 = \begin{pmatrix} \sigma_{11}^{\text{quad}} & \sigma_{12}^{\text{quad}} \\ \sigma_{21}^{\text{quad}} & \sigma_{22}^{\text{quad}} \end{pmatrix}, \tag{6.9}$$

The beam then travels through the quadrupole with strength k and length l, followed by a drift space of length d. The transfer matrix through this configuration is given by:

$$R = \begin{pmatrix} 1 & d \\ 0 & 1 \end{pmatrix} \begin{pmatrix} 1 & 0 \\ kl & 1 \end{pmatrix} = \begin{pmatrix} 1+dkl & d \\ kl & 1 \end{pmatrix}. \tag{6.10}$$

Expanding the matrix equation for the beam size at the monitor, $\sigma_{11}^{\text{Monitor}}$, leads to:

$$\begin{aligned} \sigma_{11}^{\text{Monitor}} =& (1+dkl)^2\sigma_{11}^{\text{quad}} + 2d(1+dkl)\sigma_{12}^{\text{quad}} + d^2\sigma_{22}^{\text{quad}}, \\ =& \underbrace{\left(\sigma_{11}^{\text{quad}} d^2 l^2\right)}_{A} k^2 + \underbrace{\left(2dl\sigma_{11}^{\text{quad}} + 2d^2 l\sigma_{12}^{\text{quad}}\right)}_{B} k + \underbrace{\left(\sigma_{11}^{\text{quad}} + 2d\sigma_{12}^{\text{quad}} + d^2\sigma_{22}^{\text{quad}}\right)}_{C}. \end{aligned} \tag{6.11}$$

By plotting the square of the RMS beam size against various quadrupole strengths and coefficients A, B, and C, a quadratic equation can be fitted. A rearrangement of the coefficients yields the beam matrix elements:

$$\sigma_{11}^{\text{quad}} = \frac{A}{d^2 l^2}, \qquad \sigma_{12}^{\text{quad}} = \frac{B - 2dl\sigma_{11}^{\text{quad}}}{2d^2 l}, \qquad \sigma_{22}^{\text{quad}} = \frac{C - \sigma_{11}^{\text{quad}} - 2d\sigma_{12}^{\text{quad}}}{d^2}. \tag{6.12}$$

This allows the calculation of the Twiss parameters and beam emittance at the start of the quadrupole:

$$\epsilon = \sqrt{\sigma_{11}^{\text{quad}}\sigma_{22}^{\text{quad}} - \left(\sigma_{12}^{\text{quad}}\right)^2}, \tag{6.13}$$

$$\alpha^{\text{quad}} = -\frac{\sigma_{12}^{\text{quad}}}{\epsilon}, \tag{6.14}$$

$$\beta^{\text{quad}} = \frac{\sigma_{11}^{\text{quad}}}{\epsilon}, \tag{6.15}$$

$$\gamma^{\text{quad}} = \frac{\sigma_{22}^{\text{quad}}}{\epsilon}. \tag{6.16}$$

This method is optimal at a location where the beam waist can be scanned across.

6.2.2 Twiss Parameter Rematch

Another method was developed over the course of commissioning which sped up the characterisation of a beam. Whereas the quadrupole scan relies on multiple measurements on a single beam profile monitor, this method characterises a beam from a single trajectory measurements over several beam

profile monitors.

Transfer matrix elements are related to the Twiss parameters through the relation given in eq. 2.77 [38]:

$$\begin{pmatrix} R_{11} & R_{12} \\ R_{21} & R_{22} \end{pmatrix} = \begin{pmatrix} \sqrt{\frac{\beta}{\beta_0}}\left(\cos(\mu) + \alpha_0 \sin(\mu)\right) & \sqrt{\beta\beta_0}\sin(\mu) \\ \frac{\alpha_0 - \alpha}{\sqrt{\beta\beta_0}}\cos(\mu) - \frac{1+\alpha\alpha_0}{\sqrt{\beta\beta_0}}\sin(\mu) & \sqrt{\frac{\beta_0}{\beta}}\left(\cos(\mu) - \alpha\sin(\mu)\right) \end{pmatrix}. \tag{6.17}$$

On the right side, the matrix elements are composed of Twiss parameters and the phase advance μ. The subscript zero refers to the initial Twiss parameters at the start. From eq. 6.17 the phase advance can be expressed by:

$$\mu = \arcsin\left(\frac{R_{12}}{\sqrt{\beta\beta_0}}\right). \tag{6.18}$$

Substituting eq. 6.18 into eq. 6.17 allows for β to be solved for:

$$\beta = \frac{\left(R_{12}\right)^2 + {\alpha_0}^2\left(R_{12}\right)^2 - 2\alpha_0 R_{11} R_{12}\beta_0 + \left(\beta_0 R_{11}\right)^2}{\beta_0}. \tag{6.19}$$

From this, β can be expressed in terms of the initial Twiss parameters and transfer matrix elements. For a beam with a normal distribution, the full width at half maximum (FWHM) is given by:

$$\text{FWHM} = 2\sqrt{2\ln(2)}\sigma, \tag{6.20}$$

where $\sigma = \sqrt{\beta\epsilon}$, β is the Twiss parameter and ϵ is the geometrical emittance. Substitution and rearrangement yields:

$$\beta = \frac{1}{\epsilon}\left(\frac{\text{FWHM}}{2\sqrt{2\ln(2)}}\right)^2. \tag{6.21}$$

Comparing eq. 6.19 and eq. 6.21 gives an expression relating the initial Twiss parameters to beam size measurements. Using multiple measurements along a beamline allows for a least squares minimisation:

$$S = \sum_i \left[\left(\frac{\text{FWHM}}{2\sqrt{2\ln(2)}}\right) - \sqrt{\beta_i\epsilon}\right]^2, \tag{6.22}$$

where β_i is the Twiss beta value at a detector i, as a function of the initial Twiss parameters. In

Table 6.1: Fitted Twiss parameters used to generate a vertical beam fitted to beam profile measurements using the design vertical emittance and a fitted vertical emittance. β_y represents the amplitude function, α_y the correlation function, d_y the dispersion of position y and ϵ_y is the geometrical beam emittance.

Parameters	Design Value	Optics w/ Design Emittance	Optics w/ Fitted Emittance
β_y [m]	3.0	15.5	3.0
α_y	0.0	2.5	0.22
d_y [m]	0.0	0.0	0.0
ϵ_y [π·m·rad]	7.3×10^{-7}	7.3×10^{-7}	3.8×10^{-6}

MAD-X, the coefficients for the R matrix can be found by using the `Sectormap` output at each point in the beam line. From a trajectory measurement, the minimization procedure will give an approximation of the initial Twiss parameters of a beam that best fits to all measurements.

6.3 Issues Identified during Spot Size Commissioning

Due to time constraints resulting from the need to continuously treat patients with protons on a daily basis, the number of commissioning shifts were limited. Only a few shifts were dedicated to the spot size, with most of those shifts naturally relegated to the end of the commissioning phase. However, several key issues were identified over the course of commissioning which had an effect on spot size adjustments.

6.3.1 Large Vertical Emittance

While the synchrotron was still being commissioned for carbon ions, several preliminary beam measurements were made in the HEBT. These measurements were used to approximate the beam. To characterise the beam, Twiss parameters were matched to the vertical plane profile measurements. However, there was insufficient information to determine the beam emittance.

To fit the measurements, one case was considered where the beam had different starting optics but still having the design vertical emittance [172]. The Twiss optics were manually tweaked to find a fitting. In another case, it was assumed that the beam optics were similar to the design, but the emittance was increased. In both cases, the beams were primarily matched to the first detector, EX-02-001-SFX, but also included consideration for the other detectors. A summary of the relevant fitted parameters is given in table 6.1 for the two cases. Both beams were simulated through the HEBT beam line and compared against the measurements at several detectors with the results presented in table 6.2 and in fig. 6.1.

Comparing the results in table 6.2, it can be seen that both beams start with a beam size matched to the measurement at EX-02-001-SFX. However, for the case with the design emittance, there is a

Table 6.2: Comparison of FWHM spot sizes between measurements and simulation results at several SFX and DDM monitor measurements. The beams were simulated using the fitted Twiss parameters from table 6.1.

Monitor	Measurement	Optics w/ Design Emittance	Optics w/ Fitted Emittance
EX-02-001-SFX	7.7 ± 2.2 mm	7.73 mm	7.71 mm
T2-00-000-SFX	15.2 ± 4.1 mm	8.08 mm	17.72 mm
T2-01-000-SFX	7.2 ± 2.0 mm	7.63 mm	7.66 mm
H2-00-000-SFX	29.9 ± 8.4 mm	17.37 mm	27.34 mm
H2-00-001-SFX	12.3 ± 3.7 mm	10.75 mm	12.0 mm

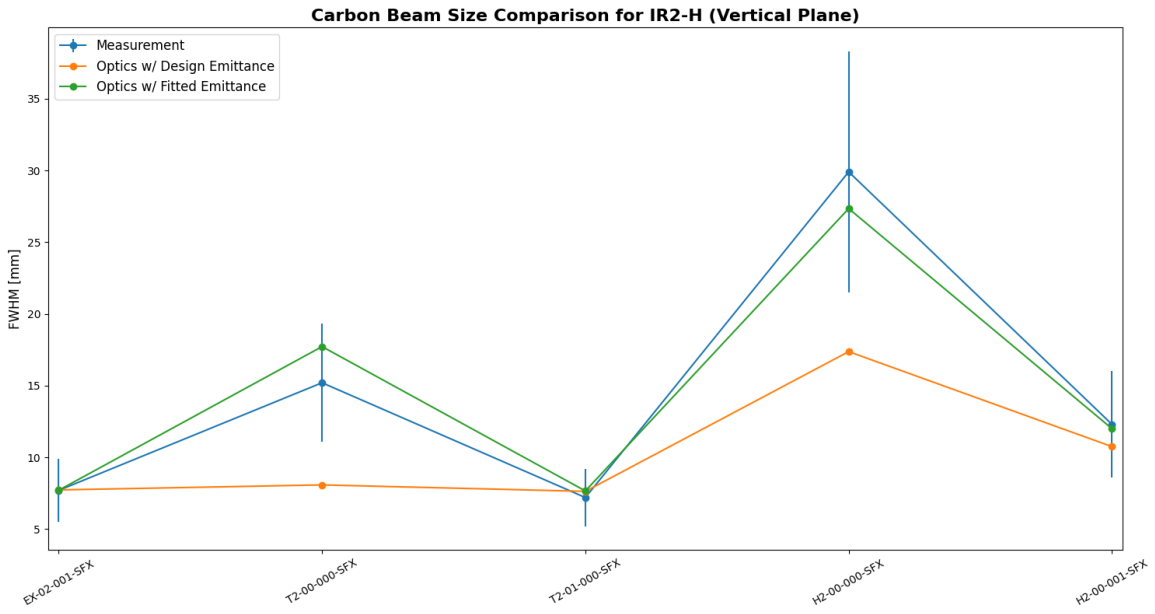

Figure 6.1: Comparison of FWHM spot sizes between measurements (in blue) and simulation results (in orange and green) at several SFX and DDM monitor measurements as shown in table 6.2.

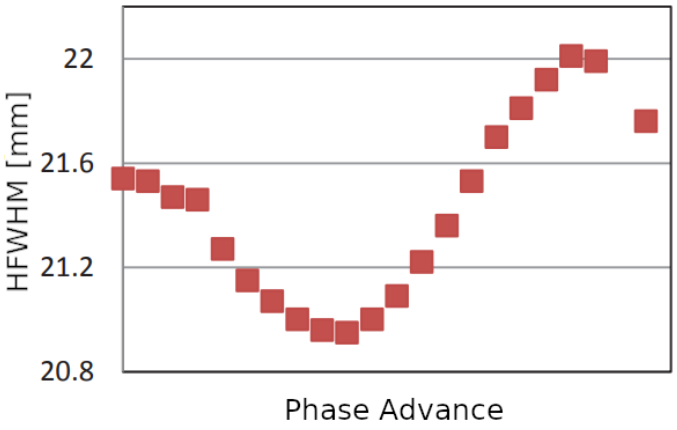

Figure 6.2: Horizontal spot size for protons at 62 MeV scanned over several settings for the PSS [173]. Uncertainty values for these measurements was not provided.

notable discrepancy for two monitors: T2-00-000-SFX and H2-00-000-SFX. Whereas for the beam using a fitted emittance, a better agreement to the measurements for all the measured detectors could be found. Of the two scenarios considered, a beam close to the design optics but with a larger emittance was more likely.

This conclusion was confirmed when the vertical emittance in the synchrotron was measured and the vertical beam emittance was found to be larger [159]. The reason for this discrepancy was attributed to a mismatch at the injection into the synchrotron. This mismatch was rectified and the injection tunes were moved away from resonance lines which lowered the vertical emittance to about 9.0×10^{-7} (π·m·rad) for carbon ions at the highest energy. This allowed for a smaller beam to be delivered.

6.3.2 Phase Shifter and Stepper Issues (PSS)

The PSS consists of six independently powered quadrupoles placed in series. It is intended to provide flexible control over the transverse beam profile. Specifically, the PSS would provide sufficient degrees of freedom to manipulate both transverse planes. When protons were first commissioned, the ability of the PSS to control the spot size was investigated. If the spot size is plotted against the phase advance, a sinusoidal shape is traced out as can be seen in fig. 6.2. In principle, the quadrupole settings could be varied for different energies to adjust the spot size. However, this full functionality was not needed and only settings for the highest and lowest proton energies were used, with settings for the intermediate energies interpolated. Finer adjustments to the spot size were left to the quadrupoles located downstream.

The capabilities of using the PSS for carbon ions was also investigated, but a different behaviour

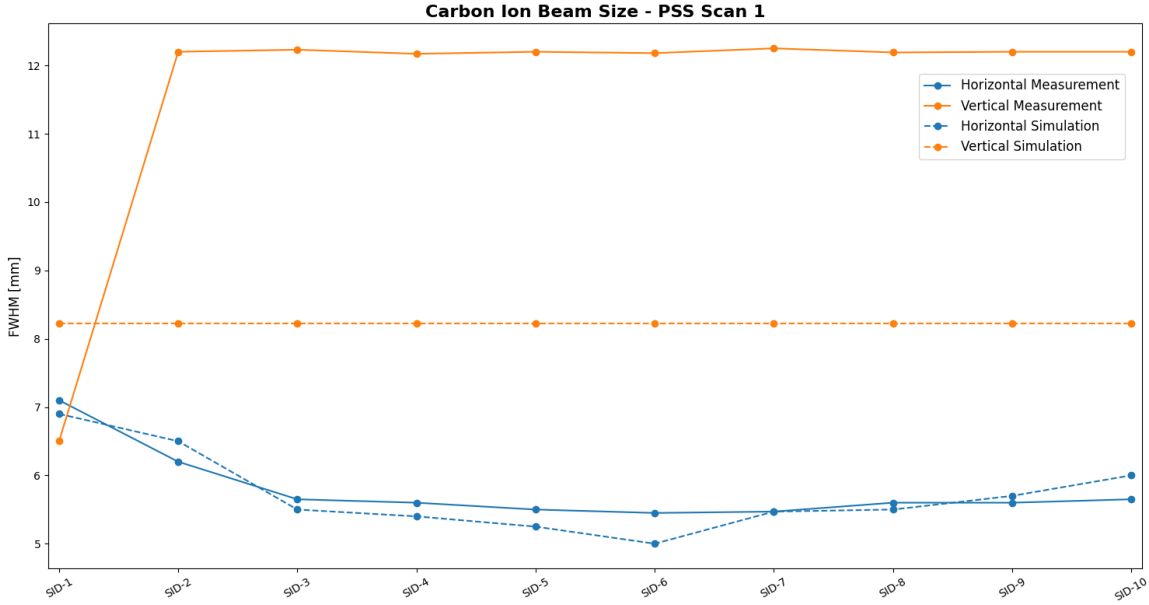

Figure 6.3: Comparison in the FWHM spot size (in units of mm) between the results from simulations and measurements at the position of the DDM when the PSS was adjusted. The horizontal axis represents the iteration of the scan corresponding different quadrupole settings to achieve a phase advance, and the vertical axis representing the FWHM. It can be seen that in the horizontal plane, the results appear quite similar though a strange plateau region can just about be observed. In the vertical plane, after the first iteration the FWHM seems to jump up to a larger value for subsequent iterations. Uncertainty values were not recorded for the measurements.

was found. A parameter scan over the phase advance for the horizontal spot size was done while keeping the vertical spot size constant, and the results were compared against MAD-X simulations as shown in fig. 6.3. For the horizontal plane it can be seen that a good match can be found between simulation and measurements for the spot size. But it can be noted that for simulations there is a small dip, whereas the measurements appear to plateau out. For the vertical plane with exception to the first quadrupole settings (SID-1), the measurements seem to have a constant offset from the simulations. Investigations of the jump in the vertical spot size showed that the discrepancy was due to this set of quadrupole settings in MAD-X having significantly different strengths and polarity compared to the others.

Fig. 6.4 shows results for a finer scan performed around the plateau region in the horizontal plane. For the horizontal plane at SID-11, it can be seen that comparable beam sizes between simulation and measurements were obtained. But a discrepancy seems to grow. Whereas the simulated beam decreases to a much smaller beam size, the measured beam does not decrease appreciably. This gives an indication that the bar of charge is not rotating as expected. In the case of the vertical plane, an offset was applied, to bring the measurements and simulation values closer. But as as seen in fig. 6.4, it appears that the measured beam is slightly increasing between different quadrupole settings.

Due to time limitations, these were the only scans performed. As a result, it is difficult to pin down

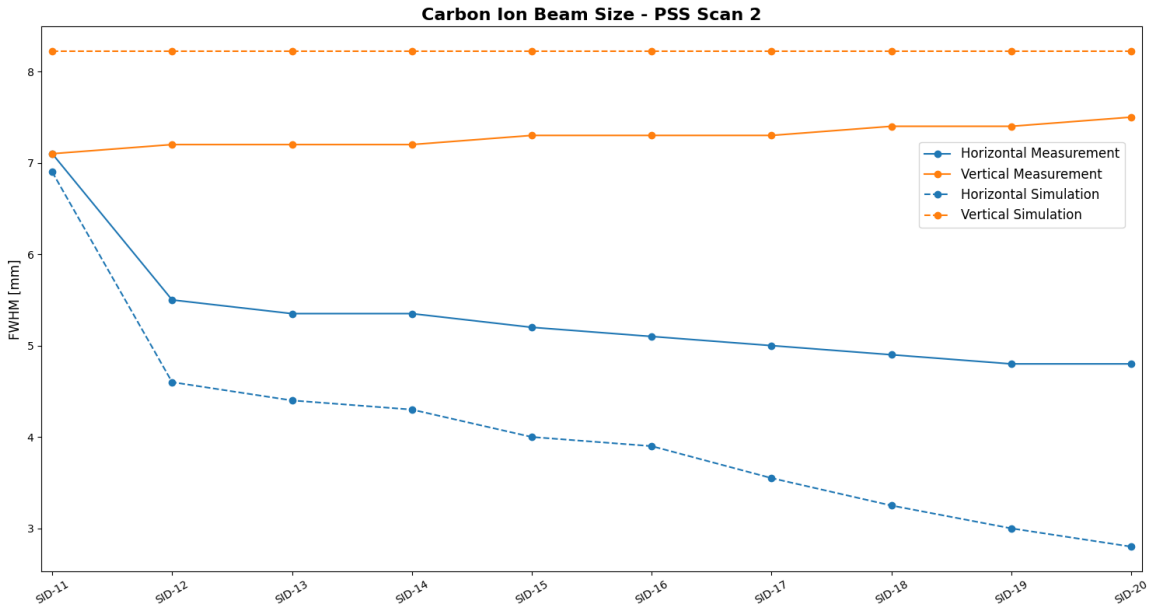

Figure 6.4: Comparison between the FWHM spot size (in units of mm) results from simulations (dashed lines) and measurements (solid lines) at the position of the DDM when adjusting the PSS for a finer scan of a perceived plateau region. The horizontal axis represents the iteration of the scan, and the vertical axis representing the FWHM. For the horizontal plane (blue) a plateau region for the measurements can be seen, despite the simulations indicating the beam should be shrinking. For the vertical plane (orange) the measured beam size slightly increases. Uncertainty values were not recorded for the measurements.

the exact reason for the observed deviations, but some hypotheses can be made. For the horizontal phase space, one possibility is related to the orientation of the bar of charge in trace space. From the schematic diagram in fig. 6.5, it can be seen that if the bar at the detector is close to horizontal, a variation of the phase advance would only give a small change in the spot size. Whereas if the bar was oriented vertically, a change in the phase advance would yield a much larger difference. Another explanation is that the sinusoidal shape that was obtained for protons is due to the larger spot size and lower energies. Under these conditions, variations in spot size can be more easily observed. On the other hand, the deviations in the vertical plane in the second scan could be explained by a beam not being centred as it passes through the quadrupole magnets. This would lead to a variation in the focusing experienced by the beam, resulting in a varying spot size.

These scans took place before the vertical emittance was recommissioned, so the vertical spot size was larger than it should have been. Although the properties of the extracted beam changed, these scans exemplified some unexpected behaviour in the beam. Similar issues were still observed when the beam emittance was lowered. In the end, the same approach as for protons was taken where quadrupole settings for the maximum and minimum energies for carbon ions were determined. The finer spot size adjustments were left to the quadrupoles that were located downstream seen in fig. 6.6.

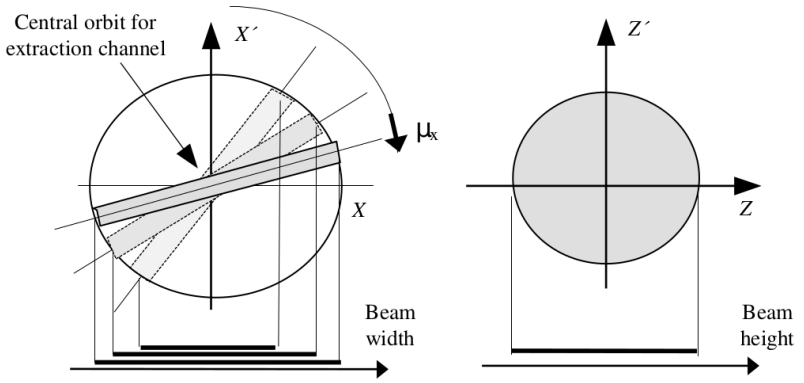

Figure 6.5: Schematic diagram of beam spot size changing with the phase advance, taken from PIMMS study [158].

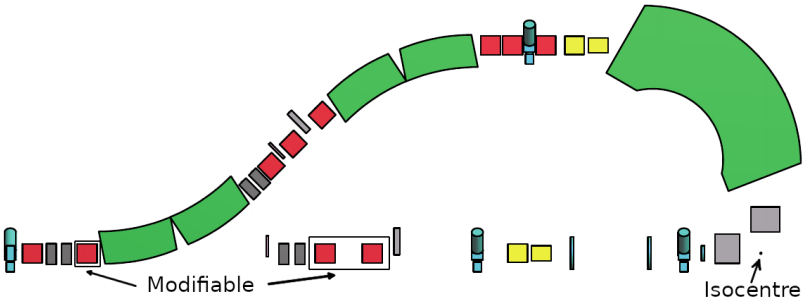

Figure 6.6: Schematic diagram of the horizontal and vertical beam line for IR2 where the quadrupoles are denoted in red, dipoles in green, scanning magnets in yellow, kicker magnets in gray, and other symbols represent various monitors. The quadrupoles in the horizontal beam line are designated.

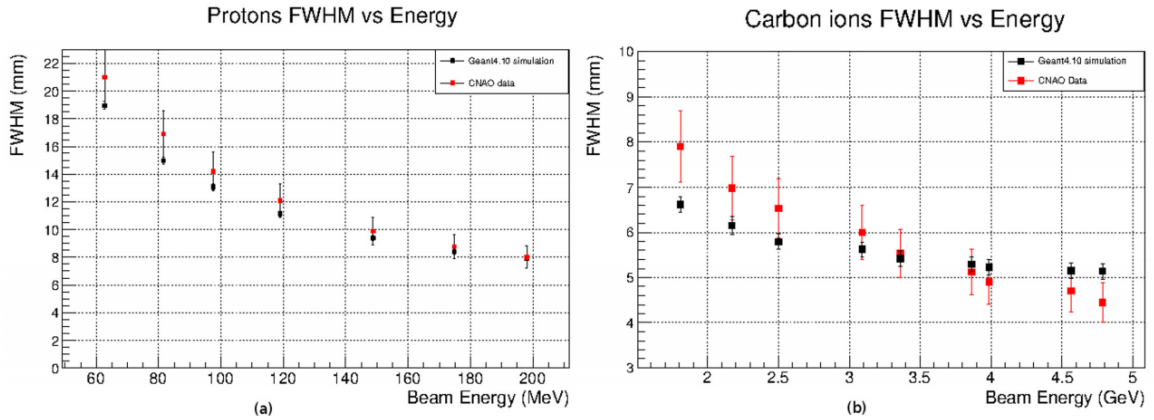

Figure 6.7: Comparison of simulated and experimental FWHM for protons (a) and carbon ions (b) from CNAO [174].

6.3.3 Discrepancies in the Scattering Physics Simulations

Another problem encountered was a discrepancy in the FWHM beam spot size between Geant4 simulations and measurements. This issue had been previously noticed at CNAO [174] where beams of protons and carbon ions simulated in Geant4 for various energies showed a smaller spot size compared to measurements. As can be seen in fig. 6.7, there is a good overlap for proton beams at CNAO, but there is a growing discrepancy as the energy is lowered. For carbon ions there is a different trend in the relationship between the beam size and energy. The authors of the paper point to the choice of the Geant4 `physics list` as being the cause of the differences in the carbon ion simulations which would be investigated in future studies. A similar phenomenon was noted at MedAustron for proton beams by Grevillot [175], where the best agreement between measurements and simulations is at high energies. A comparison has been made of three Monte Carlo simulation codes: Geant4, MCNP6, and FLUKA, which shows that Geant4 appears to underestimate lateral scattering, [176]. This study suggests that this is due to the multiple scattering algorithm used in Geant4.

For beam size optimisations, the carbon ions were simulated with BDSIM for the IR2-H beam line, and a comparison of the spot sizes at two locations can be seen in fig. 6.8. In fig. 6.8a and fig. 6.8b a good match was found for all energies at a position 50 cm upstream of the isocentre (before scattering in the air) for both planes. In comparison, fig. 6.8c and fig. 6.8d shows a discrepancy for the lower energies for measurements at the location of the isocentre. This matches the results from the past simulations. The percentage error between the simulations and measurements go beyond 10% for the lower energies in both planes. From these results it appears to support Geant4 simulations having a tendency to underestimate the lateral scattering for lower energies.

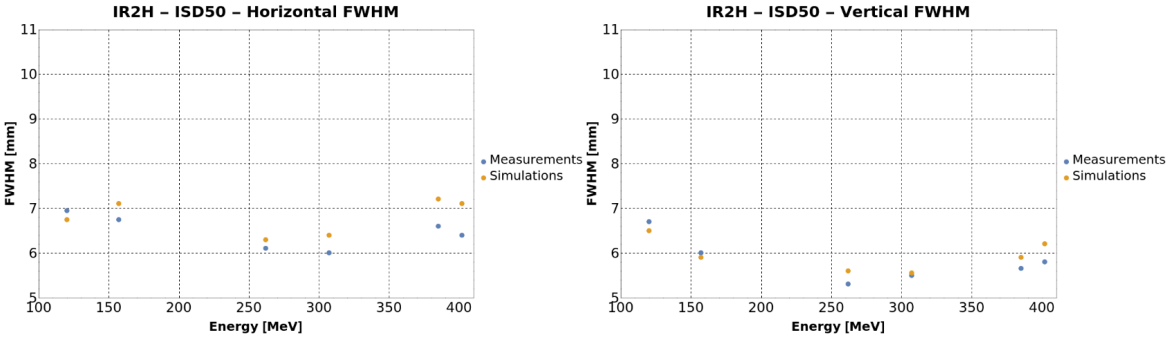

(a) Horizontal spot size at ISD50.

(b) Vertical spot size at ISD50.

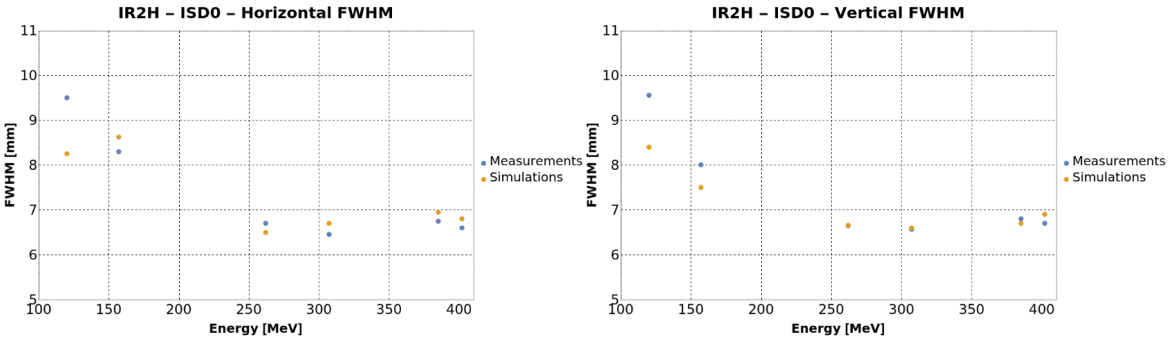

(c) Horizontal spot size at ISD0.

(d) Vertical spot size at ISD0.

Figure 6.8: Carbon ion beam spot size comparisons at ISD50 and ISD0 between Geant4 BDSIM simulations and measurements.

BDSIM allows the user to easily select which Geant4 physics libraries are used for the simulation. Different physics processes and modelled were compared to investigate if these would affect the results. These comparisons include different hadronic physics and electromagnetic models, multiple scattering models, and different threshold cuts. However, it was found that there was only a minor difference in scattering, and the same discrepant behaviour could still be observed. It can be noted that there may be other factors which cause this discrepancy for lower energies. First, the medical nozzle was only roughly simulated and a difference in the geometries could skew the results. In addition, there is an uncertainty with how well the simulations approximate the beam. A more thorough investigation would be needed in order to identify the cause of this discrepancy.

An inability to simulate the spot size at isocentre was a reoccurring problem during commissioning. However, given that the underestimation appears to be comparable for both transverse planes, the simulations did serve as a good gauge for the ellipticity. When preparing for commissioning shifts, an approximate compensation was applied to the simulation results for the various energies. As the compensation is very approximate, iterative scans were required during shifts in order to optimise the beam. But regions to scan quadrupole settings could be identified which helped to save time during shifts.

Table 6.3: Vertical Twiss parameters at EX-02-001-SFX by backtracking from the Twiss parameters measured at a downstream quadrupole for the two extreme energies of delivered carbon ions.

Parameter	Value (402.8 MeV/u)	Value (120.0 MeV/u)
ϵ_y	$0.9\,\pi \cdot$ mm $\cdot$ mrad	$2.1\,\pi \cdot$ mm $\cdot$ mrad
β_y	8.18 m	4.00 m
α_y	-1.41	-0.15

6.4 IR2-H Spot Size Commissioning

6.4.1 Spot Size Requirements

Carbon ion beam commissioning at MedAustron first focused on delivery of beam to the fixed horizontal beam line for IR2 (IR2-H). The spot sizes delivered needed to satisfy certain conditions for all energies from 120 MeV/u to 402.8 MeV/u including:

- Average FWHM spot size in both planes to be symmetric to within $\pm$10%.
- Average FWHM spot size for all energies to lie between 6 mm and 10 mm at isocentre.
- The symmetric beam spot size to be achieved at all positions from isocentre to a position 50 cm upstream of the isocentre.

In order to satisfy these conditions, accurate information needed to be obtained about the initial beam distribution and beam line configuration in order to simulate the beam. This was complicated by the fact that while the carbon ion beam was still being commissioned in the synchrotron, the extracted beam would vary between beam commissioning sessions.

6.4.2 Spot Size Commissioning

Characterising the Beam from Quadrupole Scanning

Following the quadrupole scan method outlined in subsection 6.2.1, a series of measurements gave the Twiss parameters and emittance of a beam at the location of a quadrupole. Using MAD-X, the optics at the quadrupole were backtracked. The resulting vertical Twiss parameters at the start of the IR2 beam line is given in table 6.3.

A comparison of the results of simulations and measurements for the vertical plane can be seen in fig. 6.9. It can be seen that the results of the simulations and measurements are in good agreement. The quad scan also provided parameters for the horizontal plane, but was not used due to large uncertainties. This is because in the horizontal plane, the beam was quite narrow at the position

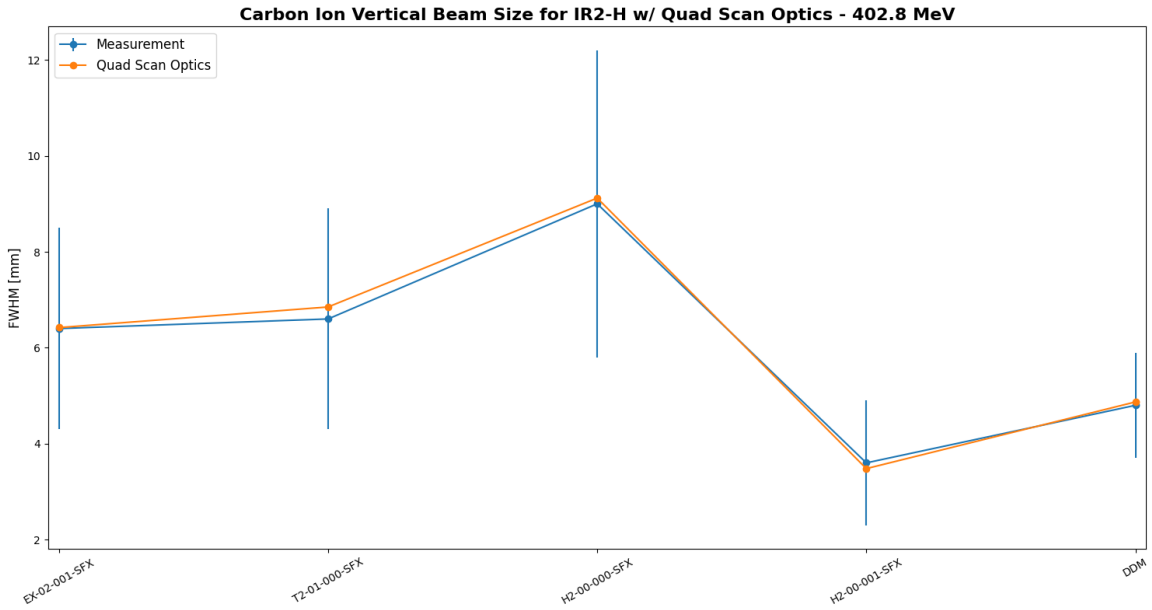

Figure 6.9: Comparison of the beam vertical FWHM measurements and simulations results using the optics from quad scans for carbon ions at 402.8 MeV/u.

of the detector [177], where it was only detected on a single fibre of the SFX monitor. Due to time constraints another part of the beam line could not be scanned.

Spot Size Adjustment

Using the reconstructed parameters from the quadrupole scan and manually adjusting the optical parameters for the horizontal plane, MAD-X was used to adjust the beam spot size. At the end of the beam line is a medical nozzle containing beam diagnostic devices such as the DDM. Following the nozzle is a gap of air between to the isocentre. In order to simulate the beam properly, scattering physics needed to be accounted for. MAD-X does not include scattering physics models, so BDSIM was used. A combination of the two codes was used for spot size adjustment. The work flow consisted of using MAD-X to do the optics matching, and then simulating the beam in BDSIM to incorporate scattering effects through the nozzle and air.

However, as previously outlined, there was a discrepancy at low energies between simulations and measurements. With little time available to investigate, a rudimentary method was used where scans over approximate Twiss parameters were used to generate magnet settings. A comparison of the parameters to measured beam sizes were then used to guide adjustments to the beam. This rudimentary method relies upon the beam being characterised well enough that a variation in the Twiss parameters would be reflected in the measured beam.

The method worked well for the vertical plane as the beam was well approximated using the parameters in table 6.3. A change in β_y would directly correspond to a change in the vertical beam

size and a constraint of $\alpha_y = 0$ would minimise the beam divergence. But extra care needed to be taken for the horizontal plane as varying both β_x and μ_x would affect the beam size. Varying the β_x parameter while keeping the phase advance constant between scans can be pictured as sequentially widening or shrinking the bar of charge. Whilst keeping β_x constant and varying the phase advance corresponds to a rotation in phase space. As the orientation of the bar of charge is not known, varying both parameters between scans could drastically affect the beam size. Furthermore, μ_x also affects the beam divergence. Due to this, a μ_x value that minimised the beam divergence was found, and β_x was used for beam size adjustments. Finally, there were constraints on the beam size to not scrape the beam pipe, which corresponded to ($\beta_{\mathrm{x,\ max}} < 80,\ \beta_{\mathrm{y,\ max}} < 85$).

Only the last three quadrupoles in the IR2-H beam line could be used for adjustments. The other quadrupoles in the beam line were not used because the presence of the bending dipole requires several quadrupoles to close the dispersion. Given the number of constraints on the parameters, three quadrupoles alone do not provide sufficient degrees of freedom. So some of these conditions were relaxed in order to best satisfy the specifications. A setting was first found for the highest energy as that would be where the magnet strengths tended to be highest, then settings were found for the lowest energy. The magnet settings for the intermediate energies are interpolated between the two strengths. Beam measurements have shown this to be an effective method to generate magnet settings without requiring the operator to specify the value. The spot sizes were first optimised at isocentre, but it was found that the beam fell out of specifications at several positions upstream of the isocentre. This required the beam to be re-optimised at a position 25 cm upstream of the isocentre. The final FWHM spot sizes and ellipticity at isocentre can be seen in fig. 6.10 and at isocentre -25 cm in fig. 6.11.

Although the spot size commissioning campaign was successful for IR2-H, the process highlighted a problem with characterising the beam. The quad scan method was very effective in reconstructing the vertical Twiss parameters, but took commissioning time to carry out. In addition, this method did not work well for the horizontal plane. But even if both planes could be characterised, there was still a discrepancy arising from the scattering simulations.

6.5 IR1 Spot Size Commissioning

6.5.1 Carbon Ion Beam

After carbon ions were commissioned for IR2-H, commissioning for IR1 quickly followed. In this case, only the HEBT needed to be commissioned. The specifications for the spot sizes are the same as specified in sec. 6.4.1 with the exception that these only needed to be achieved at isocentre.

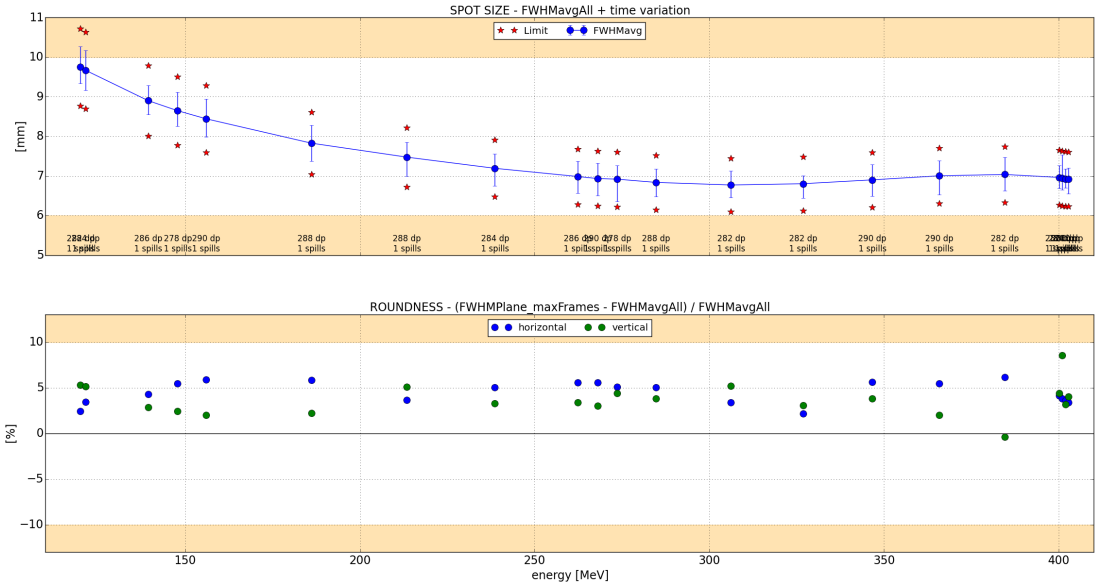

Figure 6.10: Spot size analysis after optimising for three energies at isocentre. Regions in beige are regions that exceed the constraints, the stars represent the constraint surrounding the average spot size at each energy for multiple spills, and the error bars representing the measured average spot size for multiple spills. The top plot shows the FWHM of the beam, and the bottom plot shows the beam ellipticity.

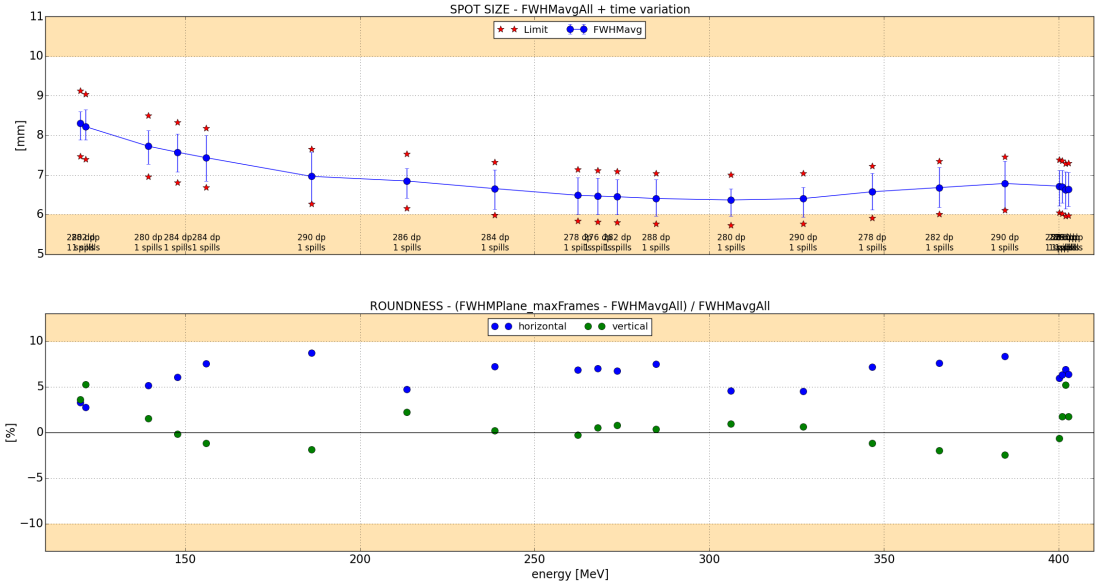

Figure 6.11: Spot size analysis after optimising for three energies at the position of isocentre - 25 cm. Regions in beige are regions that exceed the constraints, the stars represent the constraint surrounding the average spot size at each energy for multiple spills, and the error bars representing the measured average spot size for multiple spills. The top plot shows the FWHM of the beam, and the bottom plot shows the beam ellipticity.

Table 6.4: Comparison of carbon ion beam measurements and beam size simulations in the vertical plane using optics backtracked from the IR2-H quadrupole scan for 120 MeV/u carbon ions. The backtracked optics at the position EX-01-001-SFX are: $\epsilon_y = 2.1\,\pi \cdot \text{mm} \cdot \text{mrad}$, β_y =1.5 m, $\alpha_y = 0.13$.

Monitor	Measurement	Simulation
EX-01-001-SFX	5.1 ± 0.7 mm	4.2 mm
EX-01-002-SFX	8.8 ± 1.2 mm	12.9 mm
EX-01-003-SFX	7.0 ± 1.0 mm	9.7 mm
T1-00-000-SFX	11.9 ± 1.5 mm	10.9 mm
T1-01-000-SFX	11.9 ± 1.5 mm	15.5 mm
DDM	5.5 ± 0.7 mm	7.34 mm
ISD0	8.7 ± 1.1 mm	10.0 mm

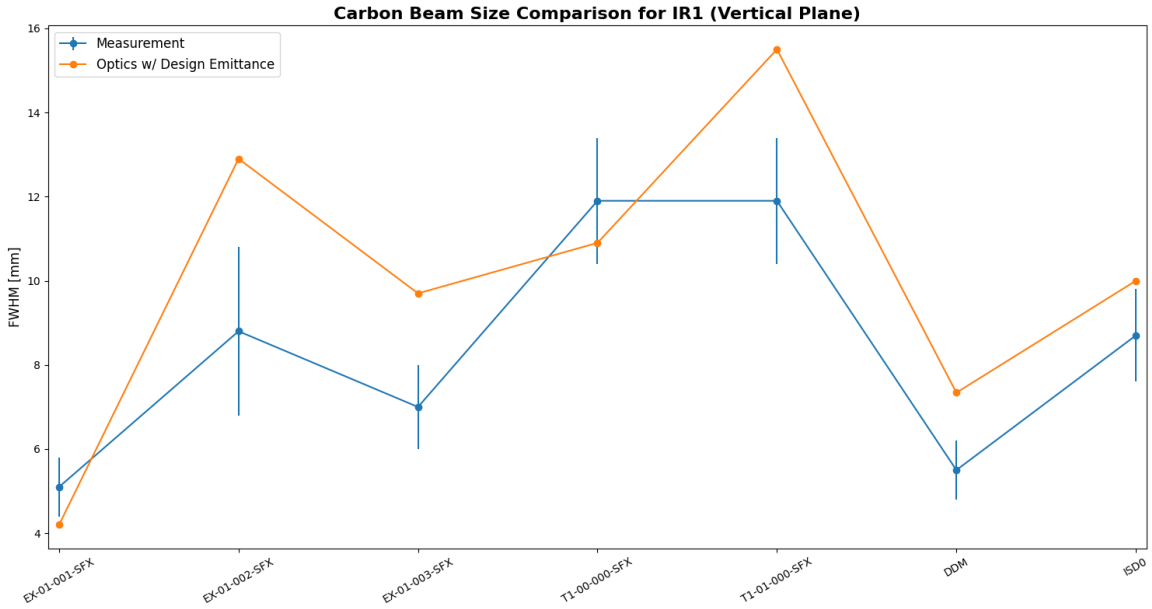

Figure 6.12: Comparison of carbon ion beam measurements and beam size simulations in the vertical plane using optics backtracked from the IR2-H quadrupole scan for 120 MeV/u carbon ions. The values in the plot are found in table 6.4.

As before, characterising the beam was important. Ideally a quad scan could be performed to reconstruct the beam entering IR1, but there was not enough time to do so. Instead, the Twiss parameters from the quad scan for IR2-H were backtracked to the entrance of IR1. Given the good comparison that was achieved previously, it was assumed that a good comparison could also be achieved for IR1. But as can be seen in table 6.4 and fig. 6.12 for 120 MeV/u carbon ions, there is a discrepancy between measurements and simulations in the vertical plane.

Despite lacking a good characterisation of the beam, quadrupole scans over the Twiss optics were used to adjust the spot size. However, due to the lack of a well characterised beam, a lot more scans were necessary to adjust the beam. The main difficulty was in minimising the divergence. Matching the lattice to a value of $\alpha_y = 0$ at the isocentre would not necessarily minimise the divergence as the starting Twiss parameters were not representative of the beam. There was a similar problem with the

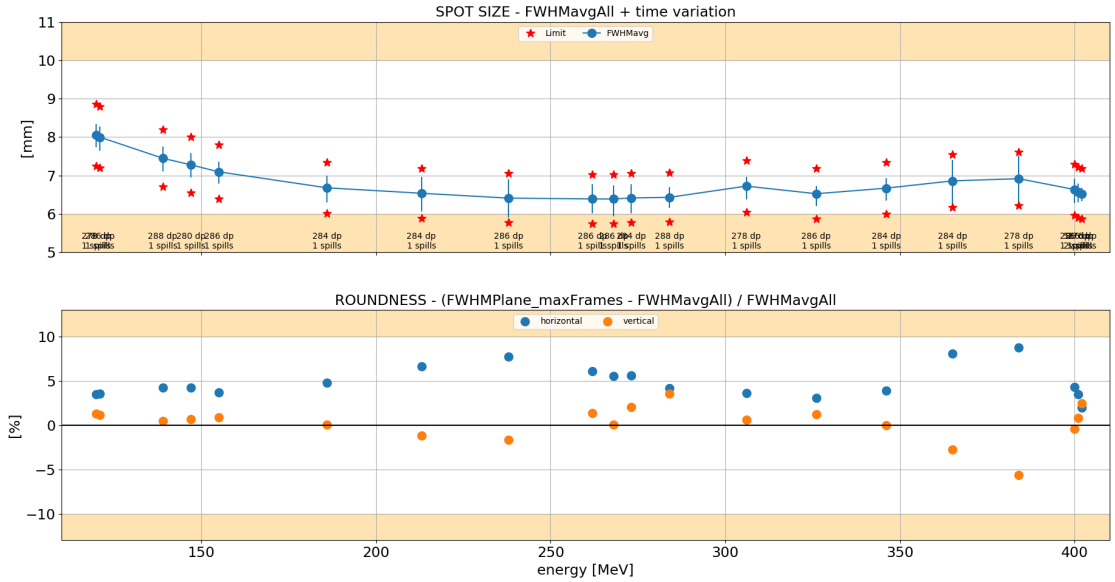

Figure 6.13: Final commissioned values for IR1 for a range of carbon ion energies at isocentre. Regions in beige are regions that exceed the constraints, the stars represent the constraint surrounding the average spot size at each energy for multiple spills, and the error bars representing the measured average spot size for multiple spills. The top plot shows the FWHM of the beam, and the bottom plot shows the beam ellipticity.

phase advance for the horizontal plane. However, as the specifications only applied at the isocentre, this mitigated some of these issues. The final values are given in fig. 6.13 for a range of energies. But it was clear that a fast method to approximate and characterise the beam was required.

6.5.2 800 MeV Proton Beam

In addition to carbon ions, highly energetic proton beams were of interest to the research groups, which led to 800 MeV protons being commissioned. In this case, three spot sizes were requested: $4{\times}4\,\mathrm{mm}^2$, $8{\times}8\,\mathrm{mm}^2$, and $20{\times}20\,\mathrm{mm}^2$. Initially an even smaller spot size was desired, but due to the vertical emittance of the 800 MeV proton beam, it was found that smaller beam sizes were not feasible.

The Twiss rematch procedure outlined in sec 6.2.2 was developed after the issues encountered for carbon ions. A key advantage of this procedure in characterising a beam compared to performing quadrupole scans is that it relies upon measurements at multiple detectors. This could be easily performed by the beam operators and does not require a commissioner to be present. In addition, it only requires a few minutes to perform. Another advantage is that a measurement of the beam waist is not necessary, but does require the beam to be well characterised by Twiss parameters.

To evaluate the effectiveness of this method in characterising a beam, a comparison was made to the commissioned carbon ion beams for IR2-H. A trajectory scan was carried out and the fitted

Table 6.5: Optics from Twiss rematch procedure from trajectory measurements of IR2-H for carbon ions.

Parameter	**Value**	
	402.8 MeV/u	120.0 MeV/u
ϵ_x	$0.18\,\pi \cdot$ mm $\cdot$ mrad	$0.18\,\pi \cdot$ mm $\cdot$ mrad
β_x	20.12 m	5.42 m
α_x	-6.87	-2.96
ϵ_y	$0.79\,\pi \cdot$ mm $\cdot$ mrad	$2.25\,\pi \cdot$ mm $\cdot$ mrad
β_y	9.07 m	3.81 m
α_y	-1.52	-0.17

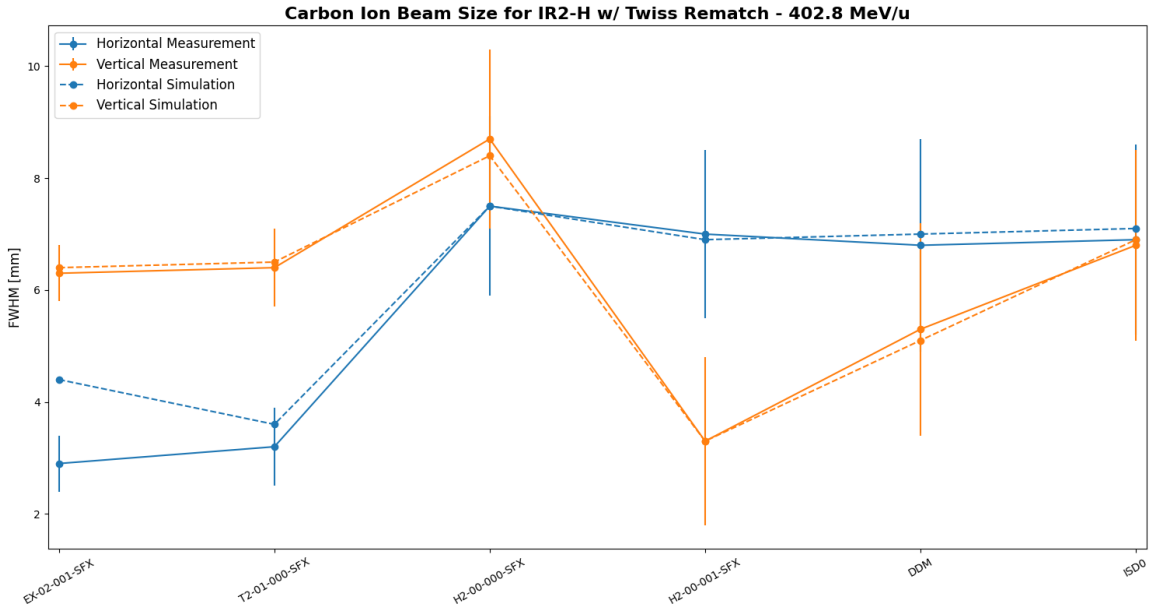

Figure 6.14: Comparison of measurements and simulations of beam size at various detectors along the IR2-H beam line for 402.8 MeV/u carbon ions. Initial optics taken from table 6.5.

optics using the Twiss rematch procedure are given in table 6.5. The beam size for the highest and lowest carbon ion energies were measured and compared against the simulations as can be seen in fig. 6.14 and fig 6.15 respectively. A good comparison can be found in both planes with the exception of the simulated beam at the start for the horizontal plane. This could be an indication of a problem in the monitor, or that the distribution of the beam is not described well by the Twiss parameters. The effectiveness of this method is also supported by a comparison of the starting parameters for the vertical plane between the quad scan (table 6.3) and the rematch procedure (table 6.5). Despite the great characterisation, the discrepancy due to scattering at low energies can still be seen.

This method was used to characterise the 800 MeV beam before the shift. Due to the intensity of the delivered beam, the medical nozzle containing the beam diagnostic devices was removed so the DDM monitor was not available. But there were sufficient SFX detectors within the beam line to characterise the beam, with the optics given in table 6.6. This description served as a good

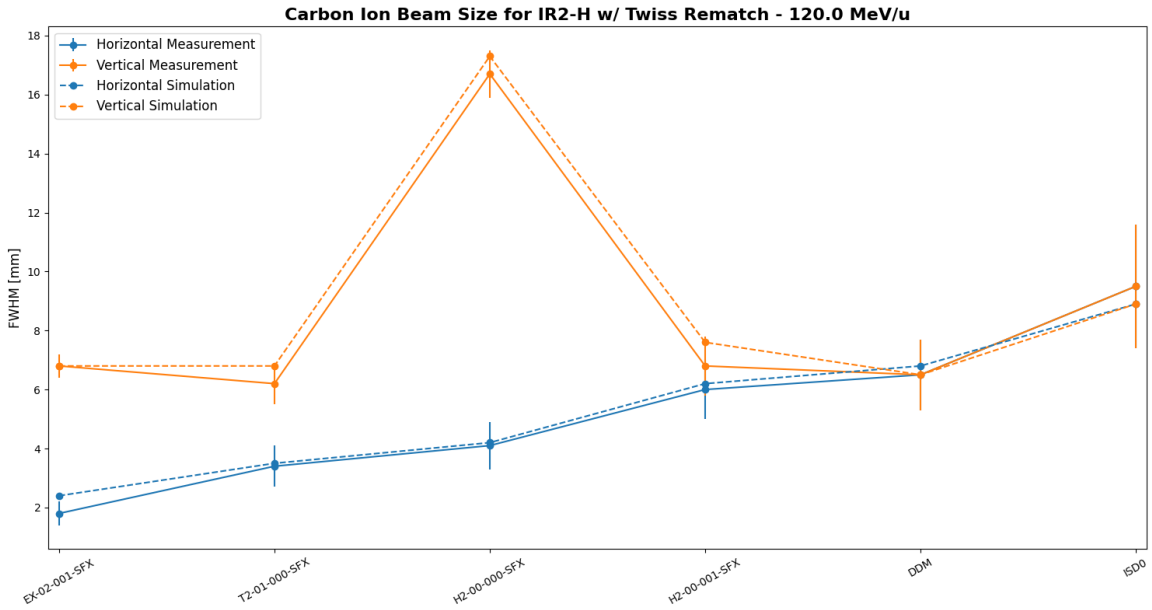

Figure 6.15: Comparison of measurements and simulations of beam size at various detectors along the IR2-H beam line for 120.0 MeV/u carbon ions. Initial optics taken from table 6.5.

Table 6.6: Optics from Twiss rematch procedure from trajectory measurements of IR1 for 800 MeV protons.

Parameter	Value
ϵ_x	$0.40\,\pi \cdot \text{mm} \cdot \text{mrad}$
β_x	3.99 m
α_x	-1.12
ϵ_y	$1.35\,\pi \cdot \text{mm} \cdot \text{mrad}$
β_y	4.41 m
α_y	0.61

characterisation of the beam, and only a couple of scans were needed to achieve the three spot sizes as seen in table 6.7 and fig. 6.16 for the smallest spot size. Due to the relatively high energy, there was minimal scattering in the air which led to the great comparison of simulations and measurements.

In conclusion, the Twiss rematch procedure proved to be both a quick and accurate way to fit and characterise a beam. It was also used to great success for various other spot size optimisations. However, there are some issues affecting the effectiveness of this method. One is that this method relies upon accurate measurements of the beam, if the detectors give inaccurate measurements (such as radiation damage) this could affect the fitted optics. A possible solution is to incorporate a weight factor to account for monitors that suffer from radiation damage. This would allow the minimisation to prioritise the detectors which give accurate measurements. Another issue is that the method only works for a centred beam. An adjustment to the method would be needed to incorporate the beam position.

Table 6.7: Comparison of measurements and simulations at various detectors along the IR1 beam line for 800 MeV protons, using optics from table 6.6. Different quadrupole settings were used in order to achieve the three different spot sizes at ISD0.

Monitor	**Horizontal [mm]**		**Vertical [mm]**	
	Measurement	Simulation	Measurement	Simulation
EX-01-001-SFX	2.7 ± 0.6	2.7	3.5 ± 0.7	3.7
EX-01-002-SFX	6.2 ± 1.3	6.0	12.0 ± 2.6	11.9
EX-01-003-SFX	8.2 ± 1.8	8.4	4.3 ± 0.9	5.0
T1-00-000-SFX	10.4 ± 2.3	9.8	14.5 ± 3.2	14.6
T1-01-000-SFX	11.5 ± 2.6	11.8	16.1 ± 3.6	16.1
T1-01-001-SFX	3.7 ± 0.8	3.4	7.5 ± 1.7	6.7
ISD0 ($4\times4\,\mathrm{mm}^2$)	4.1 ± 0.8	4.0	4.2 ± 0.8	4.6
ISD0 ($8\times8\,\mathrm{mm}^2$)	8.1 ± 1.8	8.1	7.9 ± 1.5	8.1
ISD0 ($20\times20\,\mathrm{mm}^2$)	20.2 ± 4.0	19.8	19.6 ± 3.8	19.3

Figure 6.16: Comparison of measurements and simulations at various detectors along the IR1 beam line matched to $4\times4\,\mathrm{mm}^2$ for 800 MeV protons. Initial beam optics come from table 6.6 and the beam sizes can be found in table 6.7.

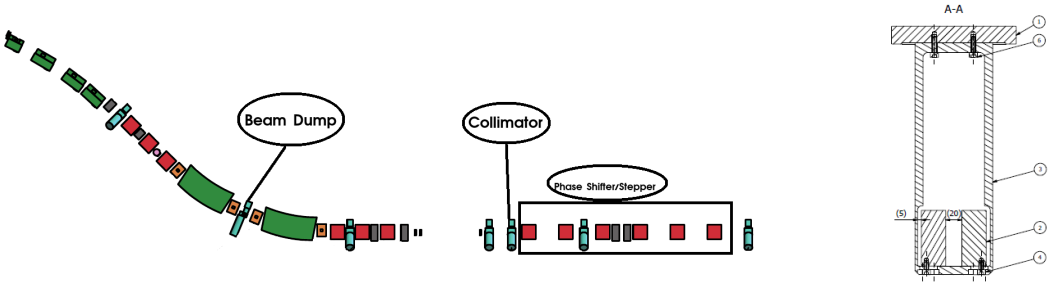

Figure 6.17: Schematic diagrams of the section of the beam line to consider the risk assessment. On the left is beam line, where the beam dump, collimator, and PSS are pictured. On the right is the collimator block that was installed just upstream of the PSS to intercept unwanted beam.

6.6 Collimator Risk Assessment

To allow for the safe delivery of carbon ions, some safety concerns needed to be addressed. In particular, it was critical to ensure that any unwanted beam from the synchrotron is intercepted before entering any of the irradiation rooms. MedAustron was designed such that by default the extracted beam is directed straight towards a beam dump. In order for beam to reach the end station, a set of dipole magnets (chopper) needs to be powered to divert the beam around the beam dump (in the horizontal plane). However, in order to ensure safe delivery, situations need to be considered where a fault in the system might result in unwanted beam irradiating one of the rooms. This was previously considered when MedAustron was first commissioned with protons [178], and this resulted in the inclusion of a collimator located right after the chopper and before the PSS as can be seen in fig. 6.17.

In the previous analysis, WinAgile [179] was used to track a beam of protons. Initially, a phase space that filled the beam pipe was tracked, and it was found that a subset of particles bypassed the beam dump even when the chopper magnets were unpowered. The addition of a collimator could intercept these extraneous particles as can be seen in fig. 6.18. A similar analysis for carbon ions was necessary to ensure the collimator was still effective [180].

6.6.1 Reproducing the Proton Beam Simulations

The first step was to reproduce the analysis for protons to ensure the same results could be obtained with MAD-X. This consisted of verifying the angular spread of particles that bypass the beam dump is the same and that the collimator is still effective.

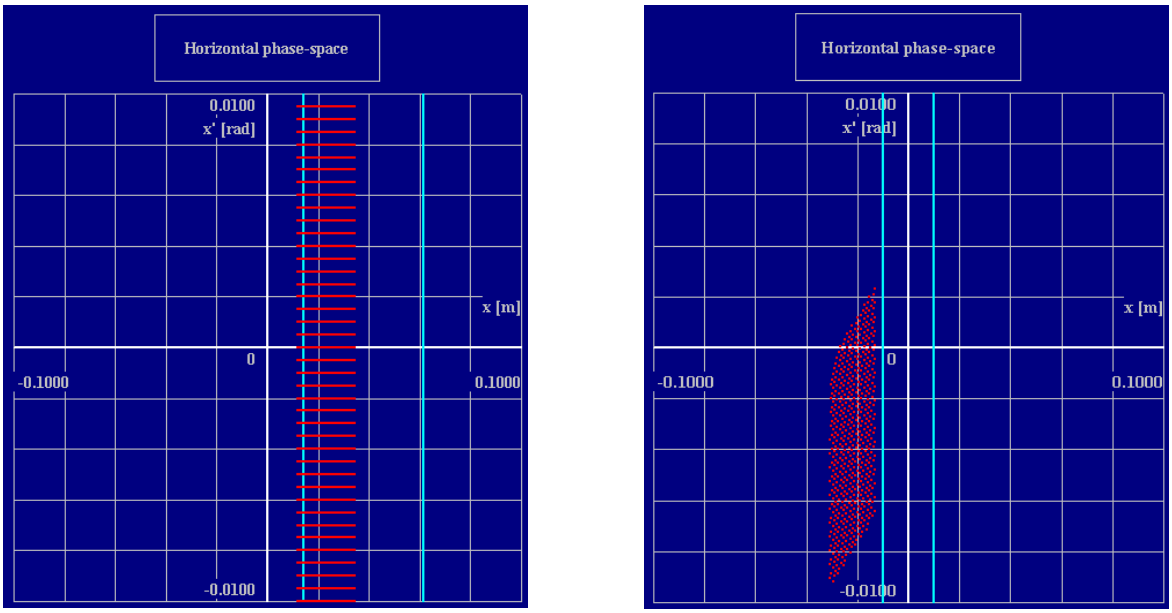

Figure 6.18: Previous simulations performed for protons where all protons which bypass the beam dump will hit the collimator walls. The image on the left shows the horizontal phase space of particles for a simulation starting at the beam dump. The image on the right shows the horizontal phase space at the position of the collimator [178]. The region between the cyan lines represents the gap in the collimator.

Particle Configurations that Bypass Beam Dump

A large beam distribution that filled the entirety of the beam pipe was generated at the start of the extraction line. Such a large distribution was simulated in order to capture all possible configurations of particles. This beam distribution was then tracked to the beam dump.

In fig. 6.19 it can be seen that only a few particles bypass the beam dump according to the MAD-X simulation. But it can be noted that the particles which bypass the beam dump fill the gap between the beam dump and beam pipe (radius of about 3.3 cm). The divergence ranges between −0.005 rad to 0.010 rad, and lies within the region given by fig. 6.18. This range is different to the previous analysis because the WinAgile simulations use the maximum angular values for both positive and negative angles to serve as a safety margin.

Simulations from Beam Dump to Collimator

A new distribution of particles starting at the gap of the beam dump was simulated with a distribution of positions that filled the gap. Following what was done in the WinAgile simulations, a large safety margin was simulated for with a divergence ranging between −0.010 rad to 0.010 rad. From the results given by fig. 6.20, it can be seen that the distribution of protons which bypass the beam dump are captured by the collimator.

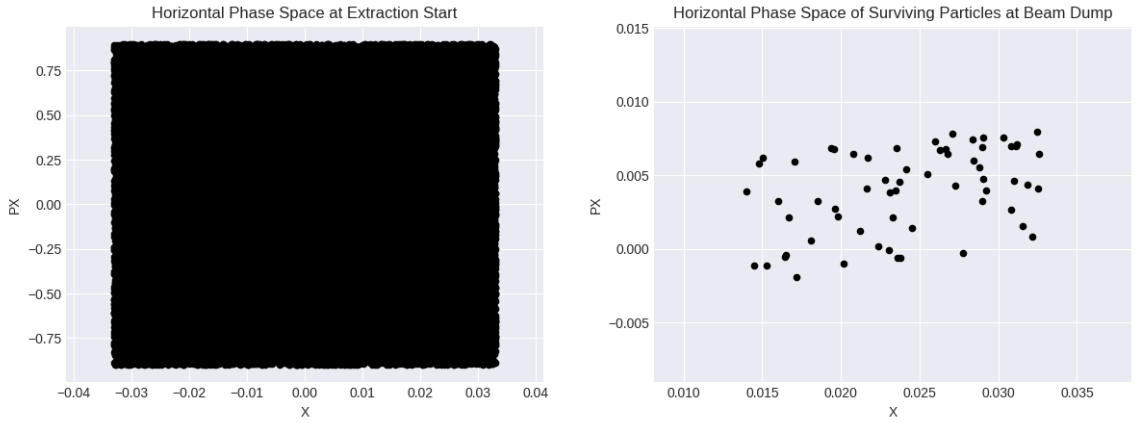

Figure 6.19: The left image shows the initial starting horizontal phase space distribution of particles at the beginning of extraction at the start of the EX-00-000-MST magnet. The image on the right shows the horizontal phase space distribution of particles which bypass the beam dump in the gap between the beam dump and the beam pipe. The vertical axis uses the MAD-X designation of 'PX' to represent the normalised horizontal momentum in radians.

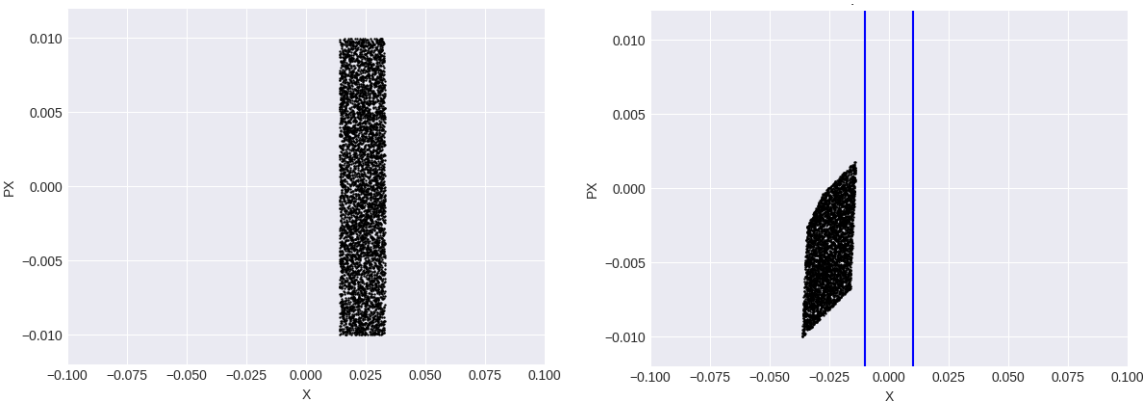

Figure 6.20: The horizontal phase space distributions simulated with MAD-X PTC are shown. On the left is the starting phase space distribution at the beam dump gap. On the right is the distribution at the position of the collimator. The lines in blue denote the boundaries of the opening of the collimator, where it is shown that all particles hit the walls of the collimator. The vertical axis uses the MAD-X designation of 'PX' to represent the normalised horizontal momentum in radians.

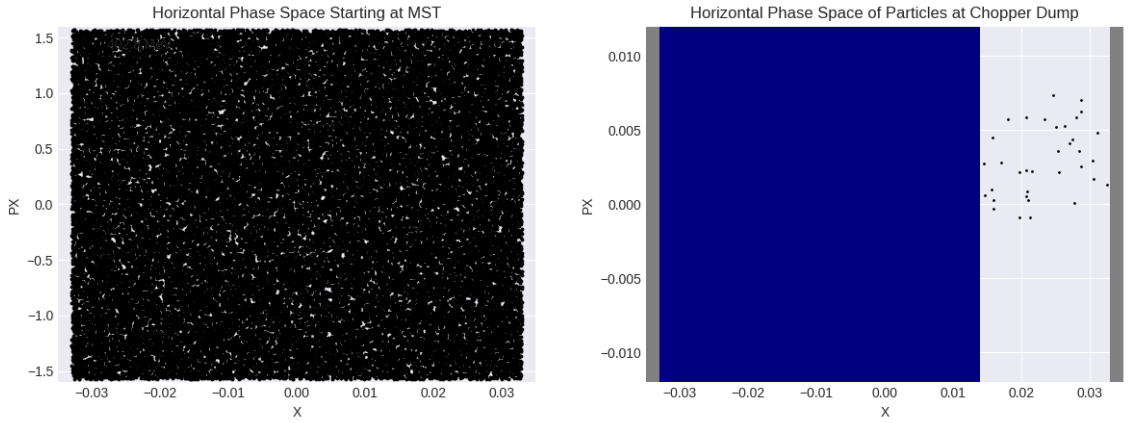

Figure 6.21: The left image shows the initial starting horizontal phase space distribution of particles at the beginning of extraction at the start of the EX-00-000-MST with a distribution filling the whole of the beam pipe for 402.8 MeV carbon. The image on the right shows the horizontal phase space distribution of particles which bypass the beam dump in the gap between the beam dump and the beam pipe. The vertical axis uses the MAD-X designation of 'PX' to represent the normalised horizontal momentum in radians.

6.6.2 Carbon Ion Simulations

For carbon ions, the previous process was repeated. This analysis was carried out with MAD-X, but a cross check with BDSIM was made which gave consistent results. As was done previously, first a large initial beam spread was simulated at the start of the HEBT and tracked to the beam dump. From Figure 6.21 it can be seen that the divergence spread of carbon ions with energies of 402.8 MeV/u that bypass the beam dump is roughly between −0.002 rad and 0.008 rad. From this divergence spread, another distribution was simulated from the beam dump gap where an additional 10% safety margin for the spread was included.

Using the nominal quadrupole settings for 402.8 MeV/u carbon ions, it can be seen in fig. 6.22 that the collimator is effective in intercepting all the carbon ions that bypass the beam dump. A trajectory plot through the beam line elements can be seen in fig. 6.23.

Several other carbon ion energies were tracked and the distributions at the beam dump and collimator can be seen in fig. 6.24 and fig. 6.25 respectively. A trajectory plot for these energies starting at the beam dump can be seen in fig. 6.26. Although there is a minor variation between the energies, the collimator is effective for all these cases. To address the safety concerns, the ramifications of these results will be scrutinised in the next section.

6.6.3 Single Fault Conditions

For the safe delivery of carbon ions, it is specified that under a single error or fault, no beam will enter any of the irradiation rooms. Under this single fault criterion there are two scenarios to consider:

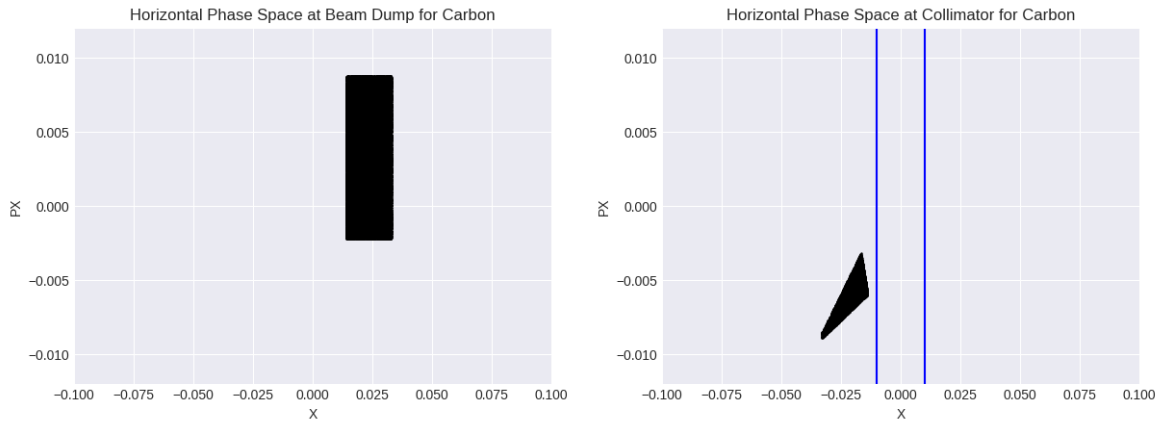

Figure 6.22: The left figure shows the initial starting horizontal phase space distribution of particles at the beam dump with a distribution filling the whole of the gap between the dump and the beam pipe for 402.8 MeV carbon. The figure on the right shows the horizontal phase space distribution of particles at the position of the collimator. The vertical axis uses the MAD-X designation of 'PX' to represent the normalised horizontal momentum in radians.

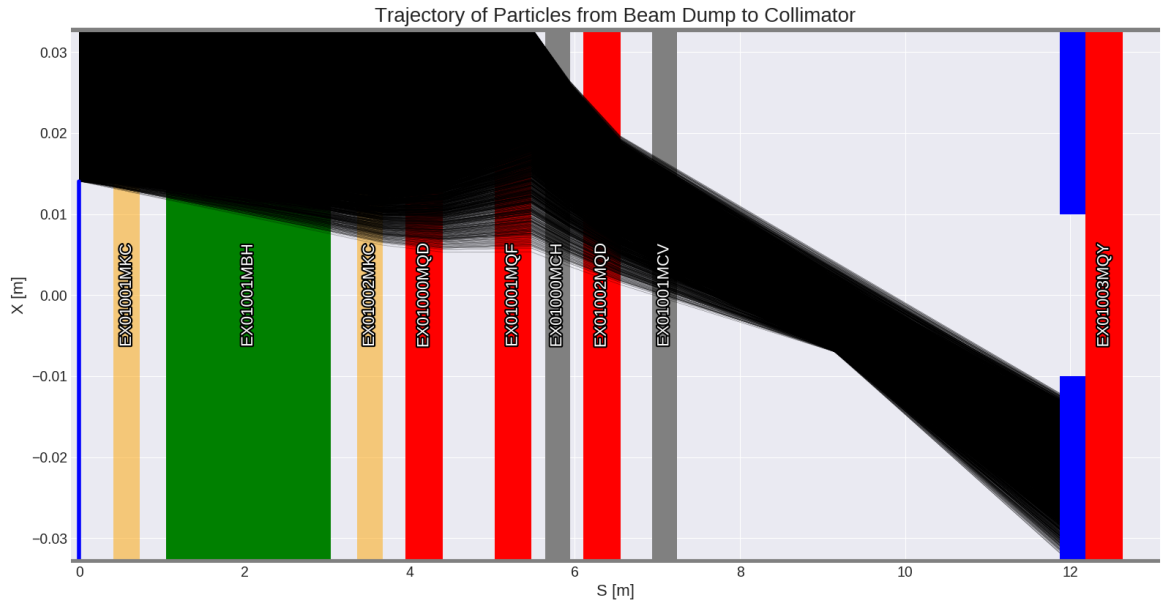

Figure 6.23: Horizontal trajectory plot from the beam dump to collimator. It is assumed that the chopper magnets pictured: EX-01-001-MKC and EX-01-002-MKC are not powered. The beam elements are overlaid behind the particle trajectories, where the element in beige represent the chopper magnets, green are dipoles, red are quadrupoles, and gray are kicker magnets.

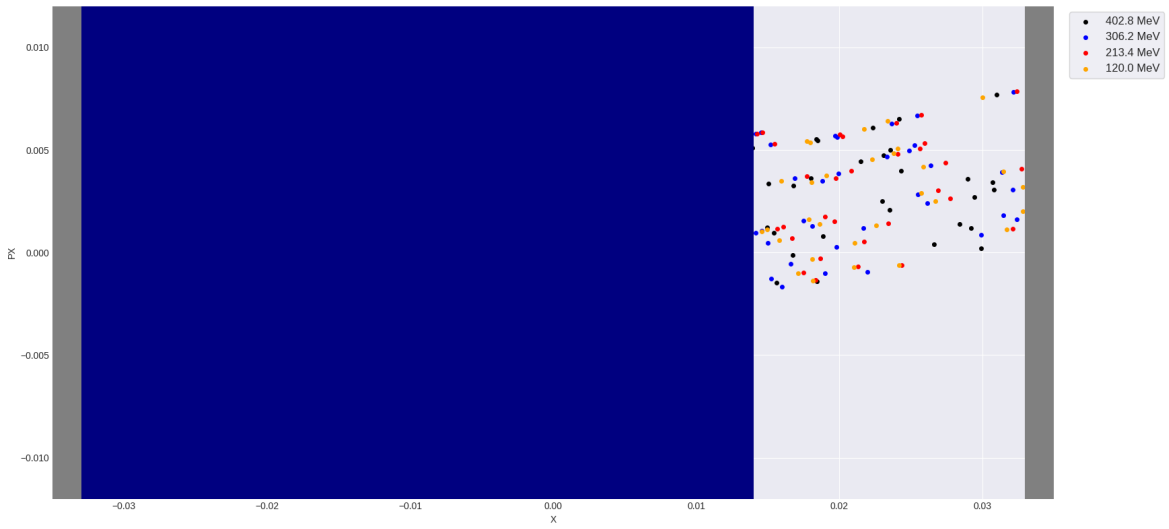

Figure 6.24: The particle distribution of carbon ion particles which bypass the chopper dump from a very extreme set of initial distribution configurations as from the left image of fig. 6.21. The vertical axis uses the MAD-X designation of 'PX' to represent the normalised horizontal momentum in radians.

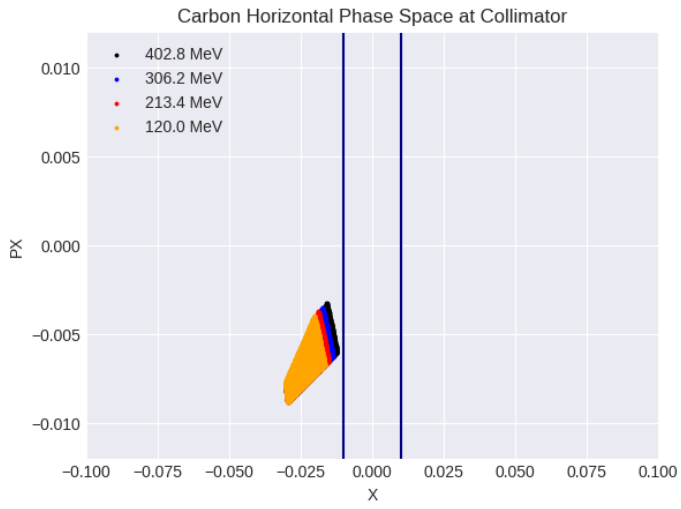

Figure 6.25: The phase space at the collimator for several energies where all particles are intercepted by the collimator. The vertical axis uses the MAD-X designation of 'PX' to represent the normalised horizontal momentum in radians.

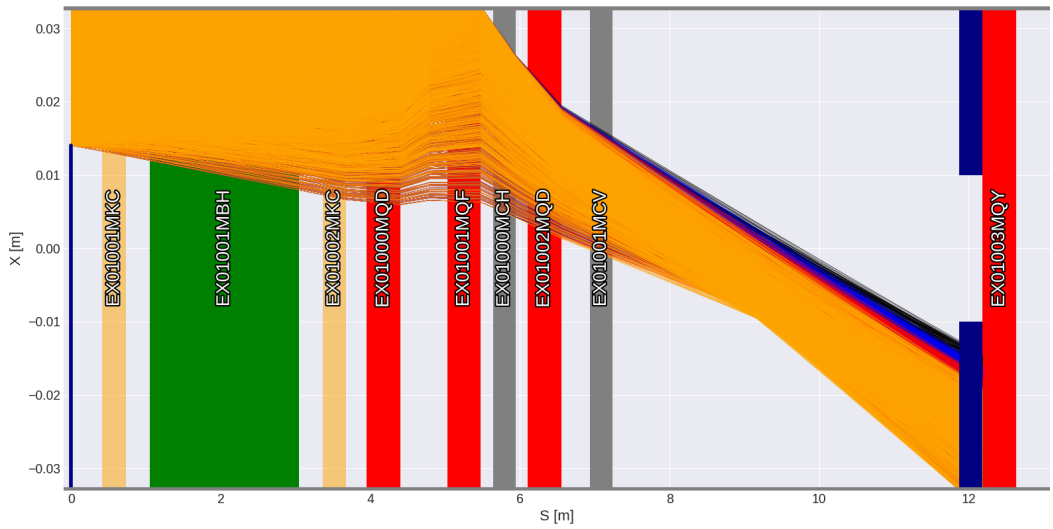

Figure 6.26: A trajectory plot to accompany fig. 6.25. The colour of the trajectory lines depict the energy of the carbon ion beam: black for 402.8 MeV/u, blue for 306.2 MeV/u, red for 213.4 MeV/u, and orange for 120.0 MeV/u. The beam elements are overlaid behind the particle trajectories, where the element in beige represent the chopper magnets, green are dipoles, red are quadrupoles, and gray are kicker magnets.

1. A single fault in an element between the chopper dump and the collimator

2. A single fault in an element upstream of the chopper dump

Since the first scenario only has an error after the chopper dump, this means that all magnetic elements starting from the source to the chopper dump function as intended. In this case, a simulation is not required as it was known from commissioning that when the chopper magnets were not powered, no beam was ever detected in any of the downstream monitors. Hence, this scenario can immediately be ruled out.

The second scenario considers where the error lies in an element located somewhere between the source and the chopper dump. The exact nature of the fault is not important, but an absolute worst case scenario needs to be considered, where such a single fault leads to a beam with a non-typical configuration. There are two ways to interpret this: the fault blows up the beam to a large emittance, or the resulting extracted beam has an unusual trace space distribution. This was what was considered in the analysis above, where it was shown that starting from a filled beam pipe at the start of extraction, no unwanted beam bypasses the collimator. Thus, under a single fault criterion, no unwanted beam reaches any of the irradiation rooms.

6.6.4 Multiple-Fault Conditions

Looking at fig. 6.25 and fig. 6.26, it can be seen that the particles are close to bypassing the collimator. Hence, a multiple-fault scenario was also considered to evaluate whether a succession of faults might

result in a beam reaching one of the irradiation rooms. But it should be stressed that this is beyond the scope of what is required for the risk assessment [180]. Under the multiple fault consideration there are three scenarios to consider:

1. Multiple faults in elements prior to the chopper dump
2. Multiple faults in elements after the chopper dump
3. A set of faults prior to the chopper dump and another set of faults after the chopper dump

The first scenario is the same as the single-fault condition scenario as the absolute worst case scenario has already been considered at the start of the HEBT. So under this scenario, any particles that bypass the chopper dump will be intercepted by the collimator.

The second scenario also falls under the single fault condition above. Since there is never beam observed downstream when the chopper dump magnets are not powered. If the faults are only downstream of the chopper dump these will not contribute to unwanted beam reaching an irradiation room.

The interesting scenario to consider is the third scenario where we have faults both prior to the chopper dump and after the beam dump. To consider this, we will assume that the faults prior to the chopper dump lead to the worst-case scenario, then we also consider faults in the magnets after the beam dump. As was the case for the single fault criterion, the entire phase space was filled coming out of the extraction line. Then magnets in the beam line were adjusted to within $\pm 15\%$ of the nominal strengths, a value that was considered to be reasonable.

In fig. 6.27, 50,000 carbon ions were tracked starting from the large emittance beam just after extraction. One of the quadrupoles (EX-01-001-MQF) was adjusted to have a reduced strength of -10% the nominal value. Further analysis is required in order to draw firm conclusions, but it can be seen that there is at least one scenario leading to beam bypassing the collimator. Although such an example was found, a multiple fault scenario is quite unlikely to occur. It also requires a very specific set of faults to occur. Furthermore, the analysis has made no consideration for any of the safety interlocks triggering which would help mitigate this problem. As the carbon ions satisfy the single fault criterion, and the likelihood of a multiple fault scenario being quite low, carbon ions were deemed to be safe for delivery.

6.7 Conclusions

This chapter presented the results of spot size adjustment at MedAustron between 2018 to the summer of 2019. Although various issues occurred during the commissioning, the effort was successful and

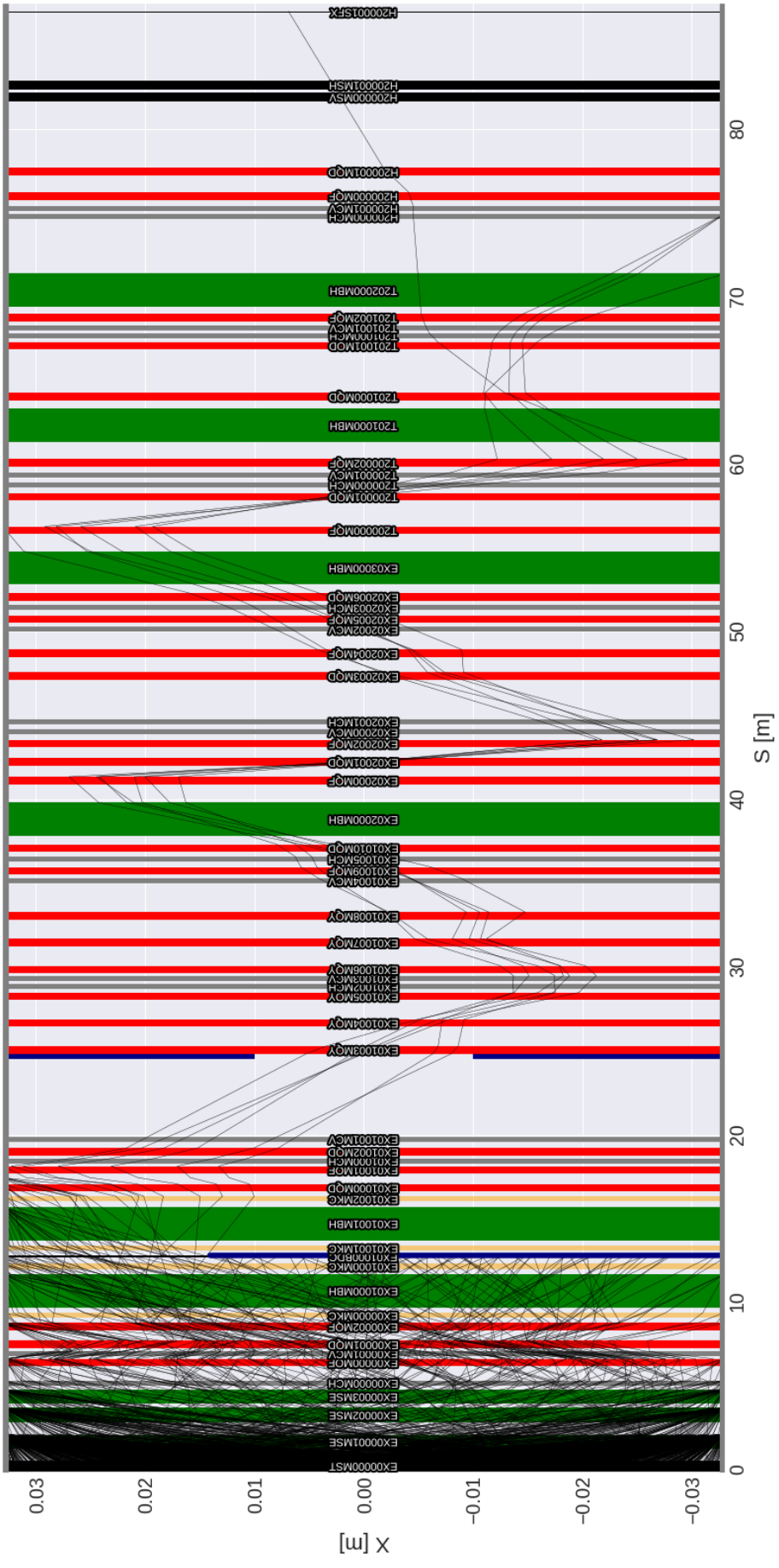

Figure 6.27: A full trajectory plot from the MST to an irradiation room (IR2). Here an error in the quadrupole element EX-01-001-MQF with a reduced strength of −10% the nominal value has led to one carbon-ion out of 50,000 total particles starting at the MST. The beam elements are overlaid behind the particle trajectories, where the element in beige represent the chopper magnets, green are dipoles, red are quadrupoles, gray are kicker magnets, black are scanning magnets, and the final element is a beam monitor.

met specified deadlines and specifications. Characterising the beam was of great importance to spot size adjustment. Throughout the commissioning effort, various attempts were made to characterise the beam, notably through quadrupole scans and through a rematch procedure that was developed.

However, the discrepancies noted for scattering simulations could not be resolved despite having a good initial beam characterisation. The underestimation of the scattering was consistently present for low energy particles. Even though the beam could not be accurately simulated from the beam line to the isocentre, the results could still be leveraged to study the beam ellipticity. Furthermore, if one had a measurement, a scaling factor could be applied to make the simulation results more comparable to measurements.

Finally, to ensure the safe delivery of carbon ions, a collimator risk assessment was carried out. Under the ALARA (As Low As Reasonably Achievable) process, it is satisfactory to fulfil single fault scenarios in reducing risks and allowing for the safe delivery of carbon ion for patient treatments. It as shown that all single fault scenarios are mitigated. Supplemental out-of-scope studies showed that a multiple faults scenario could potentially result in unwanted beam reaching a treatment room. However, in this case, safety interlocks present in the beam line and irradiation rooms would act to prevent particles from reaching the patient.

Chapter 7

LhARA Developments

Conventional particle beam therapy typically delivers treatment in several sessions over several weeks. In each session, a single fraction of about 2 Gy is delivered over a few minutes. Careful planning is needed to deliver a uniform dose to a target volume. New techniques and methodologies are being investigated to improve the treatment modality. FLASH irradiation with high dose rates has garnered renewed interest over recent years which could increase patient throughput and reduce side effects [14, 181–183]. In addition, mini- and micro-beams could spare dose to superficial tissues by segmenting beams into parallel small sized beams [184]. Experiments with novel beams are needed to investigate the underlying mechanisms of such techniques.

An example of a novel source that has garnered interest are intense lasers which can produce electrons, protons, and ion beams. One project that aims to make use of a laser driven source is the Laser-hybrid Accelerator for Radiobiological Applications (LhARA) [33, 34]. LhARA plans to exploit the TNSA mechanism to create protons and light ions. As these particles are captured at energies above those of conventional sources (∼MeV), this helps evade the current space-charge limit. These particles are then captured and focused by five strong focusing plasma lenses and transported to an *in vitro* end station, or directed to an FFA (fixed field alternating gradient accelerator) to undergo post acceleration. The FFA will accelerate the beam to higher energies to serve another *in vitro* end station or an *in vivo* end station. The vision of the LhARA collaboration is to prove the novel technologies which are needed for future facilities and to provide a dedicated research facility to aid radiobiological research.

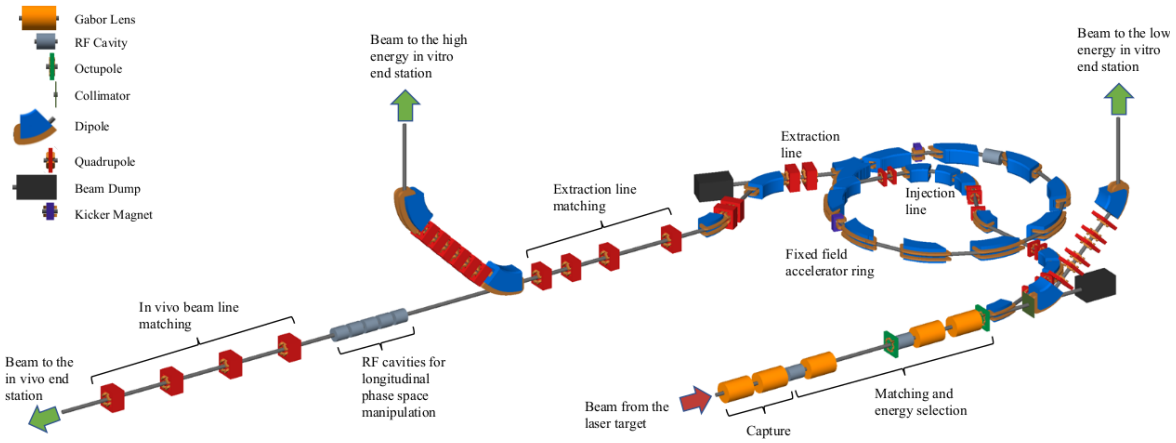

Figure 7.1: Schematic diagram of the elements of LhARA [34]. Particles from the laser source depicted by the red arrow are captured and transported by Gabor lenses to a low energy *in vitro* end station. Alternatively, the beam can be directed towards an FFA to accelerate the beam to higher energies. These high energy particles are directed to either a high energy *in vitro* or *in vivo* end station.

7.1 LhARA Facility

The LhARA facility consists of: a laser driven source, capture with five strong focusing plasma (Gabor) lenses, delivery of a vertical beam to a low energy *in vitro* end station, post acceleration with an FFA, vertical delivery to a high energy *in vitro* end station, and horizontal delivery to an in vivo end station. A schematic diagram of the facility showing the elements of LhARA is presented in fig. 7.1. The delivery of LhARA will be split in two: Stage 1 provides proton energies up to 15 MeV and Stage 2 includes commissioning the FFA to deliver both protons and other ions. LhARA will be discussed in the following sections.

7.1.1 Stage 1

Laser Driven Source

Laser systems can generally be split into single-shot systems with low repetition rates, or systems with high repetition rates. Of the two, the single-shot systems tend to produce higher energy particles. However, LhARA plans to make use of a high repetition rate laser to better serve the needs of radiobiologists.

LhARA will operate with Target Normal Sheath Acceleration, a regime discussed in sec. 4.4. An intense laser will be focused onto a target, ionising the material and producing a sheath field on the surface. Contaminants on the surface are ionised and accelerated. As LhARA is not focused on achieving the highest energies solely from the laser system, a commercial high repetition rate laser systems can be used [34]. Scaling back the energy may also help to improve the shot-to-

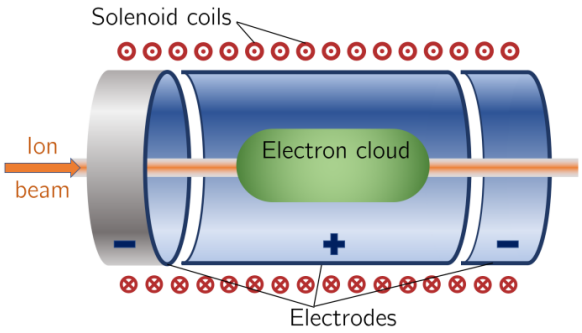

Figure 7.2: A schematic diagram of a Penning-Malmberg trap which can be used to confine an electron plasma [34].

shot reproducibility. Optimisations can be done for targets such as targets with nanostructures on the surface which make the overall density lower to improve the acceleration [185] or using foam targets [186].

Due to the nature of the interaction, the target needs to be replaced between shots. To facilitate a high repetition rate, a tape drive system is envisioned. This system can quickly deliver a fresh target between shots. Key to the operation is ensuring the target will be stretched flat to allow the laser to better couple to the target and to avoid ripples on the surface. However, an important point of concern is the debris that can result from solid target. A solution could be to use cryogenic hydrogen jets instead as these may generate higher energy ion beams without concern for debris. Gauthier *et al.* [187] have shown the capability of using cryogenic hydrogen jets for a 1 Hz repetition rate laser [187], but further research may be able to achieve higher repetition rates.

Plasma (Gabor) Lenses

In 1947, Gabor noticed that a cloud of electrons confined and distributed about a cylindrical vessel could produce an ideal focusing force in both planes for positively charged particles [188]. This is a useful property for capturing a laser driven beam which has a large divergence. The plasma can be confined using the design of a Penning-Malmberg trap as pictured in fig. 7.2.

For confinement, the Brillouin flow limit gives the maximum density of an ideal electron plasma that can be radially confined by an axially symmetric magnetic field, B_z [189]:

$$n_{e,r,\max} = \frac{\epsilon_0 {B_z}^2}{2m_e}, \tag{7.1}$$

where ϵ_0 is the permittivity of free space and m_e is the electron mass. The anode voltage confines

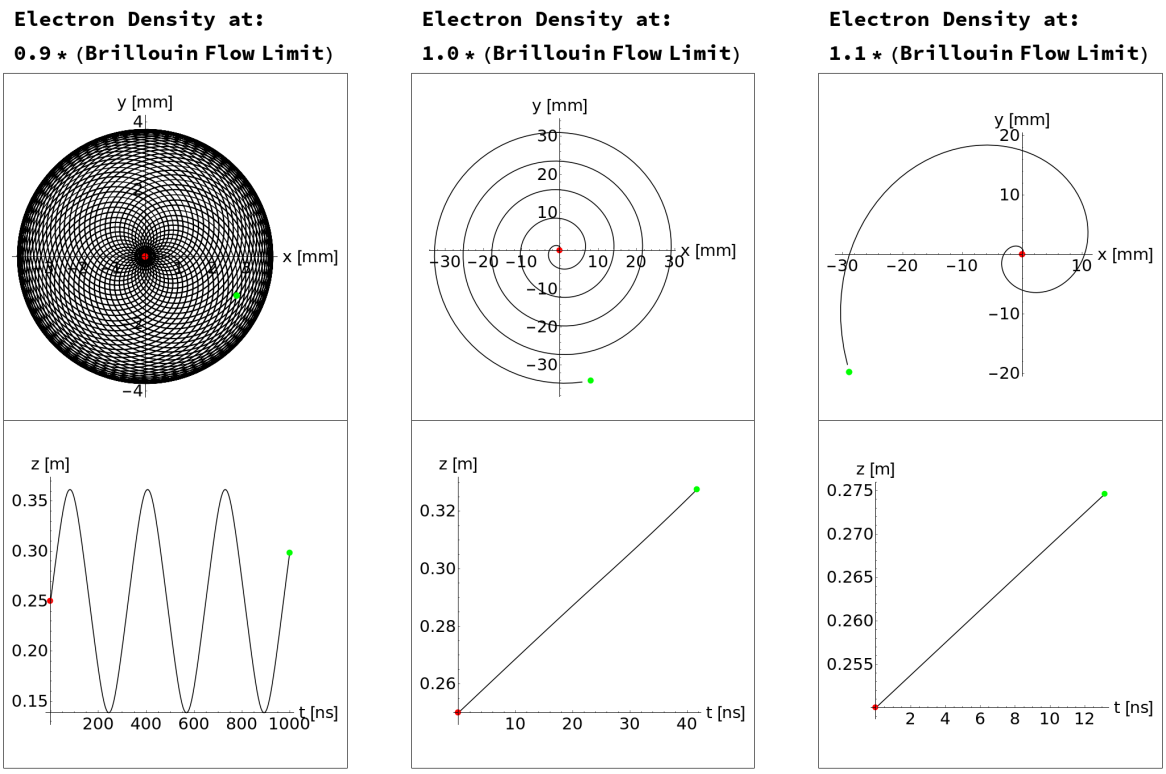

Figure 7.3: Radial (top row) and longitudinal (bottom row) motion for an electron at three electron plasma densities: below the Brillouin limit (left), at the Brillouin limit (middle), and above the Brillouin limit (right). The three cases have been simulated for 1 µs, though for the cases at and above the Brillouin limit, the electrons are lost early on. The lens was represented with a length of 500 mm, anode radius of 35 mm, anode voltage of 630 V, and axial magnetic field of 0.008 T. The electron has initial velocity: $(5.93 \times 10^5, 5.93 \times 10^5, 1.88 \times 10^6)$ m/s.

the plasma longitudinally by:

$$n_{e,z,\max} = \frac{4\epsilon_0 V_A}{eR^2}, \tag{7.2}$$

where e is the magnitude of the electron charge and R is the radius of the cylindrical anode with a potential V_A. The effect of the electron density on confinement can be seen in fig. 7.3 for an electron at three densities: below the limit, at the limit, and above the limit. Below the Brillouin limit, we see that an electron remains confined radially and oscillating longitudinally even after 1 µs. At the Brillouin limit, the particle is not confined, spiralling outwards until it hits the transverse boundary after 42 ns. Above the limit, the electron quickly is lost at 13 ns.

The electron plasma gives a radial focusing force which can act on a proton beam given by:

$$m_p \ddot{r} = eE_r = -\frac{n_e e^2}{2\epsilon_0} r, \tag{7.3}$$

where m_p is the proton mass, r is the radial position, and E_r the radial electric field. The focal length

under the thin lens approximation is then given by [189]:

$$\frac{1}{f_G} = \left(\frac{n_e e^2}{2{v_p}^2 m_p \epsilon_0}\right) \ell = \left(\frac{e^2 {B_z}^2}{4{v_p}^2 m_p m_e}\right) \ell, \tag{7.4}$$

where v_p is the longitudinal velocity, and the Brillouin flow limit from eq. 7.1 is substituted for the electron density.

As discussed in sec. 2.3.3, a solenoid can produce the same focusing effect in both planes. But when one compares the magnetic fields between the two devices, one gets the relation: [190]:

$$B_{\mathrm{GL}} = B_{\mathrm{sol}} \sqrt{Z \frac{m_e}{m_i}}, \tag{7.5}$$

which shows that for a given focal length, the magnetic field for a Gabor lens is reduced compared to a solenoid, lowering costs. However, Gabor lenses are subject to instabilities in the plasma as the electron number density increases. Research is ongoing to develop a stable lens [191,192]. For LhARA, five Gabor lenses are planned for beam capture and transport as will be discussed in sec. 7.1.1. Should the development of the Gabor lens prove too difficult, the lens can be substituted with solenoids [34], but this is not ideal as some of the solenoids may operate with high fields, nearing the regime where superconducting solenoids may be needed.

Different groups are seeking to develop plasma lenses for various applications [191, 193–196]. A prototype of the Gabor lens was developed at Imperial College London and tested at the Surrey Proton Beam Centre [191]. During the tests, the prototype lens was exposed to proton beams with energies of 1.4 MeV, an aperture plate was positioned at the entrance to the lens in order to create narrow beamlets, and a phosphor screen was installed to record the beam. However, instead of a focused beam, ring structures were recorded. It was hypothesised that the rings were a result of the plasma column being excited into a coherent off-axis rotation. This was supported by PIC simulations with VSim [197] which showed a rotation of the bulk of the plasma transformed pencil beams into rings. However, further investigations are needed to pin down the exact mechanism that causes this and if it can be avoided [191].

Beam Transport

The Stage 1 beam transport line was designed with Beamoptics [198] and MAD-X [35]. A schematic diagram of Stage 1 can be seen in fig. 7.4. The beam line has a capture section consisting of two Gabor lenses intended to reduce the transverse momentum of the beam to minimise beam losses. The matching and energy selection section contains two RF cavities to manipulate the bunch length

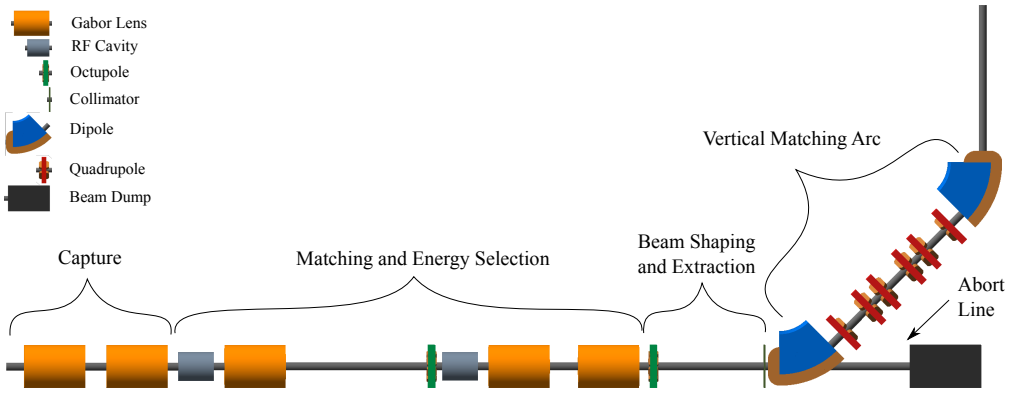

Figure 7.4: Schematic diagram of Stage 1 of LhARA starting from the capture section to the end station. The various beam line elements are given in the legend. The total length of the beam line is 17.255 m.

and longitudinal phase space. The role of the third Gabor lens is to focus the bunch to a small spot size, with the two remaining lenses used to bring the beam parallel to the entrance of the vertical arc. Octupole magnets are present to improve the uniformity of the beam. The design of the vertical arc helps to cancel vertical dispersion and preserve a one-to-one optics transfer by ensuring the phase advance in both planes is a multiple of π between the entrance and exit of the arc. The arc consists of two bending dipole magnets and six quadrupole magnets. This design allows for the beam properties at the end station to be controlled by the beam elements located upstream.

To evaluate the performance of the beam line, two simulation programs were used: BDSIM [37] and GPT [199]. BDSIM was used to evaluate beam losses and dose delivered to the end station. GPT was used to track the beam while also including space charge effects. The two programs were used in tandem, with GPT being used to add space charge effects at certain portions of the beam line, and BDSIM used for general beam line tracking.

7.1.2 Stage 2

Fixed Field Alternating Gradient Accelerator (FFA)

For post acceleration, an FFA based on the spiral scaling principle will be used to accelerate ion beams. An FFA is chosen as it has properties advantageous for radiobiology. These include: the capability to deliver a high and variable dose, rapid cycling, delivery of various energies and species without the need for energy degraders, as well as a compactness in size compared to synchrotrons. Typical FFAs can increase the momentum by a factor of three, which increases the expected maximum deliverable energy of 15 MeV in Stage 1 to 127 MeV for protons and 33.4 MeV/u for carbon ions.

Due to adiabatic damping effects, the beam emittance will shrink during acceleration. However,

the beam emittance may also grow larger due to underestimations of space charge effects [34]. These contrasting effects will impact the beam size that can be delivered.

Beam Transport

The beam extracted from the FFA will be directed to either a high energy *in vitro* end station or an *in vivo* end station through the use of a dipole magnet. The high energy *in vitro* beam transport line is a scaled version of the low energy *in vitro* transport line. It preserves the same functionalities of the low energy vertical arc but scales the magnet lengths to keep the peak magnetic fields below the saturation limits of normal conducting magnets [34].

When the bending dipole is not powered, the beam is sent to the *in vivo* end station. An extended drift section is necessary to clear the dipole and provide space for five RF cavities. Four quadrupoles are positioned to provide focusing adjustments to the beam and space is reserved for scanning magnets. The placement of the four quadrupole magnets was designed to enable deliverable spot sizes ranging from 1 mm to 30 mm.

7.1.3 Instrumentation

A variety of beam instrumentation will be needed for LhARA. To characterise the laser, a camera-based system from a commercial vendor can be used. For the beam line, conventional beam diagnostic devices will be used and the design lattice has space reserved to place these monitors.

The maximum dose delivered to a volume corresponding to the sensitive volume of a standard PTW-23343 Markus ion chamber [200] located at the end stations can be seen in Table 7.1. More detail is provided in the Pre-Conceptual Design Report [34]. With such high instantaneous dose delivered, extensive research and development will be needed to devise the instrumentation required to characterise the beam delivered. For the low energy *in vitro* end station, one of the proposed devices is the SciWire. SciWire consists of two planes of thin 250 µm scintillating optical fibres [34, 201] which measure the energy and intensity of the beam. Fibre readout can be accomplished with either cameras or photodiodes. Even though thin scintillating fibres are used, the measurements will be destructive for low energies. But it could still be useful for beam diagnostic purposes. Alternatively, radiochromic films could be used to verify the delivered beams.

For the high energy *in vitro* end station, the SmartPhantom, a conceptually similar device to the SciWire could be used. The SmartPhantom consists of several planes of thin scintillating fibres placed within a water phantom. For high energy particles, the presence of the scintillating fibres has a minimal impact on the energy deposition. Due to this, the SmartPhantom could act as an online beam monitor as will be discussed in chapter 8. Using energy deposition measurements, the Bragg

Table 7.1: Simulated maximum dose rates from simulations with BDSIM assuming bunch lengths of 7 ns for 12 MeV and 15 MeV proton beams, 41.5 ns for 127 MeV proton beam, and 75.2 ns for the 33.4 MeV/u carbon ion beam. It is assumed the laser source will have a 10 Hz repetition rate.

	12 MeV p^+	15 MeV p^+	127 MeV p^+	33.4 MeV/u C^{6+}
Dose per pulse	7.1 Gy	12.8 Gy	15.6 Gy	73.0 Gy
Instantaneous dose rate	1.0×10^9 Gy/s	1.8×10^9 Gy/s	3.8×10^8 Gy/s	9.7×10^8 Gy/s
Average dose rate	71 Gy/s	128 Gy/s	156 Gy/s	730 Gy/s

peak can be reconstructed. Other approaches are also being considered [34], such as detectors based on ionacoustics [202–204].

Since radiobiological research will be a key focus for LhARA, a fully equipped research laboratory will be housed within the facility. The research laboratory will allow for sample preparation, processing, and analysis. A robotic workstation is planned to handle the switching of multi-well cell culture plates to increase throughput. To serve *in vivo* studies, an animal-housing facility will also be located close by to allow for post-irradiation monitoring.

7.2 Laser Source Simulations

Stage 1 of LhARA consists of a laser source impinging on a thin foil target. The TNSA interaction creates a large flux of ions which is subsequently captured and focused by Gabor lenses into a beam which is transported to a vertical *in vitro* end station. To evaluate the design of the beam line, an end-to-end simulation is needed, starting from the laser and ending at the end station.

A full end-to-end simulation involved simulating the laser plasma interaction at a target. Then the accelerated ions were tracked through the beam line. The beam line consists of the vacuum nozzle vessel interface, Gabor lenses, collimators, dipole magnets, and quadrupole magnets. The beam line simulations were split into several codes. The particle-in-cell (PIC) code Smilei [122] was used to simulate the laser plasma interaction, then BDSIM and GPT (General Particle Tracer) were used to track the beam. GPT is a 3D particle tracking program which includes various 2D and 3D space-charge models [199]. Smilei is a fully-relativistic electromagnetic PIC code which makes use of parallel computing techniques, scaling well for large numbers of computing elements [122]. In this chapter, analysis was performed using BDSIM v1.4.1, Geant4 v10.04.p03, GPT v2.81, and Smilei v4.4.

7.2.1 PIC Simulations using Smilei

The scope of the laser interaction simulations is to approximate the proton flux coming from the laser source. The high-performance computing (HPC) cluster at Imperial College London was used to run

these simulations. However, it was found that it was not practical to run 3D simulations using the parameters outlined for LhARA [34]. As a result, a compromise was made where 2D simulations were run, and a 3D beam was generated from the results and subsequently tracked. But several issues needed to be addressed.

Dimensionality Differences

The dimensions of the simulation play an important role, affecting how the simulations are modelled. For the TNSA interactions, the electron cloud formed from the laser plasma interaction will be different in 2D and 3D. Due to the additional degree of freedom afforded by 3D simulations, there will be a weaker field compared to the 2D case. Macroparticles are also modelled differently, where spheres are represented by infinite cylinders in 2D.

These differences lead to higher particle energies in 2D compared to 3D. Furthermore, the energy spectrum of the particles will be different. The cut-off energy grows monotonically with time in 2D, whereas it eventually saturates in 3D [205]. This phenomenon with the cut-off energy is well known, and various empirical energy scaling laws for 2D simulations have been proposed [205–208], but depend on the laser and target.

To evaluate the discrepancy of 2D simulations to measurements, a comparison was made against experiments by Dover *et al.* [209]. The experiments compared the results of experiments in which the laser parameters were varied. In one case, the laser energy was varied and in another case, the focal width was varied. The experiments involved an intense laser ($I_L = 5 \times 10^{21}\,\mathrm{W\,cm^{-2}}$) impinging on a 5 µm stainless steel foil. In Smilei, the setup was simulated in 2D and the results compared to the results presented. An average was taken for the results (Figure 4 in Dover *et al.*) to compare against the 2D simulation results. For the energy scan, the focal width was kept constant at 1.5 µm, while the focal scan kept the laser energy constant at 10 J. From the results shown in fig. 7.5a it can be seen that in general, 2D simulations show a higher maximum energy compared to measurements when the laser energy is varied. At low laser energies, comparable results can be obtained, but becomes increasingly discrepant as the laser energy is increased. In comparison, the focal scan in fig. 7.5b shows that as the focal width increases, the maximum cut-off energy in simulations falls below the measured values. Dover *et al.* found that for larger focal spots, recirculating electrons contribute significantly to the sheath which was not accounted for in the theoretical models, leading to the lower energies seen in simulations [209]. Although modifications to scaling laws and models can be applied, this relies upon comparisons against experimental measurements which may not always be available.

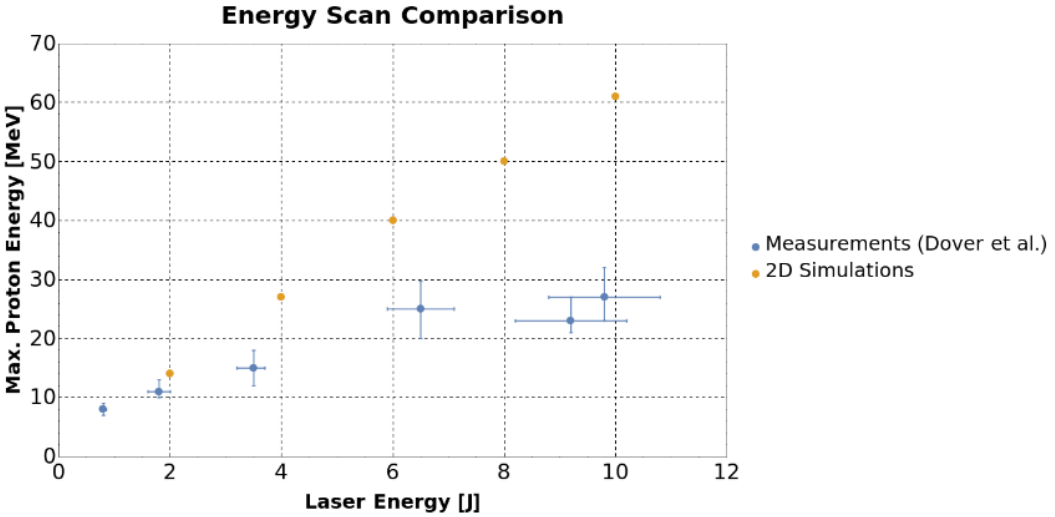

(a) Energy scan.

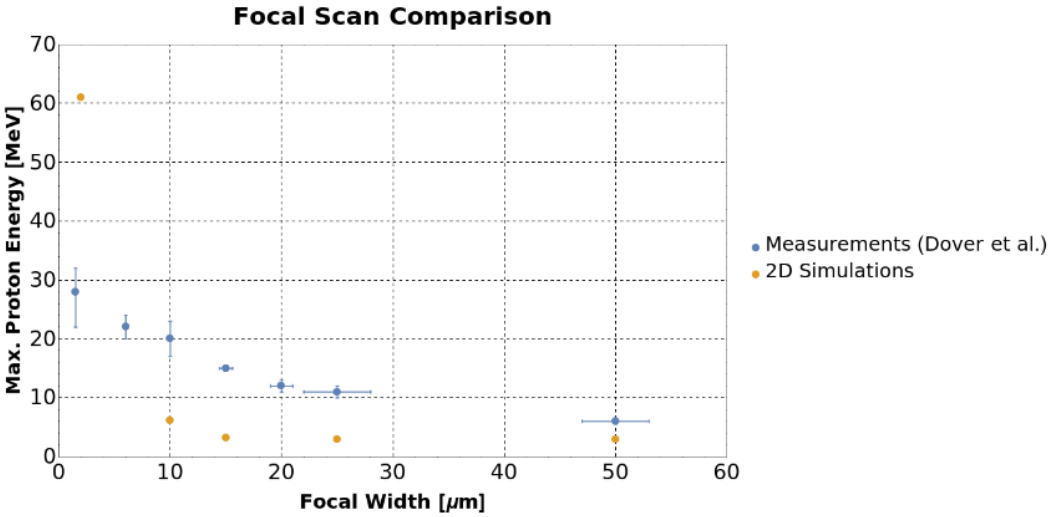

(b) Focal width scan.

Figure 7.5: A comparison of maximum proton energies in 2D simulations (orange) and measurements by Dover *et al.* [209] (blue) for an energy scan (7.5a) and focal scan (7.5b).

Sampling Method (from 2D to 3D)

Although some simulation parameters such as the particles per cell or grid mesh can be relaxed in 3D, running these simulations is still computationally expensive. By exploiting the observation that trends between 2D and 3D simulations are similar, a simple method was developed which made several assumptions to obtain an approximation of a 3D distribution from 2D results. But as this beam is only approximate, it will only give qualitative results. For particle tracking, the quantities that are of interest for an individual particle are:

$$\left(x, y, z, p_x, p_y, p_z, E\right), \tag{7.6}$$

where x, y, z are the positions, p_x, p_y, p_z the associated momentum components, and E the energy. An assumption made was that the kinematic distributions for the added transverse axis would be similar to the simulated transverse axis. Under this assumption, similar correlations would exist between the transverse axes to the longitudinal axis, momentum, and energy. Energy scaling factors were not applied in order to preserve these correlations and also due to a lack of direct experimental results to compare against. Another reason the energy was not scaled is that one would also have to scale both the momentum and position appropriately. Furthermore, as divergence is a 3D effect, a detailed scaling would not necessarily give a better representation from a fundamentally 2D simulation [210]. Hence, this leads to an implicit assumption that the energies of interest in 2D would still be a good approximation to 3D results.

From the energy (E), the total momentum (p) can be calculated for a given particle mass. For the individual momentum components, two angle quantities can be introduced:

$$\theta_p \equiv \arctan\left(\frac{p_x}{p_z}\right), \tag{7.7}$$

$$\phi_p \equiv \arctan\left(\frac{p_y}{p_z}\right), \tag{7.8}$$

where the convention used is for x and z to be the 2D simulated transverse and longitudinal axis respectively for the particle flux, and y is the added transverse axis. Here, two angles are sampled from the simulation with eq. 7.7, one is assigned to the x-axis and the other to the y-axis. By rearranging

the angles, one can determine the individual momentum components:

$$p_z = \sqrt{\frac{p^2}{\tan\left(\theta_p\right)^2 + \tan\left(\phi_p\right)^2 + 1}}, \tag{7.9}$$

$$p_x = p_z \tan\left(\theta_p\right), \tag{7.10}$$

$$p_y = p_z \tan\left(\phi_p\right). \tag{7.11}$$

To calculate the positions, they are sampled based on the existing correlations between the coordinate quantities. A simple method using 3D histograms will be described. First the longitudinal position (z) was sampled from a 3D histogram relating it to the longitudinal momentum component (p_z) and one of the transverse momentum components (p_x or p_y). The transverse momentum was randomly chosen in order to preserve the correlation of both momentum components to the longitudinal position. From the momentum, the transverse positions are sampled from separate histograms relating the positions (x or y), momentum components (p_x or p_y), and the longitudinal position (z). After this, all the quantities specified in eq. 7.6 are determined.

As can be seen in fig. 7.6, after the target there is a vacuum nozzle at the start of the beam pipe. Since it has a small entrance radius compared to the beam size (more detail will be given in sec. 7.2.2), it is important to centre the beam for the energies of interest to maximise the number of particles reaching the end station. This can be done by rotating the coordinate system with Euler angles, followed by a translation of the position. This centring process represents both a rotation and a repositioning of the foil relative to the vacuum nozzle. The resulting beam from this procedure can be seen in fig. 7.7 for the energies of interest. A summary of the steps of the method is as follows:

1. Sample energy from 2D PIC simulation.
2. Calculate the total momentum from the sampled energy.
3. Calculate the three momentum components.
4. Sample the longitudinal position from a relation relating the longitudinal position to the longitudinal momentum and one of the transverse momentum components.
5. Sample the transverse positions by relating the positions to the corresponding momentum components and longitudinal position from the previous step.
6. Iterate the previous steps to obtain a beam distribution.
7. Finally centre the distribution for the energies of interest.

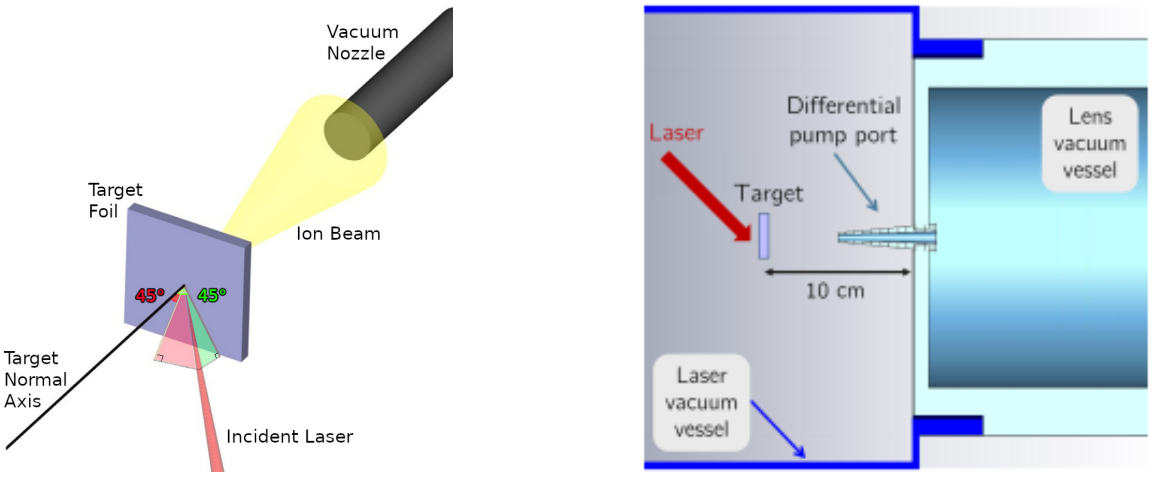

Figure 7.6: Schematic diagrams of the configuration between the laser target and the beam line, which includes the vacuum nozzle interface.

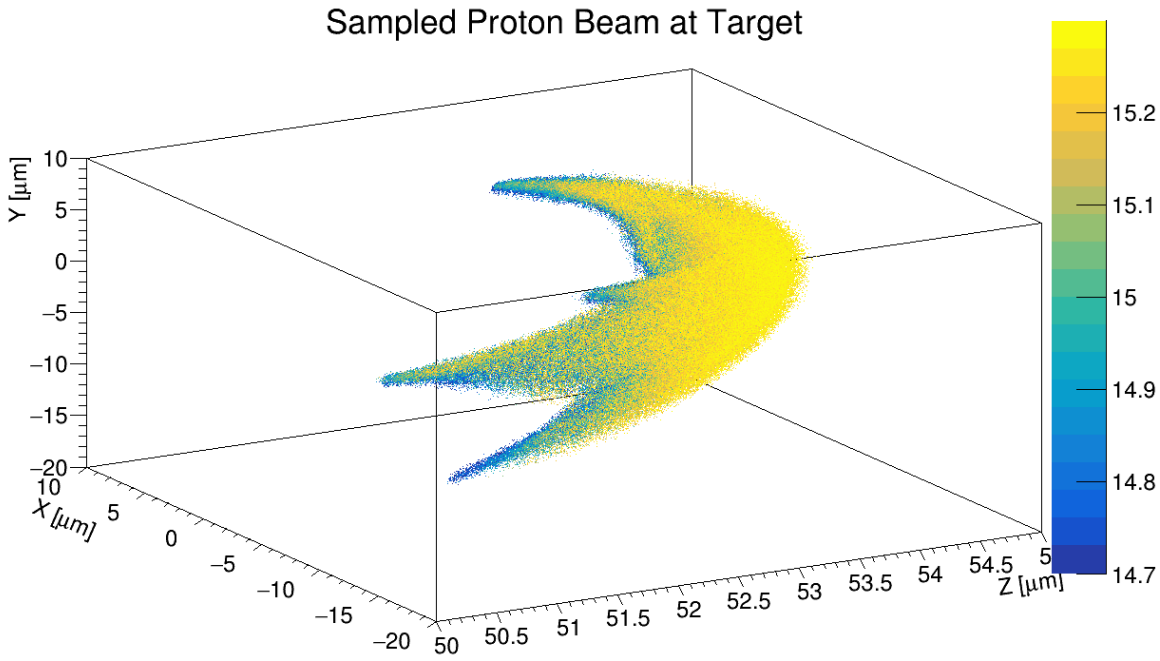

Figure 7.7: 3D proton beam generated from the sampling procedure for energies of interest (14.7 <KE< 15.3 MeV). Colours represent the kinetic energy of particles.

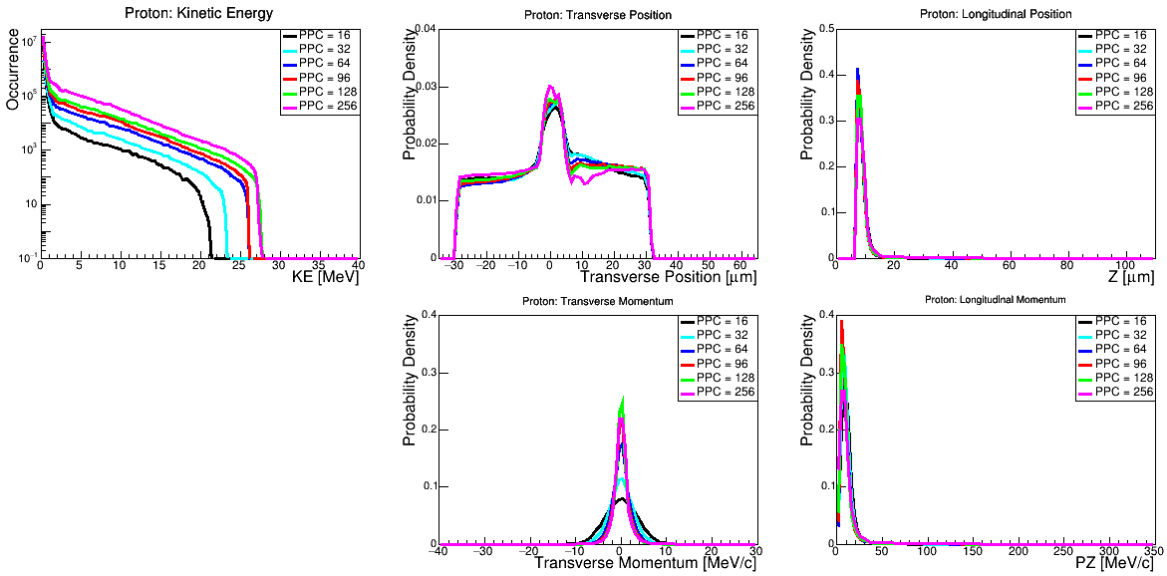

Figure 7.8: Convergence testing looking at the accelerated protons where the ppc was varied between simulations while other parameters were kept the same (a cell size with dimensions $5\times10\,\mathrm{nm}^2$ was used with the longitudinal plane specified first). The colours of the various plot refer to the different ppc values analysed at 1 ps after the start of the simulation.

Smilei Simulation Parameters

As was discussed in sec. 4.5, numerical heating effects can affect the simulation results. Convergence testing was needed to minimise these effects. To do so, parameters were varied until a convergence in the results was observed. Fig. 7.8 and fig. 7.9 show the results of the proton kinetic energy spectra analysed 1 ps after the simulation starts. The particles per cell and cell size were independently varied in the two figures. When these parameters were varied, it was found that the position and momentum distributions did not vary significantly. The main variation appears in the proton cut-off energy. The reason for the rectangular cell sizes used in fig. 7.9 is that since the acceleration primarily occurs along normal to the target, the simulation can be sped up by using coarser dimensions for the transverse plane. The total grid size and simulation time was selected based on when the increase in the proton energy slows down. The result of these tests show that a particle per cell value of 128 and a cell size of $5\times10\,\mathrm{nm}^2$ [1] for the longitudinal and transverse plane respectively are sufficient to reach convergence.

For LhARA only a small proportion of the proton flux will be of interest. Specifically energies between 12 and 15 MeV are of interest for Stage 1 [34]. Because of this, less than one percent of the protons generated are of interest, which makes the resulting distributions particularly susceptible to fluctuations when laser parameters are varied. This can be seen in fig. 7.10 and fig. 7.11 where the initial laser focal width and incidence angle are varied. Variations in the distribution can arise from

[1] Or $0.03927\frac{c}{\omega_L}\times0.07854\frac{c}{\omega_L}$ when expressed in dimensionless units.

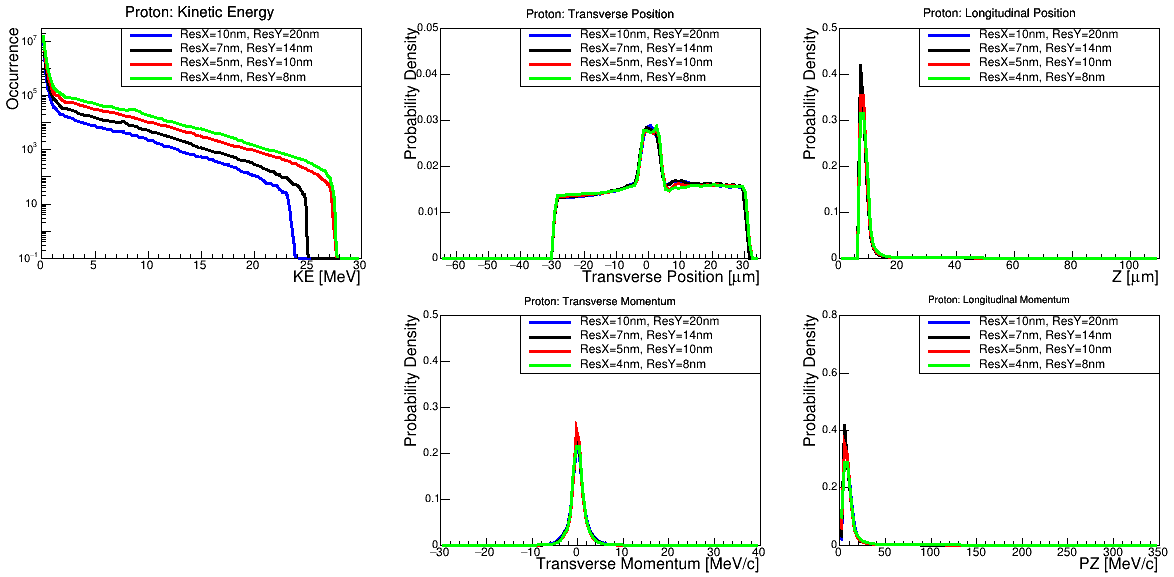

Figure 7.9: Convergence testing looking at the accelerated protons where the individual cell size was varied between simulations while other parameters were kept the same (a ppc value of 128 was used). The colours of the various plot refer to the different cell sizes analysed at 1 ps after the start of the simulation.

changes in the laser focal width and angle. This leads to different energies produced, and a different proportion of particles being analysed.

A double peak feature appears in the transverse position distribution when using the LhARA parameters [34], which is plotted in black in both fig. 7.10 and fig. 7.11. This appears to result from the sheath, but may also be an issue of statistics where only a few thousand of macroparticles are analysed. However, this double peak structure leads to an uncertainty as to which peak to centre the distribution at to maximise the number of protons entering the beam line. To avoid this issue, a different set of parameters was chosen where the focal width was increased from 3 µm to 4 µm while the angle of incidence was kept at 45°. This produces a similar looking proton energy distribution but without the double peaks. However, this lowered the cut-off energies, which reduced the number of particles at the energies of interest by about 30%. Though this also brought the cut-off energy closer to experimental measurements with the Draco laser at HZDR [152], which has similar parameters to the laser system LhARA plans to use. This may make the results a better approximation to an experimental beam. A summary of the final 2D simulation parameters used for particle tracking is presented in table 7.2.

Smilei Simulation Results

Using the parameters in table 7.2, a simulation was carried out in Smilei for 1 ps. This period of time was chosen as it corresponded approximately to when the particles approach the end of the grid and

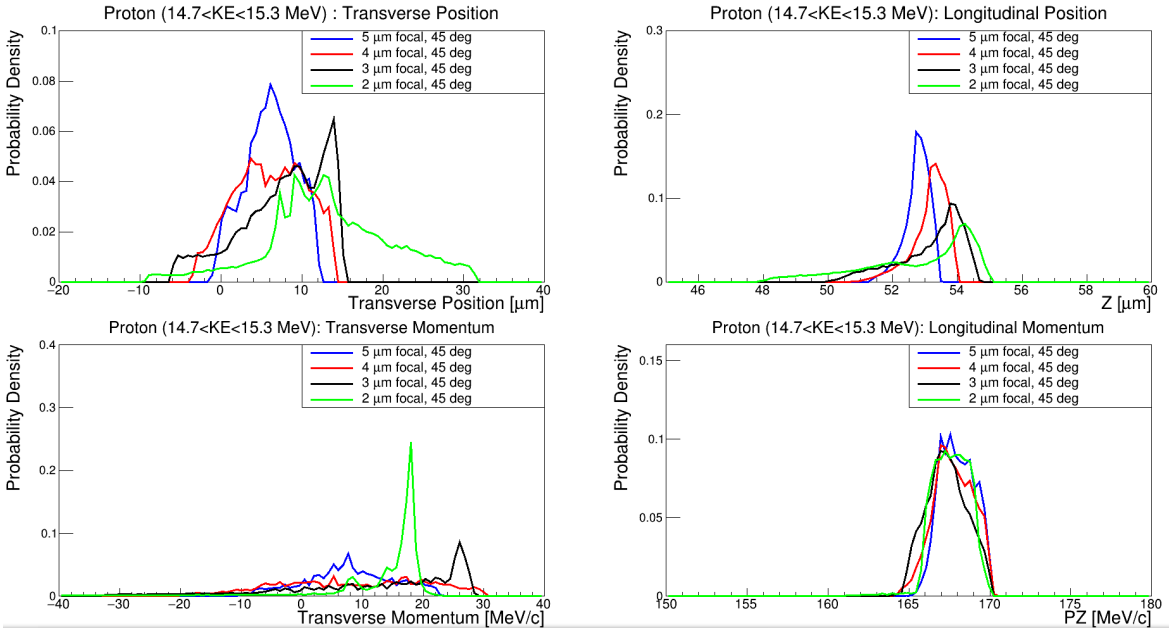

Figure 7.10: Proton macroparticles with energies of 15 MeV with a 2% energy spread, where the laser focal width is varied between 2 µm and 5 µm. The colours of the various plot refer to the different laser focal widths analysed at 1 ps after the start of the simulation. For each case the laser energy was kept constant, hence, the laser intensity differs in each case.

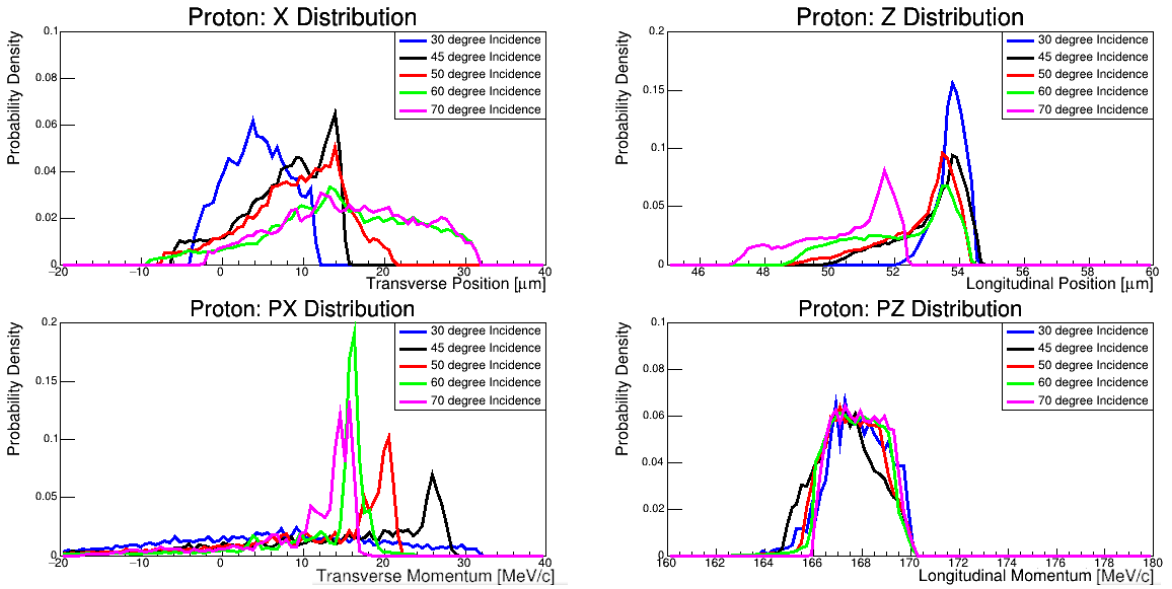

Figure 7.11: Proton macroparticles with energies of 15 MeV with a 2% energy spread, where the incident laser angle from normal is varied between 30° and 70°. The colours of the various plot refer to the different incidence angles analysed at 1 ps after the start of the simulation.

Table 7.2: Table of Smilei 2D simulation parameters used to simulate the laser source TNSA interaction.

Simulation Settings	
Duration	1 ps
Timestep	0.0148 fs (0.99×CFL)
Interpolation order	2
EM Boundary Conditions	Silver-Muller
Simulation Grid (Longitudinal × Transverse)	
Grid Size	$80\times60\,\mu m^2$
Cell Size	5×10 nm
Laser Parameters (Gaussian)	
Wavelength	800 nm
Focal Width (FWHM)	4 µm
Duration (FWHM)	25 fs
Intensity	$5.16 \times 10^{20}\,W/cm^2$
Polarisation	Linear
Incident Angle	45°
Foil Parameters ($C_{10}H_8$)	
Target Thickness	2 µm
Particles per cell	128
Total number of particles	9.42×10^8
Initial Temperature	10 keV
Initial Density	$252n_c$
Position Initialisation	Random
Momentum Initialisation (carbon ions + protons)	Cold
Momentum Initialisation (electrons)	Maxwell-Jüttner
Boundary Condition	Removed at boundary

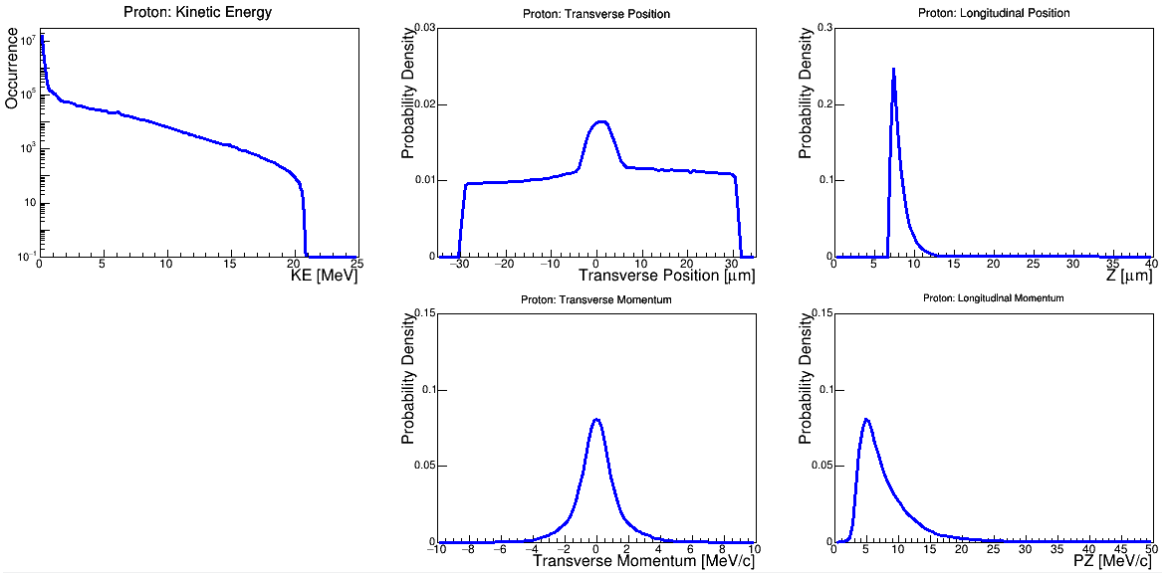

Figure 7.12: Distribution plots of proton macroparticles after 1 ps from Smilei 2D simulations using the parameters in table 7.2.

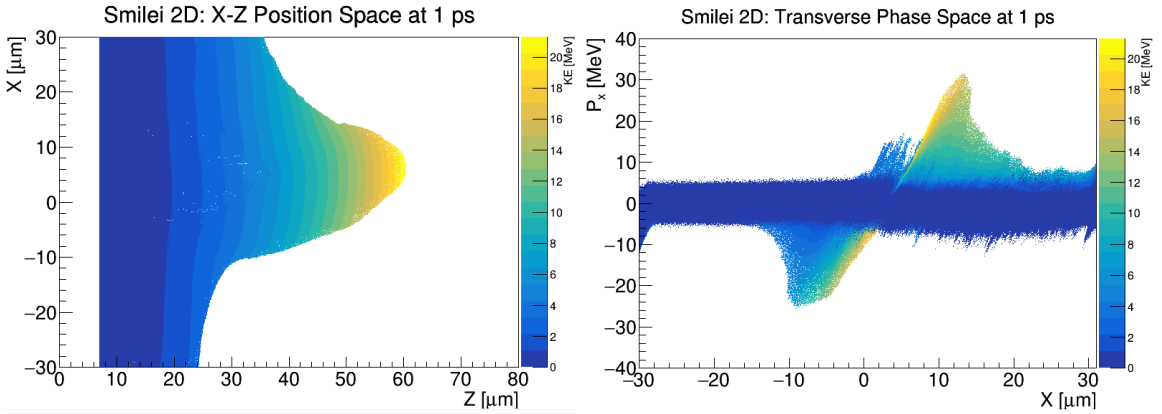

Figure 7.13: Proton macroparticle plots of the position (left) and the transverse phase space (right) after 1 ps. Colours in the plots correspond to the kinetic energy.

also when the proton energies stop growing significantly. Several of the distribution for the proton macroparticles generated can be seen in fig. 7.12.

Plots of the positions and momentum of the protons can be seen in fig. 7.13. These figures help visualise the flux of protons and shows that they are primarily accelerated along the longitudinal direction, but largely consist of low energy protons located near the foil (at $z = 5\,\mu\text{m}$). Meanwhile, one can also observe that the higher energy protons emerge both off-axis and at an angle due to the 45° angle of incidence of the laser. From these results, the sampling method was applied to approximate a 3D distribution. This distribution was then used as an input for particle tracking in the beam line.

7.2.2 Particle Tracking with BDSIM and GPT

To evaluate the performance of the Stage 1 beam line, the distribution from Smilei was tracked and compared against an ideal Gaussian distributed beam specified in the Pre-Conceptual Design Report [34]. Between the laser target and the first Gabor lens is a 5 cm drift space followed by a vacuum nozzle as seen in fig. 7.6. The vacuum nozzle can be pictured as a conical frustum with an entrance radius of 2 mm and exit radius of 2.87 mm with an overall length of 5 cm. Due to the small entrance and exit aperture, the vacuum nozzle could also function as a collimator to help filter away the lower energy protons not moving along the axis of the beam pipe.

During the first 5 cm drift space before the nozzle, there will be a substantial flux of electrons moving along with the accelerated ions. These electrons can be beneficial in neutralising space-charge effects. In the Pre-Conceptual Design Report it was assumed that the higher energy protons will eventually separate from the lower energy electrons [34]. However, even if that is not the case, there will still be a significant amount of losses that occur at the vacuum nozzle due to the aperture, decreasing the number of electrons co-moving with the protons, and may lead to space-charge effects becoming more prominent. To simplify the simulations, it was assumed the electron population would not have a major impact after the 5 cm drift space. For an ideal Gaussian beam[2], it was found that space-charge effects had a negligible effect as can be seen in fig. 7.14 [34]. Up until the entrance to the vertical arc, the three tracking codes show a similar beam evolution, but a discrepancy begins as the beam enters the arc. However, there are important details to make note of. Firstly, the plot only compares the effect of space-charge in the beam line *after* the vacuum nozzle. Secondly, the simulation lacks the placement of several collimators used for energy selection. Thirdly, the ideal beam only simulates a 15 MeV proton beam. Finally, the Gabor lenses represented by the orange boxes in the schematic diagram were modelled by solenoid lenses.

To evaluate the effect of space-charge in the vacuum nozzle, the nozzle was included in the tracking simulations. A comparison was made for an ideal beam passing through the vacuum nozzle in both BDSIM (no space-charge) and GPT (with space-charge). After the nozzle, both beams were then tracked through the rest of the beam line, but without space-charge. The results are shown in fig. 7.15 where the simulations in BDSIM are solid lines and GPT are dashed lines. In these simulations the `spacecharge3Dmesh` space-charge routine was used in this and all subsequent GPT simulations with the Poisson solver method of `MGCG` with 50, 50, 150 mesh lines for the x, y, and z-directions respectively. The electric field is calculated in the particle rest frame which is transformed to the lab frame and summed over all particles to get the electromagnetic fields. A comparable result to

[2]The idealised Gaussian beam was generated with a spot size of 4 µm FWHM, angular divergence of 50 mrad, and energy spread of 1×10^{-6} MeV

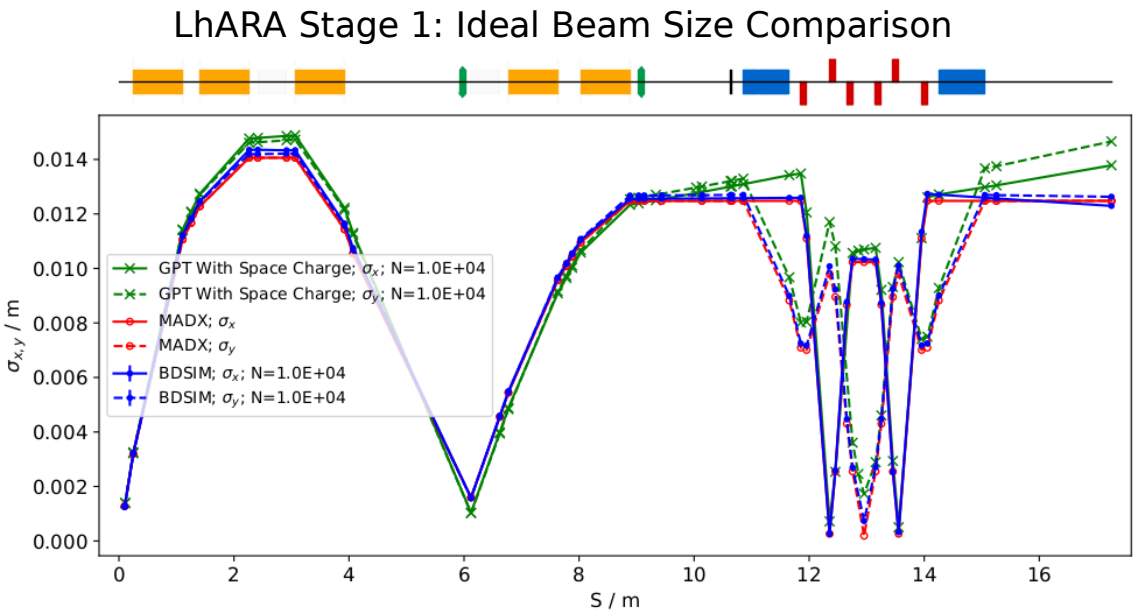

Figure 7.14: Comparison of beam size tracking for the horizontal (solid lines) and vertical (dashed line) planes. Three particle tracking codes were compared: GPT (green), MAD-X (red), and BDSIM (blue). The vacuum nozzle is not included and only GPT included space-charge in the beam line. In the schematic diagram above the plot, the orange boxes represent the Gabor lenses, green are octupoles, black are collimators, blue are dipoles and red are quadrupoles [34].

the previous simulation can be seen for the dashed line where space-charge is included, whereas a smaller initial beam is seen without space-charge until the beam is collimated at the entrance to the arc. These results indicate that space-charge needs to be considered in the vacuum nozzle where it has a substantial impact on the beam size evolution through the rest of the beam line. There is a minor discrepancy after the arc due to space charge in fig. 7.14, not seen in fig. 7.15. This could be corrected at a later point by the addition of collimators.

Another simulation was performed but included additional collimators. First, the nozzle geometry was modelled which collimates the beam at the entrance and exit to the vacuum nozzle. Then two additional collimators were added in the beam line, one at $s \sim 6\,\text{m}$, and another in the middle of the vertical arc at $s \sim 13\,\text{m}$. Like before, space-charge was only considered in the vacuum nozzle, and not in the beam line. The results of the beam evolution can be seen in fig. 7.16. In comparison to the previous result, the evolution of the beam with space-charge becomes more similar to the beam without space-charge. Despite the similarity there is still a noticeable difference, where the beam with space-charge is slightly larger in size. Hence, from the three simulations results it can be seen that space-charge has the greatest impact within the vacuum nozzle, but becomes negligible in the rest of the beam line.

Taking these results into consideration, two simulations were performed with the sampled 3D beam

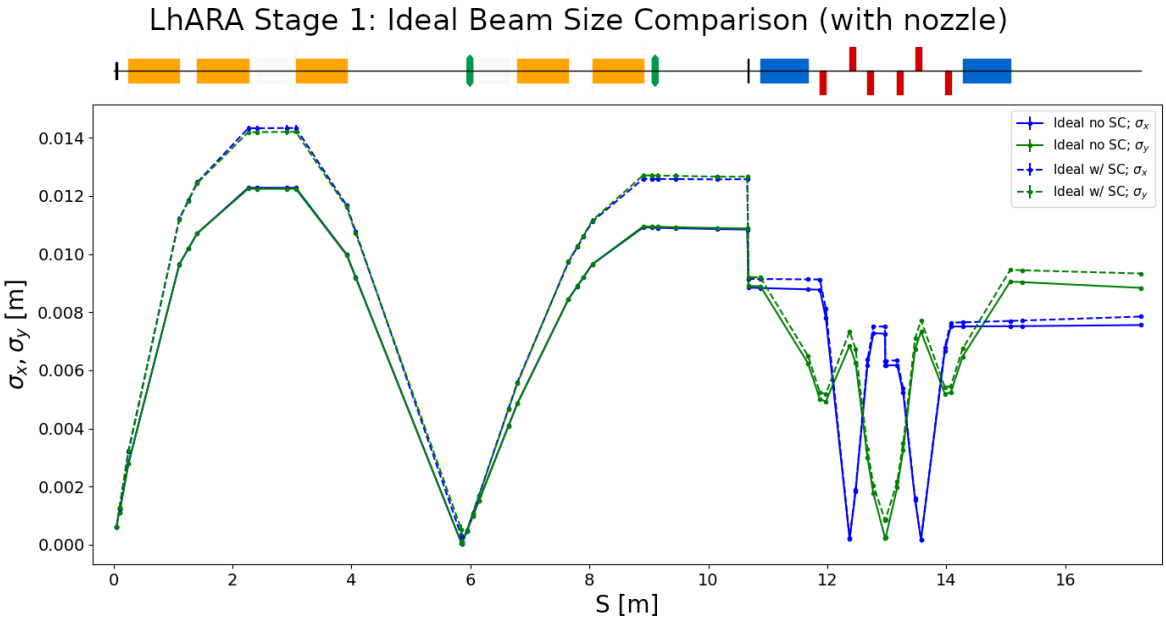

Figure 7.15: Comparison of ideal beam tracking where the vacuum nozzle space-charge effects are included (dashed lines) and not included (solid lines), however, additional collimators are not yet applied. The plots in blue and green represent the horizontal and vertical planes respectively. In the schematic diagram above the plot, the orange boxes represent the Gabor lenses, green are octupoles, black are collimators, blue are dipoles and red are quadrupoles.

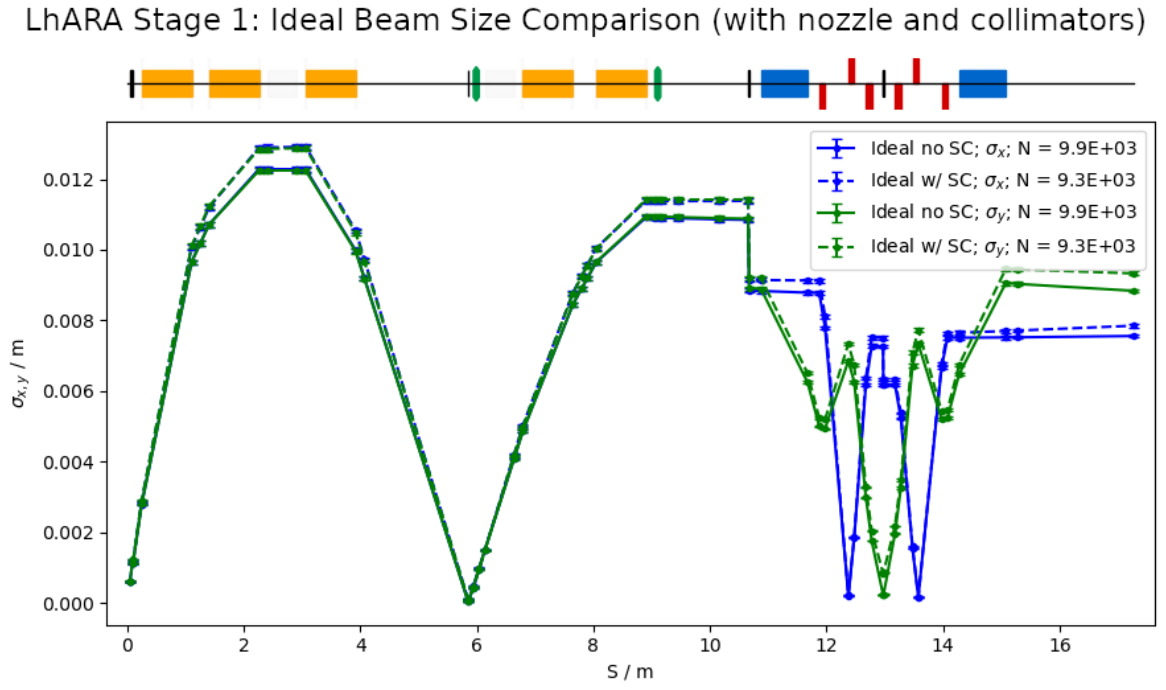

Figure 7.16: Comparison of particle tracking where vacuum nozzle space-charge effects are included (dashed lines) or not included (solid lines) in the vacuum nozzle. In addition, two additional collimators were added to the beam line. The plots in blue and green represent the horizontal and vertical planes respectively. In the schematic diagram above the plot, the orange boxes represent the Gabor lenses, green are octupoles, black are collimators, blue are dipoles and red are quadrupoles.

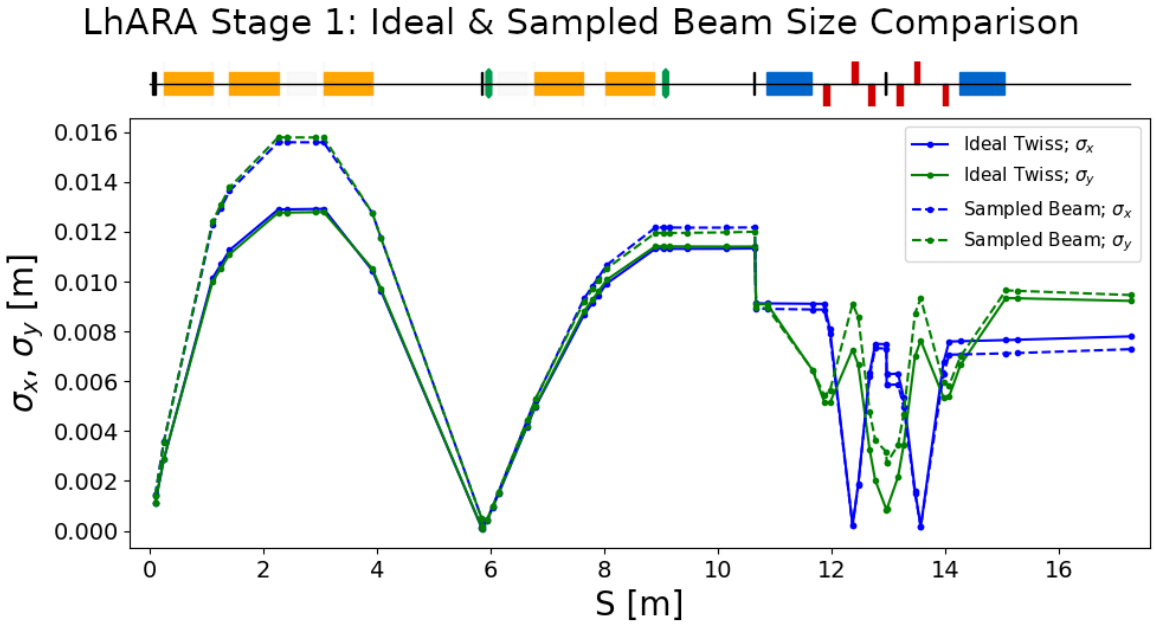

Figure 7.17: Comparison of particle tracking between an ideal beam (solid line) and sampled beam (dashed lines) where space-charge was simulated in the vacuum nozzle. The plots in blue and green represent the horizontal and vertical planes respectively. In the schematic diagram above the plot, the orange boxes represent the Gabor lenses, green are octupoles, black are collimators, blue are dipoles and red are quadrupoles.

outlined above, and the ideal beam. Starting from the target, both beams were tracked for 5 cm in drift space to the entrance of the vacuum nozzle using BDSIM. Both beams were first collimated at the entrance with a radius of 2 mm, then tracked for another 5 cm in GPT where space-charge was included. On exit, the beams were collimated with an exit radius of 2.87 mm. Finally, the beams were tracked through the rest of the beam line with BDSIM. However, since only energies of 15 MeV were tracked, this corresponded to a very small slice of the proton flux coming from the foil ($< 0.1\%$). Multiple TNSA simulations in Smilei were combined until a sufficient number of particles at the energies of interest was generated ($\sim 30,000$ particles)[3]. The resulting beam size evolution can be seen in fig. 7.17. From the figure it can be seen that both beams have similar evolutions, but the sampled beam grows larger in the capture section of the beam line. Once the beam reaches the vertical arc, collimation right before the arc brings both beams back to similar sizes, as was observed previously.

Despite the similarities in the beam size evolution of the ideal beam and the sampled beam, there are also differences to note. The first is that, due to the larger beam sizes for the sampled beam, over two thirds of the beam is lost in the beam line as seen in fig. 7.18. Another point to note is

[3]It is worth bearing in mind that macroparticles are not real particles. For 2D simulations, one can only make assumptions about the charge to estimate the number of real particles. Future studied would be needed to investigate this. But for the Monte Carlo simulations presented, only a single particle is tracked at a time so the macroparticles could be generalised as particles for the purpose of understanding the beam evolution.

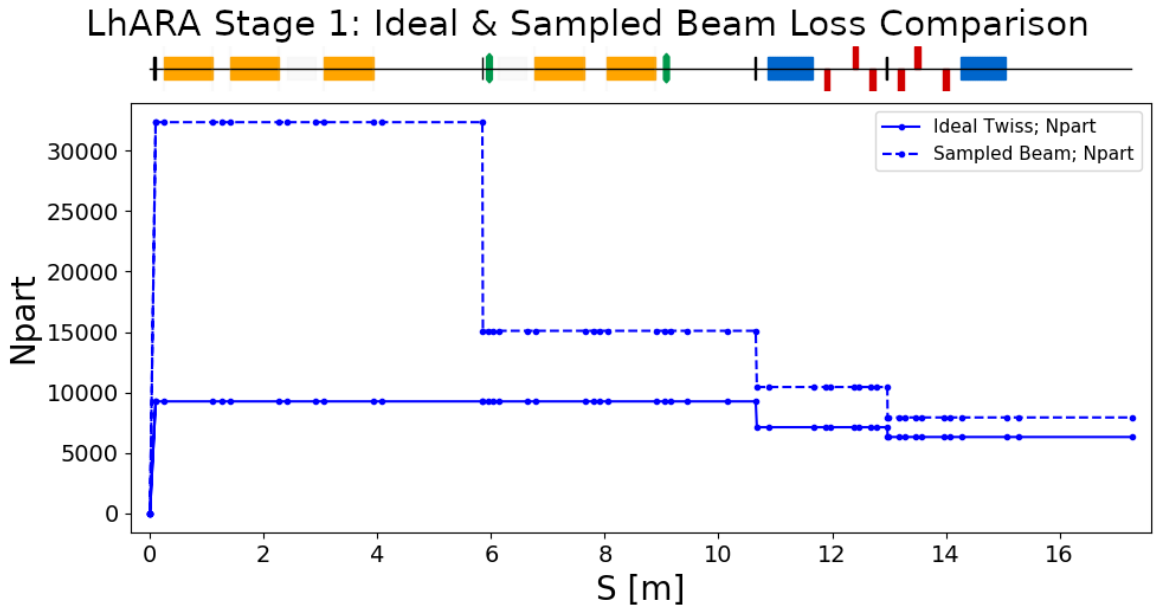

Figure 7.18: Comparison of the particle losses between an ideal beam (solid line) and sampled beam (dashed lines) as a result of the beam evolution given by fig. 7.17. In the schematic diagram above the plot, the orange boxes represent the Gabor lenses, green are octupoles, black are collimators, blue are dipoles and red are quadrupoles.

that when the sampled beam is fitted with Twiss parameters, it is different to the ideal beam as shown in table 7.3. Although the sampled beam initially has a smaller beam emittance, this grows larger than the ideal beam as seen in fig. 7.19. The difference in the parameters despite the similar beam evolution arises from the way the two beams are distributed. The ideal beam has a Gaussian profile for each of the transverse planes, which is not the case for the sampled beam as seen from the projected horizontal distributions in fig. 7.20. A difference in the way the beam is distributed will affect how well the beam can be characterised by Twiss parameters. Although the figure only shows the horizontal trace spaces, a similar distribution is found in the vertical plane for both beams. After the collimator located at 6 m, the beam emittance of both beams becomes more comparable. Due to this, the beams that arrive at the end station will have similarly shaped distributions as seen in fig. 7.21 for both the position and transverse trace space despite the discrepant initial beam emittance.

7.2.3 Improvements to the Particle Tracking

The results in the previous section show promising results when the sampled beam with energies of interest from Smilei simulations was tracked. However, it still needs to be shown that unwanted energies do not reach the end station. Another point to address is that the particle tracking simulations modelled the Gabor lenses as solenoids. It needs to be shown that the field coming from a Gabor

Table 7.3: Table of fitted parameters to the ideal beam and sampled beam at the exit of the vacuum nozzle.

Parameter	Ideal Beam	Sampled Beam
β_x [m]	5.4 ± 0.1	145.4 ± 0.7
α_x	-56.0 ± 0.4	-1458.6 ± 6.8
ϵ_x [m rad]	$(2.3 \pm 0.03) \times 10^{-7}$	$(1.4 \pm 0.008) \times 10^{-8}$
β_y [m]	5.3 ± 0.1	149.1 ± 0.8
α_y	-55.2 ± 0.4	-1496.3 ± 8.4
ϵ_y [m rad]	$(2.4 \pm 0.03) \times 10^{-7}$	$(1.3 \pm 0.008) \times 10^{-8}$

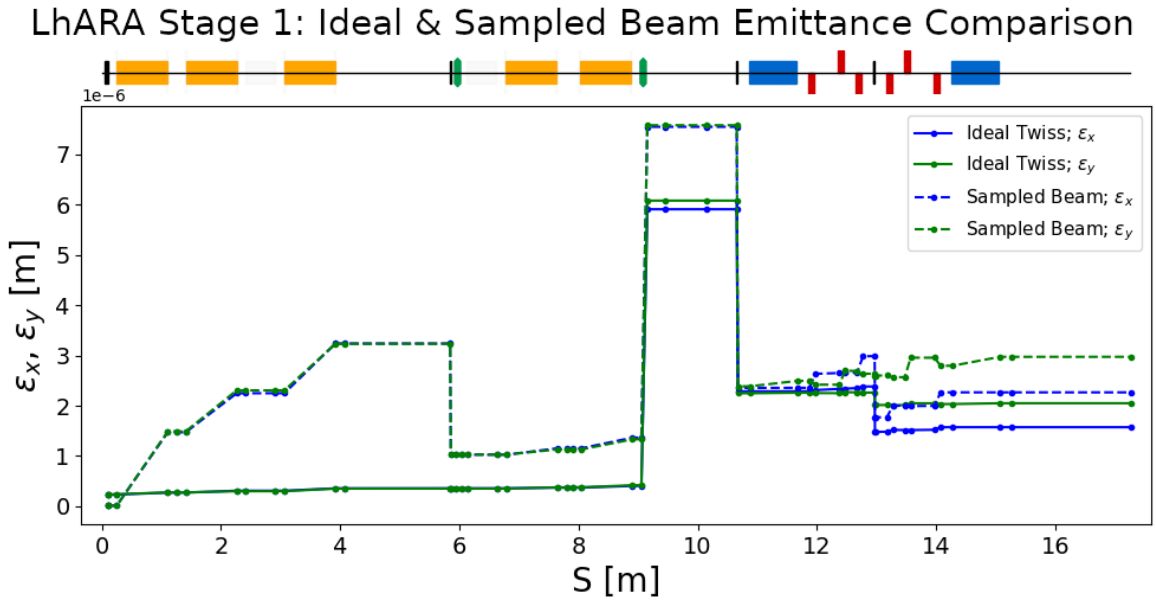

Figure 7.19: Comparison of the evolution of the fitted beam emittance between an ideal beam (solid line) and sampled beam (dashed lines) as a result of the beam evolution given by fig. 7.17. Changes in the emittance occur for the ideal beam due to collimation and non-linear optics from the octupoles. For the sampled beam, the loss of particles also affects the fitted emittance due to the effect on the beam distribution. In the schematic diagram above the plot, the orange boxes represent the Gabor lenses, green are octupoles, black are collimators, blue are dipoles and red are quadrupoles.

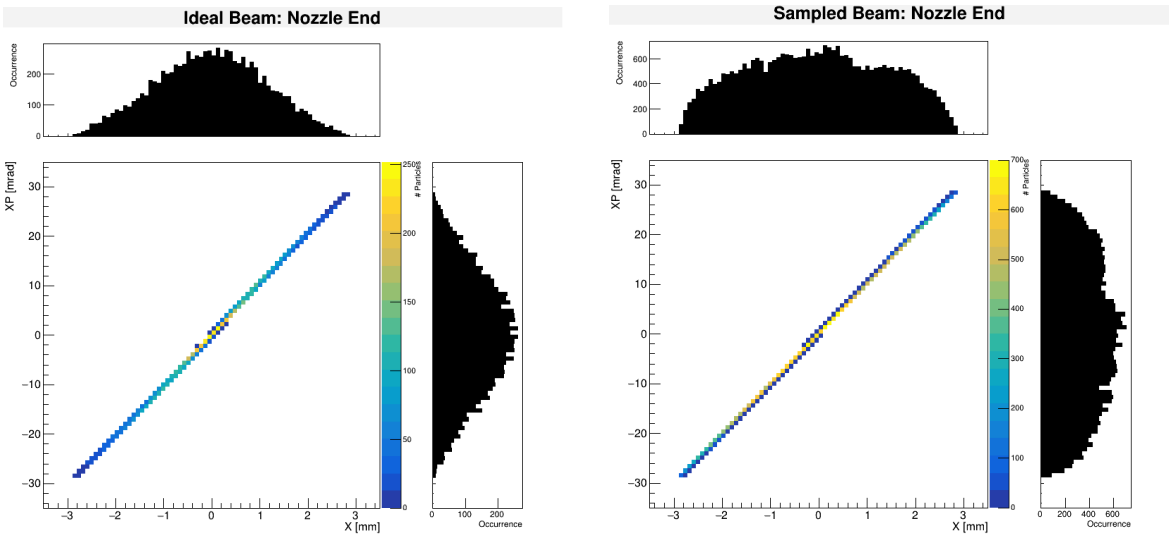

Figure 7.20: Comparison of the horizontal trace space coming out of the nozzle to the entrance of the first Gabor lens between the ideal beam and the sampled beam. Although the trace space distribution looks similar, the projected distributions look quite different. The colours represent the number of particles.

lens can still achieve the same results. It is also clear that the sampled beam coming from the PIC simulations requires optimisations of the beam line. Finally, the sampling procedure to approximate a 3D beam makes a lot of assumptions which may not be true. In order to obtain more realistic results, 3D PIC simulation are needed.

Energy Selection in the Beam Line

To show the effectiveness of the collimators and vertical arc for energy selection, a beam containing all the energies needs to be tracked. However, a problem with tracking the sampled beam containing all energies is the number of particles required. In the case of the sampled beam, less than 0.1 % of the beam consisted of particles at 15 MeV. It was found that an initial beam from the target consisting of about 4×10^7 particles was required in order to obtain about 3×10^4 particles with energies at 15 MeV. From fig. 7.18 it can be seen that this number of initial particles was necessary for about 10^4 particles to reach the end station.

However, tracking a beam with 4×10^7 particles is time consuming. Instead, the beam was separated into two separate beams, one only containing low energy protons (≤ 5 MeV) and another containing high energy protons (> 5 MeV). The kinetic energy spectrum of the beams at several locations in the beam line are shown in fig. 7.22. From the results it can be seen that a combination of the collimators and the vertical arc are quite effective at energy selection for the sampled beam. The collimators help reduce the number of particles at unwanted energies, but a significant number of particles still make it through the collimators. This is due to the fact that the collimators were

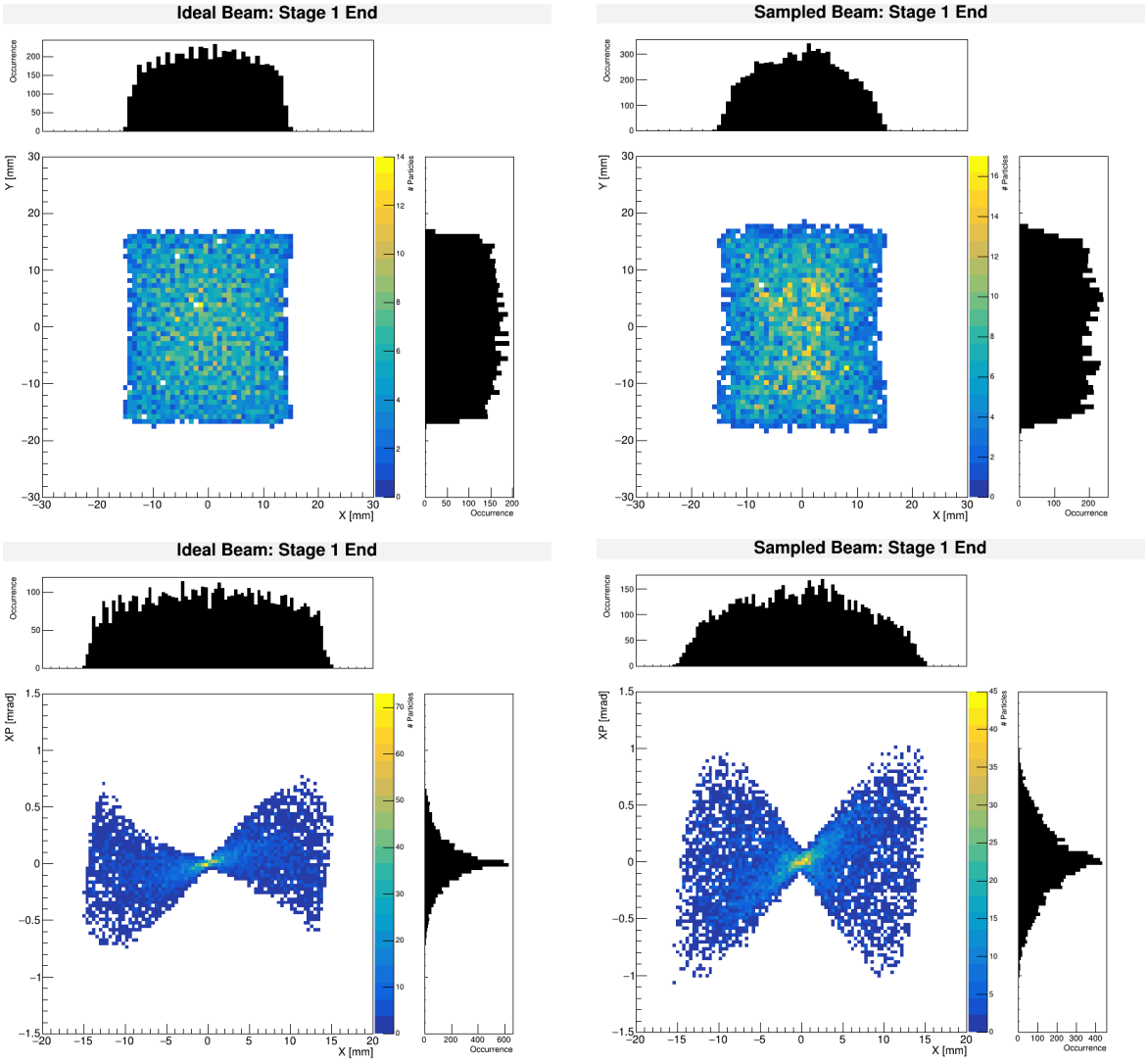

Figure 7.21: Distributions of the position (top) and horizontal trace space (bottom) at the end of the beam line for an ideal beam (left) and the sampled beam (right). Due to the vertical arc, the energy spread of the delivered beam is between 14.7 MeV and 15.3 MeV, but the sampled beam has a flatter energy spread. The colours represent the number of particles.

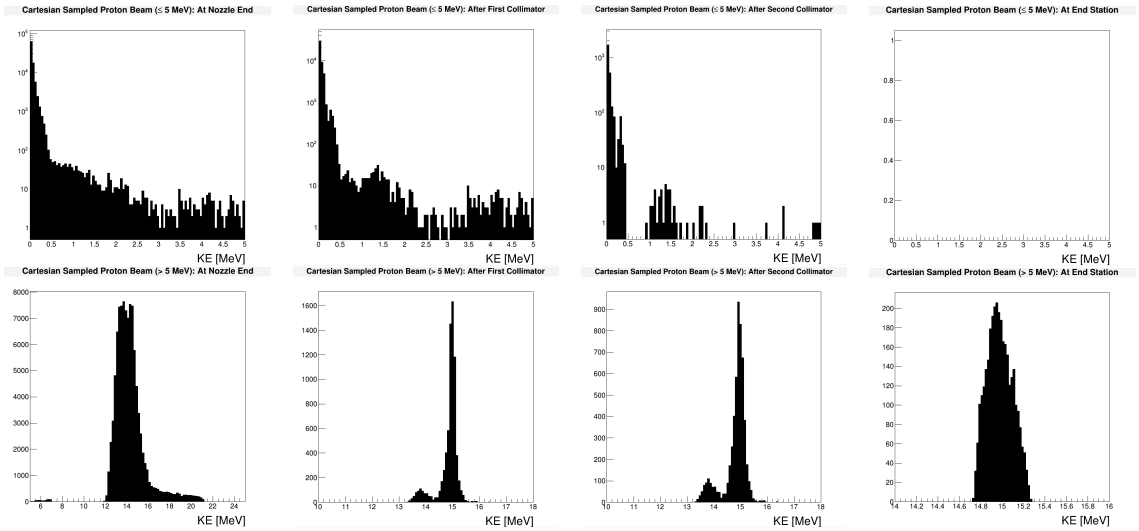

Figure 7.22: Kinetic energy spectrum after passing through the nozzle, collimators, and at the end station for the low energy sampled beam (top) and the high energy sampled beam (bottom). The vertical axis represents the number of particles.

placed according to the results of the ideal beam. But as discussed previously, the sampled beam is distributed differently to the ideal beam. Whereas the ideal beam has a Gaussian spread in energy, energies are spread a bit more uniformly in the sampled beam, making it harder to collimate the beam. In addition, a double peak feature can be observed in fig. 7.22, which is related to the beam distribution as can be seen in fig. 7.23. The first peak contains energies between 13 MeV and 14.5 MeV, appearing near the periphery of the collimator. Whereas the second peak consists of higher energies which are concentrated about the centre. One could select a smaller radius to get rid of the first peak, but would also lose some of the higher energy particles. The presence of the vertical arc helps to remove any unwanted energies that remain in the beam, but a re-optimisation discussed later will help improve both the transmission and the energy selection of the beam line.

Particle Tracking with Gabor Lens Field Maps

BDSIM defines the magnetic fields for typical accelerator magnets but also allows the user to import field maps onto geometric elements. The field map is an array of 3D Cartesian coordinates and the field 3-vector. Interpolators calculate the field value in between the specified data points. For the Gabor lenses, an ideal electric field was generated with a hard edge and applied to a cylindrical geometry. The ideal electric fields for the Gabor lens is given by:

$$E_{\mathrm{GL},r} = -\frac{eB_{\mathrm{sol}}^2}{4m_p}r, \tag{7.12}$$

$$E_{\mathrm{GL},z} = 0, \tag{7.13}$$

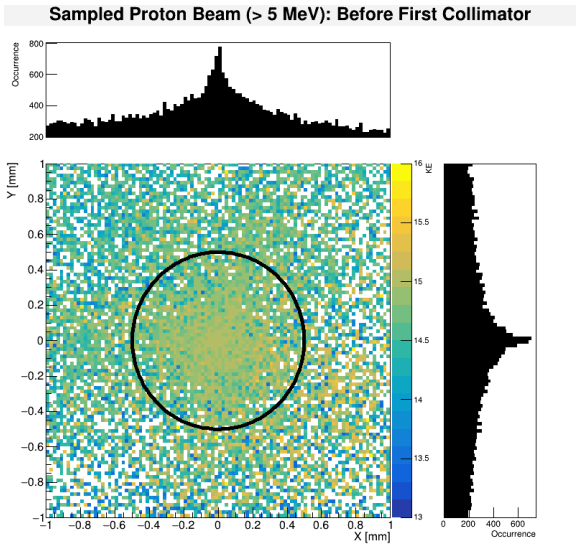

Figure 7.23: Close up position plot of sampled beam before the first collimator. The colours represent the kinetic energy. The black circle represents the aperture of the first collimator with a radius of 0.5 mm.

where B_{sol} is the magnetic field for a solenoid, m_p is the proton mass, and r is the radial position. A derivation can be found in appendix B.

Even though the ideal electric field should be zero along the longitudinal direction, it was found that a certain number of longitudinal (z-values) needed to be defined for the interpolator. In fig. 7.24, the distributions of the beam entering the end station was compared for several different field maps. It can be seen that when only five z-values are specified, the resulting distribution is different compared to the case where more values are explicitly specified for a 3D cubic interpolator. Convergent results were found when at least 43 longitudinal values were specified, where each point contains 201 horizontal and vertical points.

To evaluate any differences in the tracking results, a comparison was made of the ideal beam when the Gabor lenses were modelled by solenoids and with field maps. This can be seen in fig. 7.25 where there is a close comparison except for a minor difference observable at the end station when the beam comes out of the vertical arc. This seems to arise from the beam size decreasing as it enters the arc. The sampled beam was also tracked where there is only a minor difference between solenoids and field maps as seen in fig.7.26. In this case there is a difference after the first energy collimator, but is eliminated by the collimator located at the start of the vertical arc.

A comparison in the distributions for the position, divergence, kinetic energy, and longitudinal spread between the ideal beam and the sampled beam for the Gabor lens field maps can be seen in fig. 7.27. Overall the position and divergence distributions look similar, but the sampled beam is larger for both the beam size and divergence. However, there is a difference in the kinetic energy

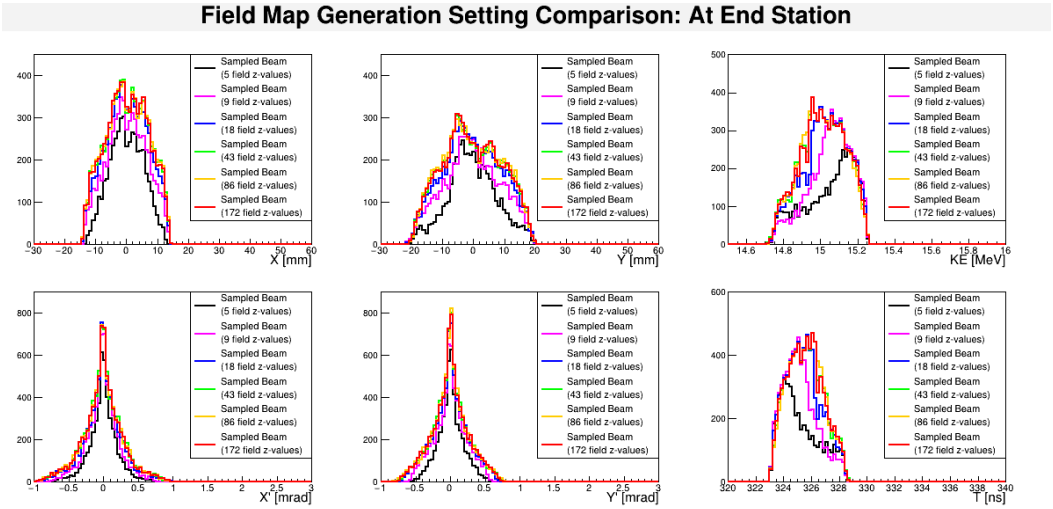

Figure 7.24: Comparison of 1D distributions for electric field maps generated for a varying number of specified z-values. In each case for each z-point 201 horizontal and vertical points were specified and a 3D cubic interpolator was used in BDSIM.

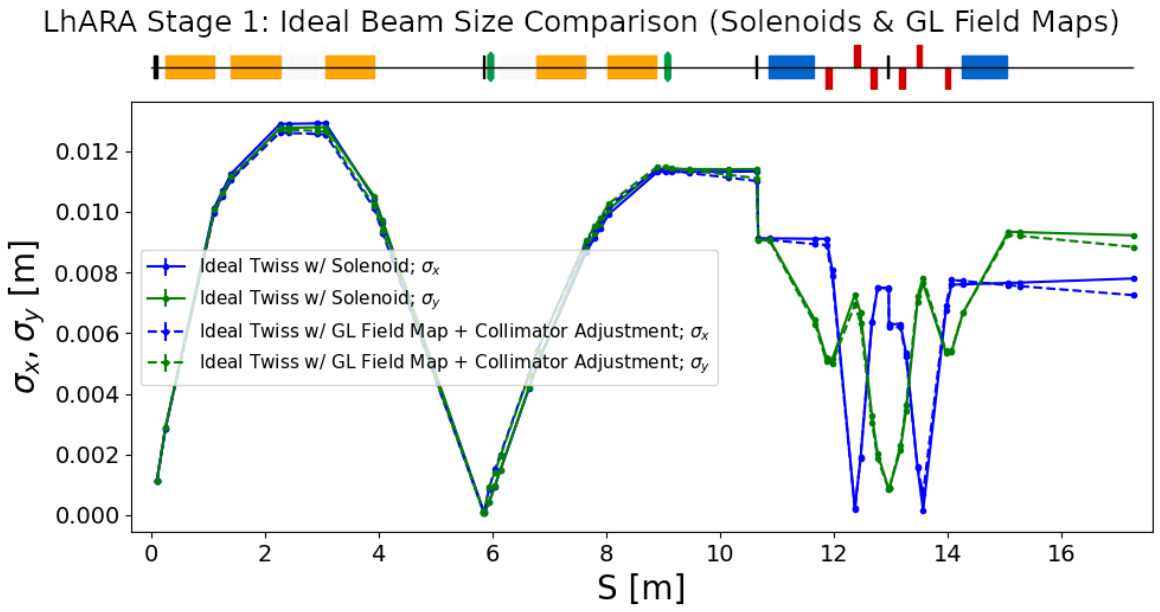

Figure 7.25: A comparison of beam size evolution for the ideal beam between tracking with Gabor lenses modelled as solenoids (solid lines) and Gabor lenses modelled with field maps (dashed lines). The position of the collimators were adjusted due to the focal point changing slightly for the field maps. In the schematic diagram above the plot, the orange boxes represent the Gabor lenses, green are octupoles, black are collimators, blue are dipoles and red are quadrupoles.

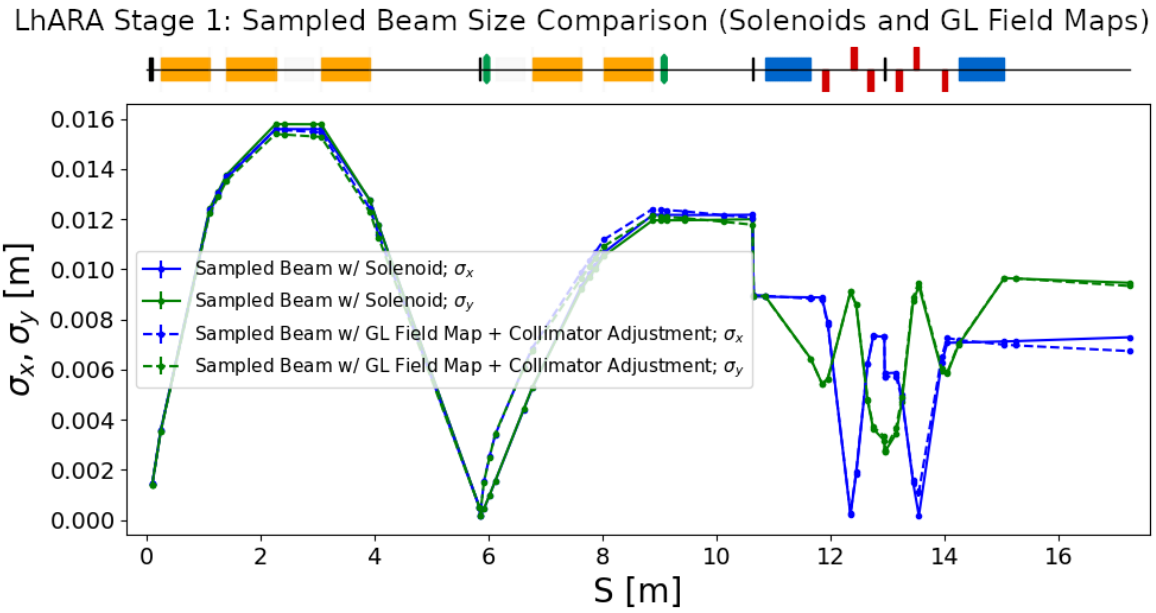

Figure 7.26: A comparison of beam size evolution for the sampled beam between tracking with Gabor lenses modelled as solenoids (solid lines) and Gabor lenses modelled with field maps (dashed lines). In the schematic diagram above the plot, the orange boxes represent the Gabor lenses, green are octupoles, black are collimators, blue are dipoles and red are quadrupoles.

spectrum and the beam spread in time. This arises because the ideal beam has a Gaussian spread in energy which is preserved as it travels through the beam line. This is quite different to the energy spread of the sampled beam which has a much flatter distribution. But this is not a major concern as the sampled beam still falls within the specified energy spread.

In summary, the results of these beam line simulations (fig. 7.25 and fig. 7.26) show that modelling the Gabor lenses as solenoids is a good approximation and validates previous simulation results. But it should be noted that the field maps used were calculated for an ideal Gabor lens with a hard edge. More sophisticated field maps will be needed in order to model a realistic Gabor lens.

Beam Loss Optimisations

Despite similar looking beam size evolutions between the idealised beam and the sampled beam, it was shown that a significant proportion of the sampled beam is lost in the beam line due to the non-Gaussian distribution spread of position and angle. In order to re-optimise the beam line, the fitted Twiss parameters of the beam in table 7.3 were used to modify several beam line elements. Changes include adjusting the focusing strengths of the Gabor lenses as well as modifying the aperture and position of the collimators. The modifications are summarised in table 7.4. The aim was to preserve the overall shape of the evolution while simultaneously improving the transmission of the beam.

The beam size evolution of the sampled beam in the re-optimised beam line can be seen in fig. 7.28. The re-optimisation increased the focusing of the first two lenses in order to decrease the beam sizes.

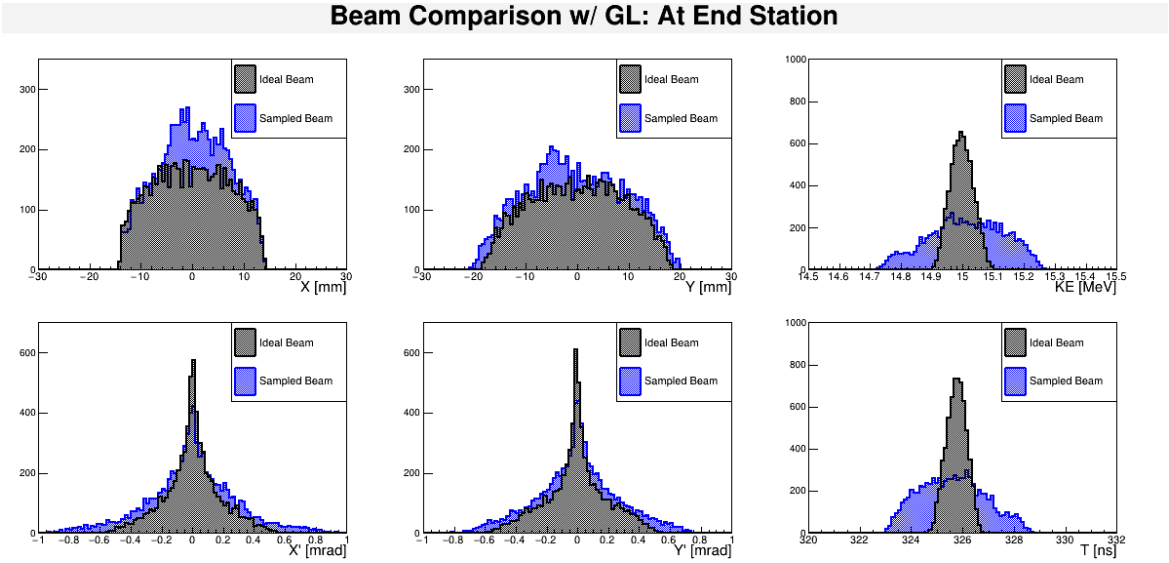

Figure 7.27: A comparison of the projected 1D distributions of the transverse x, y, kinetic energy, divergence x', y', and the longitudinal spread between the ideal beam (black) and sampled beam (blue) with the Gabor lenses modelled by field maps.

Table 7.4: Modifications to the beam line elements for the sampled beam for the relevant parameters.

Element	**Modified Parameter**	**Original Value**	**Re-optimised Value**
Gabor Lens 1	Magnetic field	$B = 1.2868\,[\mathrm{T}]$	$B = 1.4387\,[\mathrm{T}]$
Gabor Lens 2	Magnetic field	$B = 0.6671\,[\mathrm{T}]$	$B = 0.5271\,[\mathrm{T}]$
Gabor Lens 3	Magnetic field	$B = 0.8139\,[\mathrm{T}]$	(unchanged)
Collimator 1	Position Horizontal half width Vertical half width	$s = 5.856\,[\mathrm{m}]$ $r_x = 0.5\,[\mathrm{mm}]$ $r_y = 0.5\,[\mathrm{mm}]$	$s = 5.753\,[\mathrm{m}]$ $r_x = 1.5\,[\mathrm{mm}]$ $r_y = 1.5\,[\mathrm{mm}]$
Gabor Lens 4	Magnetic field	$B = 0.6852\,[\mathrm{T}]$	$B = 0.7284\,[\mathrm{T}]$
Gabor Lens 5	Magnetic field	$B = 0.6542\,[\mathrm{T}]$	$B = 0.6338\,[\mathrm{T}]$
Collimator 2	Position Horizontal half width Vertical half width	$s = 10.65\,[\mathrm{m}]$ $r_x = 20\,[\mathrm{mm}]$ $r_y = 20\,[\mathrm{mm}]$	(unchanged) $r_x = 23\,[\mathrm{mm}]$ $r_y = 23\,[\mathrm{mm}]$
Collimator 3	Position Horizontal half width Vertical half width	$s = 12.95\,[\mathrm{m}]$ $r_x = 12\,[\mathrm{mm}]$ $r_y = 6\,[\mathrm{mm}]$	(unchanged) $r_x = 19\,[\mathrm{mm}]$ $r_y = 6.9\,[\mathrm{mm}]$

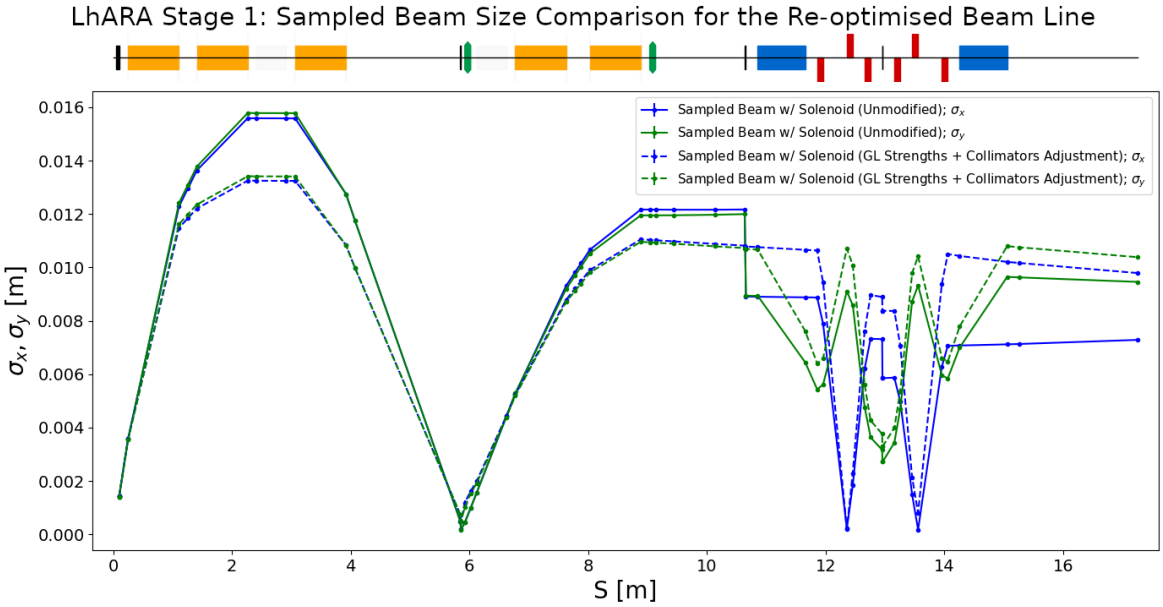

Figure 7.28: Beam size evolution for the sampled beam. A comparison of the evolution is made between the original beam line elements (solid lines) and the re-optimised elements (dashed lines). In the schematic diagram above the plot, the orange boxes represent the Gabor lenses, green are octupoles, black are collimators, blue are dipoles and red are quadrupoles.

Then the collimators were enlarged to improve the transmission of the beam. Even though the beam size decreases as it enters the arc, the final beam sizes as it exits the arc is similar to previous results. There is also an improvement to the beam ellipticity. Fig. 7.29 shows the particle losses through the beam line, and it can be seen that the re-optimised beam line vastly improves upon the previous results in terms of transmission. However, despite similar final beam sizes, the re-optimisations lead to a change in the shape, uniformity, and divergence of the beam as seen in fig. 7.30. Further optimisations such as further tweaking magnet strengths could be performed to improve the results.

Finally, the energy selection for the re-optimised beam line was verified. As was done previously, the kinetic energy spectra at the vacuum nozzle, collimators, and end station for the re-optimised beam line can be seen in fig. 7.31. These results show that the modifications to the beam line preserve the effectiveness of energy selection design.

These results give confidence that a re-optimisation of the real beam is feasible in order to deliver the specified beam parameters at the end station. There is still room for further optimisations such as improving the trace space of the delivered beam. But fine tuning the results is not of great importance given the nature of the sampled beam. A greater priority is to improve the PIC simulations.

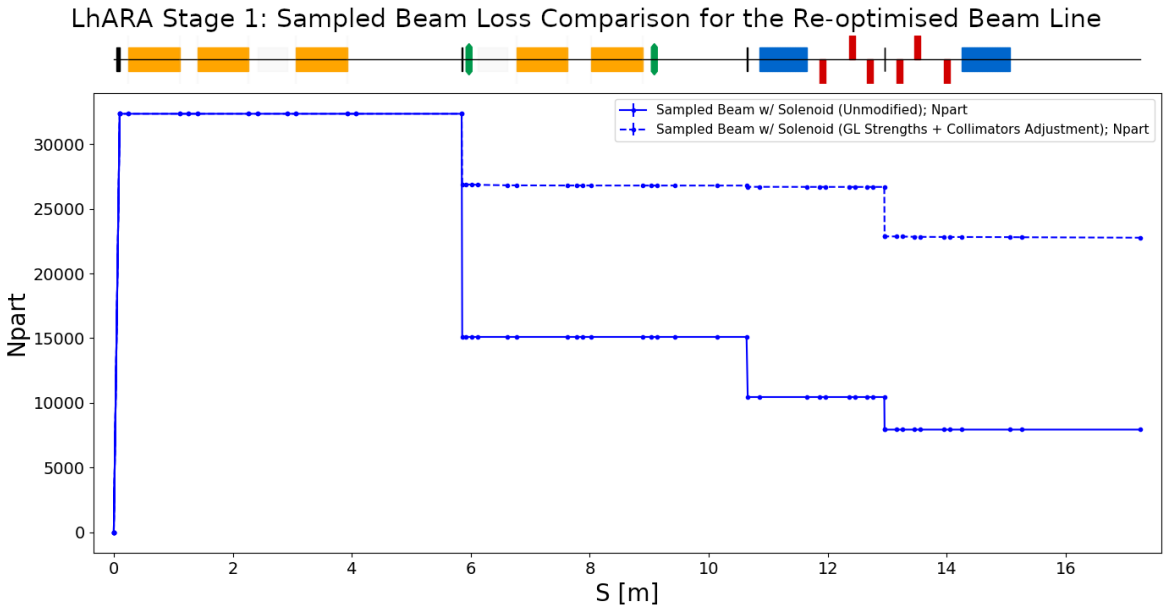

Figure 7.29: A comparison of the particle losses for the original beam line (solid line) and the re-optimised beam line (dashed line). In the schematic diagram above the plot, the orange boxes represent the Gabor lenses, green are octupoles, black are collimators, blue are dipoles and red are quadrupoles.

3D PIC Simulations

The next steps needed are to simulate a fully 3D TNSA interaction. However, there are some key issues that will need to be addressed. The first thing to consider is the time and resources that will be needed to run a 3D PIC simulation.

Secondly, the foil that was simulated in the 2D PIC simulations had a near-solid density which increases the time needed to run the simulations. For near-solid density plasmas, the Debye length is very small which the grid resolution needs to resolve. This issue is compounded in 3D with the addition of another dimension. It is clear that a compromise needs to be made for the target. The charge density could be decreased such that simulations can be run in a reasonable amount of time, such as by changing to a different material. But investigations into understanding how a change in the charge density would affect the particle distribution is needed.

Thirdly, even if the previous two issues can be resolved, the results may still not be fully representative of a real beam. Since the prepulse precedes the main pulse, it can lead to an energy enhancement which has not yet been considered in the simulations. But it may also degrade the performance depending on the thickness of the target. It can also lead to drastic effects on a very thin foil [211], affecting the particle flux and debris. Measurements and simulations will be needed to realistically model the preplasma as it can change based on the laser system and setup.

There is an ongoing effort in the LhARA consortium to address these issue. Simulations for a

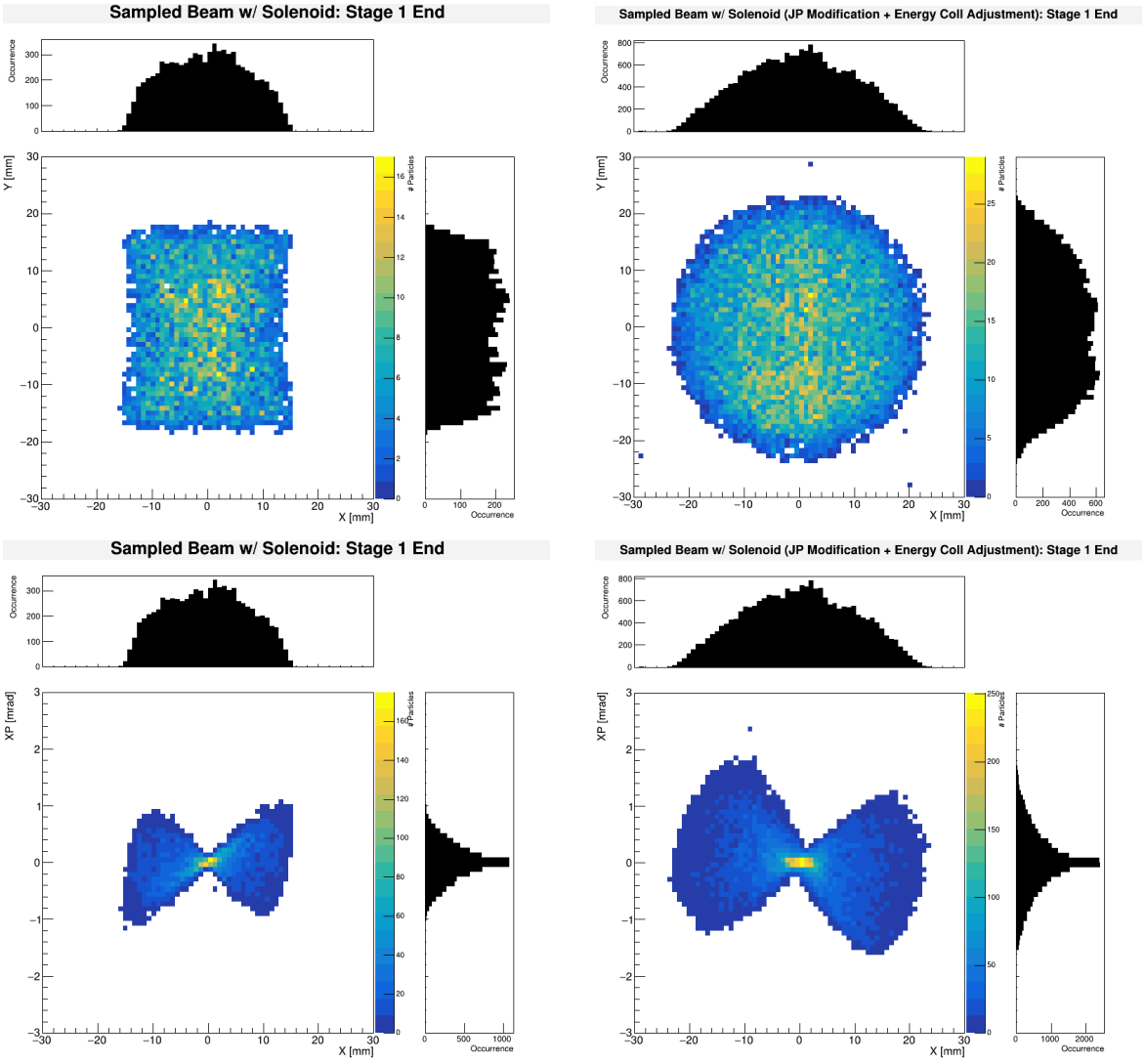

Figure 7.30: 2D Distributions of the position (top) and horizontal trace space (bottom) at the end of the beam line for the sampled beam for the unmodified beam line (left) and the re-optimised beam line (right). The colours represent the population of particles.

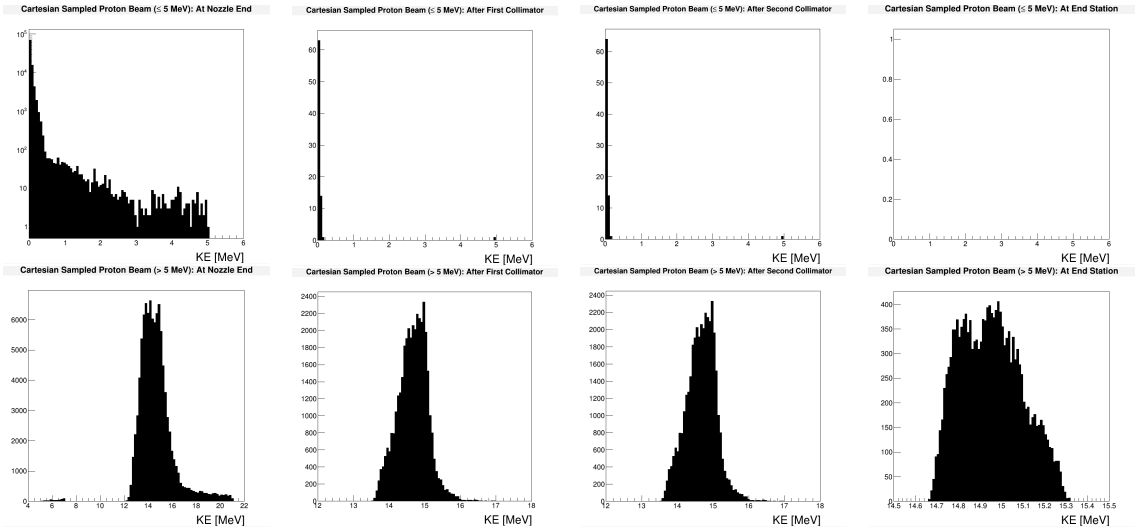

Figure 7.31: Kinetic energy spectrum of the sampled beam after passing through the nozzle, collimators for the re-optimised beam line. The top is for low energies ($\leq 5\,\mathrm{MeV}$) and the bottom for high energies ($> 5\,\mathrm{MeV}$).

plastic foil with lower charge densities were run in 3D [212]. A result can be seen in fig. 7.32 where it can be seen that there appears to be a convergence in the cut-off energy for the 3D results. In addition, the cut-off energies of the 3D results (solid lines) with lower charge densities are similar to those of a 2D simulation (dashed lines) using a high charge density (in green). But further investigations are needed.

Finally, a thorough analysis needs to be done for the co-moving electrons which have so far been neglected. From the TNSA interaction there are two populations of electrons to consider. One contains high energy electrons from the initial laser interaction and escape early on. The other population contains lower energy electrons which move with the protons. For stable operation of the Gabor lens, the effect of both these populations needs to be studied.

In summary, particle tracking simulations of the Stage 1 beam line have been performed and improve upon previous tracking simulations. A sampled proton beam approximated from the 2D PIC simulation was propagated through the beam line where comparable results to previous simulations with an ideal beam were obtained. Field maps of an ideal Gabor lens were incorporated which provided a degree of confidence to previous results that modelled the lenses as solenoids. The analysis was further improved by re-optimising the beam line and by adjusting several beam line elements. Further steps are still needed, which primarily requires propagating a full 3D PIC simulation from the laser source to the end of the beam line to improve the analysis.

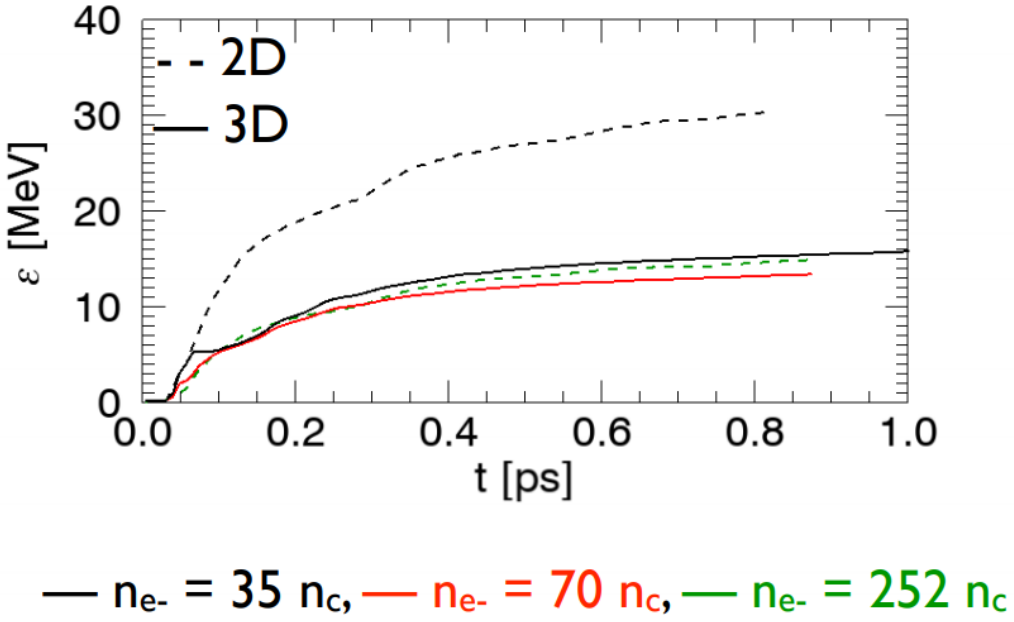

Figure 7.32: Proton cut-off energies as a function of time for a target of various charge densities for both 2D and 3D. Simulations were run using the LhARA parameters except these simulations use a normal incidence angle at 0° [212].

7.3 Stage 2 Beam Line Design

Stage 2 of LhARA involves accelerating the beam coming from the laser source to higher energies. This acceleration can be expected to increase the beam momentum by a factor of three, allowing LhARA to deliver a proton beam with a maximum energy of 127 MeV and up to 33.4 MeV/u with carbon ions [34]. Due to uncertainties in the beam that is extracted from the FFA and a requirement to deliver a range of beam sizes, a flexible design was needed for Stage 2.

The extraction line consists of two sections, the first contains two dipoles and four quadrupoles. This configuration of magnets bends the beam to make the Stage 2 beam line parallel to Stage 1, minimising the space needed for the facility. The second section consists of four quadrupoles to transport the beam to a switching dipole which directs the beam to either a high-energy *in vitro* end station, or to the *in vivo* end station. This second section can match the beam[4] from 1 mm up to 30 mm.

7.3.1 Extracted Beam Optics

The Stage 2 beam line is capable of serving a wide range of energies from 15 MeV to 127 MeV for protons. However, for the purposes of the design and study of the beam line, it was deemed that

[4]The beam spot size for LhARA is defined to be four times the sigma of the beam.

Table 7.5: Beam emittance and β Twiss values to obtain specified beam spot sizes for both nominal and pessimistic beams for a 40 MeV and 127 MeV proton beam. The beam spot size is specified to be four times the sigma of the transverse beam.

Parameter	Nominal Value	Pessimistic Value
RMS Emittance [π mm mrad]	0.137	1.37
β [m] for a 1 mm spot size	0.46	0.039
β [m] for a 10 mm spot size	46	4.5
β [m] for a 30 mm spot size	410	40

a minimum energy of 40 MeV would serve as a practical minimum energy for Stage 2. Since the carbon ion beam has the same beam rigidity as protons, the focus of the design and analysis was on proton beams. Furthermore, since the optics and acceptance of the system is approximately the same, it was hypothesised that the beam emittance would also be the same for both species [34]. But there are uncertainties in the beam arising from: beam transport in Stage 1, injection into the FFA, acceleration in the ring, extraction from the FFA, and space-charge effects. To accommodate these uncertainties, a pessimistic case was considered where the beam emittance increased by a factor of ten from the nominal value. A summary of the beam emittance and the optics used to generate ideal Gaussian beams for several sizes are given in table 7.5 for both the nominal and pessimistic beams.

7.3.2 High-Energy *in vitro* Beam Line

The arc for the high-energy *in vitro* beam line uses the same design as the vertical arc in Stage 1, but with the magnets scaled to accommodate higher energies. The magnets need to be scaled as there is a limit to the maximum magnetic fields that can be achieved with normal conducting magnets due to saturation, which for iron is at about 2 T, though a value of 1.5 T is often quoted [213]. Superconducting magnets are capable of achieving higher magnetic fields but are more costly.

The peak magnetic field for each magnet in the arc needs to be checked in order to ensure it lies below 1.5 T. To verify this, the magnetic field of a bending dipole can be expressed in terms of angle (from sec. 2.3.2):

$$B = \frac{\alpha}{\ell}\frac{p}{e}, \tag{7.14}$$

where α is the bend angle, ℓ is the bend length, p is the beam momentum, and e is the particle charge. For a quadrupole magnet, the magnetic field can be calculated from the gradient, g:

$$B = -gr, \qquad \text{where } g = k\frac{p}{e}. \tag{7.15}$$

Here r is the radius of the transverse plane and k is the normalised quadrupole strength.

Table 7.6: Comparison of magnet parameters in the vertical arc between Stage 1 and Stage 2 of LhARA. The quadrupole in the arc with the highest strength was reported in both cases which would require the highest magnetic field.

Parameter	Stage 1 Arc	Stage 2 Arc
Maximum Energy (proton)	15 MeV	127 MeV
Maximum Beam Radius	5 cm	5 cm
Dipole Bend Angle	$\frac{\pi}{4}$	$\frac{\pi}{4}$
Dipole Bend Length	0.8 m	1.2 m
Quadrupole Highest Strength	$3.15\,\mathrm{m}^{-2}$	$2.74\,\mathrm{m}^{-2}$
Quadrupole Length	0.1 m	0.3 m

A comparison of the Stage 2 arc with Stage 1 is presented in table 7.6. The dipole bending magnets had the bend length increased from 0.8 m to 1.2 m. The quadrupole magnet lengths were tripled from 0.1 m to 0.3 m. Plugging the magnet parameters into eq. 7.14 and eq. 7.15 shows the magnetic fields lie below the saturation limit, with the highest magnetic field in the Stage 2 arc requiring 1.1 T. Scaling the magnet lengths increases the arc length from 4.6 m to 6 m, which means the Stage 2 arc ends about 0.9 m higher compared to Stage 1. To compensate for this, the final drift length in the Stage 1 beam line was lengthened to ensure both arcs end at the same height.

These scaled magnet parameters were found by tweaking the values in MAD-X while ensuring the optics were preserved. This was subsequently verified with particle tracking simulations in BDSIM. To evaluate the effect of space-charge, tracking simulations were also performed with GPT using the same settings for space-charge as described in sec. 7.2.2. Three beams were simulated and tracked in both BDSIM (no space-charge) and GPT (with space-charge): a nominal 40 MeV proton beam, a nominal 127 MeV proton beam, and a pessismistic 127 MeV proton beam. A comparison of the results is given in fig. 7.33 where the beams start with $\sigma = 2.5$ mm. It can be seen that for all three cases, comparable results can be found, but near the exit of the arc differences emerge when space-charge was included. The difference appears to be small enough that an optimisation could be done by adjusting some of the quadrupoles in the extraction line and in the arc to counteract the space-charge effect as will be discussed in the next section.

7.3.3 High-Energy *in vivo* Beam Line

The *in vivo* beam line is specified to deliver a range of beam sizes from 1 mm up to 30 mm. The design is complicated by competing demands to provide a flexible design while also minimising its overall length. The magnetic fields required for the focusing magnets also had to lie below the saturation limits. In addition to the focusing magnets, sufficient space needed to be reserved to place five RF cavities, scanning magnets, and various diagnostic devices.

A series of four quadrupoles of length 0.4 m in the extraction line was found to provide sufficient

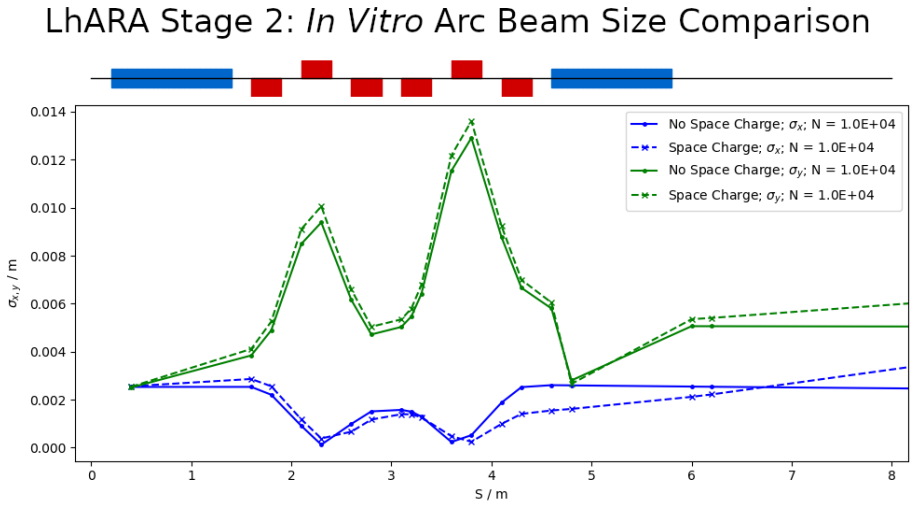

(a) Nominal 40 MeV proton beam.

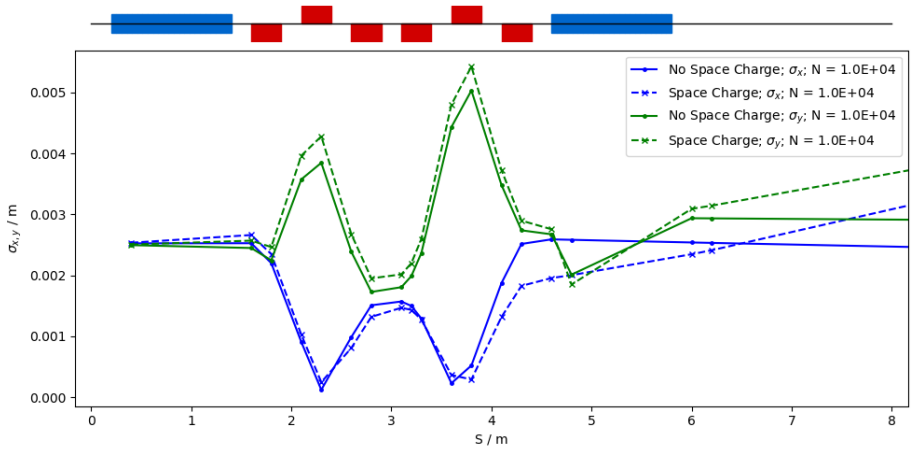

(b) Nominal 127 MeV proton beam.

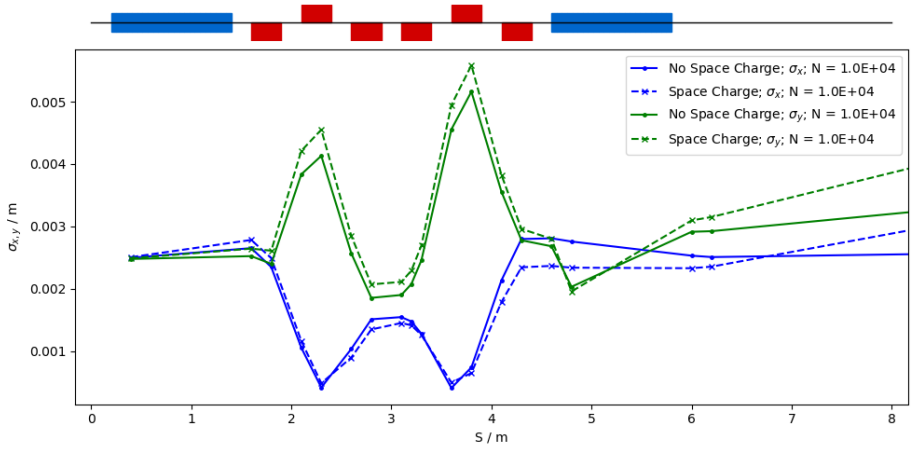

(c) Pessimistic 127 MeV proton beam.

Figure 7.33: Comparison of no space-charge (solid lines) and space-charge (dashed lines) particle tracking through the Stage 2 *in vitro* arc. All beams have been matched to start at $\sigma = 2.5$ mm corresponding to a 10 mm spot size. In the schematic diagram above the plot, the blue boxes are dipoles and red boxes are quadrupoles.

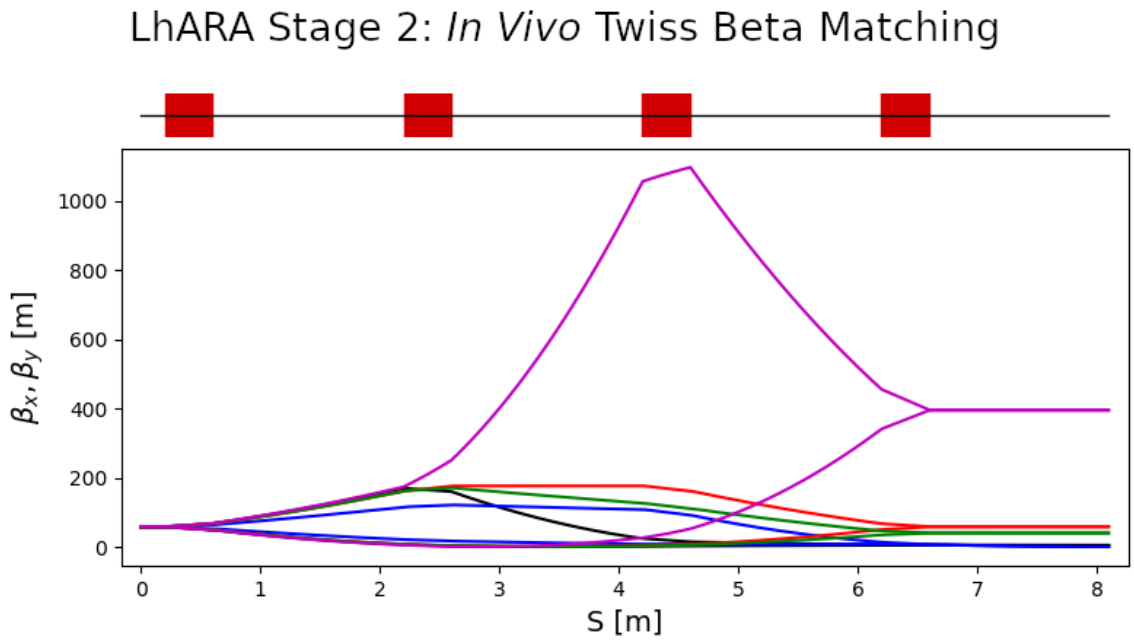

Figure 7.34: MAD-X optics matching for various Twiss beta values in the *in vivo* beam line. The input beam is for a 10 mm nominal beam coming from the extraction line. The achievable Twiss values are for $\beta = 0.46$ m (black), $\beta = 4.5$ m (blue), $\beta = 40$ m (green), $\beta = 46$ m (red), and $\beta = 410$ m (purple). In the schematic diagram above the plot, the red boxes are quadrupoles.

flexibility to achieve the optics specified in table 7.5. The peak magnetic fields also lie below the saturation limits. However, achieving a 1 mm beam spot for the pessimistic beam could not be done. Achieving such a small spot size for that beam emittance required $\beta_{x,y} = 0.039$ m which is a difficult target to achieve even without the limiting restrictions mentioned. The Stage 2 design may have to be tuned when more information about the emittance of the extracted beam is known, but it is worth bearing in mind the pessimistic assumption is a liberal estimate. Once a better understanding of the beam from Stage 1 can be made, it can be tracked through the FFA to inform any changes which need to be made to the design in order to deliver a smaller beam.

The matching capabilities of the four quadrupoles can be seen in fig. 7.34 where a range of values from $\beta = 0.46$ m to $\beta = 410$ m were matched in MAD-X. The input beam for all the cases was for a nominal 10 mm beam coming from the extraction line ($\beta = 46$ m). There is also some additional flexibility in achieving smaller and larger beta values.

Particle tracking simulations with BDSIM were performed to verify the MAD-X optics results. Good agreement was found as described in the Pre-Conceptual Design Report [34]. However, the impact of space-charge effects also needed to be evaluated. GPT simulations were performed with and without space-charge for various cases using the settings in sec. 7.2.2. The results of tracking for nominal 40 MeV and 127 MeV proton beams and the pessimistic 127 MeV beam can be seen in fig. 7.35, fig. 7.36, and fig. 7.37 respectively. A larger difference resulting from space-charge effects is

observable for the nominal beams. There is also a slightly greater difference for the 40 MeV beam compared to 127 MeV. These differences need to be addressed.

As discussed in the *in vitro* beam line section, the strength of the quadrupoles can be used to compensate for space-charge effects. To check that this could be done, a test case was considered for a nominal 15 MeV beam where the space-charge effect would be most prominent. It was found that the discrepancy in space-charge started in the drift region between the extraction line and the first quadrupoles in the *in vivo* beam line as seen in fig. 7.38a. To compensate for space-charge, the extraction line quadrupoles were matched to obtain a parallel beam entering the first *in vivo* quadrupole to match the case with no space-charge, while the *in vivo* quadrupoles strengths were kept the same. It can be seen in fig. 7.38b that an adjustment of the quadrupoles in the extraction line alone could compensate for the large discrepancy at the end of the beam line. In fig. 7.38c, the same settings for the quadrupole magnets in the extraction line were kept as in fig. 7.38b, but the *in vivo* quadrupoles were matched to get a 10 mm beam. A good comparison between no space-charge and space-charge was found, though some further tuning would be required to get a round beam. This is a promising result compared to previous plots in fig. 7.35 and fig. 7.36, in which the differences are much larger. However, it was found that there was difficulty in attaining a 1 mm spot size for the 15 MeV beam. These preliminary results show that it is feasible for the space-charge effects to be compensated by adjusting the quadrupole strengths in the beam line.

7.4 Conclusion

This chapter presented an analysis of a flux of protons coming from a 2D TNSA simulation. A 3D beam was sampled and tracked through the Stage 1 beam line and compared against an ideal beam where a similar beam evolution was found. Furthermore, the design of the energy selection system was verified to work. The transmission of the sampled beam was improved by a re-optimisation of the beam line. Field maps were also incorporated for the Gabor lenses which had previously been modelled by solenoids. Further improvements are still needed which requires simulating a full 3D TNSA simulation.

The design of the Stage 2 beam line was also presented. The Stage 2 vertical arc was scaled to ensure the peak magnetic fields were below the saturation limits. Detailed analysis was also given for the *in vivo* beam line and shown that a beam could be matched from 1 mm to 30 mm. Considerations were made if the beam emittance extracted was larger than the nominal value. Further investigation would be needed when more information about the extracted beam is known. Differences in the beam size was also found when space-charge was included in the simulations. But it was shown that these differences could be compensated by adjusting the strengths of the quadrupole magnets.

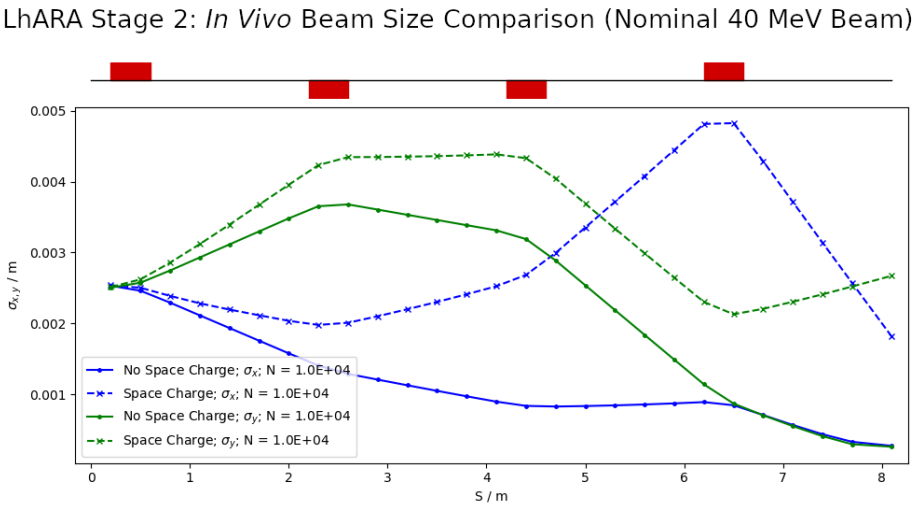

(a) Beam matching to 1 mm spot ($\beta = 0.46$ m).

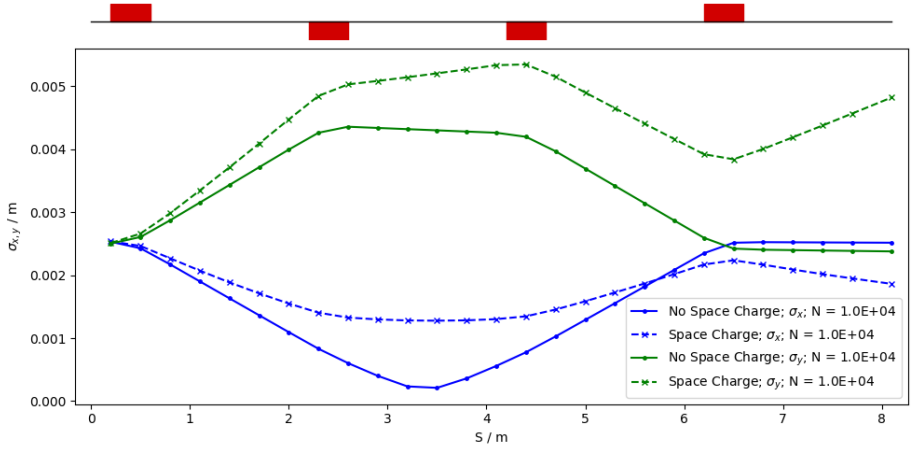

(b) Beam matching to 10 mm spot ($\beta = 46$ m).

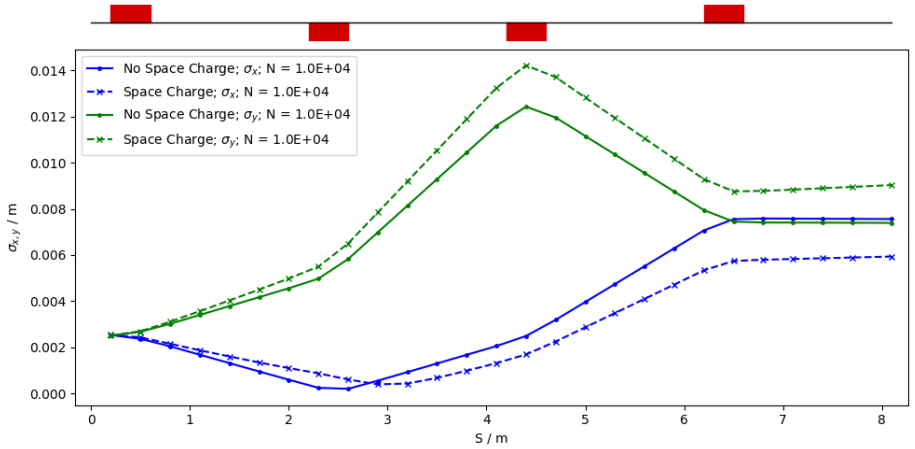

(c) Beam matching to 30 mm spot ($\beta = 410$ m).

Figure 7.35: Nominal 40 MeV beam tracking in GPT comparing no space-charge (solid line) and with space-charge (dashed lines) in the *in vivo* beam line. In the schematic diagram above the plot, the red boxes are quadrupoles.

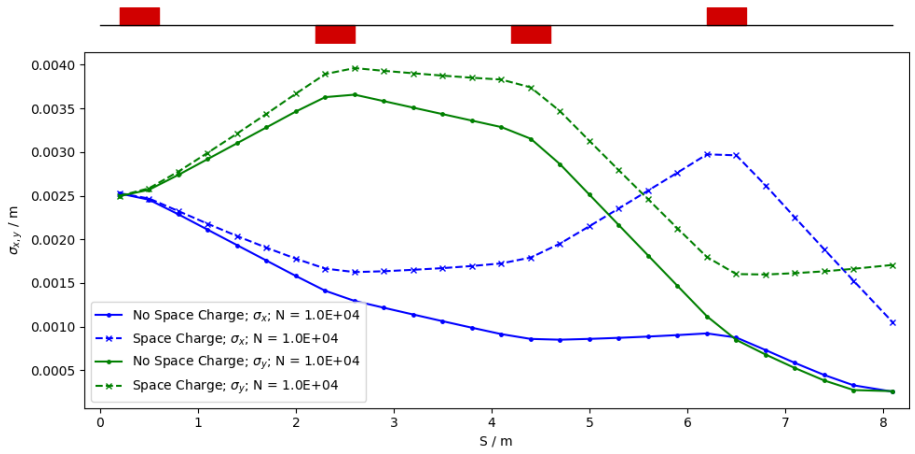

(a) Beam matching to 1 mm spot ($\beta = 0.46$ m).

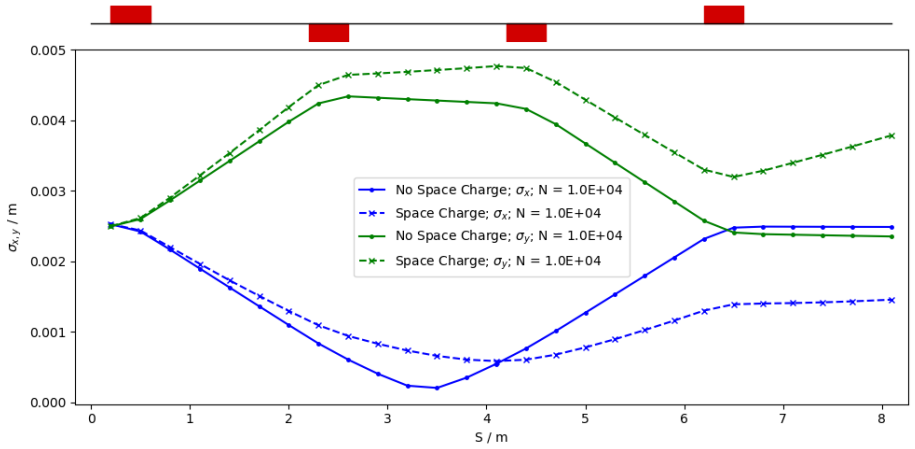

(b) Beam matching to 10 mm spot ($\beta = 46$ m).

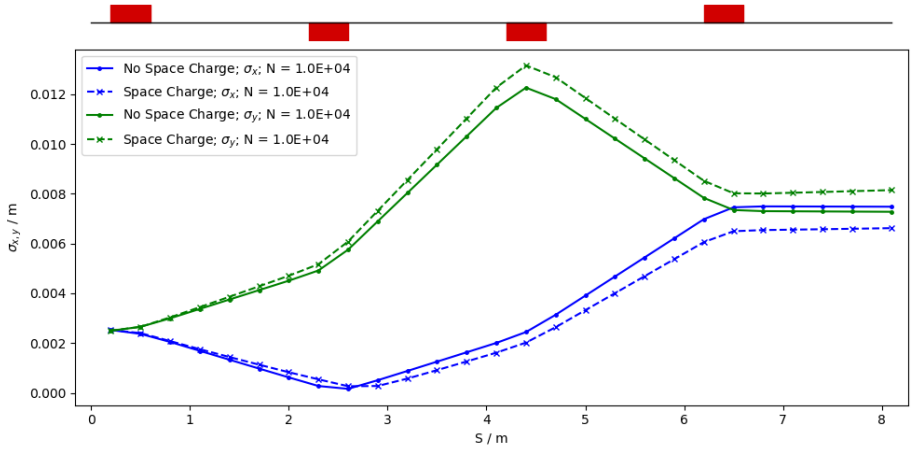

(c) Beam matching to 30 mm spot ($\beta = 410$ m).

Figure 7.36: Nominal 127 MeV beam tracking in GPT comparing no space-charge (solid line) and with space-charge (dashed lines) in the *in vivo* beam line. In the schematic diagram above the plot, the red boxes are quadrupoles.

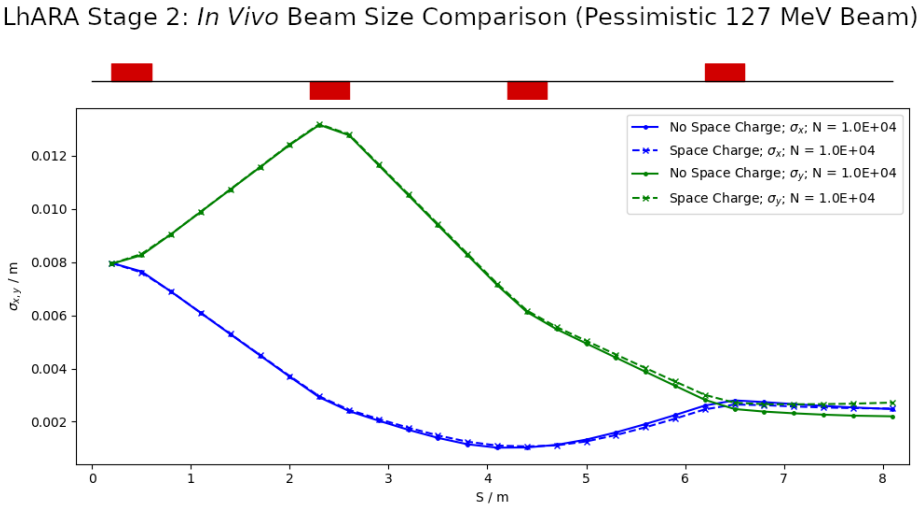

(a) Beam matching to 10 mm spot ($\beta = 4.5$ m).

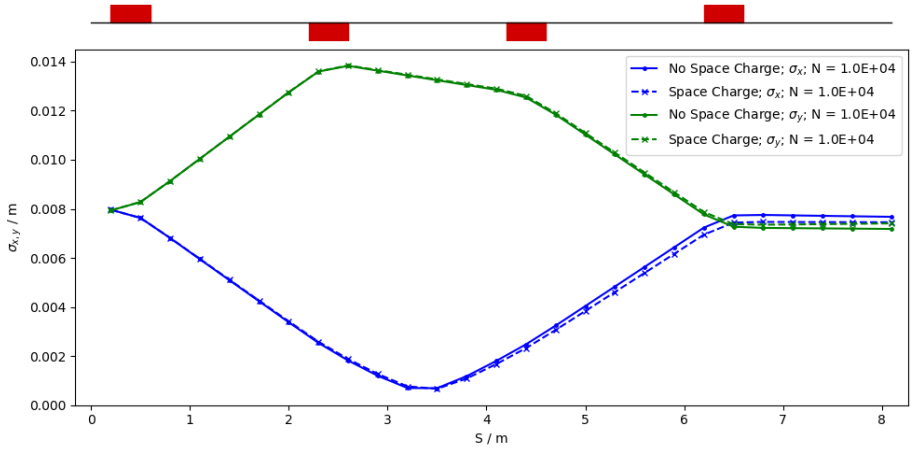

(b) Beam matching to 30 mm spot ($\beta = 40$ m).

Figure 7.37: Pessimistic 127 MeV beam tracking in GPT comparing no space-charge (solid line) and with space-charge (dashed lines) in the *in vivo* beam line. In the schematic diagram above the plot, the red boxes are quadrupoles.

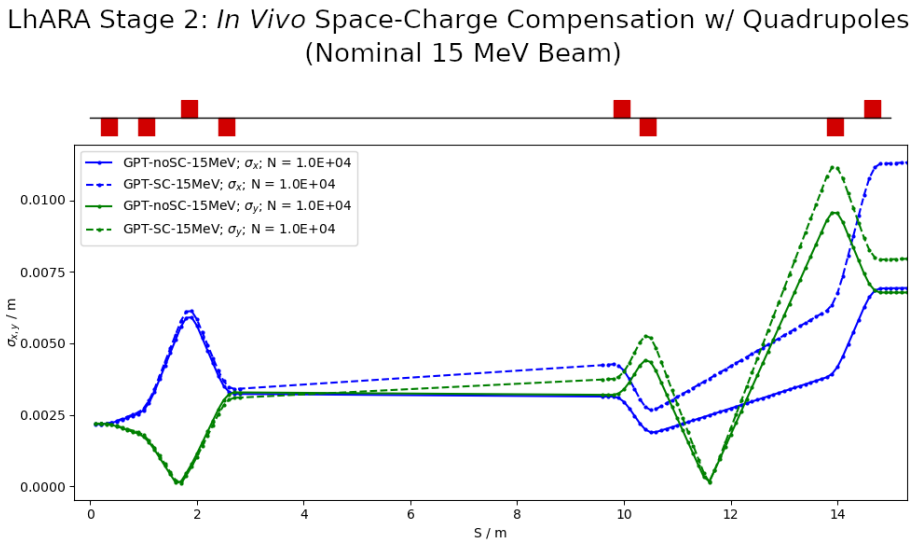

(a) Matching to 30 mm spot size without adjustments.

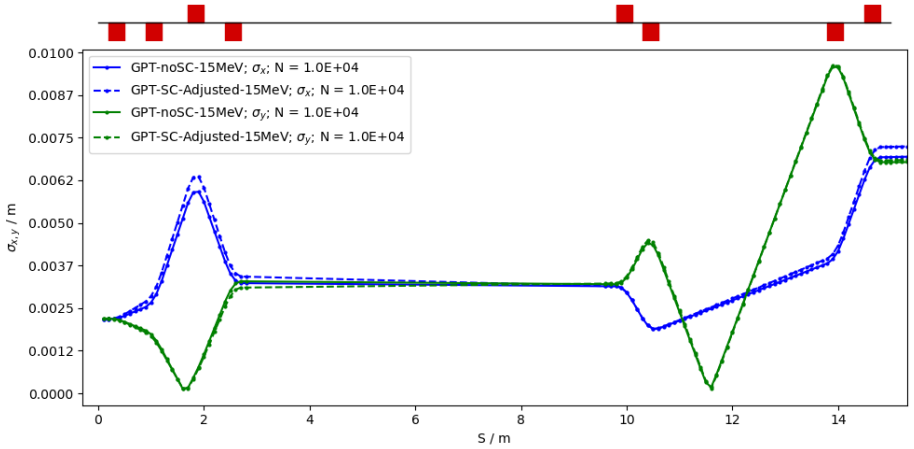

(b) Matching to 30 mm spot size with adjusted quadrupole strengths.

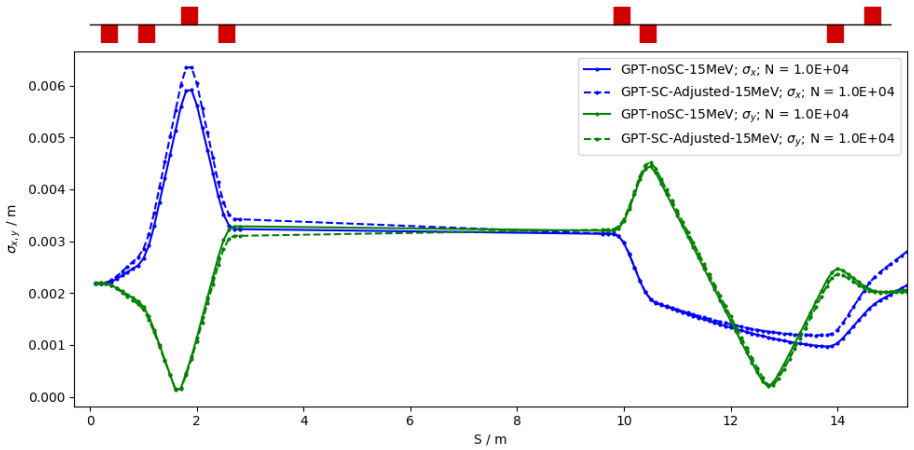

(c) Matching to 10 mm spot size with adjusted quadrupole strengths.

Figure 7.38: GPT simulations comparing no space-charge (solid line) and with space-charge (dashed line) for a nominal 15 MeV beam. Fig. 7.38a was simulated with nominal quadrupole settings in the extraction line. Fig. 7.38b and fig. 7.38c adjusted the quadrupoles in the extraction line to compensate the increase in beam size in the drift space between extraction and the *in vivo* beam line. In the schematic diagram above the plot, the red boxes are quadrupoles.

Chapter 8

SmartPhantom Design

The SmartPhantom is a proposed instrumented water phantom consisting of a series of scintillating fibre planes placed within a water phantom. This instrumentation will allow for shot-to-shot measurements of the energy deposited by a particle beam at several depths in water. From these measurements, an approximate Bragg curve can be fitted. It may also allow for analysis to be carried out on a shot-by-shot basis, allowing for an estimate of the LET and dose that irradiates a cell sample. An advantage of the SmartPhantom is that for high energies, the scintillating fibres will not have a major impact on the dose delivered to a cell sample, thus it can serve as a non-destructive beam monitoring device for radiobiological experiments. This has applications for LhARA, as it allows for shot-by-shot evaluations on the reproducibility of the beam. It could also serve as a useful monitor for both the commissioning and running of the facility.

8.1 Outline of the Initial Design

The design of the SmartPhantom was based around the PTW-T41023 water phantom [214] which can be seen in fig. 8.1. Several scintillating fibre planes are inserted into the phantom as pictured in the schematic diagram in fig. 8.2. These planes are placed in a rotated orientation to guide the fibres out of the water phantom. It also allows for the planes to be inserted and removed from the phantom without needing to unscrew the top each time.

The SmartPhantom will consist of multiple stations. Each station consists of two planes of thin 250 µm diameter scintillating fibres, the planes are oriented at 90° with respect to each other to measure both transverse axes. Each SmartPhantom plane contains a single layer of 492 fibres with a pitch (centre-to-centre distance between adjacent fibres) of 0.305 mm. The ends of each scintillating fibre are connected to clear fibre to transport scintillation photons out of the phantom to be imaged

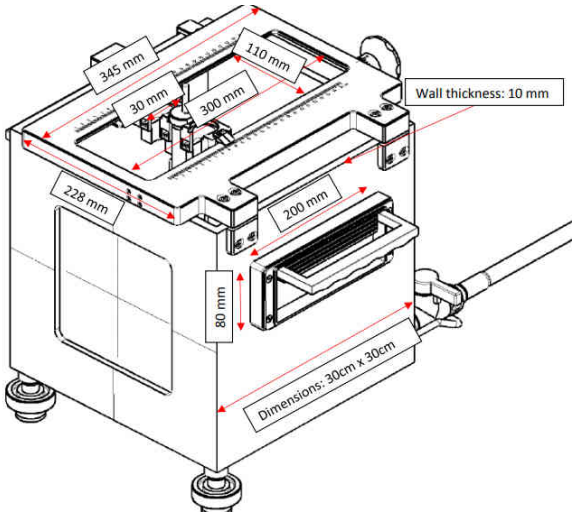

Figure 8.1: Schematic diagram of a PTW-T41023 water phantom [214].

by a camera. One station is placed near the start of the phantom, while the others are connected by a rod and can be moved depending on the energy of the beam.

8.2 Geant4 Simulations

Geant4 simulations (v10.04.p03) guided the design of the SmartPhantom and served as a proof of principle for the concept. The geometry of the water phantom and planes were modelled as can be seen in fig. 8.3 where the beam is incident from the left. The phantom wall has a thickness of 10 mm on each side, though at the centre of one side is an entrance window. The entrance window was modelled with 3.05 mm of `G4_AIR`, followed by 6.95 mm of `G4_PLEXIGLASS`, which sum up to the total thickness of the wall. The rest of the volume was modelled with `G4_WATER`.

The initial design of each SmartPhantom fibre plane was modelled and placed into the simulation. The first layer consists of mylar, modelled with `G4_MYLAR` with a thickness of 0.3 mm. Then a layer consisting of 492 cylinders was modelled with the material `G4_POLYSTYRENE` with a diameter of 250 µm and separated by a pitch of 0.305 mm to represent the scintillating fibres. An identical layer of cylinders follows the first layer but rotated by 90°. Finally, another layer of 0.3 mm of `G4_MYLAR` is modelled. The purpose of the mylar was to keep the fibres in place, but the design would be modified as discussed in appendix C. The fibre planes were designated as a sensitive detector and recorded information about the energy deposited at the end of each event. This allows for a profile to be reconstructed as can be seen in fig. 8.4.

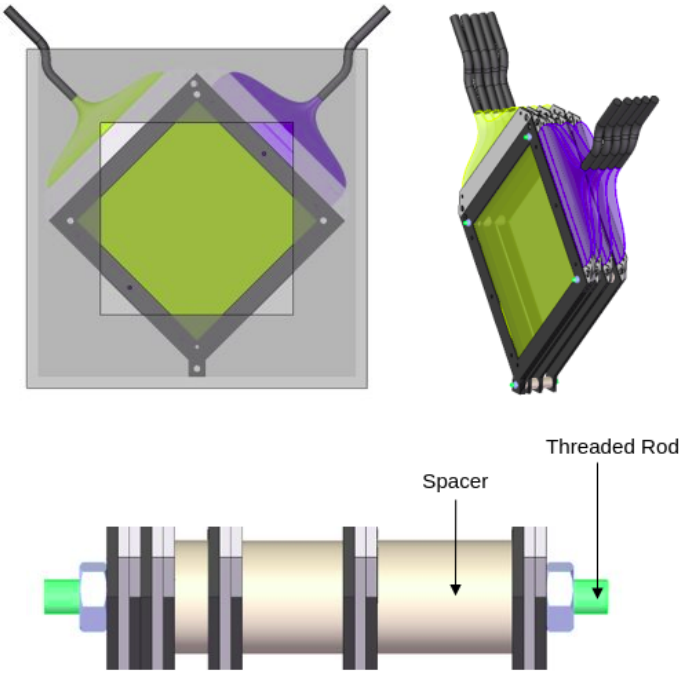

Figure 8.2: Preliminary schematic diagram of the SmartPhantom planes. Left: Transverse plane view of the phantom, with the inner square representing the entrance window. The plane of scintillating fibres (green) are positioned in a rotated orientation. Right: The scintillating fibre planes in series. The scintillating fibres are connected to clear fibres to transport light to a camera. Bottom: Rod to connect the planes through the bottom tabs.

8.2.1 Impact of SmartPhantom Planes in Phantom

The presence of the SmartPhantom planes was investigated to evaluate the impact they would have on the energy deposition. Beams of various energies were simulated through the water phantom both with and without the scintillating fibre planes. For the PTW-T41023 water phantom, its design supports typical treatment energies. For protons this ranges from about 60 to 250 MeV, and 120 to 400 MeV/u for carbon ion beams. A comparison for this range of energies can be seen in fig. 8.5. From the figure it is shown that the SmartPhantom planes have a relatively negligible effect on the energy deposition at the Bragg peak for both proton and carbon ion beams for a variety of energies. However, it should be noted that a higher deposition is seen in the planes compared to water, denoted by the bumps in the plot. Water equivalence assessments for scintillating fibres show that the dose measured tends to be within a few percent of the dose deposited to water [215]. Instead, these bumps are explained by the presence of the mylar films which increase the energy deposition. Even so, the planes have a relatively low impact on the energy delivered at the Bragg peak. But a conversion factor will be needed to bring the energy deposition in the planes down to a level matching the deposition to water as will be discussed in sec. 8.2.2. This is necessary to fit a Bragg curve to estimate the dose delivered to a cell layer located downstream.

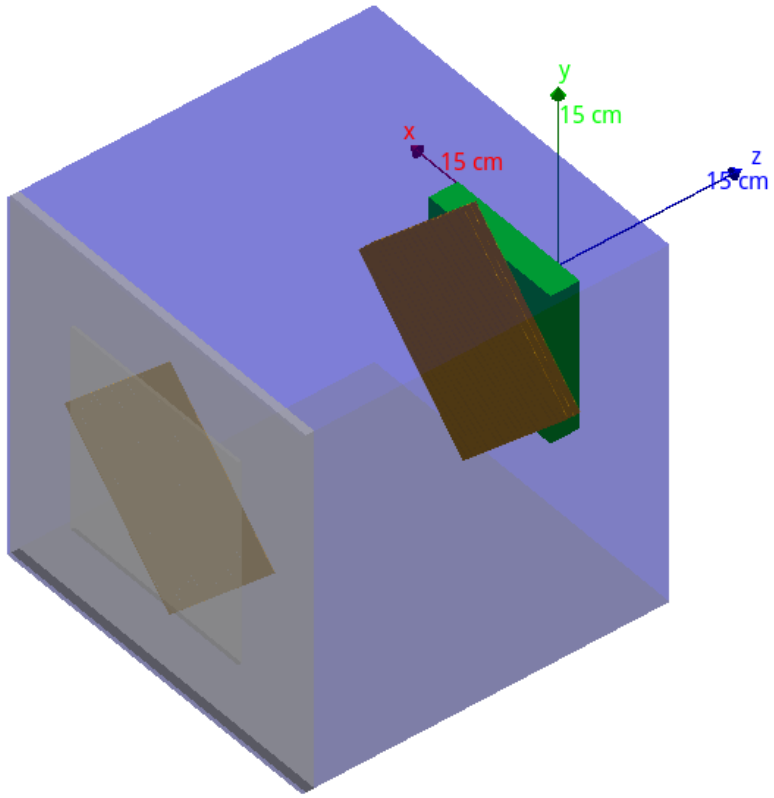

Figure 8.3: Visualisation of the SmartPhantom in Geant4 where a beam is incident from the left. The planes are represented in orange, flask represented in green, and are surrounded by water.

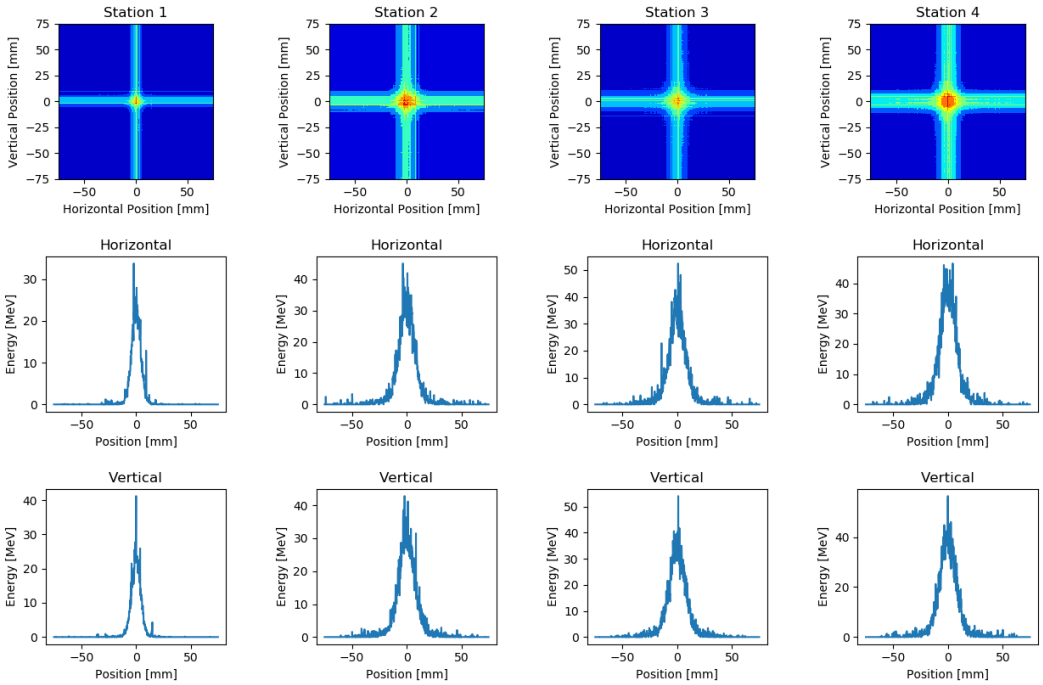

Figure 8.4: Sample output from Geant4 simulations showing the energy deposited in each fibre at each station.

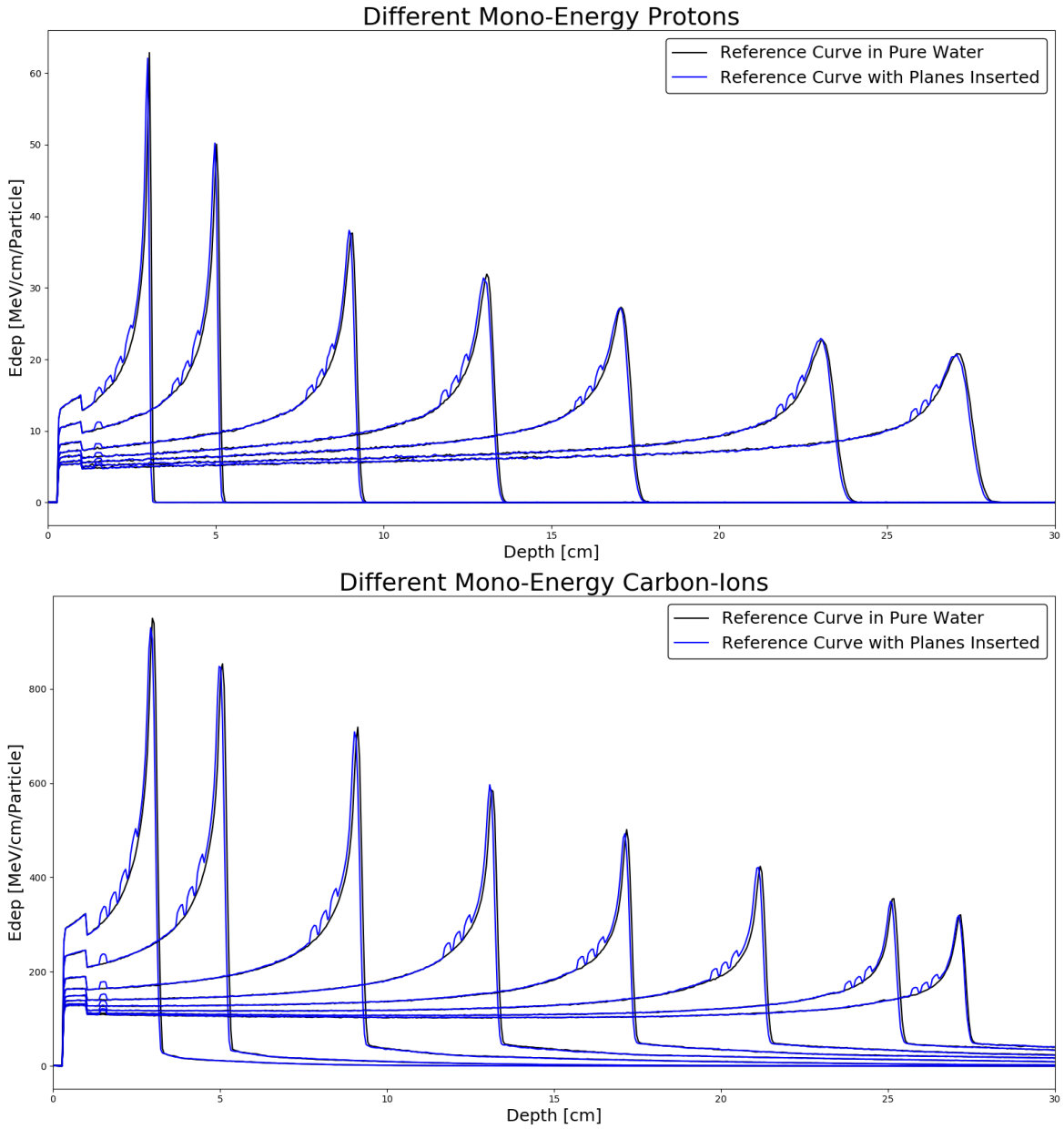

Figure 8.5: Comparison of proton (top) and carbon ion (C^{6+}) (bottom) beams travelling through a phantom with (blue) and without (black) four SmartPhantom planes inserted. Bumps in the Bragg curve are due to the scintillating fibres, with the exception of the first bump near the start which is due to the phantom wall. The proton energies range from about 60 MeV to 200 MeV and 120 MeV/u to 400 MeV/u for carbon ions.

Table 8.1: Parameters used in the Bortfeld model for protons in water.

Parameter	Name	Value	Unit
p	Exponent of range-energy relation	1.77	
α	Proportionality factor	0.0022	cm MeV^{-p}
R_0	Range	E_0^p	cm
β	Slope of fluence reduction relation	0.012	cm^{-1}
γ	Fraction of locally absorbed energy released in nonelastic nuclear interactions	0.6	
σ_{mono}	Width of Gaussian range straggling	$0.012{R_0}^{0.935}$	cm
$\sigma_{E,0}$	Width of Gaussian energy spectrum	$\approx 0.01E_0$	MeV
ϵ	Fraction of primary fluence contributing to the tail of the energy spectrum	$\approx 0.0 - 0.2$	

However, an important caveat to note is that these plots show the energy deposition recorded by the simulation, as opposed to being derived from the light output. Hence, the simulations neglect quenching effects. Quenching is described by Birks Law [216] where the light output is suppressed such that it is no longer proportional to the energy deposited. This is expressed by eq. 8.1:

$$\frac{\mathrm{d}L}{\mathrm{d}x} = L_0 \frac{\frac{\mathrm{d}E}{\mathrm{d}x}}{1 + kB \times \frac{\mathrm{d}E}{\mathrm{d}x}}, \tag{8.1}$$

where L is the relative light output, L_0 is the scintillation efficiency, kB is Birks constant, and $\frac{\mathrm{d}E}{\mathrm{d}x}$ is the energy loss. The suppression in the light output arises from the fact that as charged particles slow down, more energy will be transferred to the medium (especially for high LET particles). However, a proportion of energy will be lost from interactions that do not emit light. In order to apply Birks law accurately, the scintillation efficiency and Birks constant need to be known. These quantities can be determined empirically from measurements.

8.2.2 Fitting with Bortfeld's Model

Bortfeld's model [217] is a closed form analytical approximation of the Bragg curve. This model uses a combination of Gaussian and parabolic cylinder functions to produce the shape of the Bragg curve which can be fitted to measurements. This model applies to protons with energies between 10 and 200 MeV. A variety of parameters used in the model for protons in water is summarised in Table 8.1 [217].

From these parameters, the absorbed dose in water can be represented as a function of the depth,

$D(z)$, given by the piecewise function:

$$D(z) \approx \begin{cases} \Phi_0 \frac{(R_0-z)^{\frac{1}{p}-1}+(\beta+\gamma\beta p)(R_0-z)^{\frac{1}{p}}}{\rho p \alpha^{\frac{1}{p}}(1+\beta R_0)} & z < R_0 - 10\sigma \\ \Phi_0 \frac{e^{-\frac{\zeta^2}{4}}\sigma^{\frac{1}{p}}\Gamma(\frac{1}{p})}{\sqrt{2\pi}\rho p \alpha^{\frac{1}{p}}(1+\beta R_0)} \left[\frac{1}{\sigma}\mathscr{D}_{-\frac{1}{p}}(-\zeta) + \left(\frac{\beta}{p}+\gamma\beta+\frac{\epsilon}{R_0}\right)\mathscr{D}_{-\frac{1}{p}-1}(-\zeta)\right] & R_0 - 10\sigma \leq z \leq R_0 + 5\sigma \\ 0 & \text{otherwise,} \end{cases} \tag{8.2}$$

where Φ_0 is the primary fluence, ρ is the density of the medium, E_0 is the energy of the beam, $\Gamma(1/p) = 1.575$ is the gamma function, and

$$\sigma^2 = {\sigma_{\text{mono}}}^2 + {\sigma_{E,0}}^2 \alpha^2 p^2 {E_0}^{2p-2}, \tag{8.3}$$

$$\zeta = \frac{R_0 - z}{\sigma}. \tag{8.4}$$

A key part of the model are the parabolic cylinder functions expressed by $\mathscr{D}_y(x)$, which help describe the shape of the curve. These depth-dose curves were compared to measured data for proton beams in water where a good agreement could be found [217].

For the SmartPhantom, this model was used to fit a Bragg curve to the simulation results. The fitting parameters used in the model are: Φ_0, ϵ, R_0, β, and σ. These parameters are fitted to measurements from four SmartPhantom stations, each consisting of two planes (horizontal and vertical). One such fitting applied to a proton beam passing through the SmartPhantom can be seen in fig. 8.6 and plotted against a reference curve of the energy deposition over the entire phantom depth for several proton energies. A relatively good fit was found for the lower energies, but worsened for the higher energies, particularly on the distal edge. The fitting is affected by the measurement points where a higher energy deposition compared to water can be found on the rising edge. Another fitting was applied where the measurement points were adjusted to match the value for a reference curve in water (using the energy deposited in a volume of water). The results of a fitting using adjusted measurement values can be seen in fig. 8.7 for proton beams where an improvement to the fit can be found on both the rising edge and the distal edge. The same fitting procedure was applied for several carbon ion beams as is shown in fig. 8.8. Despite the fact that Bortfeld's model only applies to protons, the fitting is quite good. The exception is the fragmentation tail which the model does not account for. A modification to the Bortfeld approximation has been proposed by Tuomanen *et al.* [218] which adds an additional parameter to describe the fragmentation tail which could be implemented at a later stage to allow for better insight to the distal edge. Another proposed modification to the model is by Kelleter and Jolly [219], this allows one to obtain a quenched Bragg curve by including the scintillation efficiency and Birks constant into the model.

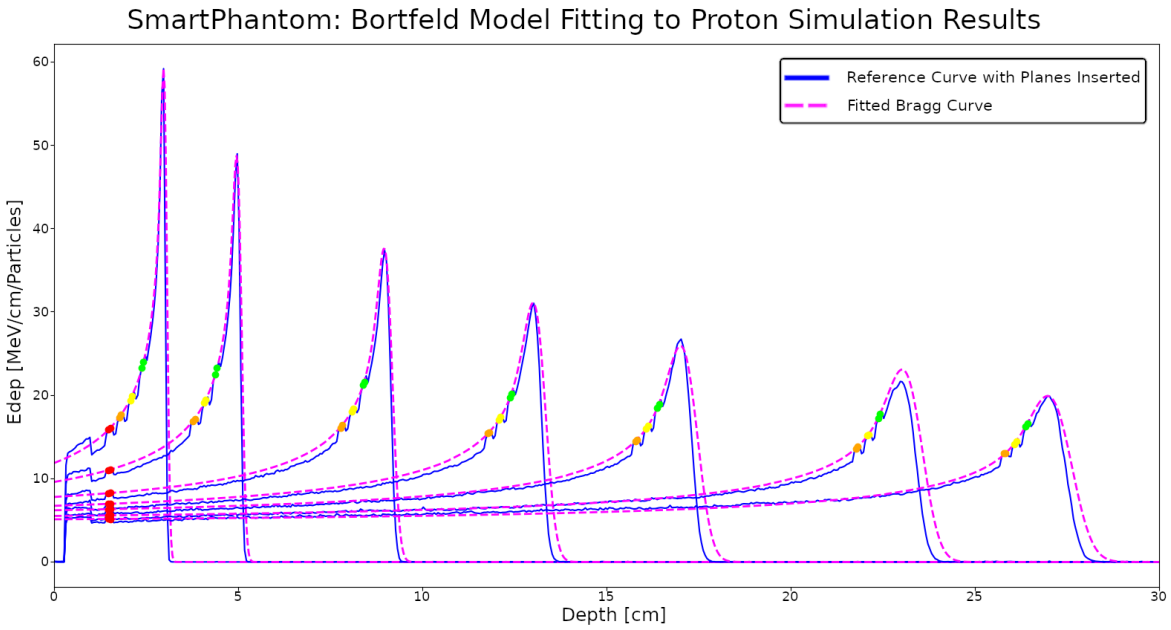

Figure 8.6: Fitted Bortfeld's model (magenta) to eight measurement points denoted by the coloured points for several proton beam energies. The curve in blue is a reference curve for the phantom with planes inserted over the entire depth.

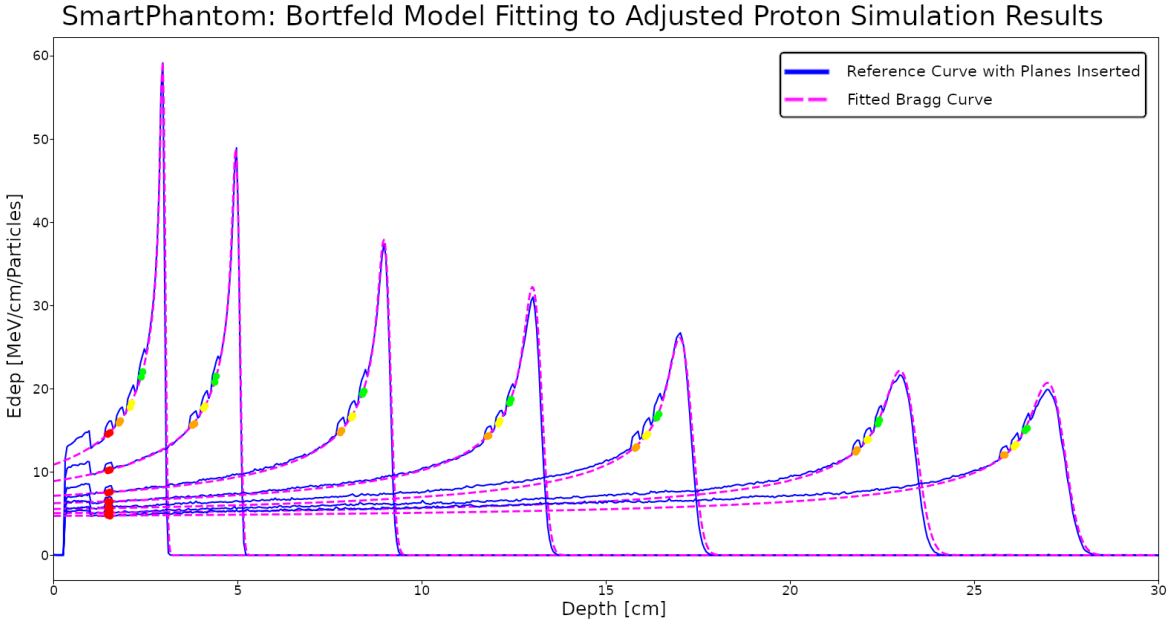

Figure 8.7: Fitted Bortfeld's model (magenta) to eight measurement points denoted by the coloured points which are adjusted to values in water for several proton beam energies. The curve in blue is a reference curve for the phantom with planes inserted over the entire depth.

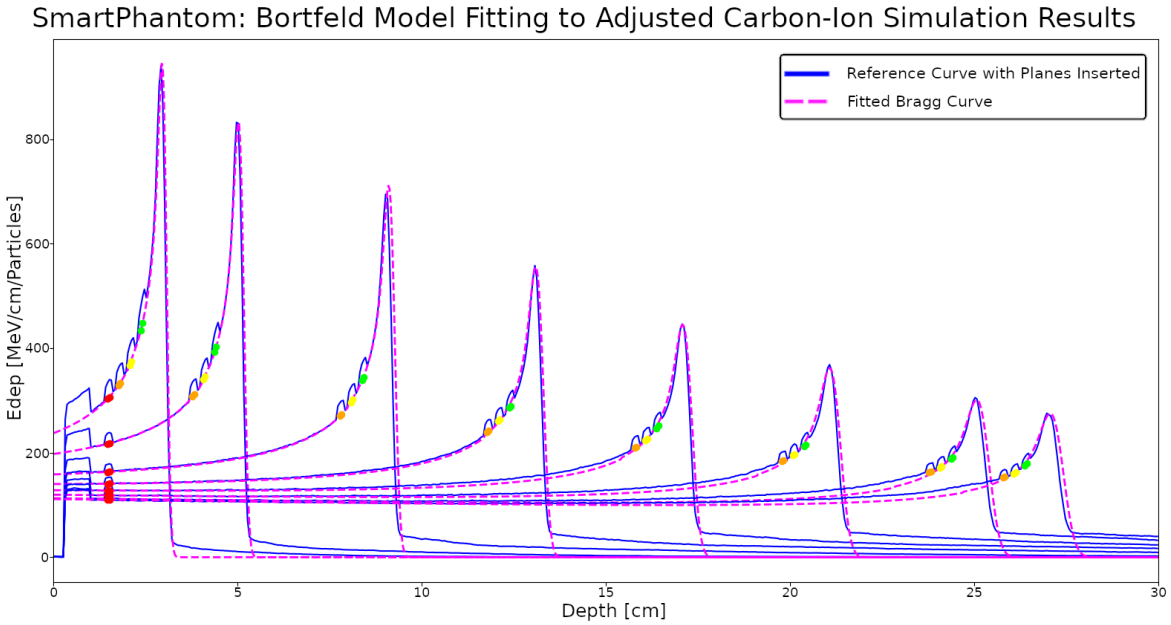

Figure 8.8: Fitted Bortfeld's model (magenta) to eight measurement points denoted by the coloured points which are adjusted to values in water for several carbon ion beam energies. The curve in blue is a reference curve for the phantom with planes inserted over the entire depth.

8.3 Scintillation Tests with Fibre Bundle

In order to test the camera readout and software needed for the SmartPhantom, fibres from Saint-Gobain Crystals were used. BCF-20 scintillating fibre with a 250 µm diameter and BCF-98 clear fibre were used. These fibres contain a polystyrene core with fluorescent dopants added for the scintillating fibres and a PMMA cladding [220].

A one-to-one connection between scintillating fibres and clear fibres is needed for the SmartPhantom to read out the light. As these initial tests were intended to test both the fibres and readout, a simple design was used. Both the scintillating and clear fibres were wound and bound together into a bundle. This bundle would be read by a camera where only the scintillating fibres produce light when exposed to a beam. This simple design is representative of a readout from the SmartPhantom where only some of the fibres would light up depending on which fibres the beam deposited energy into.

The entire fibre bundle is shown in fig. 8.9, here the scintillating fibre and clear fibre were wound and fed into a boot. The ends of the fibre in the boot were then potted with epoxy resin to both keep the fibres in place and a black pigment was added for light exclusion. The fibres on one end of the bundle would be attached to a camera, while the other end was wrapped in heat shrink and a metal cap placed on the end. A locking ring for the camera holder is slotted into the boot to affix a camera. The camera that was used in the tests was a Point Grey Chameleon3 USB3 camera with a

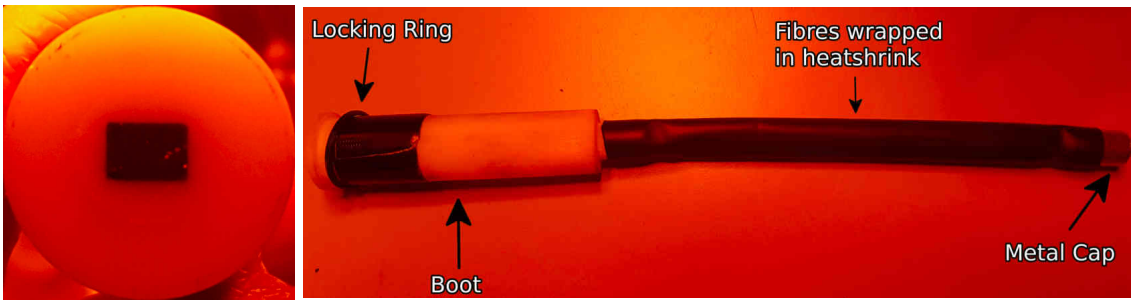

(a) Front view.

(b) Side view.

(c) Camera and holder affixed to the bundle.

Figure 8.9: Fibre bundle used for readout tests. It consists of scintillating and clear fibres fed into a boot on one end and covered with heat shrink on the other and a metal cap excludes light from the edge. The locking ring for the camera holder is slotted into the boot which locks the position of the camera and holder.

CMOS sensor (CM3-U3-31S4M-CS) [221].

8.3.1 Tests with an Ultraviolet Light Source

The fibre bundle was first exposed to an ultraviolet light source where the camera readout can be seen in fig. 8.10. There is some ambiguity when trying to differentiate between the scintillating and clear fibres. While it is clear the brightest fibres are scintillating, the duller fibres could be a result of crosstalk. This will not be an issue for the Smartphantom as only the clear fibres are captured. But an evaluation of crosstalk from adjacent fibres may be necessary.

In the SmartPhantom, the clear fibres will be bundled into a boot similar to the fibre bundle with an aperture corresponding to the area of the camera lens. To reconstruct the beam, a mapping will be needed for each station plane to correlate the readout to each scintillating fibre. To identify the fibre in an image, a script employing a flood-fill algorithm can be used. The algorithm looks for adjacent nodes connected to a start node through a condition that is specified by a user, such as the pixel intensity. An implementation was written for the readout in fig. 8.10 where the result for several cases can be seen in fig. 8.11. The script looks for any pixels with a value greater than the average background value and classifies it as belonging to a scintillating fibre, displaying it in white. In fig. 8.11a it can be seen that script is overall quite effective in filtering out the background from the readout. However, some specks in the image are picked out and some of the spots are connected

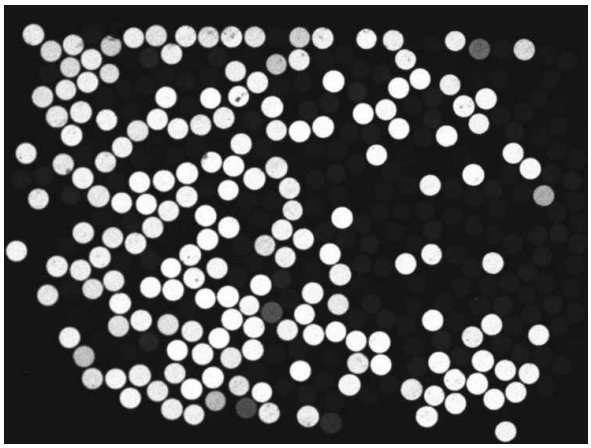

Figure 8.10: Camera readout of the fibre end when the fibre bundle was exposed to an ultraviolet light source. Due to the black and white output, it is difficult to differentiate between scintillating and clear fibre in some cases.

together. Furthermore, some of the spots are not fully picked out. The specks arise from image noise, while the incomplete spots have low pixel intensity values, indicating they come from clear fibres. These results indicate that some image processing is needed. A Gaussian filtering was used to smooth the image and the background filter was increased to filter out the clear fibres. The result of these changes to the algorithm can be seen in fig. 8.11b. It can be seen that the specks are removed, but some of the spots which are located close together are still connected. This can lead to an uncertainty in identifying which pixel corresponds to which fibre. To avoid this problem, the Gaussian blurred image was analysed and the spots were manually selected. To ensure the spots did not connect, some pixels are neglected with the result given in fig. 8.11c. A revision to the design could be made to avoid this issue for the prototype.

From the flood-fill algorithm, the pixel coordinates corresponding to each spot are also recorded. Another analysis script measures the pixel intensity for each of these coordinates in a camera readout to measure the intensity of each fibre. This can be seen in fig. 8.12 where the coordinates taken from fig. 8.11c were applied to the original readout and the 178 identified scintillating fibres marked. A conversion factor would be needed to relate the pixel intensity to the energy deposited in the scintillating fibre. For the SmartPhantom planes, this factor could be determined with the help of another detector.

8.3.2 Exposure to a Proton Beam

After the proof of principle tests with the ultraviolet source, the fibre bundle was brought to the Clatterbridge Cancer Centre and exposed to the proton beam. The purpose of this test was to verify that a signal could be obtained in the scintillating fibres from charged particles. The fibre bundle

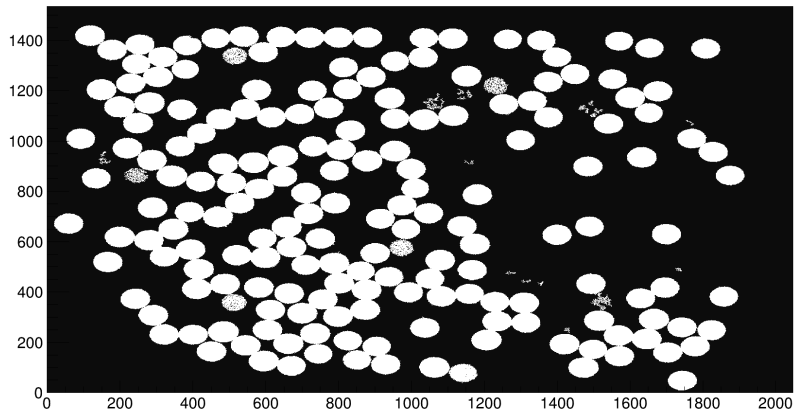

(a) Flood-fill algorithm.

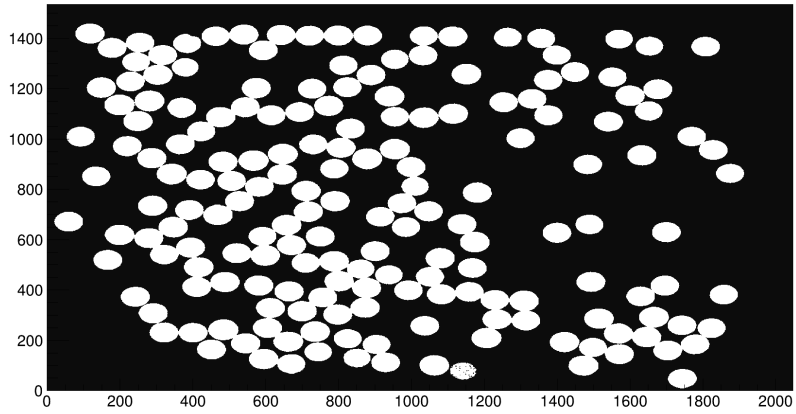

(b) Flood-fill algorithm with Gaussian filtering.

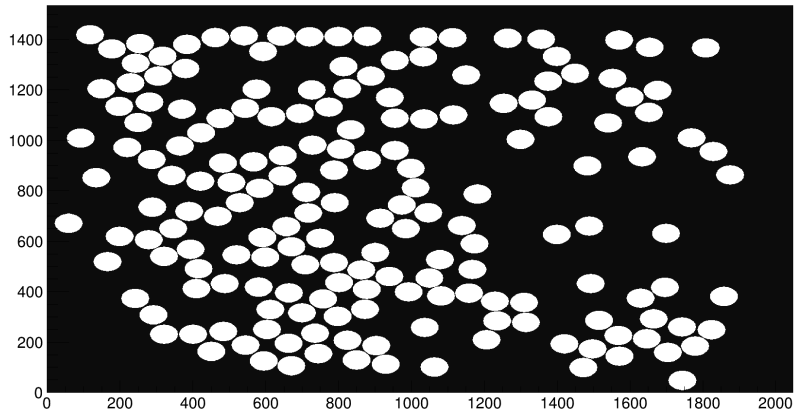

(c) Flood-fill algorithm with manual designation of scintillating fibres.

Figure 8.11: Flood-fill algorithm applied to the readout in fig. 8.10 to identify fibres. Any pixels with a value higher than the background was picked out and coloured white.

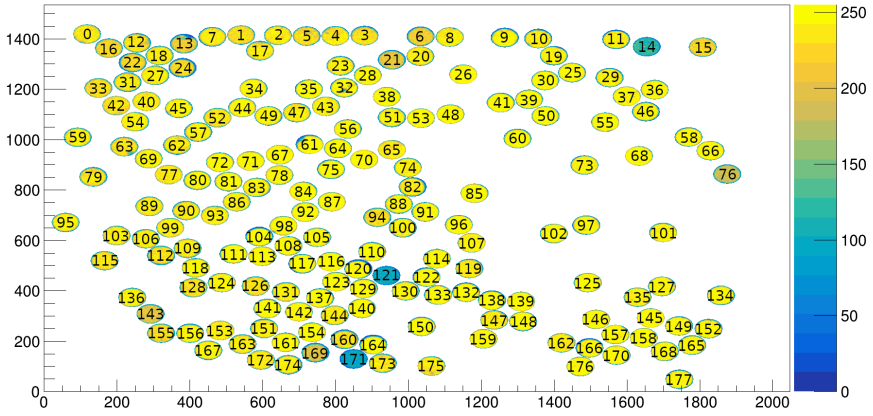

Figure 8.12: Each fibre designated according to the coordinates given from fig. 8.11c applied to the original readout image. Colours designate the pixel intensity value.

Figure 8.13: Setup of the fibre bundle positioned near the beam nozzle on the right.

was positioned on a platform behind the treatment chair and secured in place with tape and a weight as seen in fig. 8.13. In the figure it can be seen that additional black tape was applied to the boot of the fibre bundle in order to better exclude external light.

In total five separate beam exposure tests were done to see how the fibres react to different irradiation conditions. These tests involved adjustments to the delivered dose rates and insertion of modulator wheels and are summarised by:

1. Decreasing dose rates for a 59 MeV proton beam.
2. Increasing dose rates for a 59 MeV proton beam.
3. Increasing dose rates for a 11 MeV proton beam.
4. Increasing dose rates for a 11 MeV proton beam with a modulator wheel inserted.

5. Intermittent interruptions to a 11 MeV proton beam with a modulator wheel inserted.

A video was recorded for each of the tests and subsequently analysed. The integrated pixel intensity for each of the 178 scintillating fibre were calculated and plotted over different time steps corresponding to changes in the irradiation settings as seen in fig. 8.14. The results show that the scintillating fibres are effective at measuring different irradiation conditions. In the first test it can be seen that there is a general decrease in the pixel intensities as the dose rate was decreased. In the second and third test similar pixel intensities were obtained as the dose rate increased. This is explained by the fact that although the beam energies are different, the dose rate delivered is the same. For the fourth test there is a decrease in the intensity compared to the third test despite the same machine settings being used. This is explained by the insertion of a modulator wheel. At 11 MeV, the range of protons puts the Bragg peak at the location of the fibre bundle. The insertion of the modulator wheel attenuates the proton beam to produce a spread out Bragg peak, but decreases the overall dose delivered to the bundle. The final test looked at how the fibres react when the beam was interrupted with a pause period of about two seconds. It can be seen that the fibres were responsive and the same average pixel intensities were obtained between each interruption.

The results of these tests serve as an initial proof of principle that the scintillating fibres function and the mapping and analysis script could be applied to the SmartPhantom. However, one aspect that was not tested was correlating the pixel intensities to the energy deposited. This would be best done by first creating a prototype of a SmartPhantom plane. The output of the plane could then be compared against another detector.

8.4 Conclusion

This chapter summarises the developments that have went into the design of the SmartPhantom. The concept was discussed and tested with Geant4 simulations. It was shown that the presence of the SmartPhantom planes would have a negligible impact on high energy beams. It was also shown that Bortfeld's model could be fitted onto measurements to reproduce a Bragg peak. Fibre bundle tests were conducted which showed the signal response of the scintillating fibres and the mapping analysis required. Future work is needed to create a functional prototype, with some considerations discussed in appendix C. But the principle is sound and once created would serve as an effective detector. The SmartPhantom has applications in radiobiology experiments, where the beam and dose can be evaluated on a shot-by-shot basis. It can also be used in LhARA to evaluate the reproducibility of the beam, ensuring a consistent dose is delivered for experiments.

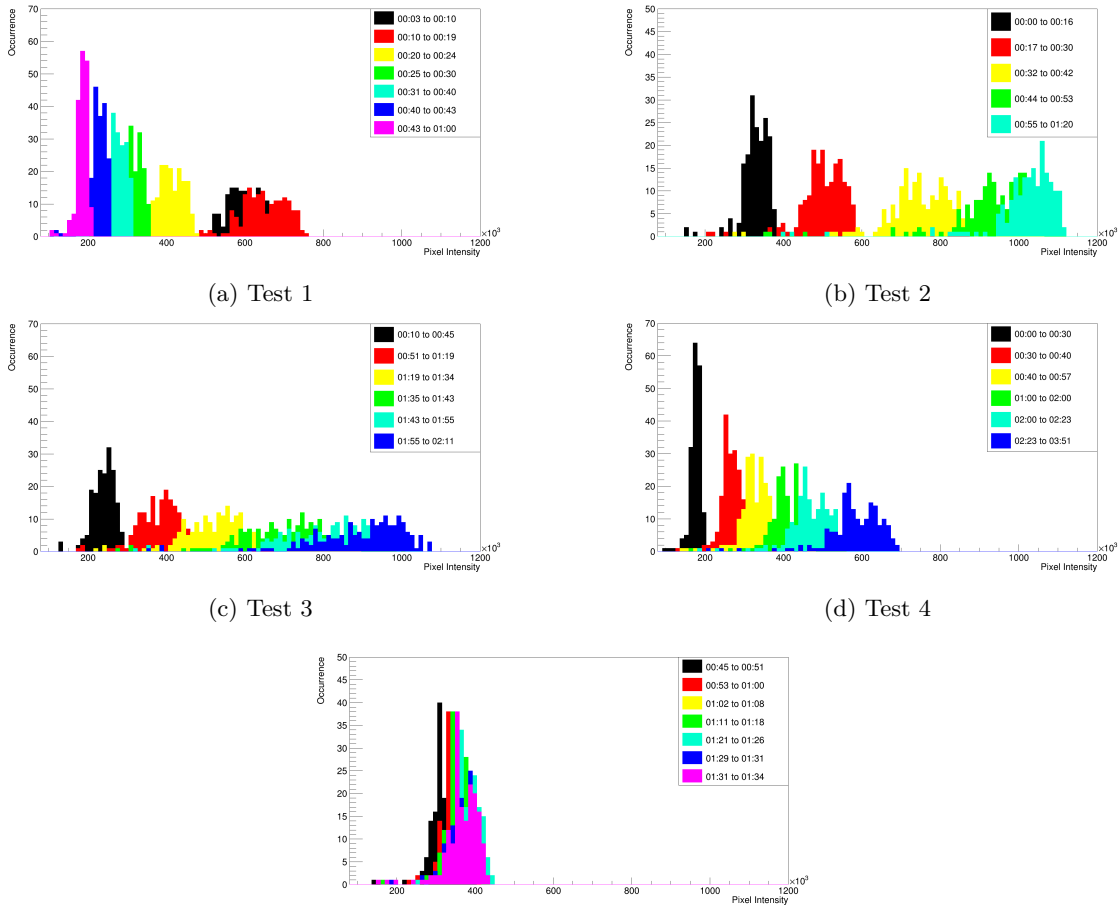

(a) Test 1

(b) Test 2

(c) Test 3

(d) Test 4

(e) Test 5

Figure 8.14: Fibre bundle tests with: (a) 59 MeV proton beam with decreasing dose rates, (b) 59 MeV proton beam with increasing dose rates, (c) 11 MeV proton beam with increasing dose rates, (d) 11 MeV proton beam with increasing dose rates and a modulator wheel inserted, and (e) 11 MeV proton beam with intermittent interruptions and a modulator wheel inserted. The integrated pixel intensity for each scintillating fibre is plotted with the colours designating the time steps analysed in each video.

Chapter 9

Conclusion and Final Remarks

This thesis presented beam simulation results which played a key role in the carbon commissioning efforts at MedAustron. A rematch procedure was developed that allowed one to approximate a Gaussian beam for tracking purposes from trajectory measurements. In addition, simulations were performed for the design and research efforts for LhARA for both Stage 1 and 2. Finally, the concept and developments for the SmartPhantom were outlined, which will aid the production of a working prototype.

9.1 Twiss Rematch Procedure

In chapter 6, the results of the spot size commissioning for carbon ions in IR1 and IR2-H as well as 800 MeV protons in IR1 at MedAustron were presented. The focus was characterising and adjusting the delivered beam to within specified parameters.

A difficulty encountered when simulating the beam was characterising the beam. Due to the commissioning schedule, the beam extracted into the HEBT would vary between sessions and updated beam measurements would not always be available. Initially, quadrupole scanning allowed for a good approximation for the beam in the vertical plane, however, due to the location of the detector, the beam was quite narrow in the horizontal plane. Due to this, a time consuming manual fit using trajectory measurements was done to approximate the horizontal plane. Although the simulated beam matched to measurements, there was a noticeable discrepancy at lower energies due to scattering. A Twiss parameter scan was performed based on this reconstructed beam which used measurements to optimise the beam for IR2-H.

For the IR1 research line, the reconstructed beam for carbon ions was backtracked in MAD-X, but no longer matched measurements. This led to the development of a Twiss rematch procedure which

allowed for an automated minimisation script to fit Twiss parameters to beam measurements along the beam line. This procedure had the benefit of only requiring beam trajectory measurements, which at MedAustron was automated and only took a few minutes to perform. Although the approximated beam was Gaussian distributed, a good fit was still found for the horizontal plane and sped up the commissioning. Future work could include refining this method to account for a beam that is off-centre. The script could also be improved by reading the measurement and beam line elements settings directly from MAPTA to reduce user input, as well as to apply a weighting to account for defects in the detectors.

9.2 LhARA Beam Line Tracking

In chapter 7, several beam line simulations were presented for LhARA. These simulations covered an approximate end-to-end simulation of Stage 1 from the laser source to the end station and the design for Stage 2.

For the Stage 1 beam line, the TNSA interaction was simulated in 2D from which an approximate sampled 3D beam was generated and tracked. Comparing this sampled beam to an ideal Gaussian beam showed a match at the end station but with a larger initial beam in the capture section which led to significant particle losses. Improvements to the simulations were made where the energy selection of the beam line design was evaluated, Gabor lens field maps were incorporated in the simulation, and the beam line was tuned to reduce beam losses for the sampled beam. Future work for these Stage 1 simulations include running a 3D TNSA simulations in order to carry out a complete end-to-end simulation, making considerations for the preplasma, and analysis of the co-moving electrons which could affect the operation of the Gabor lenses.

The design for Stage 2 was presented and evaluated using estimated extraction parameters from the FFA. From the beam line simulations it was found that the specified beam parameters could be achieved if the extracted beam had a nominal beam emittance. But a pessimistic beam emittance was also considered which would have an impact on the attainable beam sizes. Furthermore, space-charge was found to have a prominent effect on the beam size evolution. Future work will be needed to address these issues. One task is to simulate a realistic beam through the FFA which can then be tracked through the rest of the beam line. Another task is to look into compensating the space-charge effects, where an option is to adjust quadrupole strengths.

9.3 SmartPhantom Design

In chapter 8, the design and principle for the SmartPhantom was presented. Simulations in Geant4 show that the presence of several thin scintillating fibre layers in water when irradiated with high energy beams had a small impact on the dose exposed to cells. This would allow the SmartPhantom to act as an online beam monitoring device. Using the measurements from the scintillating fibre planes allows one to fit a Bragg curve to the energy deposition measurements and measure the beam profile. Some testing was done to test the fibres and prototype the mapping analysis. Future work includes making a working prototype. Improvements to the fitted Bragg curve will also be needed, this can be done by modifying Bortfeld's equation to incorporate other species and account for quenching effects.

9.4 Final Remarks

To conclude, this thesis has shown ways in which particle physics knowledge and technology plays an important role in radiotherapy and radiobiological research. Accelerators such as linacs, cyclotrons, and synchrotrons are current mainstays in delivering beams for radiotherapy. Developments in novel acceleration mechanisms have big ramifications for future particle physics research, and will find numerous applications in radiotherapy. As research and technology develop, novel sources such as laser-driven sources, may one day become a mainstay for hadron therapy, increasing the global availability of cancer treatment options for future cancer patients.

Appendix A

Normalised Phase Space

In normalised phase space, the trajectory of particles is a circle rather than an ellipse. This can be seen by considering the Courant-Snyder invariant in (u, u') space:

$$\left(\frac{1+\alpha^2}{\beta}\right) u^2 + 2\alpha u u' + \beta {u'}^2 = \epsilon,$$

where (α, β) are Twiss parameters, u is the position, and ϵ is the emittance. Rearranging the terms gives:

$$\begin{aligned} \left(1+\alpha^2\right) u^2 + 2\alpha\beta u u' + \beta^2 {u'}^2 =& \beta\epsilon, \\ u^2 + \left(\alpha^2 u^2 + 2\alpha\beta u u' + \beta^2 {u'}^2\right) =& \beta\epsilon, \\ u^2 + \left(\alpha u + \beta u'\right)^2 . =& \beta\epsilon \end{aligned} \tag{A.1}$$

This resembles the form of an equation for a circle for the $(u, (\alpha u + \beta u'))$ plane, with a radius $r = \sqrt{\beta\epsilon}$. Hence, we can introduce the normalised coordinates:

$$U = \frac{u}{\sqrt{\beta}}, \tag{A.2}$$

$$U' = \frac{\alpha}{\sqrt{\beta}} u + \sqrt{\beta} u', \tag{A.3}$$

which can be expressed in matrix notation with:

$$\begin{pmatrix} U \\ U' \end{pmatrix} = \frac{1}{\sqrt{\beta}} \begin{pmatrix} 1 & 0 \\ \alpha & \beta \end{pmatrix} \begin{pmatrix} u \\ u' \end{pmatrix}. \tag{A.4}$$

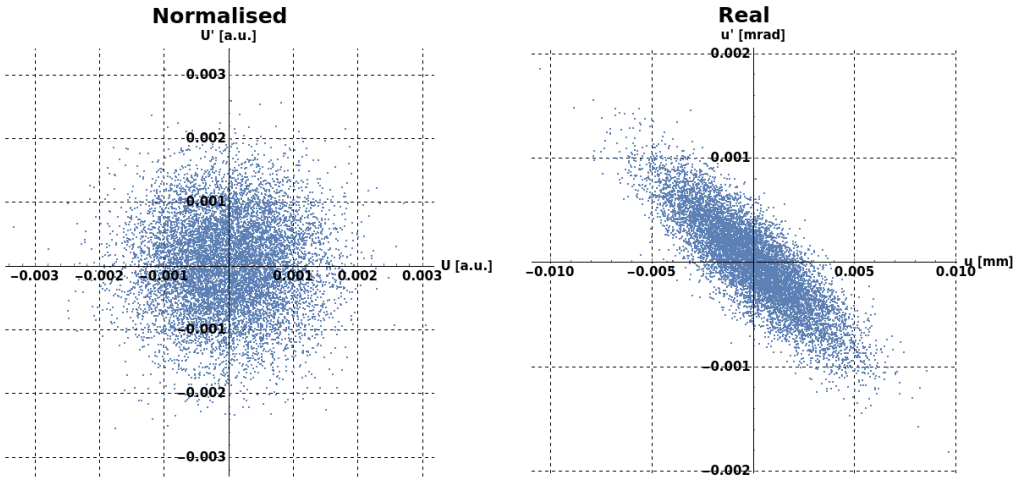

Figure A.1: Comparison of a distribution in normalised (left) and real (right) phase space. Generated using the parameters: $\beta = 10.0\,[\mathrm{m}], \alpha = 5.0, \epsilon = 7.3 \times 10^{-7}\,[\pi \cdot \mathrm{m} \cdot \mathrm{rad}]$.

The normalised phase space can be useful when generating a distribution from the Twiss parameters. To generate a distribution, one first generates a random value between zero and the emittance value to get the normalised coordinates. Then one simply transforms the normalised coordinates to real coordinates:

$$u = a\sqrt{\beta\epsilon}, \tag{A.5}$$

$$u' = (b - \alpha a)\sqrt{\frac{\epsilon}{\beta}}, \tag{A.6}$$

where a and b are Gaussian random numbers generated with a mean value of 0 and a standard deviation of 1. A comparison of the normalised and real phase space is shown in fig. A.1.

Dispersion can also be accounted for by including correction factors to get:

$$u = a\sqrt{\beta\epsilon} + D\left(c\frac{\Delta p}{p}\right), \tag{A.7}$$

$$u' = (b - \alpha a)\sqrt{\frac{\epsilon}{\beta}} + D_p\left(c\frac{\Delta p}{p}\right), \tag{A.8}$$

where D is dispersion of u, D_p is dispersion of momentum, p, and c is another Gaussian random numbers generated with a mean value of 0 and a standard deviation of 1.

Appendix B

Ideal Electric Field for the Gabor Lens

To determine the electric field for the Gabor lens, we first assume a cold and homogeneously distributed electron plasma confined within a cylindrical region with no neutralising ion background. For a cylinder of length L, radius r, and enclosed charge of Q', the field is directed outwards with an electric flux, Φ:

$$\Phi = E(2\pi rL) = \frac{Q'}{\epsilon_0}. \tag{B.1}$$

A Gaussian surface will enclose a region smaller than the total charge, which can be expressed by:

$$Q' = Q\frac{r^2}{R^2}, \tag{B.2}$$

where R is the radius from the center of a cylinder to the surface. This can be substituted into the flux to yield:

$$\Phi = E(2\pi rL) = \frac{Qr^2}{\epsilon_0 R^2} \qquad \Rightarrow \qquad E = \frac{Qr}{\epsilon_0 2\pi R^2 L}. \tag{B.3}$$

Using the fact that the volume of a cylinder is $V = \pi R^2 L$, the electron number density, n_e, can be introduced which gives for the radial electric field:

$$E_r = -\frac{n_e e}{2\epsilon_0}. \tag{B.4}$$

The Brillouin limit given by eq. 7.1 gives the maximum density of an ideal electron plasma that

an axially symmetric magnetic field, B_z, can confine. Substituting this into the radial electric field gives:

$$E_r = -\frac{eB_z^2}{4m_e}r. \tag{B.5}$$

The magnetic field required for the Gabor lens can be related to that for a solenoid in order to achieve the same focusing. By substituting eq. 7.5 into the field, it allows us to relate the radial electric field to the magnetic field for a solenoid:

$$E_r = -\frac{eB_{\text{sol}}^2 Z\left(\frac{m_e}{m_i}\right)}{4m_e}r = -\frac{eB_{\text{sol}}^2}{4m_p}r. \tag{B.6}$$

Since it is assumed the plasma will be homogeneously distributed within the lens, there will be no electric field component in the longitudinal direction:

$$E_z = 0. \tag{B.7}$$

Appendix C

Considerations for the SmartPhantom

Some plans were drafted to construct a functional prototype of the SmartPhantom planes. It was found that a revision of the design would be needed.

One aspect to require revision is with regard to the design of the frame. A station consists of two frames to measure the two transverse axes. The frame itself must be sufficiently thin in order to fit into a water phantom. However, for a thin frame there are structural issue to be considered. As fibres are wound across the frame, they must be held taut with sufficient tension. But this tensioning could induce a bending in the frames depending on the frame material and thickness. Carbon fibre has a high stiffness making it an ideal material, but the square aperture on the frame (fig. 8.2) has a relatively small surface area for the fibres to adhere to, which may lead to the frame bending. To counteract this, a smaller circular aperture would help increase the surface area available, spreading out the force while keeping the frame thickness minimised. However, care would need to be taken as this may limit the usage of the SmartPhantom if the aperture is smaller than the beam size.

Another aspect to consider is how the fibres should adhere to the frame. Careful consideration for the material is needed to ensure the adhesive will not affect the performance of the fibres. Superglue for example could be used as an adhesive but can be quite brittle. In addition, superglue is detrimental to the cladding of the fibres. A good candidate for an adhesive is an epoxy resin. Although it can take time to cure, it can be applied to easily fill in the surface area of the frames. Different ratios of epoxy resin could also be combined together. After the initial layer cures, another mixture can be applied on top to ensure the fibre ends remain in place for alignment. This improves upon the initial design which considered using mylar to vacuum seal the fibres.

Consideration also needs to be made to exclude the exposed scintillating fibres from light, which

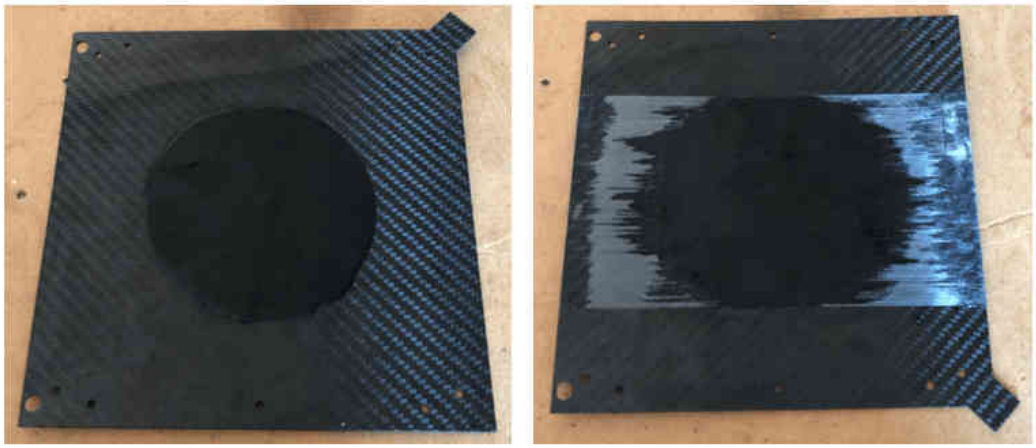

Figure C.1: Fishing wire prototype with the middle region filled with an epoxy resin with a black pigment added. The frames lack a recess for alignment and gluing.

had been neglected in the initial design. A possible solution is to use an epoxy resin mixture with a black pigment as was done for the fibre bundle. Care must be taken to minimise the amount of epoxy resin to minimise the effect on the energy deposition. Furthermore, the edges of the station would need to be covered or encased. A test with some fishing wire shows that filling the aperture region with a black resin was viable as seen in fig. C.1.

A final aspect considered was the alignment of scintillating fibres to clear fibres. An important part of the SmartPhantom is transporting light from the scintillating fibres to the clear fibres, and any misalignment would lead to signal losses. First the fibre ends would need to be polished to ensure optimal light transmission. To help with the alignment, the same number of fibres need to be wound on both the clear fibre connector and the frames. A jig was designed which could wind both components. Within the jig are two lobes with grooves onto which the fibres can be wound as seen in fig. C.2a. Ideally grooves could also be engineered into the carbon fibre connector and frames, but this would be difficult due to the material. An alternative method is to introduce a recess region to both the connector and frame as seen in fig. C.3. The introduction of a recess would also help with gluing the fibres to the frame without concerns about the resin spilling out the sides. The edges of the recess could also be used for alignment, with a finer adjustment possible with the alignment jig in fig. C.2b.

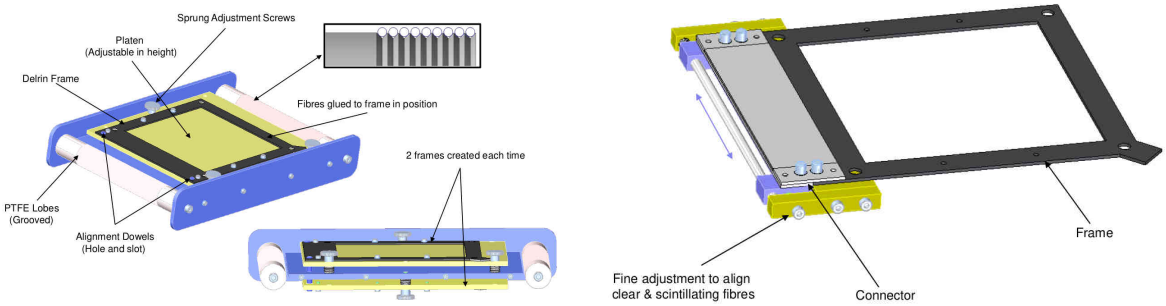

(a) Winding jig.

(b) Alignment jig.

Figure C.2: Schematic of the jigs designed to wind and align the SmartPhantom frames.

Figure C.3: Prototype clear fibre connector with a recess for the fibres to be winded.

Bibliography

[1] W. H. Organization, Cancer `https://www.who.int/news-room/fact-sheets/detail/cancer`. Accessed: 2021-09-13.

[2] B. Rachet, L. Ellis, C. Maringe, T. Chu, U. Nur, M. Quaresma, A. Shah, S. Walters, L. Woods, D. Forman, and M. P. Coleman, Socioeconomic inequalities in cancer survival in England after the NHS cancer plan *Br J Cancer*, vol. 103, pp. 446–453, Aug 2010.

[3] G. K. Singh and A. Jemal, Socioeconomic and Racial/Ethnic Disparities in Cancer Mortality, Incidence, and Survival in the United States, 1950-2014: Over Six Decades of Changing Patterns and Widening Inequalities *J Environ Public Health*, vol. 2017, p. 2819372, 2017.

[4] H. Sung, J. Ferlay, R. L. Siegel, M. Laversanne, I. Soerjomataram, A. Jemal, and F. Bray, Global Cancer Statistics 2020: GLOBOCAN Estimates of Incidence and Mortality Worldwide for 36 Cancers in 185 Countries *CA: A Cancer Journal for Clinicians*, vol. 71, no. 3, pp. 209–249, 2021, https://acsjournals.onlinelibrary.wiley.com/doi/pdf/10.3322/caac.21660.

[5] S. Siddique and J. C. L. Chow, Application of Nanomaterials in Biomedical Imaging and Cancer Therapy *Nanomaterials (Basel)*, vol. 10, Aug 2020.

[6] D. Cross and J. K. Burmester, Gene therapy for cancer treatment: past, present and future *Clin Med Res*, vol. 4, pp. 218–227, Sep 2006.

[7] R. Baskar, K. A. Lee, R. Yeo, and K. W. Yeoh, Cancer and radiation therapy: current advances and future directions *Int J Med Sci*, vol. 9, no. 3, pp. 193–199, 2012.

[8] H. Becquerel and P. Curie, Action physiologique des rayons du radium *Compt. Rend. Acad. Sci*, vol. 132, pp. 1289–1291, 1901.

[9] R. R. Wilson, Radiological Use of Fast Protons *Radiology*, vol. 47, no. 5, pp. 487–491, 1946. PMID: 20274616.

[10] V. M. Systems, FlashForward Consortium 2020. `https://www.varian.com/about-varian/research/flashforward-consortium`.

[11] D. Dewey and J. Boag, Modification of the oxygen effect when bacteria are given large pulses of radiation *Nature*, vol. 183, no. 4673, pp. 1450–1451, 1959.

[12] C. Town, Effect of high dose rates on survival of mammalian cells *Nature*, vol. 215, no. 5103, pp. 847–848, 1967.

[13] R. J. Berry, E. J. Hall, D. W. Forster, T. H. Storr, and M. J. Goodman, Survival of mammalian cells exposed to x rays at ultra-high dose-rates *The British journal of radiology*, vol. 42, no. 494, pp. 102–107, 1969.

[14] V. Favaudon, L. Caplier, V. Monceau, F. Pouzoulet, M. Sayarath, C. Fouillade, M. F. Poupon, I. Brito, P. Hupé, J. Bourhis, J. Hall, J. J. Fontaine, and M. C. Vozenin, Ultrahigh dose-rate FLASH irradiation increases the differential response between normal and tumor tissue in mice *Sci Transl Med*, vol. 6, p. 245ra93, Jul 2014.

[15] A. Dilmanian, Z. Zhong, T. Bacarian, H. Benveniste, P. Romanelli, R. Wang, J. Welwart, T. Yuasa, E. Rosen, and D. Anschel, Interlaced X-ray Microplanar Beams: A Radiosurgery Approach with Clinical Potential *Proceedings of the National Academy of Sciences of the United States of America*, vol. 103, pp. 9709–14, 07 2006.

[16] Y. Prezado and G. Fois, Proton-minibeam radiation therapy: A proof of concept *Medical physics*, vol. 40, p. 031712, 03 2013.

[17] Y. Prezado, G. Jouvion, D. Hardy, A. Patriarca, C. Nauraye, J. Bergs, W. Gonzalez, C. Guardiola, M. Juchaux, D. Labiod, R. Dendale, L. Jourdain, C. Sebrie, and F. Pouzoulet, Proton minibeam radiation therapy spares normal rat brain: Long-Term Clinical, Radiological and Histopathological Analysis OPEN *Scientific Reports*, vol. 7, 10 2017.

[18] W. Roentgen, Uber eine neue Art von Strahlen *Sitzungsber Phys Med Ges Wurtzburg*, vol. 9, pp. 132–141, 1895.

[19] D. Khiem, H. Ando, H. Matsuura, and M. Akiyoshi, Investigation of Characteristics of Low-energy X-ray Radiated from the Crookes Tube Used in Radiological Education vol. 18, pp. 9–15, 07 2019.

[20] E. L. Ginzton, W. W. Hansen, and W. R. Kennedy, A Linear Electron Accelerator *Review of Scientific Instruments*, vol. 19, no. 2, pp. 89–108, 1948, https://doi.org/10.1063/1.1741225.

[21] M. Baker, Medical linear accelerator celebrates 50 years of treating cancer `https://news.stanford.edu/news/2007/april18/med-accelerator-041807.html`. Accessed: 2021-09-15.

[22] D. Fry, R.-S. Harvie, L. Mullett, and W. Walkinshaw, Travelling-Wave Linear Accelerator for Electrons *Nature*, no. 160, pp. 351–353, 1947.

[23] D. I. Thwaites and J. B. Tuohy, Back to the future: the history and development of the clinical linear accelerator *Physics in Medicine and Biology*, vol. 51, pp. R343–R362, jun 2006.

[24] E. O. Lawrence and M. S. Livingston, The Production of High Speed Light Ions Without the Use of High Voltages *Phys. Rev.*, vol. 40, pp. 19–35, Apr 1932.

[25] E. L. Clark, K. Krushelnick, J. R. Davies, M. Zepf, M. Tatarakis, F. N. Beg, A. Machacek, P. A. Norreys, M. I. K. Santala, I. Watts, and A. E. Dangor, Measurements of Energetic Proton Transport through Magnetized Plasma from Intense Laser Interactions with Solids *Phys. Rev. Lett.*, vol. 84, pp. 670–673, Jan 2000.

[26] A. Maksimchuk, S. Gu, K. Flippo, D. Umstadter, and V. Y. Bychenkov, Forward Ion Acceleration in Thin Films Driven by a High-Intensity Laser *Phys. Rev. Lett.*, vol. 84, pp. 4108–4111, May 2000.

[27] R. A. Snavely, M. H. Key, S. P. Hatchett, T. E. Cowan, M. Roth, T. W. Phillips, M. A. Stoyer, E. A. Henry, T. C. Sangster, M. S. Singh, S. C. Wilks, A. MacKinnon, A. Offenberger, D. M. Pennington, K. Yasuike, A. B. Langdon, B. F. Lasinski, J. Johnson, M. D. Perry, and E. M. Campbell, Intense High-Energy Proton Beams from Petawatt-Laser Irradiation of Solids *Phys. Rev. Lett.*, vol. 85, pp. 2945–2948, Oct 2000.

[28] M. Borghesi, Laser-driven ion acceleration: State of the art and emerging mechanisms *Nuclear Instruments and Methods in Physics Research Section A: Accelerators, Spectrometers, Detectors and Associated Equipment*, vol. 740, pp. 6–9, 2014. Proceedings of the first European Advanced Accelerator Concepts Workshop 2013.

[29] F. Wagner, O. Deppert, C. Brabetz, P. Fiala, A. Kleinschmidt, P. Poth, V. Schanz, A. Tebartz, B. Zielbauer, M. Roth, T. Stöhlker, and V. Bagnoud, Maximum Proton Energy above 85 MeV from the Relativistic Interaction of Laser Pulses with Micrometer Thick CH 2 Targets *Physical Review Letters*, vol. 116, 05 2016.

[30] T. Esirkepov, M. Borghesi, S. V. Bulanov, G. Mourou, and T. Tajima, Highly Efficient Relativistic-Ion Generation in the Laser-Piston Regime *Phys. Rev. Lett.*, vol. 92, p. 175003, Apr 2004.

[31] A. Higginson *et al.*, Near-100 MeV protons via a laser-driven transparency-enhanced hybrid acceleration scheme *Nature Communications*, vol. 9, p. 724, 02 2018.

[32] M. Benedikt *et al.*, Overview of the MedAustron Design and Technology Choices *Conf. Proc.*, vol. C100523, p. MOPEA020, 2010.

[33] G. Aymar *et al.*, LhARA: The Laser-hybrid Accelerator for Radiobiological Applications *Frontiers in Physics*, vol. 8, p. 432, 2020.

[34] G. Aymar *et al.*, The Laser-hybrid Accelerator for Radiobiological Applications 2020, physics.acc-ph/2006.00493.

[35] CERN, MAD - Methodical Accelerator Design 2018.

[36] H. Wiedemann, *Particle Accelerator Physics*. Springer-Verlag Berlin Heidelberg, 2007.

[37] B. Collaboration, *BDSIM Documentation*. Royal Holloway, University of London.

[38] CERN, *CERN Accelerator School Fifth General Accelerator Physics Course*, (Geneva), CERN, 1994. 2 volumes, consecutive pagination.

[39] B. Muratori, J. Jones, and A. Wolski, Analytical expressions for fringe fields in multipole magnets *Physical Review Special Topics - Accelerators and Beams*, vol. 18, Jun 2015.

[40] V. Kain, Beam Dynamics and Beam Losses - Circular Machines 8 2016.

[41] V. Kumar, Understanding the focusing of charged particle beams in a solenoid magnetic field *American Journal of Physics*, vol. 77, no. 8, pp. 737–741, 2009, https://doi.org/10.1119/1.3129242.

[42] I. Hofmann, Performance of solenoids versus quadrupoles in focusing and energy selection of laser accelerated protons *Phys. Rev. ST Accel. Beams*, vol. 16, p. 041302, Apr 2013.

[43] M. Martini, An Introduction to transverse beam dynamics in accelerators 3 1996.

[44] W. Magnus and S. Winkler, *Hill's Equation*. Dover Publications, January 2004.

[45] J. Walecka, *Fundamentals of Statistical Mechanics*. World Scientific Publishing Co., November 2000.

[46] J. Buon, Beam phase space and emittance; rev. version p. 27 p, Feb 1992.

[47] K. Schindl, Space charge 2006.

[48] M. Ferrario, M. Migliorati, and L. Palumbo, Space Charge Effects 01 2016.

[49] S. H. Park and J. O. Kang, Basics of particle therapy I: physics *Radiat Oncol J*, vol. 29, pp. 135–146, Sep 2011.

[50] J. Allison *et al.*, Recent developments in Geant4 *Nuclear Instruments and Methods in Physics Research Section A: Accelerators, Spectrometers, Detectors and Associated Equipment*, vol. 835, pp. 186–225, 2016.

[51] E. Mladenov, S. Magin, A. Soni, and G. Iliakis, DNA double-strand break repair as determinant of cellular radiosensitivity to killing and target in radiation therapy *Front Oncol*, vol. 3, p. 113, 2013.

[52] B. B. Rossi, *High-energy particles*. Prentice-Hall physics series, New York, NY: Prentice-Hall, 1952.

[53] P. D. Group, Review of Particle Physics *Progress of Theoretical and Experimental Physics*, vol. 2020, August 2020, https://academic.oup.com/ptep/article-pdf/2020/8/083C01/34673722/ptaa104.pdf.

[54] C. Grupen, *Particle Detectors*. Cambridge University Press, March 2008.

[55] ICRU, Fundamental quantities and units for ionizing radiation, Report 85 *International Commission on Radiation Units and Measurements*, vol. 11, pp. 1–31, Apr 2011.

[56] ICRU, Linear Energy Transfer, Report 16 *International Commission on Radiation Units and Measurements*, June 1970.

[57] A. M. Kellerer, K. Hahn, and H. H. Rossi, Intermediate Dosimetric Quantities *Radiation Research*, vol. 130, no. 1, pp. 15–25, 1992.

[58] H. Paganetti, *Proton Therapy Physics*. CRC Press, November 2018.

[59] M. Berger, J. Coursey, M. Zucker, and J. Chang, ESTAR, PSTAR, and ASTAR:Computer Programs for Calculating Stopping-Power and Range Tables for Electrons, Protons, and Helium Ions 2005.

[60] *Radiation Oncology Physics*. Non-serial Publications, Vienna: International Atomic Energy Agency, 2005.

[61] W. H. B. M.A. and R. K. B.Sc., XXXIX. On the particles of radium, and their loss of range in passing through various atoms and molecules *The London, Edinburgh, and Dublin Philosophical Magazine and Journal of Science*, vol. 10, no. 57, pp. 318–340, 1905, https://doi.org/10.1080/14786440509463378.

[62] G. V. Dalrymple, I. R. Lindsay, J. D. Hall, J. C. Mitchell, J. J. Ghidoni, H. L. Kundel, and I. L. Morgan, The Relative Biological Effectiveness of 138-Mev Protons as Compared to Cobalt-60 Gamma Radiation *Radiation Research*, vol. 28, no. 2, pp. 489–506, 1966.

[63] H. Paganetti, N. A., M. Ancukiewicz, L. Gerweck, M. Goitein, J. Loeffler, and H. Suit, Relative biological effectiveness (RBE) values for proton beam therapy *International Journal of Radiation Oncology Biology Physics*, vol. 53, pp. 407–421, 2002.

[64] H. Paganetti, Relative biological effectiveness (RBE) values for proton beam therapy. Variations as a function of biological endpoint, dose, and linear energy transfer *Phys Med Biol*, vol. 59, pp. R419–472, Nov 2014.

[65] W. D. Newhauser and R. Zhang, The physics of proton therapy *Physics in Medicine and Biology*, vol. 60, pp. R155–R209, Mar 2015.

[66] M. Cianchetti, Sinonasal Malignancies and Charged Particle Radiation Treatment: A Systematic Literature Review *International journal of otolaryngology*, vol. 2012, p. 325891, 05 2012.

[67] U. Schneider and R. Hälg, The Impact of Neutrons in Clinical Proton Therapy *Front Oncol*, vol. 5, p. 235, 2015.

[68] P. Horton and D. Eaton, *Design and Shielding of Radiotherapy Treatment Facilities*. 2053-2563, IOP Publishing, 2017.

[69] G. Molière, Theorie der Streuung schneller geladener Teilchen II. Mehrfach- und Vielfachstreuung *Zeitschrift Naturforschung Teil A*, vol. 3, pp. 78–97, Feb. 1948.

[70] S. Striganov, Modified Moliere's screening parameter and its impact on multiple coulomb scattering in *12th Meeting of Task-Force on Shielding Aspects of Accelerators, Targets and Irradiation Facilities*, pp. 315–320, 2014.

[71] H. A. Bethe, Molière's Theory of Multiple Scattering *Phys. Rev.*, vol. 89, pp. 1256–1266, Mar 1953.

[72] U. Fano, Inelastic Collisions and the Molière Theory of Multiple Scattering *Phys. Rev.*, vol. 93, pp. 117–120, Jan 1954.

[73] A. O. Hanson, L. H. Lanzl, E. M. Lyman, and M. B. Scott, Measurement of Multiple Scattering of 15.7-Mev Electrons *Phys. Rev.*, vol. 84, pp. 634–637, Nov 1951.

[74] V. L. Highland, Some practical remarks on multiple scattering *Nuclear Instruments and Methods*, vol. 129, no. 2, pp. 497–499, 1975.

[75] B. Gottschalk, On the scattering power of radiotherapy protons *Medical Physics*, vol. 37, no. 1, pp. 352–367, 2010, https://aapm.onlinelibrary.wiley.com/doi/pdf/10.1118/1.3264177.

[76] B. Gottschalk, A. Koehler, R. Schneider, J. Sisterson, and M. Wagner, Multiple Coulomb scattering of 160 MeV protons *Nuclear Instruments and Methods in Physics Research Section B: Beam Interactions with Materials and Atoms*, vol. 74, no. 4, pp. 467–490, 1993.

[77] G. R. Lynch and O. I. Dahl, Approximations to multiple Coulomb scattering *Nuclear Instruments and Methods in Physics Research Section B: Beam Interactions with Materials and Atoms*, vol. 58, no. 1, pp. 6–10, 1991.

[78] D. R. Grimes, W. D. R., and M. Partridge, An approximate analytical solution of the Bethe equation for charged particles in the radiotherapeutic energy range *Scientific Reports*, 2017.

[79] R. Cambria, J. Hérault, N. Brassart, M. Silari, and P. Chauvel, Proton beam dosimetry: A comparison between the Faraday cup and an ionization chamber *Physics in Medicine and Biology*, vol. 42, pp. 1185–1196, jun 1997.

[80] L. H. Gray, An Ionization Method for the Absolute Measurement of γ-Ray Energy *Proceedings of the Royal Society of London. Series A, Mathematical and Physical Sciences*, vol. 156, no. 889, pp. 578–596, 1936.

[81] IAEA, Implementation of the International Code of Practice on Dosimetry in Radiotherapy (TRS 398): Review of testing results *International Atomic Energy Agency*, June 2005.

[82] L. V. Spencer and F. H. Attix, A Theory of Cavity Ionization *Radiation Research*, vol. 3, no. 3, pp. 239–254, 1955.

[83] T. Kato, Current Status of Dosimetry Tools for Clinical Proton Beams 2019.

[84] F. F. Chen, *Introduction to Plasma Physics and Controlled Fusion*. Springer US, 2 ed., 1984.

[85] P. Gibbon, Introduction to Plasma Physics in *CAS - CERN Accelerator School: Plasma Wake Acceleration*, (Geneva), pp. 51–65, CERN, 2016, 1705.10529.

[86] H. Schaub, G. Parker, and L. King, Coulomb Thrusting Application Study p. 120, 01 2006.

[87] A. L. Schawlow and C. H. Townes, Infrared and Optical Masers *Phys. Rev.*, vol. 112, pp. 1940–1949, Dec 1958.

[88] A. E. Siegman, *Lasers*. University Science Books, 1990.

[89] H. Takabe, *The Physics of Laser Plasmas and Applications - Volume 1*. Springer Series in Plasma Science and Technology, Spring,Cham, 2020.

[90] D. Strickland and G. Mourou, Compression of amplified chirped optical pulses *Optics Communications*, vol. 55, no. 6, pp. 447–449, 1985.

[91] M. Kaluza, J. Schreiber, M. I. K. Santala, G. D. Tsakiris, K. Eidmann, J. Meyer-ter Vehn, and K. J. Witte, Influence of the Laser Prepulse on Proton Acceleration in Thin-Foil Experiments *Phys. Rev. Lett.*, vol. 93, p. 045003, Jul 2004.

[92] D. Batani, R. Jafer, M. Veltcheva, R. Dezulian, O. Lundh, F. Lindau, A. Persson, K. Osvay, C.-G. Wahlström, D. C. Carroll, P. McKenna, A. Flacco, and V. Malka, Effects of laser prepulses on laser-induced proton generation *New Journal of Physics*, vol. 12, p. 045018, apr 2010.

[93] F. Wagner, C. Brabetz, O. Deppert, M. Roth, T. Stöhlker, A. Tauschwitz, A. Tebartz, B. Zielbauer, and V. Bagnoud, Accelerating ions with high-energy short laser pulses from submicrometer thick targets *High Power Laser Science and Engineering*, vol. 4, p. e45, 2016.

[94] S. Keppler, A. Sävert, J. Körner, M. Hornung, H. Liebetrau, J. Hein, and M. C. Kaluza, The generation of amplified spontaneous emission in high-power CPA laser systems *Laser & Photonics Reviews*, vol. 10, p. 264—277, March 2016.

[95] Földes, István B, Gilicze, Barnabás, Kovács, Zsolt, and Szatmári, Sándor, Plasma Mirrors for Cleaning Laser Pulses from the Infrared to the Ultraviolet *EPJ Web of Conferences*, vol. 167, p. 04001, 2018.

[96] S. Witte and K. S. E. Eikema, Ultrafast Optical Parametric Chirped-Pulse Amplification *IEEE Journal of Selected Topics in Quantum Electronics*, vol. 18, no. 1, pp. 296–307, 2012.

[97] P. Mora and T. M. Antonsen, Jr., Kinetic modeling of intense, short laser pulses propagating in tenuous plasmas *Physics of Plasmas*, vol. 4, no. 1, pp. 217–229, 1997, https://doi.org/10.1063/1.872134.

[98] V. Karanpreet, A review on self focusing in laser plasma interaction *Materials Today: Proceedings*, vol. 37, pp. 2786–2791, 2021. International Conference on Newer Trends and Innovation in Mechanical Engineering: Materials Science.

[99] M. Moll, M. Schlanges, T. Bornath, and V. P. Krainov, Inverse bremsstrahlung heating beyond the first Born approximation for dense plasmas in laser fields *New Journal of Physics*, vol. 14, p. 065010, jun 2012.

[100] W. Bang, G. Dyer, H. J. Quevedo, A. C. Bernstein, E. Gaul, J. Rougk, F. Aymond, M. E. Donovan, and T. Ditmire, Optimum laser intensity for the production of energetic deuterium ions from laser-cluster interaction *Physics of Plasmas*, vol. 20, no. 9, p. 093104, 2013, https://doi.org/10.1063/1.4821611.

[101] S. K. Rajouria, M. K. K K, and V. K. Tripathi, Nonlinear resonance absorption of laser in an inhomogeneous plasma *Physics of Plasmas*, vol. 20, no. 8, p. 083112, 2013, https://doi.org/10.1063/1.4818588.

[102] W. Kruer, *The Physics of Laser Plasma Interactions*. Westview Press, 2003.

[103] Y. Ping, R. Shepherd, B. F. Lasinski, M. Tabak, H. Chen, H. K. Chung, K. B. Fournier, S. B. Hansen, A. Kemp, D. A. Liedahl, K. Widmann, S. C. Wilks, W. Rozmus, and M. Sherlock, Absorption of Short Laser Pulses on Solid Targets in the Ultrarelativistic Regime *Phys. Rev. Lett.*, vol. 100, p. 085004, Feb 2008.

[104] F. Brunel, Not-so-resonant, resonant absorption *Phys. Rev. Lett.*, vol. 59, pp. 52–55, Jul 1987.

[105] H.-B. Cai, W. Yu, S.-P. Zhu, C.-Y. Zheng, L.-H. Cao, and W.-B. Pei, Vacuum heating in the interaction of ultrashort, relativistically strong laser pulses with solid targets *Physics of Plasmas*, vol. 13, no. 6, p. 063108, 2006, https://doi.org/10.1063/1.2206548.

[106] S. C. Wilks, W. L. Kruer, M. Tabak, and A. B. Langdon, Absorption of ultra-intense laser pulses *Phys. Rev. Lett.*, vol. 69, pp. 1383–1386, Aug 1992.

[107] W. L. Kruer and K. Estabrook, J×B heating by very intense laser light *The Physics of Fluids*, vol. 28, no. 1, pp. 430–432, 1985, https://aip.scitation.org/doi/pdf/10.1063/1.865171.

[108] S. C. Wilks, A. B. Langdon, T. E. Cowan, M. Roth, M. Singh, S. Hatchett, M. H. Key, D. Pennington, A. MacKinnon, and R. A. Snavely, Energetic proton generation in ultra-intense laser–solid interactions *Physics of Plasmas*, vol. 8, no. 2, pp. 542–549, 2001, https://doi.org/10.1063/1.1333697.

[109] L. Yin, B. J. Albright, B. M. Hegelich, and J. C. Fernández, GeV laser ion acceleration from ultrathin targets: The laser break-out afterburner *Laser and Particle Beams*, vol. 24, no. 2, p. 291–298, 2006.

[110] M. Roth and M. Schollmeier, Ion Acceleration - Target Normal Sheath Acceleration in *CAS - CERN Accelerator School: Plasma Wake Acceleration*, (Geneva), pp. 231–270, CERN, 2016, 1705.10569.

[111] K. Zeil, J. Metzkes, T. Kluge, M. Bussmann, T. Cowan, S. Kraft, R. Sauerbrey, and U. Schramm, Direct observation of prompt pre-thermal laser ion sheath acceleration *Nature communications*, vol. 3, p. 874, 06 2012.

[112] M. Passoni, L. Bertagna, and A. Zani, Target normal sheath acceleration: theory, comparison with experiments and future perspectives *New Journal of Physics*, vol. 12, p. 045012, apr 2010.

[113] S. Kumar and D. N. Gupta, Optimization of laser parameters for proton acceleration using double laser pulses in TNSA mechanism *Laser and Particle Beams*, vol. 38, no. 2, p. 73–78, 2020.

[114] H. Alfvén, On the Motion of Cosmic Rays in Interstellar Space *Phys. Rev.*, vol. 55, pp. 425–429, Mar 1939.

[115] J. Davies, The Alfvén limit revisited and its relevance to laser-plasma interactions *Laser and Particle Beams*, vol. 24, no. 2, p. 299–310, 2006.

[116] P. Mora, Plasma Expansion into a Vacuum *Phys. Rev. Lett.*, vol. 90, p. 185002, May 2003.

[117] P. Mora, Thin-foil expansion into a vacuum *Phys. Rev. E*, vol. 72, p. 056401, Nov 2005.

[118] T. Kluge, T. Cowan, A. Debus, U. Schramm, K. Zeil, and M. Bussmann, Electron Temperature Scaling in Laser Interaction with Solids *Phys. Rev. Lett.*, vol. 107, p. 205003, Nov 2011.

[119] J. Schreiber, F. Bell, F. Grüner, U. Schramm, M. Geissler, M. Schnürer, S. Ter-Avetisyan, B. M. Hegelich, J. Cobble, E. Brambrink, J. Fuchs, P. Audebert, and D. Habs, Analytical Model for Ion Acceleration by High-Intensity Laser Pulses *Phys. Rev. Lett.*, vol. 97, p. 045005, Jul 2006.

[120] M. Passoni and M. Lontano, Theory of Light-Ion Acceleration Driven by a Strong Charge Separation *Phys. Rev. Lett.*, vol. 101, p. 115001, Sep 2008.

[121] C. Perego, A. Zani, D. Batani, and M. Passoni, Extensive comparison among Target Normal Sheath Acceleration theoretical models *Nuclear Instruments and Methods in Physics Research Section A: Accelerators, Spectrometers, Detectors and Associated Equipment*, vol. 653, no. 1, pp. 89–93, 2011. Superstrong 2010.

[122] J. Derouillat, A. Beck, F. Pérez, T. Vinci, M. Chiaramello, A. Grassi, M. Flé, G. Bouchard, I. Plotnikov, N. Aunai, J. Dargent, C. Riconda, and M. Grech, Smilei : A collaborative, open-source, multi-purpose particle-in-cell code for plasma simulation *Computer Physics Communications*, vol. 222, pp. 351 – 373, 2018.

[123] A. Pukhov, Particle-In-Cell Codes for Plasma-based Particle Acceleration in *CAS - CERN Accelerator School: Plasma Wake Acceleration*, (Geneva), CERN, 2016, 1510.01071.

[124] A. Beck, J. Dérouillat, M. Lobet, A. Farjallah, F. Massimo, I. Zemzemi, F. Perez, T. Vinci, and M. Grech, Adaptive SIMD optimizations in particle-in-cell codes with fine-grain particle sorting 10 2018.

[125] T. Esirkepov, Exact charge conservation scheme for Particle-in-Cell simulation with an arbitrary form-factor *Computer Physics Communications*, vol. 135, no. 2, pp. 144–153, 2001.

[126] K. Yee and J. Chen, The finite-difference time-domain (FDTD) and the finite-volume time-domain (FVTD) methods in solving Maxwell's equations *IEEE Transactions on Antennas and Propagation*, vol. 45, no. 3, pp. 354–363, 1997.

[127] C. Birdsall and A. Langdon, *Plasma Physics via Computer Simulation*. CRC Press, 1991.

[128] R. Courant, K. Friedrichs, and H. Lewy, On the Partial Difference Equations of Mathematical Physics *IBM Journal of Research and Development*, vol. 11, no. 2, pp. 215–234, 1967.

[129] A. Degiovanni and U. Amaldi, History of hadron therapy accelerators *Physica Medica*, vol. 31, no. 4, pp. 322–332, 2015.

[130] R. Jones and O. Lodge, The Discovery of a Bullet Lost in the Wrist by Means of the Roentgen Rays *The Lancet*, vol. 147, no. 3782, pp. 476–477, 1896. Originally published as Volume 1, Issue 3782.

[131] T. C. Evans, X-Ray Treatment-Its Origin, Birth and Early History. Emil H. Grubbe *The Quarterly Review of Biology*, vol. 26, no. 2, pp. 223–223, 1951, https://doi.org/10.1086/398163.

[132] L. Freund, *Elements of general radio-therapy for practitioners*. Rebman, 1904.

[133] R. H. Varian and S. F. Varian, A High Frequency Oscillator and Amplifier *Journal of Applied Physics*, vol. 10, no. 5, pp. 321–327, 1939, https://doi.org/10.1063/1.1707311.

[134] R. Wideröe, Über ein neues Prinzip zur Herstellung hoher Spannungen *Archiv für Elektrotechnik*, no. 21, pp. 387–406, 1928.

[135] J. H. Lawrence, P. C. Aebersold, and E. O. Lawrence, Comparative Effects of X-Rays and Neutrons on Normal and Tumor Tissue *Proceedings of the National Academy of Sciences*, vol. 22, no. 9, pp. 543–557, 1936, https://www.pnas.org/content/22/9/543.full.pdf.

[136] V. Ullmann, Microworld particles, their origin, properties and application in research and technology `https://astronuclphysics.info/JadRadFyzika5.htm`. Accessed: 2021-10-15.

[137] H. Owen, A. Lomax, and S. Jolly, Current and future accelerator technologies for charged particle therapy *Nuclear Instruments and Methods in Physics Research Section A: Accelerators, Spectrometers, Detectors and Associated Equipment*, vol. 809, pp. 96–104, 2016. Advances in detectors and applications for medicine.

[138] U. Amaldi, P. Berra, K. Crandall, D. Toet, M. Weiss, R. Zennaro, E. Rosso, B. Szeless, M. Vretenar, C. Cicardi, C. De Martinis, D. Giove, D. Davino, M. Masullo, and V. Vaccaro, LIBO—a linac-booster for protontherapy: construction and tests of a prototype *Nuclear Instruments and Methods in Physics Research Section A: Accelerators, Spectrometers, Detectors and Associated Equipment*, vol. 521, no. 2, pp. 512–529, 2004.

[139] P. Berra, Design, construction and tests of a 3 GHz proton linac booster (LIBO) for cancer therapy 2007, 0712.0830.

[140] C. De Martinis, D. Giove, U. Amaldi, P. Berra, K. Crandall, M. Mauri, M. Weiss, R. Zennaro, E. Rosso, B. Szeless, M. Vretenar, M. Masullo, V. Vaccaro, L. Calabretta, and A. Rovelli, Acceleration tests of a 3GHz proton linear accelerator (LIBO) for hadrontherapy *Nuclear Instruments and Methods in Physics Research Section A: Accelerators, Spectrometers, Detectors and Associated Equipment*, vol. 681, pp. 10–15, 2012.

[141] D. Ungaro, A. Degiovanni, and P. Stabile, LIGHT: A Linear Accelerator for Proton Therapy p. FRB1IO02. 5 p, 2017.

[142] K. R. Symon, D. W. Kerst, L. W. Jones, L. J. Laslett, and K. M. Terwilliger, Fixed-Field Alternating-Gradient Particle Accelerators *Phys. Rev.*, vol. 103, pp. 1837–1859, Sep 1956.

[143] M. Craddock and K. Symon, Cyclotrons and Fixed-Field Alternating-Gradient Accelerators *Reviews of Accelerator Science and Technology*, vol. 01, 12 2008.

[144] K. R. Symon, D. W. Kerst, L. W. Jones, L. J. Laslett, and K. M. Terwilliger, Fixed-Field Alternating-Gradient Particle Accelerators *Phys. Rev.*, vol. 103, pp. 1837–1859, Sep 1956.

[145] M. Aiba, Y. Mori, R. Muramatsu, C. Ohmori, I. Sakai, Y. Sato, A. Takagi, R. Ueno, T. Yokoi, M. Yoshimoto, and Y. Yuasa, DEVELOPMENT OF A FFAG PROTON SYNCHROTRON 2000.

[146] S. Machida, Y. Mori, K. Mishima, S. Shiroya, M. Tanigaki, S. Fukumoto, Y. Ishi, and M. Inoue, Construction of FFAG Accelerators in KURRI for ADS Study *Conf. Proc. C*, vol. 0505161, p. 350, 2005.

[147] R. Barlow *et al.*, EMMA—The world's first non-scaling FFAG *Nuclear Instruments and Methods in Physics Research Section A: Accelerators, Spectrometers, Detectors and Associated Equipment*, vol. 624, no. 1, pp. 1–19, 2010.

[148] S. Machida, R. Barlow, J. Berg, N. Bliss, R. Buckley, J. Clarke, M. Craddock, R. Edgecock, J. Garland, Y. Giboudot, P. Goudket, S. Griffiths, C. Hill, S. Hill, K. Hock, D. Holder, M. Ibi-

son, F. Jackson, S. Jamison, and T. Yokoi, Acceleration in the linear non-scaling fixed-field alternating-gradient accelerator EMMA *Nature Physics*, vol. 8, pp. 243–247, 01 2012.

[149] K. Peach *et al.*, PAMELA Overview and Status *Conf. Proc. C*, vol. 100523, p. MOPEA021, 2010.

[150] R. Appleby, J. Garland, H. Owen, S. Tygier, and K. Hock, NORMA - The Normal-Conducting, Scaling Racetrack FFAG in *5th International Particle Accelerator Conference*, 7 2014.

[151] S. M. Wiggins *et al.*, Application programmes at the Scottish Centre for the Application of Plasma-based Accelerators (SCAPA) in *Relativistic Plasma Waves and Particle Beams as Coherent and Incoherent Radiation Sources III* (D. A. Jaroszynski and M. Hur, eds.), vol. 11036, pp. 93 – 103, International Society for Optics and Photonics, SPIE, 2019.

[152] K. Zeil *et al.*, Dose-controlled irradiation of cancer cells with laser-accelerated proton pulses *Appl. Phys. B*, vol. 110, pp. 1–8, 03 2012.

[153] M. Siebold *et al.*, PENELOPE: a high peak-power diode-pumped laser system for laser-plasma experiments in *High-Power, High-Energy, and High-Intensity Laser Technology; and Research Using Extreme Light: Entering New Frontiers with Petawatt-Class Lasers* (G. Korn, L. O. Silva, and J. Hein, eds.), vol. 8780, pp. 31 – 44, International Society for Optics and Photonics, SPIE, 2013.

[154] D. Margarone *et al.*, ELIMAIA: A Laser-Driven Ion Accelerator for Multidisciplinary Applications *Quantum Beam Science*, vol. 2, Apr. 2018.

[155] P. Mckenna, M. Borghesi, D. Neely, Z. Najmudin, M. Zepf, and K. Prise, Progress in Laser-Driven Ion Acceleration towards Applications in Radiotherapy 06 2014.

[156] T. R. C. of Radiologists, Radiotherapy Dose Fractionation Third Edition 2019.

[157] R. Leroy, N. Benahmed, F. Hulstaert, F. Mambourg, N. Fairon, E. Van Eycken, and D. Ruysscher, Hadron therapy in children – an update of the scientific evidence for 15 paediatric cancers. 01 2015.

[158] L. Badano *et al.*, Proton-Ion Medical Machine Study (PIMMS), 1 p. 232 p, Mar 1999.

[159] M.T.F.Pivi *et al.*, Status of the Carbon Commissioning and Roadmap Projects of the MedAustron Ion Therapy Center Accelerator May 2019.

[160] A. Maillot, W. Rupprecht, A. Wastl, and U. P., MA-004929-a-AMA-v4.2_Master_Layout_160420 2020.

[161] E. Sargsyan, MedAustron Injector Design Report Tech. Rep. 1.0, ebg MedAustron, September 2010.

[162] M. Vretenar, The radio-frequency quadrupole in *Proceedings, CERN Accelerator School on High Power Hadron Machines (CAS 2011): Bilbao, Spain, May 24-June 02, 2011*, pp. 207–223, 2013, 1303.6762. [,207(2013)].

[163] P. Bryant and U. Dorda, MedAustron Synchrotron Design Report Tech. Rep. 1.1, ebg MedAustron, October 2010.

[164] P. Bryant and U. Dorda, MedAustron MEBT Design Report Tech. Rep. 1.1, ebg MedAustron, October 2010.

[165] P. Bryant and U. Dorda, MedAustron HEBT Design Report Tech. Rep. 1.4, ebg MedAustron, November 2010.

[166] M. Feurstein, A. Gyorgy, A. Kerschbaum, F. Osmic, M. Repovz, S. M. Schwarz, and G. Burtin, Overview of the Beam Diagnostics in the MedAustron Accelerator: Design Choices and Test Beam Commissioning *Conf. Proc. C*, vol. 1205201, pp. 774–776, 2012.

[167] S. Tuma, J. Dedič, M. Klun, L. Šepetavc, A. Kerschbaum, F. Osmić, M. Repovž, and J. Sanchez Arias, Integration of Beam Diagnostics Devices for a Therapy Accelerator in *5th International Particle Accelerator Conference*, 7 2014.

[168] M. Repovz, A. Gyorgy, A. Kerschbaum, F. Osmic, S. Schwarz, M. Gmbh, W. Neustadt, A. Burtin, and G. Switzerland, Profile Grid Monitor and First Measurement Results at the MedAustron Accelerator 09 2013.

[169] S. Giordanengo, M. A. Garella, F. Marchetto, F. Bourhaleb, M. Ciocca, A. Mirandola, V. Monaco, M. A. Hosseini, C. Peroni, R. Sacchi, R. Cirio, and M. Donetti, The CNAO dose delivery system for modulated scanning ion beam radiotherapy *Medical Physics*, vol. 42, no. 1, pp. 263–275, 2015, https://aapm.onlinelibrary.wiley.com/doi/pdf/10.1118/1.4903276.

[170] F. Schmidt, E. Forest, and E. McIntosh, Introduction to the polymorphic tracking code: Fibre bundles, polymorphic taylor types and exact tracking 7 2002.

[171] S. Skelton, Multi-quadrupole scan for emittance determination at PITZ tech. rep., University of St Andrews, Scotland, 2007.

[172] P. J. Bryant *et al.*, Proton-Ion Medical Machine Study (PIMMS), 2 8 2000.

[173] A. Garonna *et al.*, Status of Proton Beam Commissioning of the MedAustron Particle Therapy Accelerator 06 2016.

[174] E. Farina, P. Piersimoni, C. Riccardi, A. Rimoldi, A. Tamborini, and M. Ciocca, Geant4 simulation for a study of a possible use of carbon ion pencil beams for the treatment of ocular melanomas with the active scanning system at CNAO *Journal of Physics: Conference Series*, vol. 664, no. 7, p. 072048, 2015.

[175] L. Grevillot, T. Frisson, N. Zahra, D. Bertrand, F. Stichelbaut, N. Freud, and D. Sarrut, Optimization of GEANT4 settings for Proton Pencil Beam Scanning simulations using GATE *Nuclear Instruments and Methods in Physics Research Section B: Beam Interactions with Materials and Atoms*, vol. 268, pp. 3295–3305, 10 2010.

[176] J. Rambo Sølie, H. E. Seime Pettersen, I. Meric, O. Harald Odland, H. Helstrup, and D. Röhrich, A comparison of proton ranges in complex media using GATE/Geant4, MCNP6 and FLUKA *arXiv e-prints*, p. arXiv:1708.00668, Aug. 2017, 1708.00668.

[177] L. Adler, Implementation of emittance and transmission measurement and analysis procedures along the MedAustron accelerator Master's thesis, Technischen Universität Wien, 12 2018.

[178] MedAustron, Cause-Effect Analysis on MAPTA Industrial Device Component Systems Tech. Rep. DD050_ MAPTA_ 1807181, MedAustron. 3.0.

[179] P. Bryant, AGILE, a tool for interactive lattice design in *7th European Particle Accelerator Conference (EPAC 2000)*, pp. 1357–1359, 7 2000.

[180] H. Lau, A. D. Franco, and R. Filippini, Effectiveness of the Collimator downstream the Chopper to Intercept the Carbon Ions Beam tech. rep., MedAustron, December 2018.

[181] R. M. de Kruijff, FLASH radiotherapy: ultra-high dose rates to spare healthy tissue *Int J Radiat Biol*, vol. 96, pp. 419–423, 04 2020.

[182] J. R. Hughes and J. L. Parsons, FLASH Radiotherapy: Current Knowledge and Future Insights Using Proton-Beam Therapy *Int J Mol Sci*, vol. 21, Sep 2020.

[183] J. Hendry, Taking Care with FLASH Radiation Therapy *Int J Radiat Oncol Biol Phys*, vol. 107, pp. 239–242, 06 2020.

[184] P. Lansonneur, H. Mammar, C. Nauraye, A. Patriarca, E. Hierso, R. Dendale, Y. Prezado, and L. De marzi, First proton minibeam radiation therapy treatment plan evaluation *Scientific Reports*, vol. 10, p. 7025, 04 2020.

[185] L. Torrisi, L. Calcagno, M. Cutroneo, J. Badziak, M. Rosinski, A. Zaras-Szydlowska, and A. Torrisi, Nanostructured targets for TNSA laser ion acceleration *Nukleonika*, vol. 61, 06 2016.

[186] M. Passoni, A. Sgattoni, I. Prencipe, L. Fedeli, D. Dellasega, L. Cialfi, I. W. Choi, I. J. Kim, K. A. Janulewicz, H. W. Lee, J. H. Sung, S. K. Lee, and C. H. Nam, Toward high-energy laser-driven ion beams: Nanostructured double-layer targets *Phys. Rev. Accel. Beams*, vol. 19, p. 061301, Jun 2016.

[187] M. Gauthier, C. B. Curry, S. Göde, F.-E. Brack, J. B. Kim, M. J. MacDonald, J. Metzkes, L. Obst, M. Rehwald, C. Rödel, H.-P. Schlenvoigt, W. Schumaker, U. Schramm, K. Zeil, and S. H. Glenzer, High repetition rate, multi-MeV proton source from cryogenic hydrogen jets *Applied Physics Letters*, vol. 111, no. 11, p. 114102, 2017, https://doi.org/10.1063/1.4990487.

[188] D. Gabor, A Space-Charge Lens for the Focusing of Ion Beams *Nature*, vol. 160, pp. 89–90, 1947.

[189] H. Lau, Gabor Lens Theory and Mathematica Results CCAP-TN-ACCL 1, Imperial College London, March 2018.

[190] J. Pozimski and M. Aslaninejad, Gabor lenses for capture and energy selection of laser driven ion beams in cancer treatment, *Laser and Particle Beams*, vol. 31, no. 4, pp. 723 – 733, 2013.

[191] P. Posocco, J. Pozimski, Y. Xia, and M. Merchant, First Test of The Imperial College Gabor (Plasma) Lens prototype at the Surrey Ion Beam centre in *Proceedings of the 7th International Particle Accelerator Conference (IPAC 2016)*, pp. 1598–1600, Medical Research Council (MRC), Joint Accelerator Conferences, 2016.

[192] K. Schulte, M. Droba, O. Meusel, U. Ratzinger, A. Adonin, R. Berezov, R. Hollinger, and J. Pfister, Gabor Lens Performance Studies at the GSI High Current Test Injector in *4th International Particle Accelerator Conference*, 6 2013.

[193] J. Palkovic, F. Mills, C. Schmidt, and D. Young, Gabor lens focusing of a negative ion beam pp. 304 – 306 vol.1, 04 1989.

[194] O. Meusel, M. Droba, B. Glaeser, and K. Schulte, Experimental studies of stable confined electron clouds using Gabor lenses *Conf. Proc. C*, vol. 1206051, pp. 157–160, 2013, 1309.4654.

[195] J. S. T. Ng *et al.*, Observation of plasma focusing of a 28.5-GeV positron beam *Phys. Rev. Lett.*, vol. 87, p. 244801, 2001, physics/0110015.

[196] C. Joshi, B. Blue, C. E. Clayton, E. Dodd, C. Huang, K. A. Marsh, W. B. Mori, S. Wang, M. J. Hogan, C. O'Connell, R. Siemann, D. Watz, P. Muggli, T. Katsouleas, and S. Lee, High energy density plasma science with an ultrarelativistic electron beam *Physics of Plasmas*, vol. 9, no. 5, pp. 1845–1855, 2002, https://doi.org/10.1063/1.1455003.

[197] Tech-X, VSim for Plasma `https://txcorp.com/vsim/`. Accessed: 2021-08-17.

[198] C. Carli, T. D'Amico, O. Grobner, M. Martini, and E. Wildner, Beam Optics: A program for analytical beam optics 8 1998.

[199] *Applications of the General Particle Tracer Code*, 1996.

[200] P.-F. P.-T. W. D. P. GmbH, Ionizing Radiation Detectors `https://www.ptwdosimetry.com/fileadmin/user_upload/DETECTORS_Cat_en_16522900_12/blaetterkatalog/blaetterkatalog/pdf/complete.pdf`, 2019/2020. Accessed: 2020-09-23.

[201] A. Kurup, Diagnostics for LhARA 2019.

[202] S. Hickling, L. Xiang, K. C. Jones, K. Parodi, W. Assmann, S. Avery, M. Hobson, and I. El Naqa, Ionizing radiation-induced acoustics for radiotherapy and diagnostic radiology applications *Med Phys*, vol. 45, pp. e707–e721, Jul 2018.

[203] A. Jathoul, J. Laufer, O. Ogunlade, B. Treeby, B. Cox, E. Zhang, P. Johnson, A. Pizzey, B. Philip, T. Marafioti, M. Lythgoe, R. Pedley, M. Pule, and P. Beard, Deep in vivo photoacoustic imaging of mammalian tissues using a tyrosinase-based genetic reporter *Nature Photonics*, vol. 9, p. 239, 03 2015.

[204] S. Kellnberger, W. Assmann, S. Lehrack, S. Reinhardt, P. Thirolf, D. Queirós, G. Sergiadis, G. Dollinger, K. Parodi, and V. Ntziachristos, Ionoacoustic tomography of the proton Bragg peak in combination with ultrasound and optoacoustic imaging *Scientific reports*, vol. 6, p. 29305, 07 2016.

[205] S. Sinigardi, J. Babaei, and G. Turchetti, TNSA proton maximum energy laws for 2D and 3D PIC simulations *Nuclear Instruments and Methods in Physics Research Section A: Accelerators, Spectrometers, Detectors and Associated Equipment*, vol. 909, pp. 438 – 440, 2018. 3rd European Advanced Accelerator Concepts workshop (EAAC2017).

[206] K. D. Xiao, C. T. Zhou, K. Jiang, Y. C. Yang, R. Li, H. Zhang, B. Qiao, T. W. Huang, J. M. Cao, T. X. Cai, M. Y. Yu, S. C. Ruan, and X. T. He, Multidimensional effects on proton acceleration using high-power intense laser pulses *Physics of Plasmas*, vol. 25, no. 2, p. 023103, 2018, https://doi.org/10.1063/1.5003619.

[207] J. Babaei, L. A. Gizzi, P. Londrillo, S. Mirzanejad, T. Rovelli, S. Sinigardi, and G. Turchetti, Rise time of proton cut-off energy in 2D and 3D PIC simulations *Physics of Plasmas*, vol. 24, no. 4, p. 043106, 2017, https://doi.org/10.1063/1.4979901.

[208] A. Sgattoni, P. Londrillo, A. Macchi, and M. Passoni, Laser ion acceleration using a solid target coupled with a low-density layer *Phys. Rev. E*, vol. 85, p. 036405, Mar 2012.

[209] N. P. Dover *et al.*, Effect of Small Focus on Electron Heating and Proton Acceleration in Ultrarelativistic Laser-Solid Interactions *Phys. Rev. Lett.*, vol. 124, no. 8, p. 084802, 2020.

[210] M. Afshari, J. Hornung, A. Kleinschmidt, P. Neumayer, D. Bertini, and V. Bagnoud, Proton acceleration via the TNSA mechanism using a smoothed laser focus *AIP Advances*, vol. 10, no. 3, p. 035023, 2020, https://doi.org/10.1063/1.5117236.

[211] P. Antici, E. Boella, S. Chen, D. Andrews, M. Barberio, J. Boeker, F. Cardelli, J. Feugeas, M. Glesser, P. Nicolaï, L. Romagnani, M. Scisciò, M. Starodubtsev, O. Willi, J. C. Kieffer, H. Pépin, L. Silva, E. D'Humières, and J. Fuchs, Acceleration of collimated 45 MeV protons by collisionless shocks driven in low-density, large-scale gradient plasmas by a 10^{20} W/cm^2, 1 micron wavelength laser *Scientific Reports*, vol. 7, 11 2017.

[212] E. Boella, Progress towards 3D simulations of laser-target interactions 2021.

[213] T. Zickler, Basic design and engineering of normal-conducting, iron-dominated electromagnets in *CERN Accelerator School: Course on Magnets*, 3 2011, 1103.1119.

[214] PTW, *User Manual Water Phantom T41023.* PTW-Freiburg Physikalisch-Technische Werkstatten Dr. Pychlau GmbH, Freiburg, Germany, d738.131.00/02 en ed., 9 2009.

[215] L. Archambault, J. C. Polf, L. Beaulieu, and S. Beddar, Characterizing the response of miniature scintillation detectors when irradiated with proton beams *Phys Med Biol*, vol. 53, pp. 1865–1876, Apr 2008.

[216] J. Birks, *The Theory and Practice of Scintillation Counting.* Pergamon Press, January 1964.

[217] T. Bortfeld, An analytical approximation of the Bragg curve for therapeutic proton beams *Medical Physics*, vol. 24, no. 12, pp. 2024–2033, 1997, https://aapm.onlinelibrary.wiley.com/doi/pdf/10.1118/1.598116.

[218] S. Tuomanen, V. Moskvin, and J. Farr, SU-F-T-144: Analytical Closed Form Approximation for Carbon Ion Bragg Curves in Water *Medical Physics*, vol. 43, pp. 3495–3495, 06 2016.

[219] L. Kelleter and S. Jolly, A mathematical expression for depth-light curves of therapeutic proton beams in a quenching scintillator *Medical Physics*, vol. 47, no. 5, pp. 2300–2308, 2020, https://aapm.onlinelibrary.wiley.com/doi/pdf/10.1002/mp.14099.

[220] Saint-Gobain, Scintillating Fiber `https://www.crystals.saint-gobain.com/products/scintillating-fiber`. Accessed: 2021-09-01.

[221] T. FLIR, Chameleon3 USB3 `https://www.flir.co.uk/products/chameleon3-usb3/`. Accessed: 2021-09-01.